Triply-Resonant Cavity-Enhanced Spontaneous Parametric Down-Conversion

Dissertation

zur Erlangung des akademischen Grades

doctor rerum naturalium

(Dr. rer. nat.)

im Promotionsfach Physik

eingereicht an der
Mathematisch-Naturwissenschaftlichen Fakultät
der Humboldt-Universität zu Berlin

von

Dipl.-Phys. Andreas Ahlrichs

Präsidentin der Humboldt-Universität zu Berlin:
Prof. Dr.-Ing. Dr. Sabine Kunst

Dekan der Mathematisch-Naturwissenschaftlichen Fakultät:
Prof. Dr. Elmar Kulke

Gutachter: 1. Prof. Dr. Benson
2. Prof. Dr. Jürgen Eschner
3. Prof. Dr. Günter Steinmeyer

Tag der mündlichen Prüfung: 14. Juni 2019

Licence

Erklärung

Hiermit erkläre ich, die Dissertation selbstständig und nur unter Verwendung der angegebenen Hilfen und Hilfsmittel angefertigt zu haben. Ich habe mich anderwärts nicht um einen Doktorgrad beworben und besitze einen entsprechenden Doktorgrad nicht. Ich erkläre die Kenntnisnahme der dem Verfahren zugrunde liegenden Promotionsordnung der Mathematisch-Naturwissenschaftlichen Fakultät der Humboldt-Universität zu Berlin vom 06. Juli 2009.

Berlin, den 01.03.2019 Andreas Ahlrichs

Abstract

The consistent generation of single photons with well-defined properties in all degrees of freedom is crucial for the development of photonic quantum technologies. Today, the most prominent sources of single photons are based on the process of spontaneous parametric down-conversion (SPDC) where a pump photon spontaneously decays into a pair of signal and idler photons inside a nonlinear medium.

Cavity-enhanced SPDC, i.e., placing the nonlinear medium inside an optical cavity, is widely used to build photon-pair sources with increased brightness and tailored spectral properties. This spectral tailoring by selective adjustment of the cavity parameters is of particular importance for hybrid quantum technologies which seek to combine dissimilar quantum systems in a way that their advantages complement each other.

This thesis provides a comprehensive theoretical and experimental analysis of triply-resonant cavity-enhanced SPDC. We improve the theoretical model found in the literature such that the influence of all resonator properties on the important experimental parameters (e.g., the generation rate) can be analyzed in detail. This convenient and highly accurate model of cavity-enhanced SPDC represents an important basis for the design and optimization of novel photon-pair sources.

The experimental part of this thesis presents the setup and characterization of a triply-resonant photon-pair source. We describe the digital control system used to operate this source over days without manual intervention, and we present a highly stable, narrow-linewidth monochromator based on cascaded, polarization-independent monolithic Fabry-Pérot cavities.

Utilizing these temperature-stabilized cavities as a spectrum analyzer, we verify, for the first time, the frequency comb spectral structure of photons generated by cavity-enhanced SPDC. We further simulate and measure the impact of the pump resonance on the temporal wave-packets and the two-photon interference of signal and idler photons.

Finally, we present a series of experiments in the context of hybrid quantum networks where we employ quantum frequency conversion (QFC) to transfer the generated signal photons into the telecommunication band. We verify the preservation of the temporal wave-packet upon QFC and highlight how quantum networks can benefit from advanced commercial telecommunication technologies.

Zusammenfassung

Die verlässliche Erzeugung einzelner Photonen mit wohldefinierten Eigenschaften in allen Freiheitsgraden ist entscheidend für die Entwicklung photonischer Quantentechnologien. Derzeit basieren die wichtigsten Einzelphotonenquellen auf dem Prozess der spontanen parameterischen Fluoreszenz (SPF), bei dem ein Pumpphoton in einem nichtlinearen Medium spontan in ein Paar aus Signal- und Idlerphotonen zerfällt.

Resonator-überhöhte SPF, also das Plazieren des nichtlinearen Mediums in einem optischen Resonator, ist ein weit verbreitetes Verfahren, um Einzelphotonenquellen mit erhöhter Helligkeit und angepassten spektralen Eigenschaften zu konstruieren. Das Anpassen der spektralen Eigenschaften durch gezielte Auswahl der Resonatoreigenschaften ist besonders für hybride Quantentechnologien von Bedeutung, welche darauf abzielen, unterschiedliche Quntensysteme so zu kombinieren, dass sich deren Vorteile ergänzen.

Diese Arbeit stellt eine umfassende theoretische und experimentelle Analyse der dreifach resonanten SPF vor. Das aus der Literatur bekannte theoretische Modell wird diesbezüglich verbessert, dass der Einfluss sämtlicher Eigenschaften des Resonators auf die wichtigen experimentellen Größen (z.B. die Erzeugungsrate) gezielt ausgewertet werden kann. Dieses verbesserte und hoch genaue Modell stellt eine wichtige Grundlage für die Entwicklung und Optimierung neuartiger Photonenpaarquellen dar.

Im experimentellen Teil dieser Arbeit wird der Aufbau und die Charakterisierung einer dreifach resonanten Photonenpaarquellen präsentiert. Die neu entwickelte digitale Regelelektronik sowie ein hochstabiler, schmalbandiger Monochromator welcher auf monolitischen, polarisationsunabhängigen Fabry-Pérot Resonatoren basiert, werden vorgestellt.

Indem diese temperaturstabilisierten Resonatoren als Spetrumanalysator verwendet werden, wird zum ersten Mal die Frequenzkammstruktur des Spektrums der erzeugten Signal- und Idlerphotonen nachgewiesen. Des Weiteren wird der Einfluss der Pumpresonanz auf die Korrelationsfunktion und die Zweiphotoneninterferenz von Signal- und Idlerphotonen simuliert und vermessen.

Abschließend werden Experimente aus dem Bereich der hybriden Quantennetzwerke präsentiert, in welchen Quantenfrequenzkonversion verwendet wird um die erzeugten Signalphotonen in das Telekommunikationsband zu transferieren. Dabei wird nachgewiesen, dass das temporale Wellenpaket durch die Konversion nicht beeinflusst wird und aufgezeigt, wie Quantennetzwerke von kommerziellen Telekommunikationstechnologien profitieren können.

Contents

List of Figures

List of Abbreviations

ADC analog to digital converter

AMP amplifier

APD avalanche photodiode

AR anti reflection (coating)

AWG arbitrary waveform generator

BP bandpass (filter)

BS beam splitter

CIRC circulator

DAC digital to analog converter

DM dichroic mirror

FBG fiber Bragg grating

FC filter cavity

FM flat mirror

FPGA field-programmable gate array

FSR free spectral range

FWHM full width at half maximum

HOM Hong-Ou-Mandel

HR high-reflection (coating)

HWP half-wave plate

IRF instrument response function

JSA joint spectral amplitude

KTP potassium titanyl phosphate

LIN linear polarizer

LP lowpass (filter)

MZM Mach-Zehnder modulator

OPO optical parametric oscillator

PBS polarizing beam splitter

PD photodiode

PMF polarization-maintaining fiber

PPKTP periodically poled potassium titanly phosphate

PZT piezo-electric transducer

QFC quantum frequency conversion

QWP quarter-wave plate

RMS root mean squared

SHG second harmonic generation

SMF single-mode fiber

SNR signal-to-noise ratio

SP shortpass (filter)

SPD single-photon detector

SPDC spontaneous parametric down-conversion

SSPD superconducting single-photon detector

TA tapered amplifier

TCSPC time-correlated single-photon counting

WG waveguide

Introduction

In recent years, enormous progress has been made in the field of quantum technology.[1] After a period of steady progress towards major goals in quantum computing, quantum simulation, quantum communication, and quantum-enhanced sensing, quantum technology has arrived at a stage where the transition from basic research to applied science is eminent. Governments all around the world recently are launching large research programs to promote quantum technologies. The most prominent field, namely quantum computation, has gained much public attention since large multinational companies have teamed up with research institutes in the development of quantum computers and have invested heavily in this field.

In quantum computing, the most promising technologies[2–4] have recently taken important steps towards scaling laboratory setups to larger qubit numbers and towards fault tolerant computations.[5–7] The science community vividly discusses whether the next generation of quantum computers can outperform classical super computers in certain computational tasks.[8–13] The related field of quantum simulation also profits from the upscaling of the experimental setups to larger qubit numbers.[14,15]

Current experiments in the field of quantum sensing[16] show how the revolutionary developments in this field pave the way to an everyday use of quantum technologies in various applications. Both in basic research as well as in applications quantum-enhanced sensing shows the potential to outperform classical measurements.[17] Entanglement-enhanced microscopes[18] and gyroscopes[19] have recently been presented, for example. Another example are photonic quantum technologies which can be utilized to overcome the classical shot-noise limit in interferometry.[20]

The fields of quantum communication and quantum information distribution are also rapidly evolving. Advances in the field of optically interfaced solid-state spins[21] have led to spectacular[22,23] experiments presenting, e.g., entanglement distillation between solid-state quantum network nodes,[24] or a deterministic delivery of entanglement on a quantum network.[25] Currently, researchers are discussing possible realizations of global quantum networks and their potential applications in the near future.[26,27] Even the first functional

implementations of space-borne, satellite-relayed quantum networks have been demonstrated.[22,23,28]

Single and entangled photons. Single and entangled photons play a key role in quantum technology. Especially in the fields of quantum sensing and quantum communication, photonic quantum systems are ubiquitous. With the success of hybrid quantum systems in recent years, the demand for high-brightness sources of (entangled) photons tailored to specific transitions of various quantum emitters has increased. To optimize the interaction of photons with other quantum systems, one needs to tailor the properties of the photon wave-packets in all degrees of freedom.

Recent conducted experiments verify that semiconductor quantum dots can meet these requirement. They feature outstanding properties in terms of single-photon purity, on-demand generation and brightness.[29–31] Therefore, quantum-dot-based single-photon sources are approaching the ideal of a *photon gun* which would be highly useful for many applications.

But, these kinds of single-photon sources require sophisticated cryogenic setups and rely on complicated manufacturing processes. Given these practical limitations, the widely applied process of spontaneous parametric down-conversion is a viable alternative to state-of-the-art single-photon sources like quantum dots or vacancy centers in crystals.

Spontaneous parametric down-conversion. The process of spontaneous parametric down-conversion (SPDC) is of eminent importance for a wide range of experiments in quantum optics.[32–39] Due to its ease of use[40] and its versatility, spontaneous parametric down-conversion is the most prominent source of non-classical light. The non-classicality stems from the principle that a photon from a (classical) pump beam can spontaneously decay into a pair of so-called *signal* and *idler* photons inside a nonlinear medium (Fig. 0.1). The simultaneous generation of the two photons in a single process gives rise to a rich structure of non-classical correlations between the signal and idler photons.

Key advantages of SPDC. There are several advantages of photon-pair sources based on spontaneous parametric down-conversion over other known photon-pair sources: They can be operated at room temperature and do not require elaborate cryogenic or vacuum setups. One can exploit the simultaneity[32,41] of the generation process for so-called *heralded single-photon sources*. The detection of an idler photon at a specific point in time *heralds* the presence of the corresponding signal photon. This localization in time[32] of a single photon wave packet offers a convenient method to enhance the signal-to-noise ratio in

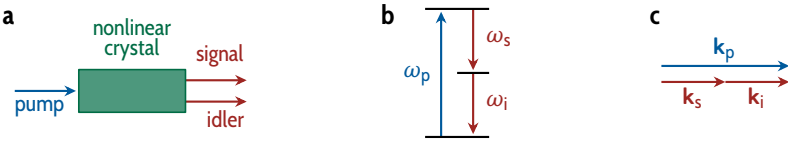

Figure 0.1 | Simplistic picture of spontaneous parametric down-conversion. **a**,A photon from the pump beam can spontaneously decay into a pair of so-called signal and idler photons inside a nonlinear crystal under energy and momentum conservation. **b**, The energy of the pump photon is conserved, i.e. the sum of signal and idler energies corresponds to the pump photon energy: $\hbar\omega_s + \hbar\omega_i = \hbar\omega_p$, where ω_n is the frequency of the corresponding field. **c**,An analogous expression for the photon momenta k_n can be found: $k_p = k_s + k_i$. In spontaneous parametric down-conversion, conservation of momentum is called *phase-matching*.

many experiments analogous to a lock-in amplifier which localizes a signal in frequency space.

Additionally, due to the nonlinear correlations between signal and idler photons, photon-pair sources based on SPDC can produce pairs of photons which are entangled in various degrees of freedom.[42–50] The central wavelength can be tuned from the ultraviolet[51] to the far infrared[52] and the spectral bandwidth of the generated photons can vary over many orders of magnitude.[53,54] Under certain conditions, the spectral structure of photons generated by SPDC is nearly independent of laboratory parameters. Therefore, SPDC allows for defining a primary radiation standard.[55]

Shortcomings and limitations. Despite their wide use in quantum optics experiments, photon-pair sources based on spontaneous parametric down-conversion also have several drawbacks:

- Due to the spontaneous nature of the process, photon pairs are always generated stochastically. With continuous wave pumping, the exact point in time when a photon pair is generated cannot be predicted. If a pulsed pump is employed, the experimenter cannot influence which pump pulse produces a photon pair.
- The photon pairs have thermal statistics:[56–58] There is always a non-vanishing probability to generate more than one pair simultaneously. The probability to generate double pairs can be made arbitrarily small, but only to the expense of a strong reduction in brightness.
- The process is very inefficient. Typically, not even one in 10^9 pump photons is converted into a photon pair with bulk nonlinear crystals.[59] This ratio can be improved by several orders of magnitude with integrated structures, e.g. waveguides[60,61] or micro resonators,[62–65] but these kinds of structures increase the experimental complexity and often suffer from higher losses than bulk optics.

- In general, the photons are not generated in a pure quantum state required for many applications in quantum computing,[66] quantum information processing and quantum communication.[67] The generation of photons in pure quantum states involves either lossy filtering[68,69] or a careful design of the down-conversion source.[70,71] This limits the flexibility of SPDC based photon-pair sources.

Historical overview. Louisell and coworkers[72] first predicted the generation of photon pairs by zero-point fluctuations or a spontaneously decaying pump photon in 1961. The first experimental evaluation of the spectral characteristics and the brightness of the parametric fluorescence was performed some years later by Harris and colleagues.[73] About the same time, Mollow[74,75] theoretically analyzed the photon statistics of parametric processes and Graham derived a quantum theory for optical parametric oscillation.[76,77]

In the beginning of the 1970s with the advent of low-noise single-photon detectors, this led to the first experimental realization of a photon-pair source by Burnham and Weinberg,[78] who also evaluated the simultaneity, energy and momentum conservation.

A full quantum theory of spontaneous parametric down-conversion with emphasis on the very short correlation time (small time separation) was derived by Hong and Mandel[41] in the 1980s. The theory was verified by time-resolved photon counting in 1985.[79] Shortly thereafter, Hong and colleagues published the first experimental realization of a localized one-photon state (heralded single-photon source).[32] With this novel source of single photons, Hong, Ou and Mandel[33] were able to realize genuine two-photon interference at a beam splitter for the first time. Recently, even three-photon interference with photons generated by spontaneous parametric down-conversion has been shown.[37,38]

Improved single-photon detectors and a deeper theoretical understanding paved the way for the first demonstration of entanglement between the photons in a pair. The first (polarization) entanglement of down-converted photons was shown in 1988.[42,43] Later on, time-energy entanglement,[44] time-bin entanglement,[80–83] momentum-position entanglement,[46] orbital angular momentum entanglement,[45,84] path entanglement,[48] and, recently, frequency-bin entanglement[50] have been shown.

Even photon-pair states entangled (or hyper-entangled) in all degrees of freedom have been generated.[47] And, by combining multiple photon-pair sources, it became possible to entangle more than two photons. While, in 1997, Bouwmeester and coworkers generated an entangled state of three photons,[85] the

number steadily increased,[49,86–90] culminating in the entanglement of 10 photons in 2017[90] and the entanglement of 18 qubits[91] using six photons with three degrees of freedom each in 2018.

Application of SPDC in modern experiments. Ambitious long-term goals such as large-scale quantum communication[67,92–95] or quantum computation based on photonic quantum states[66,96–98] have high demands on the fidelity, purity, and determinism in the generation process of single photons or photon pairs. Due to the aforementioned shortcomings, photon-pair sources based on SPDC are limited in their usefulness for these kinds of applications.

In recent years, mayor improvements of single-photon sources based on quantum dots have been achieved.[99–105] Even on-demand generation of polarization-entangled photon-pairs is feasible with quantum dots.[31]

Despite the aforementioned shortcomings and the major improvements of alternative technologies, SPDC based photon-pair sources are still ubiquitous in experimental quantum optics and in research projects working towards the aforementioned long-term goals. Due to their ease of use and their flexibility, they are often the mechanism of choice to generate single or entangled photons in prove-of-principle experiments. This makes SPDC based photon-pair sources a versatile tool for prototyping and verification of novel ideas. It is, for example, not surprising that the first realisation of space-borne entanglement distribution is based on SPDC.[22]

Hybrid quantum systems. Hybrid quantum systems[106] are increasingly successful at combining different quantum systems with complementary properties and functionalities to overcome fundamental barriers which cannot be overcome by the individual quantum systems. The spectral width of photons generated by spontaneous parametric down-conversion is typically of the order 100 GHz to THz. If one wants to interface the generated photon pairs with other systems (e.g. atomic transitions,[107] quantum dots,[108] or quantum memories) bandwidths on the order of several MHz to GHz are required. This normally requires aggressive spectral filtering[109,110] of the photon pairs with an associated dramatic reduction in brightness.

Cavity-enhanced spontaneous parametric down-conversion. A convenient method to overcome this limitation of SPDC is to place the nonlinear material into an optical cavity with an appropriate linewidth (see Fig. 0.2).[111] The bandwidth of the generated photons then depends on the cavity decay rate and can easily be adjusted via the reflectivity of the cavity mirrors. Additionally, the cavity can enhance the brightness of the source: Compared to a non-resonant photon-pair

source with the same non-linear crystal, the cavity can increase the photon-pair generation rate by orders of magnitude.

The concept of placing a nonlinear crystal into an optical cavity to generate non-classical light originates in 1984.[112–114] It was first discussed and applied in the context of squeezed-state preparation where an optical parametric oscillator is operated close to its threshold. The first proposals of cavity-enhanced photon-pair generation via SPDC date back to 1999.[111,115,116]

Soon thereafter, several groups presented various experimental realizations of cavity-enhanced sources of heralded or entangled photons.[111,117–121] Since then, these sources of non-classical light have been improved and optimized for various applications.[53,65,82,122–141] Recently, the results of several experiments have been published which no longer merely focus on the design and optimization of these photon-pair sources, but, instead, present practical applications thereof.[107,142–150]

Currently, in the literature, new realizations of cavity-enhanced photon-pair sources are still being published. All of these novel publications have in common that they aim at an interaction of the generated photons with other quantum systems, i.e., to build hybrid quantum systems. Various groups have recently presented atom-resonant photon-pair sources.[151–154] Interfacing photons generated by cavity-enhanced SPDC with rare-earth doped crystals[155–159] or single ions[140] is receiving much attention.

Outline of this thesis

Against the background of continuing scientific interest in the development and experimental applications of cavity-enhanced photon-pair sources, this thesis provides a comprehensive analysis of triply-resonant cavity-enhanced SPDC. The analysis covers three aspects: Following a theoretical discussion of cavity-enhanced SPDC, we describe the experimental implementation of a cavity-enhanced photon-pair source and its characterization. Finally, this thesis presents the results of a series of experiments that exploit the specific properties of the above-mentioned photon-pair source.

Theoretical foundations. Chapter 1 presents the theoretical foundations of this thesis. We derive the quantum theory of cavity-enhanced SPDC with a focus on the analysis of double-pass pumping and pump-resonant linear cavities. The main objective of this chapter is to derive a convenient model with which the cavity geometry can be optimized to maximize the photon-pair generation rate while maintaining a high heralding ratio.

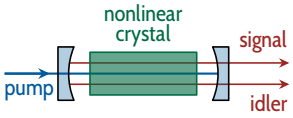

Figure 0.2 | Schematic of cavity-enhanced spontaneous parametric down-conversion. The generation of signal and idler photons can be enhanced by placing the nonlinear crystal into an optical resonator. This configuration is also called an *optical parametric oscillator*. The cavity increases not only the brightness of the photon-pair source, it also alters the spectral structure of the generated photons. Signal and idler photons are generated only at the resonance frequencies of the cavity. Additionally, the two photons of a pair must still obey energy conservation.

At the heart of the theoretical analysis lies the *joint spectral amplitude* of the two-photon state generated by cavity-enhanced spontaneous parametric down-conversion. Building on established theoretical models of cavity-enhanced parametric down-conversion,[111,129,130,136,137,160–162] this thesis refines the expression for the joint spectral amplitude. Specifically, the refined expression takes account of the interaction of Gaussian beams inside (linear) cavities and covers a wide range of different cavity configurations and geometries.

The refined expression for the joint spectral amplitude also takes the loss of photons inside the cavity and at the cavity mirrors into account. Exploiting this model, chapter 1 highlights the strong impact of photon losses on the brightness and the cavity-escape efficiency for larger values of the cavity finesse. These two parameters cannot be optimized independently. Regarding experimental implementation, this indicates that the trade-off between brightness and heralding ratio has to be taken into account in the design process of a cavity-enhanced photon-pair source.

Most importantly, the first chapter of this thesis contributes to the literature on cavity-enhanced SPDC by deriving and verifying a theoretical expression for *absolute* values of the photon-pair generation rate depending on the pump power and the cavity geometry. Special care has been taken to specify the brightness only in terms of parameters which are directly accessible in the design process of a new experimental setup.

The model is in good agreement with experimental results gathered for a broad range of different cavity configurations ranging from low-finesse conventional cavities to high-finesse monolithic resonators. Therefore, the first chapter of this thesis provides researchers in the field of quantum optics with an approachable, ready-to-use model which can serve as a basis for the development and optimization of novel cavity-enhanced photon-pair sources. Accordingly, chapter 1 provides the theoretical background for our experimental implementation of a cavity-enhanced photon-pair source and its characterization, which we describe in the subsequent chapter of this thesis.

Experimental implementation of a triply-resonant photon-pair source. In the second part of this thesis, we describe the experimental implementation of a cavity-enhanced photon-pair source based on SPDC which is resonant to the cesium D_1-line. The linewidth of the generated photons is larger than the natural linewidth of the hyperfine transitions. It is designed to match the storage-bandwidth of several quantum memories based on room-temperature cesium vapor.[163–166] Furthermore, this combination of wavelength and linewidth also matches the properties of photons generated by InGaAs quantum dots.[108,167,168]

Regarding the technical aspects, chapter 2 addresses two important building blocks for the experimental implementation of cavity-enhanced photon-pair sources: the development of improved monolithic filter cavities as well as the use of digital cavity locking electronics. Chapter 2 presents an important technical improvement of the concept of a monolithic Fabry-Pérot cavity, which allows for polarization-independent spectral filtering. Additionally, we use the intrinsic frequency stability of the filter cavity to develop a novel high-precision monochromator and a high-resolution spectrum analyzer. Combined with single-photon detectors, this setup provides excellent spectral resolution for extremely weak signals. Furthermore, experiments based on cavity-enhanced SPDC with conventional cavities require a sophisticated feedback control system to stabilize the mirror spacing over long measurement durations. By the introduction of a digital locking scheme instead of the previously-employed analog control system, we achieve a significant improvement in the long-term stability of our experimental setup.

Characterization of a triply-resonant photon-pair source. Apart from the technical improvements introduced in the first part of chapter 2, we also present an in-depth experimental characterization of cavity-enhanced photon-pair sources. In this aspect, the main contribution of chapter 2 lies in the special emphasis on the pump resonance condition and the direct comparison of high-resolution spectral and temporal measurements of the two-photon wave packet. Due to the interference of photons generated in the forward direction and photons generated in the backward direction, we are able to identify and experimentally verify a rich spectral and temporal structure. The theoretical model developed in chapter 1 and the measurements presented in chapter 2 are in excellent agreement, which further corroborates the theoretical findings presented in chapter 1. Furthermore, chapter 2 provides the verification that our designed photon-pair source generates entangled photons. Thereby, this thesis opens the way towards building prove-of-principle experiments like quantum teleportation between pair photons and quantum dot spins, or pair photons and collective spin excitations in room-temperature cesium vapor, that fall into research field of hybrid quantum networks.

Hybrid quantum networks. Chapter 3 discusses experimental results which are also linked to the field of hybrid quantum networks. Hybrid quantum systems[106] aim at combining different quantum systems with complementary properties and functionalities to overcome fundamental barriers which cannot be overcome by the individual quantum systems. If quantum information is transferred from one such quantum system to another via single photons over optical fibers, often, quantum frequency conversion to telecommunication wavelengths is beneficial to avoid photon losses inside the fiber.

Chapter 3 presents the quantum frequency conversion of heralded single photons generated by the cavity-enhanced photon-pair source presented in chapter 2. We provide evidence that the structure of the temporal wave packets of the heralded photons is unaffected by the conversion process. Operation at telecom wavelength allows us to use advanced telecommunication technology, e.g., for fast wave-packet modulation. Therefore, in chapter 3, we present a potential route to interface dissimilar quantum systems via optical fibers. We match the spectral as well as the temporal wave packets from one quantum system to another and, thus, optimize their interaction.

Chapter 4 summarizes the main results of this thesis and points out promising areas of future research.

1 Triply-resonant cavity-enhanced spontaneous parametric down-conversion

This chapter lays the theoretical foundations of this thesis by providing a detailed model of triply-resonant spontaneous parametric down-conversion. In the following, we introduce cavity-enhanced photon-pair sources with the description of a exemplary realization. Subsequently, we define the main objective of this thesis, namely the design and optimization of a cesium-resonant photon-pair source with a linewidth of 100 MHz. Finally, we summarize the outline and contributions of this chapter.

Cavity-enhanced photon-pair sources. An example of a cavity-enhanced source of frequency-degenerate pairs of photons is shown in Fig. 1.1. It utilizes type-II phase matching, where signal and idler photons are polarized vertically. Type-II phase matching offers the advantage that signal and idler photon – even at frequency degeneracy – can be deterministically split by a polarizing beam splitter. This splitting is especially important in applications where the down-conversion source is used as a heralded single-photon source and signal and idler photons are degenerate in frequency. Another advantage of type-II phase matching is that a cavity-enhanced source can be used to produce polarization-entangled photons with a small spectral bandwidth.[118,125]

Example of a small-bandwidth cavity-enhanced SPDC source. To introduce the main objective of this thesis, the following paragraphs discuss a practical example of a cavity-enhanced source of photon pairs. The original setup of Scholz et al.[128] consists of a 2 cm long periodically poled potassium titanyl phosphate (PPKTP) crystal placed in a 6 cm long, spherical cavity with a high finesse ($\mathcal{F} = 265$) at the signal and idler wavelength. This results in a linewidth of only 3 MHz. The cavity is locked to a resonance of the pump beam via a piezo-electric transducer. To achieve simultaneous resonance of all three fields, an additional (non-poled) KTP crystal is placed next to the down-conversion crystal. This compensation crystal has the same length as the PPKTP crystal but is turned by 90° around the optical axis. With this configuration, the free spectral range (FSR) of the cavity is identical for signal and idler photons. By tuning the temperature of

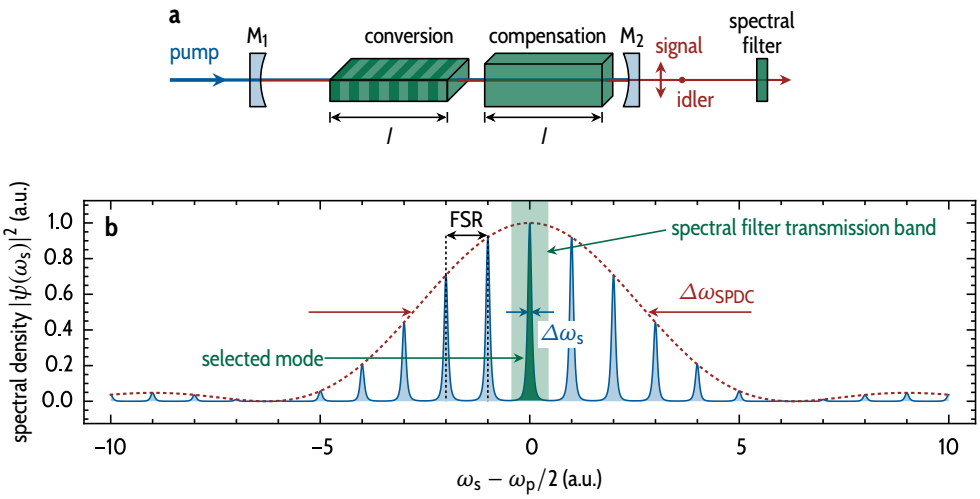

Figure 1.1 | Cavity-enhanced parametric down-conversion with compensation crystal. **a**, Experimental setup of the cavity with the periodically poled KTP down-conversion crystal of length *l* placed at the focus of pump beam. The non-poled compensation crystal of the same length is made from the same material and is cut the same way. It is rotated about the optical axis by 90° with respect to the down-conversion crystal. The free spectral ranges (FSR) of signal and idler fields are identical, since the two polarization directions share the same optical round-trip path length. A spectral filter is used to select only signal and idler photons which are degenerate in frequency. **b**, The signal spectral density $|\psi(\omega_s)|^2$ (—) is the product of the non-resonant parametric gain envelope (----) and a joint resonance function. With the configuration depicted in **a**, the signal and idler free spectral range is identical, giving rise to a series of equally-spaced spectral modes. The spectral width $\Delta\omega_{SPDC}$ of non-resonant down-conversion is defined by the length and dispersion of the nonlinear crystal. The width of the individual modes $\Delta\omega_s$ is given by the length and signal/idler finesse of the cavity. Here, the degenerate case is shown, where there is a mode in the center of the spectrum for which signal and idler photons are indistinguishable in frequency. For many experiments, only this mode is needed and all other photons are discarded by spectral filtering.

the crystals individually, the resonance frequencies of the three fields can be adjusted to achieve the desired triple resonance condition.

The mirrors are coated so that the cavity is triply resonant for both pump, signal and idler fields. The first mirror M_1 is highly reflective for signal and idler photons and is partially reflective at the pump wavelength. For the second mirror M_2 the reflectivity is reversed, being highly reflective at the pump wavelengths and partly reflective at the signal/idler wavelength. Therefore, the cavity can be pumped from the left, while most of the generated photons leave the cavity through mirror M_2. The spectrum of the signal and idler photons is determined by the length and temperature of the crystals, the reflectivity of the mirrors and the absolute length of the cavity.

Objective: Design of a 100 MHz bandwidth SPDC photon-pair source. One important objective of this thesis is the design and optimization of a photon-pair source based on the design of M. Scholz and coworkers, but with a broader spectral bandwidth. The following requirements should be met:

Wavelength and triple resonance: The wavelength of signal and idler photons should be degenerate at the cesium D_1-line of 894.3 nm. To generate signal and idler photons, which are indistinguishable in frequency, the cavity resonances of the pump, signal and idler fields should be independently tunable to achieve triple resonance.

Spectral bandwidth: The bandwidth of the spectral modes of the generated photons should correspond to the bandwidth of photons generated by solid-state quantum dots, i.e. in the range[169,170] of 100 MHz to 1 GHz. This bandwidth would also allow for storage of the generated photons in a quantum memory based on neutral cesium atoms.[110,166,171,172]

Brightness and pump power: The brightness (i.e. the number of generated photon pairs per second per mW of pump power) of the photon-pair source should be as high as possible. The pump power required to produce 0.01 photon pairs per temporal mode[138,173] (this corresponds to a photon-pair generation rate of about 5 MHz) should not exceed 100 mW so that a convenient (frequency-doubled) diode laser can be used as a pump.

Extraction and collection efficiency: The probability that the photon pairs exit the cavity through the desired cavity mirror and can be efficiently coupled into a single-mode optical fiber, should be as high as possible to obtain a high probability of detecting both signal and idler photons from one pair.

Stability: The source should be mechanically and spectrally stable in order to allow for continuous operation over many hours without manual intervention.

Outline and contribution. The first two requirements listed above can easily be met: It is trivial to find a nonlinear crystal phase-matched for the desired wavelength of pump, signal, and idler photons. Furthermore, the spectral bandwidth of the generated photon pairs can also easily be brought to the target value by choosing appropriate values for the reflectivities of the cavity mirrors to tune the cavity decay rate to the desired value.

In contrast, designing a photon-pair source with a certain brightness requires a theory which predicts (absolute) values for the photon-pair generation rate. Such a theory is not available in the literature. Existing theories which predict absolute values[111,129,161,162] have the following deficiencies: They assume an interaction of plane waves instead of more realistic Gaussian beams. Also, the impact of the cavity geometry on the generation rate and the spectral characteristics has so far not been studied. Especially the impact of the positions and lengths of the nonlinear and compensation crystals inside the cavity have not been analyzed in detail. Furthermore, triply-resonant configurations have only been discussed for a lossless cavity.[129]

The theory presented in this chapter addresses these issues by providing a detailed quantitative model of triply-resonant cavity-enhanced spontaneous parametric down-conversion. This model can be directly applied to the design and optimization of a photon-pair source with realistic experimental parameters.

This chapter is organized as follows: In section 1.1 we provide convenient expressions for the two-photon quantum state and the (joint) spectral amplitude of signal and idler photons generated by triply-resonant cavity-enhanced parametric down-conversion. In standing-wave cavities, photon pairs can be generated in both directions leading to an interference effect. The impact of double-pass pump and pump-resonant configurations on the spectral density is covered in detail and the theory of Jeronimo-Moreno and colleagues[129] is extended to the case of a lossy cavity.

In the subsequent section 1.2, we rewrite this plane-wave model to cover the interaction of Gaussian beams. Care is taken to describe arbitrary cavity geometries in closed-form expressions. With this approach, one can analyze the influence on the photon-pair generation rate of the relative position of the nonlinear crystal and the focal point of the pump. This section heavily relies on the works of Boyd and Kleinman[174] as well as Bennink,[59] but transfers their findings to cavity-enhanced SPDC.

These first two sections lay the foundation for section 1.3, in which we derive an expression for the brightness in terms of photon-pair generation rate per mW of pump power. With this model, absolute values for the generation rate

can be computed. All expressions can be traced back to experimental accessible parameters which need to be specified in the design process of a cavity-enhanced photon-pair source.

We evaluate the model by comparing it with generation rates measured for various cavity configurations (section 1.3.5). Subsequently, we also utilize the model to optimize the cavity geometry (especially the length of the nonlinear crystal) for maximum generation rate and photon extraction efficiency (section 1.3.6). A similar study cannot straightforwardly be performed with models found in the literature.

Finally, in section 1.4, we analyze the purity of heralded single photons generated by triply-resonant cavity-enhanced SPDC. With these calculates, we confirm the qualitative findings of Jeronimo-Moreno an coworerks.[129] The analysis indicates that a pump with sufficient spectral bandwidth is required to produce pure single photons.[137] Additionally, the cavity decay rate for the pump field needs to be much larger than the signal/idler cavity decay rate. Both findings are evaluated quantitatively.

1.1 | Spontaneous parametric down-conversion

The spontaneous decay of a pump photon into a pair of signal and idler photons can only be explained by the quantum theory of light. The strong correlations between the generated photons in various degrees of freedom and the photon statistics have no classical counterpart. Nevertheless, the classical theory of three-wave-mixing we present in the following gives valuable insights into the generation process.

Therefore, we split this section into two parts. First, starting from classical three-wave-mixing, we derive a set of coupled differential equations for the three interacting fields and introduce the concept of phase matching. From the coupled equations we also derive an expression for the spectral properties of the generated fields.

Subsequently, we contrasts the classical picture with the quantum mechanical Hamiltonian. In contrast to the classical interaction of waves, the signal and idler photons generated by spontaneous parametric down-conversion do not require initial seeding fields. But, their spectral properties are identical to their classical counterparts.

While discussing these spectral properties, we introduce the most important theoretical construct for this thesis: the *joint spectral amplitude* of the generated two-photon state. The joint spectral amplitude encodes the spectral and temporal properties of signal and idler photons as well as the spectro-temporal *correlations* between the two photons from one pair.

1.1.1 | Classical three-wave-mixing

The classical theory of difference-frequency generation of plane waves inside a nonlinear crystal provides an intuitive understanding why conservation of momentum requires a phase matching between the involved fields. The purpose of this section is to show that the process of parametric down-conversion (or difference-frequency generation) is most efficient if there is a fixed phase relation between the nonlinear polarizations and generated fields. Phase matching also determines the spectral properties of the generated fields. This section follows the theory detailed by Boyd[175] and is adapted to the case of parametric down-conversion.

Nonlinear polarization. In classical three-wave-mixing, the polarization $\tilde{\boldsymbol{P}}$ of the nonlinear medium is related to the electrical field $\tilde{\boldsymbol{E}}$ of the involved optical fields by the nonlinear susceptibility tensor $\boldsymbol{\chi}^{(2)}$ by:

$$\tilde{\boldsymbol{P}} = \tilde{\boldsymbol{E}} \otimes \boldsymbol{\chi}^{(2)} \otimes \tilde{\boldsymbol{E}}. \tag{1.1.1}$$

The electrical field can be expressed as a superposition of the pump (p), signal (s) and idler (i) fields:

$$\tilde{\boldsymbol{E}} = \tilde{\boldsymbol{E}}_\mathrm{p} + \tilde{\boldsymbol{E}}_\mathrm{s} + \tilde{\boldsymbol{E}}_\mathrm{i}. \tag{1.1.2}$$

When assuming a fixed geometry where the three fields are propagating collinearly along the z-axis and are polarized in the same direction, all relations become scalar and the fields can be written as:

$$\tilde{E}_n(z,t) \equiv E_n(z)e^{-i\omega_n t} + \text{c.c.} \equiv A_n(z)e^{i[k_n z - \omega_n t]} + \text{c.c.}, \qquad n = \text{p, s, i}, \tag{1.1.3}$$

where $A_n(z)$ is the electric field amplitude along the polarization direction, k_n is the wave vector and ω_n is the angular frequency. $E_n(z)$ is defined as $E_n(z) = A_n(z)e^{ik_n z}$. Analogously, the polarization is given by:

$$\tilde{P}_n(z,t) \equiv P_n(z)e^{-i\omega_n t} + \text{c.c.}, \qquad n = \text{p, s, i}. \tag{1.1.4}$$

Plugging Eqs. 1.1.2 to 1.1.4 into Eq. 1.1.1, the polarization can be written[176] analogously to the electrical field (Eq. 1.1.2):

$$\begin{aligned} P_\mathrm{p}(z) &= 4\epsilon_0 d_\mathrm{eff} E_\mathrm{s}(z) E_\mathrm{i}(z) \\ &= 4\epsilon_0 d_\mathrm{eff} A_\mathrm{s}(z) A_\mathrm{i}(z) e^{i[k_\mathrm{s}+k_\mathrm{i}]z} \\ P_\mathrm{s}(z) &= 4\epsilon_0 d_\mathrm{eff} A_\mathrm{p}(z) A_\mathrm{i}^*(z) e^{i[k_\mathrm{p}-k_\mathrm{i}]z} \\ P_\mathrm{i}(z) &= 4\epsilon_0 d_\mathrm{eff} A_\mathrm{p}(z) A_\mathrm{s}^*(z) e^{i[k_\mathrm{p}-k_\mathrm{s}]z}, \end{aligned} \tag{1.1.5}$$

where d_eff is the effective nonlinear coefficient.[175] It depends on the material of the nonlinear crystal, its orientation and geometry, as well as the chosen polarization direction of the pump field. ϵ_0 is the permittivity of free space.

Coupled wave equations and phase matching. Maxwell's equation can be utilized to derive[175] coupled differential equations for the electric field amplitudes A_p, A_s and A_i. In the slowly varying envelope approximation, which requires that the amplitude A_n varies only marginally on the scale of the wavelength (i.e. $\left|\mathrm{d}^2 A_n \middle/ \mathrm{d}z^2\right| \ll \left|k_n \, \mathrm{d}A_n/\mathrm{d}z\right|$), one obtains:

$$\begin{aligned} \frac{\mathrm{d}A_\mathrm{p}}{\mathrm{d}z} &= i\frac{2d_\mathrm{eff}\omega_\mathrm{p}^2}{k_\mathrm{p}c^2} A_\mathrm{s} A_\mathrm{i} e^{-i\Delta k z} \\ \frac{\mathrm{d}A_s}{\mathrm{d}z} &= i\frac{2d_\mathrm{eff}\omega_s^2}{k_s c^2} A_\mathrm{p} A_i^* e^{i\Delta k z} \\ \frac{\mathrm{d}A_i}{\mathrm{d}z} &= i\frac{2d_\mathrm{eff}\omega_i^2}{k_i c^2} A_\mathrm{p} A_s^* e^{i\Delta k z}, \end{aligned} \tag{1.1.6}$$

where $\Delta k = k_\mathrm{p} - k_\mathrm{s} - k_\mathrm{i}$ is the so-called *phase mismatch* between the involved fields.

It is essential to note that for perfect phase matching, i.e., $\Delta k = 0$, the amplitudes of the generated signal and idler field are monotonically increasing functions with the position along the crystal axis. In this case, there is a fixed phase relation between the nonlinear polarizations and the generated waves:

$$\Delta k = 0 \Rightarrow \begin{cases} \tilde{E}_n(z,t) &= A_n e^{i[k_n z - \omega_n t]} \\ \tilde{P}_n(z,t) &= p_n e^{i[k_n z - \omega_n t]} \end{cases}, \qquad n = \mathrm{p,\, s,\, i}, \tag{1.1.7}$$

where the value of p_n can be inferred from Eq. 1.1.6, e.g., $p_\mathrm{p} = 4\epsilon_0 d_\mathrm{eff} A_\mathrm{s} A_\mathrm{i}$. The process of spontaneous parametric down-conversion is most efficient if the phases of electrical fields and nonlinear polarizations are *matched* in this way,

as will be shown below. In quantum theory, where photon momentum p is related to the wave vector k by $p = \hbar k$, the phase-matching condition $\Delta k = 0$ corresponds to momentum conservation.

Note, that collinear parametric interaction as described by Eq. 1.1.6 is experimentally achievable by *quasi phase matching*,[175] where the ferroelectric domain structure of a nonlinear crystal is periodically inverted with poling period Λ. This introduces an additional wave vector in the phase-matching condition:

$$\Delta k_{\mathrm{qpm}} = k_{\mathrm{p}} - k_{\mathrm{s}} - k_{\mathrm{i}} + \frac{2\pi}{\Lambda}, \tag{1.1.8}$$

and each field acquires an additional phase factor $\exp\left(i2\pi l/\Lambda\right)$ upon traversal of the crystal of length l. In the following discussion, is always assumed that the nonlinear crystal is collinearily phase-matched. The extra contributions from the periodic poling are omitted for simplicity.

Spectral properties. For small parametric gain, one can take the amplitudes A_n on the right hand side of Eq. 1.1.6 to be constants. Then, Eq. 1.1.6 can be integrated, yielding the values of the amplitudes after traversal of the nonlinear crystal of length l:

$$\begin{aligned} A_{\mathrm{p}}(l) &= A_{\mathrm{p}}(0) - \chi_{\mathrm{p}}^{*} A_{\mathrm{s}}(0) A_{\mathrm{i}}(0) \\ A_{\mathrm{s}}(l) &= A_{\mathrm{s}}(0) - \chi_{\mathrm{s}} A_{\mathrm{p}}(0) A_{\mathrm{i}}^{*}(0) \\ A_{\mathrm{i}}(l) &= A_{\mathrm{i}}(0) - \chi_{\mathrm{i}} A_{\mathrm{p}}(0) A_{\mathrm{s}}^{*}(0). \end{aligned} \tag{1.1.9}$$

The coupling coefficient χ_n is given by:[175]

$$\chi_n = il\frac{2d_{\mathrm{eff}}\omega_n^2}{k_n c^2}\,\mathrm{sinc}\left(\frac{\Delta kl}{2}\right)e^{-i\Delta kl/2}. \tag{1.1.10}$$

Eq. 1.1.9 indicates that for classical fields there is no *spontaneous* down-conversion. If both $A_{\mathrm{s}}(0) = A_{\mathrm{i}}(0) = 0$, the pump field inside the nonlinear crystal generates no signal and idler fields ($A_{\mathrm{s/i}}(z) \equiv 0$). There always needs to be a seed from either the signal or the idler field ($A_{\mathrm{s}}(0) \neq 0$ or $A_{\mathrm{i}}(0) \neq 0$) for conversion to take place.

To show that the efficiency of the down-conversion process is highest for perfect phase matching, the spectral intensity of the signal/idler field $I_{\mathrm{s/i}}$ at the output facet of the nonlinear crystal can be evaluated:[175]

$$I_{\mathrm{s/i}}(\omega_{\mathrm{s}}, \omega_{\mathrm{i}}) \propto \left|A_{\mathrm{s/i}}(\omega_{\mathrm{s}}, \omega_i, l)\right|^2 \propto l^2\,\mathrm{sinc}^2\left(\frac{\Delta k(\omega_{\mathrm{s}}, \omega_{\mathrm{i}})l}{2}\right). \tag{1.1.11}$$

Even for a monochromatic pump, signal and idler fields are not monochromatic but exhibit a sinc^2-shaped spectral distribution as a function of the phase mismatch Δk.[41] The process is most efficient for $\Delta k = 0$. The width of the spectral distribution is inversely proportional to the length of the nonlinear crystal.

In the following, we derive the corresponding quantum-mechanical expressions for the spectrum of the signal and idler photons generated by spontaneous parametric down-conversion.

1.1.2 | Quantum theory of spontaneous parametric down-conversion

The classical theory predicts the same spectral characteristics for the signal and idler fields as the quantum theory predicts for the signal and idler photons. In contrast to the classical theory, quantum theory predicts the generation of signal and idler photons even without initial signal and idler fields, i.e., even for a vacuum state of the signal and idler modes.

This section follows an approach similar to Mosley's[70] excellent quantum theory of spontaneous parametric down-conversion which is based on earlier works.[41,177] In some cases we adapt the notation so that we can extend this theory in a later section to the case of the interaction of focussed Gaussian beams discussed by Bennink.[59] As opposed to the classical theory, the starting point is not the set of coupled wave equations but the Hamiltonian of the system.

Quantization. First, the electric field needs to be quantized: The electric field operator of a plane wave traveling in z-direction, polarized along the unit vector $\boldsymbol{e}$, is of the form:

$$\widehat{\boldsymbol{E}}(z,t) = \widehat{\boldsymbol{E}}^{(+)}(z,t) + \widehat{\boldsymbol{E}}^{(-)}(z,t), \quad \text{with} \quad \widehat{\boldsymbol{E}}^{(-)}(z,t) = \left[\widehat{\boldsymbol{E}}^{(+)}(z,t)\right]^{\dagger} \tag{1.1.12}$$

and

$$\widehat{\boldsymbol{E}}^{(+)}(z,t) = \boldsymbol{e}\widehat{E}^{(+)}(z,t) = i\boldsymbol{e}\int_0^\infty \mathrm{d}\omega\, A(\omega)\mathcal{E}(k(\omega),z)\hat{a}(\omega)e^{-i\omega t}. \tag{1.1.13}$$

Here, $\hat{a}(\omega)$ is the photon annihilation operator with the usual commutation relation $\left[a(\omega), a^{\dagger}(\omega')\right] = \delta(\omega-\omega')$ and the amplitude factor $A(\omega)$ is defined by:[177]

$$A(\omega) = \sqrt{\frac{\hbar\omega}{2\epsilon_0 n(\omega)^2 V_{\mathrm{Q}}}}, \tag{1.1.14}$$

where V_Q is the quantization volume and $n(\omega)$ is the refractive index. For a plane wave, the mode function $\mathcal{E}(k(\omega), z)$ is given by:

$$\mathcal{E}(k(\omega), z) = e^{ik(\omega)z}. \tag{1.1.15}$$

The dispersion relation is $k(\omega) = \omega n(\omega)/c$.

Hamiltonian. The Hamiltonian of parametric down-conversion in the interaction picture is:[41,177]

$$\begin{aligned} \widehat{H}_I(t) &= \epsilon_0 d_{\text{eff}} \int_V \mathrm{d}V\, \widehat{E}_p \widehat{E}_s \widehat{E}_i \\ &= \epsilon_0 d_{\text{eff}} \int_V \mathrm{d}V\, \widehat{E}_p^{(+)} \widehat{E}_s^{(-)} \widehat{E}_i^{(-)} + \quad \text{h.c.}, \end{aligned} \tag{1.1.16}$$

where the integral is performed over the volume V of the nonlinear crystal and $\widehat{E}_p$, $\widehat{E}_s$ and $\widehat{E}_i$ are the quantized fields of the pump, signal and idler photons. The Hamiltonian depends only implicitly on the polarization directions of the fields, since these determine the value of the effective nonlinear coefficient d_{eff}.

If the pump beam is a bright undepleted laser, the pump field operator can be replaced by a classical field:

$$\widehat{E}_p^{(+)}(z,t) \longrightarrow E_p^{(+)}(z,t) = A_p \int_0^\infty \mathrm{d}\omega\, s(\omega) \mathcal{E}_p e^{-i\omega t}. \tag{1.1.17}$$

The factor A_p is the pump amplitude and $s(\omega)$ is the spectral amplitude distribution. The corresponding pump spectral density $\left|s(\omega)\right|^2$ is normalized to 1:

$$\int_0^\infty \mathrm{d}\omega \left|s(\omega)\right|^2 = 1. \tag{1.1.18}$$

For a (monochromatic) pump with a spectral width much smaller than the bandwidth of the generated photons, the pump spectral density can be approximated by a delta distribution:[178]

$$s(\omega) = \delta(\omega - \omega_p). \tag{1.1.19}$$

State evolution. In contrast to the classical process of three-wave-mixing, in quantum theory, the initial state of the signal and idler fields can also be the vacuum state:

$$\left|\psi(t=0)\right\rangle = \left|0\right\rangle_{\mathrm{s}} \left|0\right\rangle_{\mathrm{i}} \equiv \left|0,0\right\rangle . \tag{1.1.20}$$

Expanding the Dyson-series[179] to first order yields the evolved state at time t in the interaction picture:

$$\begin{aligned}\left|\psi(t)\right\rangle &\approx \left[1 + \frac{i}{\hbar}\int_0^t \mathrm{d}t'\, H_{\mathrm{I}}(t')\right]\left|0,0\right\rangle \\ &= \left|0,0\right\rangle + \kappa \int_0^t \mathrm{d}t' \int_0^\infty \mathrm{d}\omega_{\mathrm{p}} \int_0^\infty \mathrm{d}\omega_{\mathrm{s}} \int_0^\infty \mathrm{d}\omega_{\mathrm{i}} \\ &\quad s(\omega_{\mathrm{p}})\mathcal{O}(\omega_{\mathrm{s}},\omega_{\mathrm{i}})e^{-i\Delta\omega t}\hat{a}_{\mathrm{s}}^{\dagger}(\omega_{\mathrm{s}})\hat{a}_{\mathrm{i}}^{\dagger}(\omega_{\mathrm{i}})\left|0,0\right\rangle ,\end{aligned} \tag{1.1.21}$$

with $\Delta\omega = \omega_{\mathrm{p}} - \omega_{\mathrm{s}} - \omega_{\mathrm{i}}$. The amplitude factors $A_n(\omega_n)$ (Eq. 1.1.14) vary only slowly with the frequency $\omega(\omega_n)$ and have been pulled out of the integral in Eq. 1.1.21. Therefore, the constant κ is defined by:

$$\kappa = i\frac{\epsilon_0 d_{\mathrm{eff}} A_{\mathrm{p}} A_{\mathrm{s}}(\omega_s) A_{\mathrm{i}}(\omega_{\mathrm{i}})}{\hbar}. \tag{1.1.22}$$

We discuss the so-called *spatial mode overlap* $\mathcal{O}(\omega_{\mathrm{s}},\omega_{\mathrm{i}})$ in the following paragraph.

Spatial mode overlap. The following discussion assumes that the nonlinear crystal of length l is placed with the front facet at poistion $z = 0$. The spatial overlap $\mathcal{O}(\omega_{\mathrm{s}},\omega_{\mathrm{i}})$ of the plane wave mode functions defined in Eq. 1.1.15 is, in the case of collinear phase matching, just an integral over z:

$$\mathcal{O}(\omega_{\mathrm{s}},\omega_{\mathrm{i}}) = \int_0^l \mathrm{d}z\, \mathcal{E}_{\mathrm{p}}\mathcal{E}_{\mathrm{s}}\mathcal{E}_{\mathrm{i}} \tag{1.1.23}$$

$$= \int_0^l \mathrm{d}z\, e^{i\Delta k z} \tag{1.1.24}$$

$$= l\,\mathrm{sinc}\big(\Delta k l/2\big)e^{i\Delta k l/2}. \tag{1.1.25}$$

The pertubative expansion in Eq. 1.1.21 is only valid if the probability to generate a photon pair in the interaction time t is small. It is therefore appropriate to

take the limit $t \to \infty$. The time integral in Eq. 1.1.21 then evaluates to a delta function which reflects energy conservation:

$$\begin{aligned} \int_0^t \mathrm{d}t'\, e^{-i\Delta\omega t} &= t e^{-i\Delta\omega t/2}\,\mathrm{sinc}\big(\Delta\omega t/2\big) \\ &\to \pi\delta(\omega_\mathrm{p} - \omega_\mathrm{s} - \omega_\mathrm{i}) \quad \text{for } t \to \infty. \end{aligned} \tag{1.1.26}$$

Joint spectral amplitude. Finally, the state after the interaction can be written as:

$$\big|\psi\big\rangle = |0,0\rangle + \pi l\kappa \int_0^\infty \mathrm{d}\omega_\mathrm{s} \int_0^\infty \mathrm{d}\omega_\mathrm{i}\, s(\omega_\mathrm{s}+\omega_\mathrm{i})\,\mathrm{sinc}\big(\Delta kl/2\big) e^{i\Delta kl/2} \hat{a}_\mathrm{s}^\dagger(\omega_\mathrm{s}) \hat{a}_\mathrm{i}^\dagger(\omega_\mathrm{i})\,|0,0\rangle\,. \tag{1.1.27}$$

Now, we introduce the *joint spectral amplitude* $\psi(\omega_\mathrm{s}, \omega_\mathrm{i})$ of signal and idler photon by rewriting Eq. 1.1.27:

$$\big|\psi\big\rangle = |0,0\rangle + \int_0^\infty \mathrm{d}\omega_\mathrm{s} \int_0^\infty \mathrm{d}\omega_\mathrm{i}\, \psi(\omega_\mathrm{s}, \omega_\mathrm{i}) \hat{a}_\mathrm{s}^\dagger(\omega_\mathrm{s}) \hat{a}_\mathrm{i}^\dagger(\omega_\mathrm{i})\,|0,0\rangle\,. \tag{1.1.28}$$

The joint spectral amplitude (JSA) is the most important theoretical concept of this thesis. It encodes the complete spectro-temporal structure of the two-photon state.

In chapter 2, we will discuss the experimental characterization of photon-pair sources based on SPDC. As we will show, most of the important experimental accessible parameters are directly connected to the joint spectral amplitude. From the JSA we cannot only derive the spectrum of signal and idler photons (section 2.3), but also the spectral correlations between signal and idler photons (see section 1.4). The JSA encodes temporal correlations between signal and idler photons which we measure via the second-order signal-idler correlation function (section 2.4). We also utilize the JSA to theoretically evaluate the two-photon interference of signal and idler photons discussed in section 2.5.

Phase-matching function. We define the joint spectral amplitude as the product of pump spectral amplitude and *phase-matching function* $f(\omega_\mathrm{s}, \omega_\mathrm{i})$:

$$\psi(\omega_\mathrm{s}, \omega_\mathrm{i}) = s(\omega_\mathrm{s} + \omega_\mathrm{i}) f(\omega_\mathrm{s}, \omega_\mathrm{i}), \tag{1.1.29}$$

where, with Eq. 1.1.27, the phase-matching function is:

$$f(\omega_\mathrm{s}, \omega_\mathrm{i}) \propto \mathrm{sinc}\big(\Delta kl/2\big) e^{i\Delta kl/2}. \tag{1.1.30}$$

The modulus squared of the phase-matching function is proportional to the classical intensity of the generated signal and idler fields (see Eq. 1.1.11)

$$\left|f(\omega_\mathrm{s},\omega_\mathrm{i})\right|^2 \propto l^2\,\mathrm{sinc}^2\big(\Delta k(\omega_\mathrm{s},\omega_\mathrm{i})l/2\big). \tag{1.1.31}$$

Signal/Idler spectrum. From the JSA, we can derive the spectrum (i.e. the spectral densities) of signal and idler photons by:[129]

$$\left|\psi(\omega_\mathrm{s})\right|^2 = \int_{-\infty}^{\infty} \mathrm{d}\omega_\mathrm{i}\left|\psi(\omega_\mathrm{s},\omega_\mathrm{i})\right|^2, \tag{1.1.32}$$

and

$$\left|\psi(\omega_\mathrm{i})\right|^2 = \int_{-\infty}^{\infty} \mathrm{d}\omega_\mathrm{s}\left|\psi(\omega_\mathrm{s},\omega_\mathrm{i})\right|^2. \tag{1.1.33}$$

Photon-pair generation rate. The *joint spectral density* $\left|\psi(\omega_\mathrm{s},\omega_\mathrm{i})\right|^2$ is the expected number of photon pairs emitted per signal/idler bandwidth per unit time for a given pump power.[59]

The photon-pair generation rate $\mathcal{R}$ is proportional to the expectation value:[59,161]

$$\begin{aligned}\mathcal{R} &\propto \langle\psi|\psi\rangle \\ &= \int_0^{\infty}\mathrm{d}\omega_s \int_0^{\infty}\mathrm{d}\omega_i\left|\psi(\omega_\mathrm{s},\omega_\mathrm{i})\right|^2.\end{aligned} \tag{1.1.34}$$

For a monochromatic pump, the photon-pair generation rate integrated over all frequencies is proportional to the length of the nonlinear crystal:

$$R \propto \int_0^{\infty}\mathrm{d}\omega_s\left|f(\omega_\mathrm{s},\omega_\mathrm{p}-\omega_\mathrm{s})\right|^2 \propto l. \tag{1.1.35}$$

This result applies only for plane waves. As will be shown below, for optimally focussed Gaussian beams, the photon-pair generation rate is independent of l.

Higher order terms and thermal photon statistics. We can, of course, evaluate the higher order contributions of the Dyson-series in Eq. 1.1.21. The higher order terms correspond to a simultaneous generation of multiple photon pairs. For example, the second order contribution in Eq. 1.1.28 is of the form:[136]

$$\int_0^\infty \mathrm{d}\omega_\mathrm{s} \int_0^\infty \mathrm{d}\omega_\mathrm{s}' \int_0^\infty \mathrm{d}\omega_\mathrm{i} \int_0^\infty \mathrm{d}\omega_\mathrm{i}' \psi(\omega_\mathrm{s}, \omega_\mathrm{i}) \psi(\omega_\mathrm{s}', \omega_\mathrm{i}') \\ \hat{a}_\mathrm{s}^\dagger(\omega_\mathrm{s}) \hat{a}_\mathrm{s}^\dagger(\omega_\mathrm{s}') \hat{a}_\mathrm{i}^\dagger(\omega_\mathrm{i}) \hat{a}_\mathrm{i}^\dagger(\omega_\mathrm{i}') \, |0, 0\rangle \tag{1.1.36}$$

The expected number of double pairs per signal/idler bandwidth per unit time for a given pump power is therefore proportional to $\left|\psi(\omega_\mathrm{s}, \omega_\mathrm{i})\right|^4$. The ratio of the expected number of double pairs to the expected number of single pairs is identical to the ratio of expected number of single pairs to the expected number of cases, where no photon pair is generated. This behavior corresponds to thermal photon statistics.[56]

Discussion. The quantum theory of spontaneous parametric down-conversion gives exactly the same sinc^2 shaped spectral characteristics as the classical theory for the signal and idler fields. The main differences are, on the one hand, the deterministic correlation between signal and idler photons in the quantum mechanical model manifested by the joint spectral amplitude. On the other hand, in the case of quantum theory, there is the possibility to spontaneously generate signal and idler photons even without any seeding.

The thermal photon statistics limits the usefulness as a single-photon source. A pure single-photon state cannot be produced with spontaneous parametric down-conversion since there are always admixtures of higher-order photon numbers. Of course, the probability to generate multiple pairs simultaneous can be made arbitrarily small by reducing the pump power. But, reducing the pump power also reduces the photon-pair generation rate by the same amount.

Nevertheless, photon-pair sources based on SPDC are routinely used as heralded single-photon sources. The detection of an idler photon *heralds* the presence of the paired photon in the signal mode.[32] Due to the intrinsic correlation between signal and idler photons, the measurement of the idler photon projects the signal photon into a state which can be highly localized in time and space. In a sense, a source of heralded single-photons can be regarded as a lock-in amplifier which does not act in frequency space but in the time domain. The advantage of lock-in amplifier is that it can even tiny signal over a (spectrally) broad background by selecting only signal which are modulated with a certain frequency. In contrast, a heralded single-photon source allows for the detection

of a tiny signal (a single photon) by heralding the precise moment in time when this signal is present at the detector.

As discussed in this section, the joint spectral density is key concept in the theoretical description of the two-photon state. Therefore, we will gradually refine our expression for JSA to accurately define the two-photon state generated by cavity-enhanced SPDC. In the following sections, the theory will be extended to account for the effect a linear cavity placed around the nonlinear crystal has on the generated photon pairs. Here, two aspects are of importance: on the one hand, parametric interaction can take place in two directions in a linear cavity this the pump beam is reflected on the mirrors. This gives rise to an interference between photons generated in the forward direction and photons generated in the backward direction (section 1.1.3). On the other hand, the photons can only be generated at the resonance frequencies of the cavity, which dramatically changes the JSA and thus their spectro-temporal properties (section 1.1.4).

1.1.3 | Double-pass parametric interaction

If the nonlinear crystal is placed inside a linear cavity (Fig. 1.2), parametric interaction of the three waves can take place in both directions. For a cavity pumped through mirror M_1 (Fig. 1.2a), the second mirror M_2 needs to reflect all three waves to allow for this type of double-pass parametric interaction.

Before we analyze a complete cavity with two mirrors (see section 1.1.4), we simplify the problem and discuss the double-pass interaction where only the second mirror M_2 is present. This section analyzes the situation without the first mirror (Fig. 1.2b) to evaluate the effect of the double-pass interaction on the spectrum of the generated photon pairs. There is a coherent superposition of photons generated in the forward direction and the photons generated in the backward direction. There are two different possibilities to generate a photon pair traveling to the left (backward direction). Either the photons are generated in the first pass of the pump and then are reflected by the mirror. Or the pump is reflected and the photon pair is generated in the backward direction. Therefore, the relative phase relation between the two possible interaction directions modifies the joint spectral amplitude and thus determines the spectral shape of photons generated in the double-pass scheme[160] (see Fig. 1.2c).

Relative phase. There is no significant parametric interaction of waves traveling in opposite directions, if the nonlinear crystal is phase-matched for the interaction of co-propagating fields. Nevertheless, counter-propagating (or *backward-wave* interaction) is possible in principle.[162,180] The phase-matching condition can be engineered such that the signal photon is generated traveling in direction of

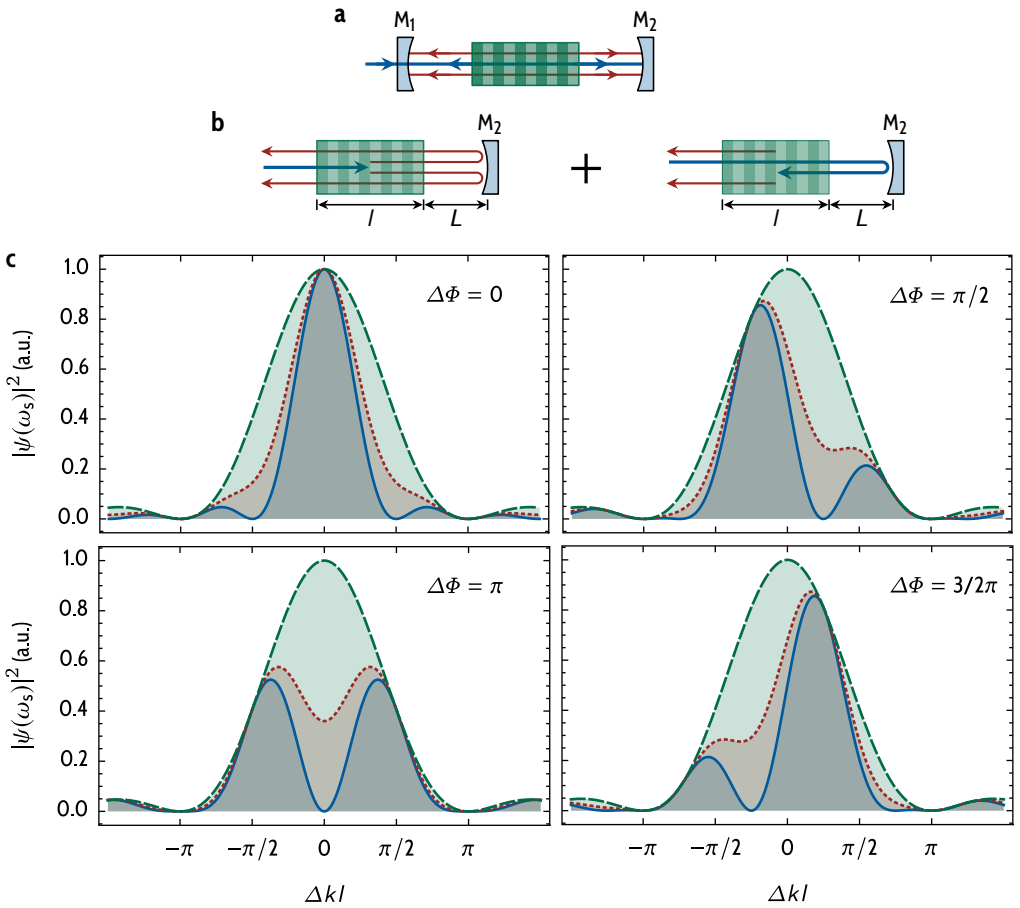

Figure 1.2 | Double-pass parametric interaction. **a**, In a linear cavity, where the second mirror (M_2) reflects both pump, signal and idler fields, parametric interaction in both directions is possible. Since parametric down-conversion is a coherent process, the relative phase $\Delta\Phi$ between the interaction in the forward direction and the interaction in the backward direction affects the spectrum of the generated photon pairs. **b**, To study the effect of double-pass parametric interaction, here we omit the first mirror M_1. The generation of photon pairs in the forward direction can be treated independently from the generation in the backward direction. There are two different realizations how a photon pair traveling to the left can be generated. Either the photon pair is generated in the first pass of the pump and is then reflected by the mirror or it is generated in the second pass. In the latter case the pump has acquired an addition phase between the two passes. In the former case, the reflected photon pair acquires an additional phase. Together these two phase factors and the reflectivity of the mirror determine the spectral shape of the generated photon pairs. **c**, The interference changes the shape of the spectral density $\left|\psi(\omega_s)\right|^2$ (Eq. 1.1.50), which is shown here normalized for $r = r_p = r_s = r_i = 1$ (—), $r = 0.25$ (----), and $r = 0$ (– –). If the relative phase $\Delta\Phi = 0$, there is constructive interference and the spectral width is decreased due to the increased interaction length. For $\Delta\Phi = \pi$, there is destructive interference for $\Delta kl = 0$ and the spectral profile is redistributed. The spectra shown here are normalized by a factor of $1/(r_s r_i + r_p)^2$.

the pump photon while the idler photon is generated traveling in the opposite direction. But, for these kinds of parametric processes, a vastly different poling period would be required.[162,181] Therefore, we assume that both signal and idler photons are generated in the travel direction of the pump photons and the two interactions can be treated independently.

In double-pass parametric down-conversion (see Fig. 1.2b), the quantum state of photon pairs traveling to the left is a superposition[182] of a photon pair generated in the forward (fw) and in the backward directions (bw), respectively:

$$\left|\psi_{\mathrm{dp}}\right\rangle = \left|\psi^{\mathrm{fw}}\right\rangle + \left|\psi^{\mathrm{bw}}\right\rangle \tag{1.1.37}$$

To analyze the interference, the relative phase between $\left|\psi_{\mathrm{fw}}\right\rangle$ and $\left|\psi_{\mathrm{bw}}\right\rangle$ must be found: The mode functions of the pump, defined in Eq. 1.1.17, for the forward and backward direction are:

$$\mathcal{E}_{\mathrm{p}}^{\mathrm{fw}}(k_{\mathrm{p}}, z) = e^{ik_{\mathrm{p}}z}, \tag{1.1.38}$$

and

$$\mathcal{E}_{\mathrm{p}}^{\mathrm{bw}}(k_{\mathrm{p}}, z) = r_{\mathrm{p}} e^{-ik_{\mathrm{p}}z + \phi_{\mathrm{p}}^{\mathrm{bw}}}, \tag{1.1.39}$$

where r_p it the amplitude reflection coefficient which is related to the reflection coefficient R_n by $r_n = \sqrt{R_n}$. Assuming the center of the crystal is at position $z = 0$, the reflected pump wave has a phase relative to the forward direction of:

$$\phi_{\mathrm{p}}^{\mathrm{bw}} = k_{\mathrm{p}} l + 2\phi_{2\mathrm{p}} + \delta_{2\mathrm{p}}. \tag{1.1.40}$$

This expression is the total phase acquired by the pump field between the first and the second interaction measured from the center of the nonlinear crystal. Here, $\delta_{2\mathrm{p}}$ is the phase shift upon reflection on the mirror and $\phi_{2\mathrm{p}}$ is the phase acquired over the optical path length L between the crystal and the mirror M_2 (Fig. 1.2b):

$$\phi_{2\mathrm{p}} = \frac{\omega_{\mathrm{p}}}{c} L. \tag{1.1.41}$$

Mode overlap and interference. The signal/idler mode functions (Eq. 1.1.15) are of the form:

$$\mathcal{E}_{\mathrm{s/i}}^{\mathrm{fw}} = e^{ik_{\mathrm{s/i}}z} \tag{1.1.42}$$

$$\mathcal{E}_{\mathrm{s/i}}^{\mathrm{bw}} = e^{-ik_{\mathrm{s/i}}z}. \tag{1.1.43}$$

The corresponding creation operators are labeled $\hat{a}^{\dagger}_{\mathrm{fw}}(\omega_{\mathrm{s/i}})$ and $\hat{a}^{\dagger}_{\mathrm{bw}}(\omega_{\mathrm{s/i}})$, respectively. Since the two interactions can be considered independently, there is no relative phase between $\mathcal{E}^{\mathrm{fw}}_{\mathrm{s/i}}$ and $\mathcal{E}^{\mathrm{bw}}_{\mathrm{s/i}}$.

The double-pass Hamiltonian (Eq. 1.1.16) is:

$$\widehat{H}^{\mathrm{dp}}_{\mathrm{I}}(t) = \epsilon_0 d_{\mathrm{eff}} \int_0^l \mathrm{d}z \left[E^{\mathrm{fw}}_{\mathrm{p}} \widehat{E}^{\mathrm{fw}}_{\mathrm{s}} \widehat{E}^{\mathrm{fw}}_{\mathrm{i}} + E^{\mathrm{bw}}_{\mathrm{p}} \widehat{E}^{\mathrm{bw}}_{\mathrm{s}} \widehat{E}^{\mathrm{bw}}_{\mathrm{i}} \right], \tag{1.1.44}$$

As discussed above, mixed terms with contributions of both backward and forward fields are discarded, since these interactions are not phase-matched.

The generated two-photon state (Eq. 1.1.37) consists of photon pairs generated in the forward direction and photon pairs generated in the backward direction:

$$\begin{aligned} |\psi\rangle = &\int_0^{\infty} \mathrm{d}\omega_{\mathrm{s}} \int_0^{\infty} \mathrm{d}\omega_{\mathrm{i}}\, \psi_{\mathrm{sp}}(\omega_{\mathrm{s}}, \omega_i) \hat{a}^{\dagger}_{\mathrm{fw}}(\omega_{\mathrm{s}}) \hat{a}^{\dagger}_{\mathrm{fw}}(\omega_{\mathrm{i}}) |0,0\rangle \\ &+ r_{\mathrm{p}} e^{i\phi^{\mathrm{bw}}_{\mathrm{p}}} \int_0^{\infty} \mathrm{d}\omega_{\mathrm{s}} \int_0^{\infty} \mathrm{d}\omega_{\mathrm{i}}\, \psi_{\mathrm{sp}}(\omega_{\mathrm{s}}, \omega_i) \hat{a}^{\dagger}_{\mathrm{bw}}(\omega_{\mathrm{s}}) \hat{a}^{\dagger}_{\mathrm{bw}}(\omega_{\mathrm{i}}) |0,0\rangle , \end{aligned} \tag{1.1.45}$$

where the single-pass joint spectral amplitude $\psi_{\mathrm{sp}}(\omega_{\mathrm{s}}, \omega_{\mathrm{i}})$ is defined in Eq. 1.1.29.

The photon pairs which are generated in the forward direction are reflected by the mirror and have acquired a phase $\phi^{\mathrm{bw}}_{\mathrm{s/i}}$ once they are again situated at the center of the nonlinear crystal. This phase is defined analogously to Eq. 1.1.40. Therefore, the creation operators fulfill the relation:

$$\hat{a}^{\dagger}_{\mathrm{fw}}(\omega_{\mathrm{s/i}}) = r_{2\mathrm{s/i}} \hat{a}^{\dagger}_{\mathrm{bw}}(\omega_{\mathrm{s/i}}) e^{i\phi^{\mathrm{bw}}_{\mathrm{s/i}}}. \tag{1.1.46}$$

Plugging Eq. 1.1.46 into Eq. 1.1.45, the state of photon pairs traveling to the left is:

$$|\psi_{\mathrm{dp}}\rangle = \int_0^{\infty} \mathrm{d}\omega_{\mathrm{s}}\, \mathrm{d}\omega_{\mathrm{i}}\, \psi_{\mathrm{dp}} \hat{a}^{\dagger}_{\mathrm{bw}}(\omega_{\mathrm{s}}) \hat{a}^{\dagger}_{\mathrm{bw}}(\omega_{\mathrm{i}}). \tag{1.1.47}$$

Now, we write the double-pass joint spectral amplitude as a product of the single-pass amplitude multiplied by the *phase-balancing amplitude*[129] $p(\omega_{\mathrm{s}}, \omega_{\mathrm{i}})$:

$$\psi_{\mathrm{dp}}(\omega_{\mathrm{s}}, \omega_{\mathrm{i}}) = \psi_{\mathrm{sp}}(\omega_{\mathrm{s}}, \omega_{\mathrm{i}}) p(\omega_{\mathrm{s}}, \omega_{\mathrm{i}}) \tag{1.1.48}$$

with

$$p(\omega_{\mathrm{s}}, \omega_{\mathrm{i}}) = r_{2\mathrm{s}} r_{2\mathrm{i}} e^{i[\phi^{\mathrm{bw}}_{\mathrm{s}} + \phi^{\mathrm{bw}}_{\mathrm{i}}]} + r_{2\mathrm{p}} e^{i\phi^{\mathrm{bw}}_{\mathrm{p}}}. \tag{1.1.49}$$

Joint spectral density. The corresponding joint spectral density after the double-pass is proportional to the single-pass joint spectral density $\left|\psi_{\mathrm{sp}}(\omega_\mathrm{s},\omega_\mathrm{i})\right|^2$ (see Eq. 1.1.11) multiplied by a phase-balancing factor[129] $P(\omega_\mathrm{s},\omega_\mathrm{i}) = \left|p(\omega_\mathrm{s},\omega_\mathrm{i})\right|^2$:

$$\begin{aligned}\left|\psi_{\mathrm{dp}}(\omega_\mathrm{s},\omega_\mathrm{i})\right|^2 &\propto l^2\,\mathrm{sinc}\left(\frac{\Delta k l}{2}\right)\left[r_{2\mathrm{s}}^2 r_{2\mathrm{i}}^2 + r_{2\mathrm{p}}^2 + 2r_{2\mathrm{p}}r_{2\mathrm{s}}r_{2\mathrm{i}}\cos(\Delta k l + \Delta\Phi)\right]\\ &\equiv \left|\psi_{\mathrm{sp}}(\omega_\mathrm{s},\omega_\mathrm{i})\right|^2 P(\omega_\mathrm{s},\omega_\mathrm{i}),\end{aligned} \tag{1.1.50}$$

where $\Delta\Phi = 2\Delta\phi_2 + \Delta\delta_2$, and $\Delta\delta_2 = \delta_{2\mathrm{p}} - \delta_{2\mathrm{s}} - \delta_{2\mathrm{i}}$.

Note, that any free space of length L between crystal and mirror does not contribute to $\Delta\phi_2$ due to energy conservation:

$$\Delta\phi_2 = (\omega_\mathrm{p} - \omega_\mathrm{s} - \omega_\mathrm{i})\frac{L}{c} = 0. \tag{1.1.51}$$

But, in principle, we can tune the relative phase to any value. This can be achieved by using a dielectric coating with appropriate phase shifts or by placing a suitable compensation crystal between the nonlinear crystal and the mirror, for example.

Double-pass spectrum. In Fig. 1.2c the signal spectral density:

$$\left|\psi_{\mathrm{dp}}(\omega_s)\right|^2 = \int_{-\infty}^{\infty} \mathrm{d}\omega_i \left|\psi_{\mathrm{dp}}(\omega_\mathrm{s},\omega_\mathrm{i})\right|^2 = \left|\psi_{\mathrm{dp}}(\omega_\mathrm{s},\omega_\mathrm{p}-\omega_\mathrm{s})\right|^2 \tag{1.1.52}$$

for a monochromatic pump with $s(\omega_\mathrm{s}+\omega_\mathrm{i}) = \delta(\omega_\mathrm{p}-\omega_\mathrm{s}-\omega_\mathrm{i})$ is shown for different values of $\Delta\Phi$ and $r_{2\mathrm{p}} = r_{2\mathrm{s}} = r_{2\mathrm{i}} = r$. For $r = 1$ and $\Delta\Phi = 0$ the effective interaction length is doubled (see Eq. 1.1.30) and the spectrum corresponds to single-pass parametric down-conversion with a nonlinear crystal of length $2l$:

$$\left|\psi_{\mathrm{dp}}(\omega_\mathrm{s},\omega_\mathrm{i})\right|^2 \propto [2l]^2\,\mathrm{sinc}\left(\frac{\Delta k\,[2l]}{2}\right). \tag{1.1.53}$$

Even for a mirror with low values of the reflection coefficients, the spectral width of the generated photons decreases considerably.

If a metallic mirror is used, $\Delta\Phi = \pi$. In this case, there is destructive interference for $\Delta k = 0$. For double-pass second-harmonic generation, a metallic mirror would result in a vanishing conversion efficiency. This is not the case for double-pass parametric down-conversion, since signal and idler photons can be generated at different wavelengths. For $\Delta\Phi = \pi$, only degenerate photon pairs

interfere destructively and the spectral density is redistributed to signal/idler frequencies with $\Delta k \neq 0$. For other values of $\Delta\Phi$, there is a smooth transition between the sinc^2-shaped spectrum for $\Delta\Phi = 0$ and the double-peaked structure for $\Delta\phi = \pi$.

The total photon-pair generation rate (Eq. 1.1.35) is increased by a factor of

$$\left[r_{2s}^2 r_{2i}^2 + r_{2p}^2\right] \leq 2 \tag{1.1.54}$$

compared to single-pass interaction. The increase is independent of the relative phase $\Delta\Phi$. For $\Delta\Phi = 0$, the maximum of the joint spectral density at $\Delta k = 0$ is larger by a factor of

$$\left[r_{2s} r_{2i} + r_{2p}\right]^2 \leq 4 \tag{1.1.55}$$

compared to the single-pass joint spectral density.

Discussion. Double-pass parametric down-conversion offers a convenient way to double the effective length of the nonlinear crystal. Under optimal conditions ($r_{2n} = 1$), this results in an enhancement of the photon-pair generation rate by a factor of 2 (integrated of the whole spectrum). More importantly, for the application in mind, only photon pairs at the center of the parametric gain envelope are spectrally selected by filters external to the cavity. The spectral brightness (at degeneracy $\Delta k = 0$) is increased by double-pass pumping by a factor of up to 4 for $\Delta\Phi = 0$. Therefore, if the filtered region is much smaller than the full width of the gain envelope, a filtered double-pass photon-pair source would be a factor of up to 4 brighter than a single-pass source filtered with the same spectral filter.

For optimum performance, the relative phase must be tuned to $\Delta\Phi = 0$. This can be achieved either with the use of a compensation crystal or by applying a dielectric coating with appropriate phase shifts for the three fields onto the mirror. Note, that the preceding discussion assumes a perfect collinear alignment of the three beams. If the pump beam is not perfectly collinear with the signal and idler fields (e.g. caused by walk-off in a tilted crystal), the visibility of the interference between photon pairs generated in the forward direction and photon pairs generated in the backward direction is reduced. This corresponds to a reduction of the parameter $\bar{r}$, as observed in the experiment (see the discussion of the experiments in section 2.3.6). Further studies are required analyze this reduction of $\bar{r}$ as function of, e.g., the tilt crystals inside the cavity or a misalignment of the mirrors.

In the case of cavity-enhanced parametric down-conversion in a linear *triply-resonant* cavity signal and idler photons can also be generated in both directions.

Therefore, we observe the same interference effect. We will analyze triply resonant photon-pair sources in the following section.

1.1.4 | Triply-resonant cavity

Several authors already treated photon-pair generation by cavity-enhanced parametric down-conversion. To pinpoint the contributions of this section, we detail the existing literature on this topic in the following.

The first theoretical studies of triply-resonant three-wave mixing were conducted in the 1960ies.[182–184] A thorough analysis of type-II parametric interaction inside a cavity was performed by Debuisschert and colleagues.[185] All of these studies have in common that they aim at optical parametric oscillation above the oscillation threshold. Therefore, only part of their analysis applies here and e.g. below the threshold, the spectral structure of the generated photon pairs was not analyzed. Nevertheless, the interference effect of parametric interaction in both directions present in a linear triply-resonant cavity was already described in these works.

Cavity-enhanced parametric down-conversion in the context of photon-pair generation was first theoretically analyzed by Ou and Lu.[111] Starting from expressions derived in the context of squeezed state generation,[113] they derived an expression for the generation rate enhancement per cavity mode compared to single-pass down-conversion. Their theory treats just a single cavity mode but takes into account losses inside the cavity.

A fully quantum mechanical model of a singly and doubly-resonant down-converter including multiple cavity modes was developed by Herzog[160] and Scholz and colleagues.[161] They derived an expression for the two-photon quantum state from which the generation rate, spectral densities and signal/idler correlation functions could be obtained. Triply-resonant cavity were not covered.

Jeronimo-Moreno and coworkers[129] published a multi-mode theory for a triply-resonant linear (standing wave) cavity. Their model assumes a cavity without losses. As a consequence, their theory does not provide an expression for absolute count-rates. There is an emphasis on the spectral characteristics of the generated photon pairs in their work. They derived the joint spectral amplitude by starting with a photon pair being generated in the cavity and summing over all possible realizations of the photons being reflected or transmitted by the cavity mirrors. While Scholz et al. found the joint spectral density in terms of an infinite sum over Lorenztian-shaped resonances spaced by the free spectral

range, Jeronimo-Moreno et al. obtained a joint spectral density in terms of more intuitive Airy functions.

For a single-mode doubly-resonant cavity, Chuu and coworkers[130,162] derived a theory similar to Ou and Lu with more details. They derived an expression for the absolute generation rate in terms of the finesse and the losses inside the cavity.

In the context of doubly-resonant down-conversion inside a nonlinear waveguide, Luo et al.[136,137] also provided (but did not derive) an expression for the joint spectral density in terms of Airy functions including losses inside the cavity. They further analyzed in detail the signal/idler second order correlation functions for a resonator for which the signal free spectral range differs from the idler free spectral range.

This section develops an expression for the joint spectral amplitude of a monolithic, triply-resonant cavity. In contrast to Jeronimo-Moreno, we include losses inside the cavity and we derive the Airy functions with a different approach inspired by works on resonant second-harmonic generation.[186] In the limit of a lossless cavity, the results found here coincide with Jeronimo-Moreno's.

The comparable expression found by Luo et al. is inherently non-quantitative in nature due to a normalization of the Airy functions. In contrast, with the theory presented here, it is possible to derive an expression for the absolute brightness of the photon-pair source.

In a linear cavity, photon pairs can be generated in both directions, giving rise to interference effects similar to the double-pass parametric interaction discussed in section 1.1.3. But, as will be shown, the form of the phase-balancing amplitude differs slightly from Eq. 1.1.49, since we assume that the photon pairs leave the cavity through mirror M_2 instead of being reflected by it (Figs. 1.2 and 1.3).

Fields inside the cavity. To describe the process of parametric down-conversion inside a linear cavity, we require an expression for the mode functions (Eq. 1.1.15). The discussion presented here follows the theory of Fujimura and coworkers[186,187] on second-harmonic generation inside a monolithic resonator.

In a monolithic cavity (Fig. 1.3a) with mirrors M_j, a dielectric coating with amplitude reflection coefficient $r_j e^{i\delta_j}$ and amplitude transmission coefficients t_j is applied onto the front and back facets of the nonlinear crystal. To distinguish fields inside and outside the cavity, the following photon creation operators are introduced: For photons generated inside the cavity, $a^\dagger_{\mathrm{fw}}$ and $\hat{a}^\dagger_{\mathrm{bw}}$ are the creation operator for the forward and the backward direction, respectively. For photons

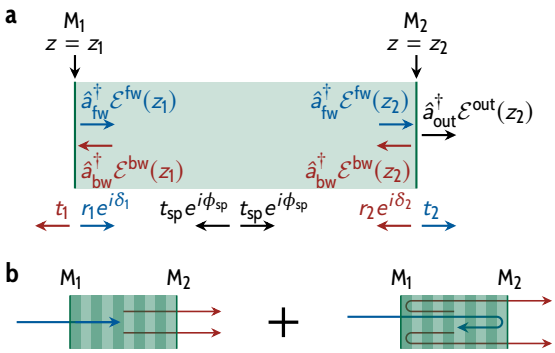

Figure 1.3 | Resonating field inside a monolithic cavity. **a**, To derive an expression for the signal/idler mode functions $\mathcal{E}^{\mathrm{fw}}_{\mathrm{s/i}}(z)$ and $\mathcal{E}^{\mathrm{bw}}_{\mathrm{s/i}}(z)$ inside the resonator, photon creation operators $\hat{a}^{\dagger}_{\mathrm{fw}}(\omega_{\mathrm{s/i}})$ for the generation in the forward and $\hat{a}^{\dagger}_{\mathrm{bw}}(\omega_{\mathrm{s/i}})$ for the generation in the backward direction are introduced. The mirrors are located at the positions z_1 and z_2. The mirrors have the (amplitude) transmission coefficient t_n and amplitude reflection coefficients $r_n e^{i\delta_n}$. In a single pass through the cavity, the amplitude of the mode function is reduced by a factor t_{sp} and it acquires a phase ϕ_{sp}. **b**, Interference of photons generated in the forward direction and photons generated in the backward direction: The quantum state for photon pairs leaving the cavity through mirror M_2 is a superposition of the following processes. Either the photons are generated in the forward direction and exit the cavity after a certain number of round trips or they are generated in the backward direction and exit the cavity after a certain number of round trips. In the latter case, the pump acquires an additional phase factor, since it is reflected by mirror M_2 and the photon pair acquires an additional phase factor compared to the former case by being reflected by mirror M_1. Due to the resonance condition, all contributions from the individual round trips interfere constructively and do not have to be analyzed separately.

leaving the cavity at the desired output port through mirror M_2, the creation operator $a^\dagger_{\text{out}}$ is used. Signal and idler photons leaving the cavity through M_1 are lost for the experiment. Upon traversal of the cavity, the photons acquire a single-pass phase $\phi_{\text{sp}} = kl$ and their amplitude is multiplied by the single-pass transmission t_{sp}.

In a triply-resonant cavity pumped from the left through mirror M_1, there are two interfering ways for a generated photon pair to exit the cavity through mirror M_2 (Fig. 1.3b). The photon pair can be generated in the forward direction, perform a certain number of cavity round trips and leave through M_2, or it can be generated in the backward direction. In the latter case, the pump has acquired a different phase compared to the generation in the forward direction and the photon pair acquires an additional phase by first being reflected by mirror M_1 and leaving through M_2 after a certain amount of round trips. Note, that on resonance, all contributions from different round trips interfere constructively due to the resonance condition derived below.

Boundary conditions. The signal/idler mode functions $\mathcal{E}^{\text{fw}}(z)$ and $\mathcal{E}^{\text{bw}}(z)$ for photon pairs generated in the forward and backward directions can be found by considering their boundary conditions in the steady state (Fig. 1.3a). For photon pairs generated in the forward direction, we find at the first mirror M_1:

$$\hat{a}^\dagger_{\text{fw}}\mathcal{E}^{\text{fw}}(z_1) = \hat{a}^\dagger_{\text{bw}} r_1 e^{i\delta_1}\mathcal{E}^{\text{bw}}(z_1) + \hat{a}^\dagger_{\text{fw}} \tag{1.1.56}$$

$$\hat{a}^\dagger_{\text{bw}}\mathcal{E}^{\text{bw}}(z_1) = \hat{a}^\dagger_{\text{bw}} t_{\text{sp}} e^{i\phi_{\text{sp}}}\mathcal{E}^{\text{bw}}(z_2), \tag{1.1.57}$$

and at mirror M_2:

$$\hat{a}^\dagger_{\text{fw}}\mathcal{E}^{\text{fw}}(z_2) = \hat{a}^\dagger_{\text{fw}} t_{\text{sp}} e^{i\phi_{\text{sp}}}\mathcal{E}^{\text{fw}}(z_1) \tag{1.1.58}$$

$$\hat{a}^\dagger_{\text{bw}}\mathcal{E}^{\text{bw}}(z_2) = \hat{a}^\dagger_{\text{fw}} r_2 e^{i\delta_2}\mathcal{E}^{\text{fw}}(z_2). \tag{1.1.59}$$

These are four equations for the four unknown boundary values of the forward and backward fields. The extra creation operator $a^\dagger_{\text{fw}}$ on the right hand side of Eq. 1.1.56 is the source term in this system of equations. It corresponds to the creation of a photon pair at the front section of the nonlinear crystal.

Cavity mode functions. With the solutions for the boundary values, we can construct the signal/idler mode functions for photons generated in the forward direction:

$$\mathcal{E}^{\text{fw}}_{\text{s/i}}(\omega_{\text{s/i}}, z) = \mathcal{T}_{\text{s/i}}(\omega_{\text{s/i}}) e^{ik_{\text{s/i}}z} \tag{1.1.60}$$

with the complex cavity round-trip transmission function:

$$\mathcal{T}_n(\omega_n) = \frac{1}{1 - r_{1n} r_{2n} t_{\mathrm{sp},n}^2 e^{i[\delta_{1n} + \delta_{2n} + \phi_{\mathrm{rt},n}(\omega_n)]}}, \tag{1.1.61}$$

where $\phi_{\mathrm{rt}} = 2\phi_{\mathrm{sp}}$ in the round-trip phase and the coordinate system is chosen such that $z_1 = -l/2$ and $z_2 = l/2$.

For photons generated in the backward direction, Eqs. 1.1.56 and 1.1.59 have to be replaced by:

$$\hat{a}^\dagger_{\mathrm{fw}} \mathcal{E}^{\mathrm{fw}}(z_1) = \hat{a}^\dagger_{\mathrm{bw}} r_1 e^{i\delta_1} \mathcal{E}^{\mathrm{bw}}(z_1) \tag{1.1.62}$$

$$\hat{a}^\dagger_{\mathrm{bw}} \mathcal{E}^{\mathrm{bw}}(z_2) = \hat{a}^\dagger_{\mathrm{fw}} r_2 e^{i\delta_2} \mathcal{E}^{\mathrm{fw}}(z_2) + \hat{a}^\dagger_{\mathrm{bw}}. \tag{1.1.63}$$

Thus, the mode function in the backward direction is:

$$\mathcal{E}^{\mathrm{bw}}_{\mathrm{s/i}}(\omega_{\mathrm{s/i}}, z) = \mathcal{T}_{\mathrm{s/i}}(\omega_{\mathrm{s/i}}) e^{-ik_{\mathrm{s/i}} z}. \tag{1.1.64}$$

We can set up an analogous set of boundary conditions for the classical pump field (where no creation operators are required). The only difference is that in the first equation, Eq. 1.1.56, the mode function of the incoupling field $\mathcal{E}^{\mathrm{in}}_{\mathrm{p}}(z)$ is the source term:

$$\mathcal{E}^{\mathrm{fw}}_{p}(z_1) = t_{1\mathrm{p}} \mathcal{E}^{\mathrm{in}}_{\mathrm{p}}(z_1) + r_{1\mathrm{p}} e^{i\delta_{1\mathrm{p}}} \mathcal{E}^{\mathrm{bw}}_{\mathrm{p}}(z_1). \tag{1.1.65}$$

The solutions are:

$$\mathcal{E}^{\mathrm{fw}}_{\mathrm{p}}(\omega_{\mathrm{p}}, z) = t_{1\mathrm{p}} \mathcal{E}^{\mathrm{in}}_{\mathrm{p}}(z_1) \mathcal{T}_{\mathrm{p}}(\omega_{\mathrm{p}}) e^{ik_{\mathrm{p}} z} \tag{1.1.66}$$

$$\mathcal{E}^{\mathrm{bw}}_{\mathrm{p}}(\omega_{\mathrm{p}}, z) = t_{1\mathrm{p}} \mathcal{E}^{\mathrm{in}}_{\mathrm{p}}(z_1) t_{\mathrm{sp,p}} r_{2\mathrm{p}} e^{i[\delta_{2\mathrm{p}} + \phi_{\mathrm{sp}}(\omega_{\mathrm{p}})]} \mathcal{T}_{\mathrm{p}}(\omega_{\mathrm{p}}) e^{-ik_{\mathrm{p}} z}. \tag{1.1.67}$$

Joint spectral amplitude. Now, we can plug the expressions for the forward and backward fields into Eq. 1.1.44 to obtain the intra-cavity state $|\psi_{\text{intra-cavity}}\rangle$. Since the z-dependence of the mode functions ($\exp(ik_n z)$) is identical to the single-pass case, we can express the state in terms of the single-pass joint spectral amplitude (Eq. 1.1.29):

$$\begin{aligned} |\psi_{\text{intra-cavity}}\rangle = \int_0^\infty \mathrm{d}\omega_{\mathrm{s}}\, \mathrm{d}\omega_{\mathrm{i}}\, \psi_{\mathrm{sp}}(\omega_{\mathrm{s}}, \omega_i) t_{1\mathrm{p}} \mathcal{T}_{\mathrm{p}}(\omega_{\mathrm{s}} + \omega_{\mathrm{i}}) \mathcal{T}_{\mathrm{s}}(\omega_{\mathrm{s}}) \mathcal{T}_{\mathrm{i}}(\omega_{\mathrm{i}}) \\ \times \left[\hat{a}^\dagger_{\mathrm{fw}}(\omega_{\mathrm{s}}) \hat{a}^\dagger_{\mathrm{fw}}(\omega_{\mathrm{i}}) \right. \\ \left. + r_{2\mathrm{p}} t_{\mathrm{sp,p}} \hat{a}^\dagger_{\mathrm{bw}}(\omega_{\mathrm{s}}) \hat{a}^\dagger_{\mathrm{bw}}(\omega_{\mathrm{i}}) e^{i[k_{\mathrm{p}} + \delta_{2\mathrm{p}})} \right] |0, 0\rangle . \end{aligned} \tag{1.1.68}$$

With the help of the relation $\hat{a}^{\dagger}_{\mathrm{bw}}(\omega_{\mathrm{s/i}}) = r_{1\mathrm{s/i}} t_{\mathrm{sp,s/i}} \hat{a}^{\dagger}_{\mathrm{fw}}(\omega_{\mathrm{s/i}})$, the intra-cavity joint spectral amplitude can be expressed as:

$$\begin{aligned}\psi_{\text{intra-cavity}}(\omega_{\mathrm{s}}, \omega_{\mathrm{i}}) = \psi_{\mathrm{sp}}(\omega_{\mathrm{s}}, \omega_i) t_{1\mathrm{p}} \mathcal{T}_{\mathrm{p}}(\omega_{\mathrm{s}} + \omega_{\mathrm{i}}) \mathcal{T}_{\mathrm{s}}(\omega_{\mathrm{s}}) \mathcal{T}_{\mathrm{i}}(\omega_{\mathrm{i}}) \\ \times \left[1 + r_{2\mathrm{p}} r_{1\mathrm{s}} r_{1\mathrm{i}} t_{\mathrm{sp,p}} t_{\mathrm{sp,s}} t_{\mathrm{sp,i}} e^{i[k_{\mathrm{p}} + k_{\mathrm{s}} + k_{\mathrm{i}} + \delta_{2\mathrm{p}} + \delta_{1\mathrm{s}} + \delta_{1\mathrm{i}}]}\right].\end{aligned} \tag{1.1.69}$$

To compute the state behind the output port (mirror M_2), an additional boundary condition can be found (Fig. 1.3):

$$\hat{a}^{\dagger}_{\mathrm{out}}(\omega_n) \mathcal{E}^{\mathrm{out}}(z_2) = \hat{a}^{\dagger}_{\mathrm{fw}}(\omega_n) t_2 \mathcal{E}^{\mathrm{fw}}(z_2), \tag{1.1.70}$$

from which $\hat{a}^{\dagger}_{\mathrm{out}}(\omega_n) = t_{2n} \hat{a}^{\dagger}_{\mathrm{fw}}(\omega_n)$ can be deduced. Therefore, the joint spectral amplitude $\psi_{\mathrm{cavity}}(\omega_{\mathrm{s}}, \omega_{\mathrm{i}})$ behind the output mirror is:

$$\begin{aligned}\psi_{\mathrm{cavity}}(\omega_{\mathrm{s}}, \omega_{\mathrm{i}}) &= t_{2\mathrm{s}} t_{2\mathrm{i}} \psi_{\text{intra-cavity}}(\omega_{\mathrm{s}}, \omega_{\mathrm{i}}) \\ &= \psi_{\mathrm{sp}}(\omega_{\mathrm{s}}, \omega_{\mathrm{i}}) t_{1\mathrm{p}} \mathcal{T}_{\mathrm{p}}(\omega_{\mathrm{s}} + \omega_{\mathrm{i}}) t_{2\mathrm{s}} \mathcal{T}_{\mathrm{s}}(\omega_{\mathrm{s}}) t_{2\mathrm{i}} \mathcal{T}_{\mathrm{i}}(\omega_{\mathrm{i}}) p_{\mathrm{cavity}}(\omega_{\mathrm{s}}, \omega_{\mathrm{i}}),\end{aligned} \tag{1.1.71}$$

(1.1.72)

with the phase-balancing amplitude corresponding to Eq. 1.1.49

$$p_{\mathrm{cavity}}(\omega_{\mathrm{s}}, \omega_{\mathrm{i}}) = 1 + r_{2\mathrm{p}} r_{1\mathrm{s}} r_{1\mathrm{i}} t_{\mathrm{sp,p}} t_{\mathrm{sp,s}} t_{\mathrm{sp,i}} e^{i[\Sigma kl + \Sigma\delta]} \tag{1.1.73}$$

$$\equiv 1 + \bar{r} e^{i[\Sigma kl + \Sigma\delta]}, \tag{1.1.74}$$

with $\Sigma k = k_{\mathrm{p}} + k_{\mathrm{s}} + k_{\mathrm{i}}$, $\Sigma\delta = \delta_{2\mathrm{p}} + \delta_{1\mathrm{s}} + \delta_{1\mathrm{i}}$ and

$$\bar{r} = r_{2\mathrm{p}} r_{1\mathrm{s}} r_{1\mathrm{i}} t_{\mathrm{sp,p}} t_{\mathrm{sp,s}} t_{\mathrm{sp,i}}. \tag{1.1.75}$$

Analogous expressions for $\psi_{\mathrm{cavity}}(\omega_{\mathrm{s}}, \omega_{\mathrm{i}})$ and $p_{\mathrm{cavity}}(\omega_{\mathrm{s}}, \omega_{\mathrm{i}})$ have been found for a lossless cavity by Jeronimo-Moreno and coworkers.[129]

The joint spectral density can be expressed in terms of (non-normalized)[136] Airy functions:

$$\mathcal{A}_{\mathrm{s/i}}(\omega_{\mathrm{s/i}}) = \left|t_{2\mathrm{s/i}} \mathcal{T}_{\mathrm{s/i}}(\omega_{\mathrm{s/i}})\right|^2 \quad \text{and} \tag{1.1.76}$$

$$\mathcal{A}_{\mathrm{p}}(\omega_{\mathrm{p}}) = \left|t_{1\mathrm{p}} \mathcal{T}_{\mathrm{p}}(\omega_{\mathrm{p}})\right|^2. \tag{1.1.77}$$

It is:

$$\left|\psi_{\mathrm{cavity}}(\omega_{\mathrm{s}}, \omega_{\mathrm{i}})\right|^2 = \left|\psi_{\mathrm{sp}}(\omega_{\mathrm{s}}, \omega_{\mathrm{i}})\right|^2 \mathcal{A}_{\mathrm{p}}(\omega_{\mathrm{s}} + \omega_{\mathrm{i}}) \mathcal{A}_{\mathrm{s}}(\omega_{\mathrm{s}}) \mathcal{A}_{\mathrm{i}}(\omega_{\mathrm{i}}) P(\omega_{\mathrm{s}}, \omega_{\mathrm{i}}). \tag{1.1.78}$$

The phase-balancing factor $P_{\text{cavity}}(\omega_s, \omega_i)$ is:

$$P_{\text{cavity}}(\omega_s, \omega_i) = 1 + \bar{r}^2 + 2\bar{r}\cos(\Sigma kl + \Sigma\delta). \tag{1.1.79}$$

One might assume that the appearance of Σkl in Eq. 1.1.79 instead of Δkl in Eq. 1.1.50 might change the spectral properties compared to the double-pass interaction. But, since a triply-resonant down-conversion source it normally operated at a mirror distance close to a pump resonance, the pump resonance condition can be applied:

$$\phi_{\text{rt,p}} = 2k_p l + \delta_{1p} + \delta_{2p} = 2\pi m, \quad m \in \mathbb{N} \tag{1.1.80}$$

$$\Rightarrow k_p l + \delta_{2p} = 2\pi m - k_p l - \delta_{1p}. \tag{1.1.81}$$

Therefore, the phase-balancing factor can, again, be expressed in terms of the phase mismatch Δkl:

$$P_{\text{cavity}}(\omega_s, \omega_i) = 1 + \bar{r}^2 + 2\bar{r}\cos(\Delta kl + \Delta\delta_1), \tag{1.1.82}$$

which describes the same spectral features as discussed in section 1.1.3 and shown in Fig. 1.2, albeit with a different definition of the relative phase $\Delta\Phi$.

Discussion. In the limit of a lossless cavity ($t_{\text{sp},n} = 1$ and $r_{1s/i} = 1$), Eq. 1.1.72 corresponds to the expression found by Jeronimo-Moreno and colleagues.[129] For practical purposes, e.g. when calculating absolute generation rates, it is nevertheless vital to include the losses. Especially for larger values of the signal/idler cavity finesse, the losses dramatically decrease the escape efficiency (i.e. the chance that the generated photons exit the cavity through the desired output port). We will discussed this finding in detail in section 1.3.3.

The theory of cavity-enhanced parametric down-conversion presented here, can easily be extended to more complex configurations of the cavity (e.g. Figs. 1.1a and 1.4a). For this, the single-pass transmission t_{sp} and the phase ϕ_{sp} have to be modified accordingly. If there are additional elements inside the cavity, the phase-balancing factor also needs to be modified to account for additional phase contributions. An expression for $\left|\psi_{\text{cavity}}(\omega_s, \omega_i)\right|^2$ for arbitrary cavity geometries will be given in section 1.3.1.

The spectral density of the signal photons (for a cavity which is resonant to a monochromatic pump beam) can be derived from Eq. 1.1.78 to be:

$$\left|\psi_{\text{cavity}}(\omega_s)\right|^2 = \left|\psi_{\text{sp}}(\omega_s)\right|^2 P(\omega_s, \omega_p - \omega_s)\mathcal{A}_s(\omega_s)\mathcal{A}_i(\omega_p - \omega_s). \tag{1.1.83}$$

The modified parametric gain envelope $\left|\psi_{\text{sp}}(\omega_s)\right|^2 P(\omega_s, \omega_p - \omega_s)$ is multiplied by a factor $\mathcal{A}_s(\omega_s)\mathcal{A}_i(\omega_p - \omega_s)$ which describes *joint resonances* of signal and

idler fields. Only where both fields are resonant and energy conservation $\omega_s + \omega_i = \omega_p$ is satisfied simultaneously, a joint resonance can be found. If the free spectral ranges for signal and idler fields differ, this results in the formation of *clusters*[162,188] of joint resonances (Fig. 1.4). If the free spectral range is identical, a full comb of joint resonances can be observed (Fig. 1.1).

Note, that the two-photon state produced by cavity-enhanced parametric down-conversion is closely related to the two-photon state of conventional spontaneous parametric down-conversion spectrally filtered by a cavity placed after the nonlinear crystal (Fig. 1.5). If, in the latter case, the state is post-selected for the case where both signal and idler photons are transmitted by the cavity, the joint spectral density of the photon pairs is:[36]

$$\left|\psi_{\text{filtered}}(\omega_s, \omega_i)\right|^2 = \left|\psi_{\text{sp}}(\omega_s, \omega_i)\right|^2 \mathcal{A}^{\text{s}}_{\text{filter}}(\omega_s)\mathcal{A}^{\text{i}}_{\text{filter}}(\omega_i), \tag{1.1.84}$$

where $\mathcal{A}_{\text{filter}}(\omega)$ is the filter-cavity transmission function:

$$\mathcal{A}_{\text{filter}}(\omega) = \left|t_1 t_2 t_{\text{sp}} \mathcal{T}(\omega)\right|^2. \tag{1.1.85}$$

Of course, in Eq. 1.1.84, neither a phase-balancing factor nor the pump Airy function $\mathcal{A}_p(\omega_p)$ enter since there is only a single interaction of the pump with the nonlinear crystal. Another major difference is that the brightness of a photon-pair source which is filtered after the generation of signal and idler photons is much lower than the brightness of a cavity-enhanced photon-pair source with the same cavity linewidth. In fact, if the photons are filtered after the generation (Fig. 1.5), the source is always less bright than an unfiltered down-conversion source, while a cavity-enhanced source can even exhibit a larger brightness than an unfiltered source. The cavity enhancement is discussed in detail in section 1.3.2.

1.2 | Interaction of Gaussian beams

In the previous sections, we studied the parametric interaction of plane waves. Although many of the observed phenomena can be explained with this simple model, some experiments presented in this thesis can only be explained if one extends the theory to the interaction of Gaussian fields. Since focussing the pump beam has a strong impact on the brightness of the photon-pair source, absolute photon-pair generation rates can only be calculated if the beam profiles of the interacting fields are taken into account.

The parametric interaction of Gaussian beams in classical nonlinear optics was studied in great detail in the seminal work of Boyd and Kleinman[174] in the

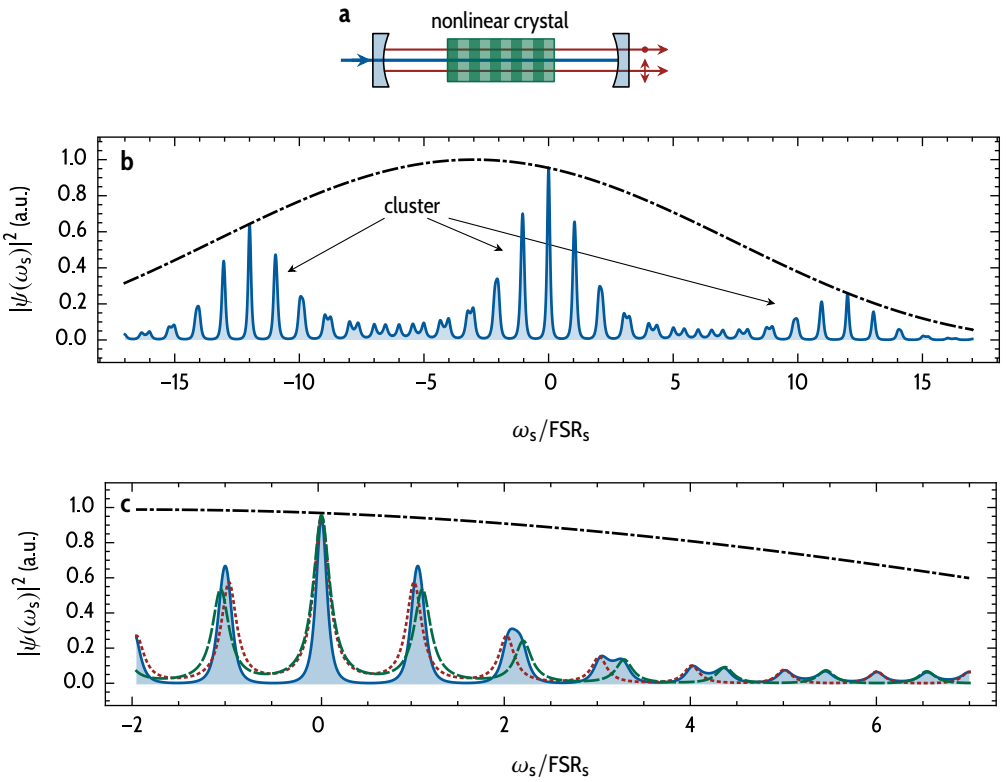

Figure 1.4 | Spectrum of photons generated by cavity-enhanced parametric down-conversion. **a**, Single-crystal cavity-enhanced parametric down-conversion: If there is no compensation crystal inside the cavity, the free spectral range of the signal photons is not identical to the free spectral range of the idler photons, in general. E.g. for type-II phase matching, signal and idler photons experience a different refractive index inside the nonlinear crystal. Therefore, the spectral structure is different to the one shown in Fig. 1.1. **b**, Cluster effect in cavity-enhanced parametric down-conversion: Here, the signal spectral density $\left|\psi(\omega_s)\right|^2$ (——) for unequal free spectral range of the signal and idler photons is plotted. For this plot, the signal/idler finesse is $\mathcal{F}_{s/i} = 5$ and the ratio of the free spectral ranges is $1 : 1.09$. Note, that the maximum of the parametric gain envelope $\left|\psi_{sp}(\omega_s)\right|^2 P(\omega_s, \omega_p - \omega_s)$ (–·–) does not in general coincide with the center of a cluster. **c**,Detail of the plot shown in **a**: Each cluster consists of several joint resonances where signal (----) and idler (– –) resonances partially overlap. To guide the eye, each of the resonances defined by $\mathcal{A}_s(\omega_s)$ and $\mathcal{A}_i(\omega_p - \omega_s)$ is scaled by $\left|\psi(\omega_s)\right|^2$. For larger values of the signal/idler finesse, the overlap of adjacent signal/idler resonances is reduced, resulting in fewer modes per cluster.

late 1960ies. Their work covers a broad range of parametric interactions and does not solely target difference-frequency generation. With the advent of bright sources of non-classical light based on spontaneous parametric down-conversion, the need to provide a more comprehensive theory targeting photon-pair generation and absolute generation rates arose. Numerous works addressed various configurations under different conditions.[189–194] The discussion in this section is based on the theory of Bennink[59] since it is specifically targeted at collinear spontaneous parametric down-conversion. It is therefore the most suitable theory which can be extended to describe cavity-enhanced photon-pair generation, and it is thoroughly tested and verified experimentally.[195]

To provide an intuitive approach, this section will start from classical (non-resonant) nonlinear optics to discuss the effect of focussing on the phase-matching condition and the brightness of the source. The modified phase matching results in a modified spectrum of the generated photons, which we will discuss in detail. Subsequently, we will analyze the parametric interaction inside a cavity, taking into account the Gaussian nature of the fundamental mode of the cavity. To account e.g. for additional compensation crystals inside the cavity, this section studies cavities of arbitrary geometry and with an arbitrary number of optical media. For triply-resonant standing-wave cavities, the beam profile of the three fields cannot be chosen independently. In the final part of this section, we will discuss how this affects the brightness of the photon-pair source.

Gouy phase shift in classical nonlinear optics. In the case of focused Gaussian beams interacting with a nonlinear medium, the so called *Gouy phase shift* has to be taken into account as it affects the phase matching between the electrical fields and the nonlinear polarizations.[175] Upon propagation through the focus with beam waist w_0, an incident wave acquires a phase shift ϕ_{Gouy} of π

$$\phi_{\text{Gouy}}(z) = -\arctan\left(\frac{z}{z_{\text{R}}}\right), \tag{1.2.1}$$

where z_{R} is the *Rayleigh length* $z_{\text{R}} = (\pi w_0^2)/\lambda$. One can show that the parametric interaction is most efficient if the Rayleigh length of the generated fields is identical to the Rayleigh length of the pump field.[59,174] Then, according to Eq. 1.2.1, the Gouy phase shift for all involved fields is the same.

Since the Gouy phase is an entirely classical phenomenon, the notation introduced in section 1.1.1 can be reused. The field amplitudes are replaced by:

$$A_n(z) \longrightarrow A'_n(z)e^{i\phi_{\text{Gouy}}(z)}, \qquad n = \text{p, s, i.} \tag{1.2.2}$$

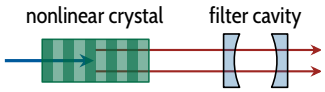

Figure 1.5 | Filtering with a cavity after the generation of photon pairs. Instead of placing the nonlinear crystal inside the cavity, a cavity can be used to spectrally filter the photon pairs generated by spontaneous parametric down-conversion. The two-photon state can be post-selected for the case that both photons are transmitted by the filter cavity. Then, the state cannot be distinguished from the two-photon state generated by (non pump resonant) cavity-enhanced parametric down-conversion, given that the free spectral range and linewidth of the cavity are identical. The key difference between these two photon-pair sources is, that a cavity-enhanced source can be much brighter in terms of photon-pair generation rate per pump power.

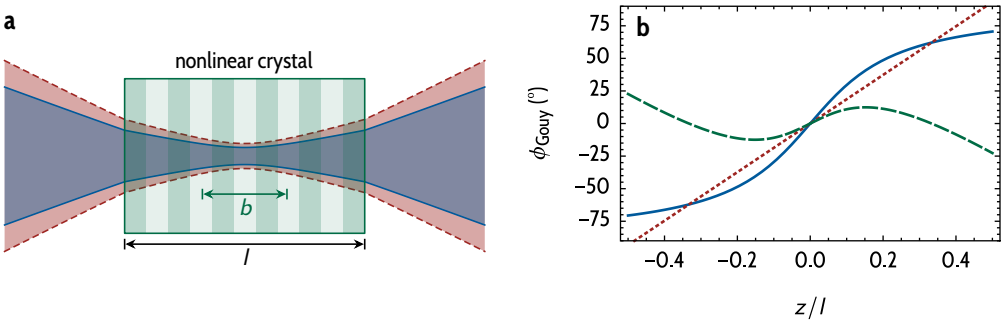

Figure 1.6 | Compensation of the Gouy phase shift. **a**, Simulation of the pump (—) and signal/idler (----) beam profile with a nonlinear crystal of length l and identical confocal parameters $b = 2z_R$. At degeneracy, the waist of the signal/idler field is a factor of $\sqrt{2}$ larger than the waist of the pump field. The confocal parameter is chosen so that the ratio $\xi = l/b = 2.838$ and the conversion efficiency is maximum.[174] **b**, Partial compensation of the Gouy phase shift for a nonzero phase mismatch $\Delta k > 0$. The Gouy phase causes a spatially varying phase mismatch between the electrical fields and the corresponding nonlinear polarization. At nominal phase matching ($\Delta k = 0$), a phase mismatch of $\phi_{\text{Gouy}}(z)$ (—) would occur, which reduces the conversion efficiency. A positive phase mismatch yields a spatial phase of Δkz (----). At the optimum phase mismatch $\Delta k = 3.254/l$ and when $\xi = 2.838$, the phase mismatch $\Phi_{\text{Gouy}} - \Delta kz$ (– –) is minimum and the spectral density is maximized.

In the case of degenerate parametric down-conversion with perfect phase matching, the nonlinear polarization at the pump frequency acquires an additional phase shift of $2\phi_{\text{Gouy}}$:

$$\tilde{P}_{\text{p}}(z,t) = 4\epsilon_0 d_{\text{eff}} A'_{\text{s}} A'_{\text{i}} e^{-i2\phi_{\text{Gouy}}(z)} e^{-i[\omega_{\text{p}} t + k_{\text{p}} z]}, \qquad \text{for } \Delta k = 0. \tag{1.2.3}$$

Therefore, there is a phase difference of ϕ_{Gouy} between the nonlinear polarization $\tilde{P}_{\text{p}}(z,t)$ and the electrical field

$$\tilde{E}_{\text{p}}(z,t) = A'_{\text{p}} e^{-i\phi_{\text{Gouy}}(z)} e^{-i[\omega_{\text{p}} t + k_{\text{p}} z]}, \tag{1.2.4}$$

which results in a reduced conversion efficiency for $\Delta k = 0$. The same is true for the signal and idler fields. But, for a positive wave-vector mismatch $\Delta k > 0$, there is a partial compensation of this phase difference between the nonlinear polarization and the corresponding electrical field. The effective phase mismatch is shown in Fig. 1.6. It is given by:

$$\phi_{\text{Gouy}} - \Delta k z. \tag{1.2.5}$$

Therefore, the largest values of the joint spectral density can no longer be found for $\Delta k = 0$ but for $\Delta k > 0$.

Intuitively, one would assume that by focussing the pump beam more tightly one would obtain a higher pump intensity and thus a higher photon-pair generation rate. The overall brightness does indeed increase monotonically (up to a point where the Rayleigh length is much smaller than the crystal length, i.e. $\xi \gtrsim 10$)[59] But, due to the Gouy phase shift, the spectral width of the generated photon pairs gets larger and the *spectral* brightness is reduced. Therefore, there is an optimum beam waist (and a corresponding phase mismatch $\Delta k > 0$) for which the parametric gain envelope reaches its maximum value.

Boyd-Kleinman factor. For focussed Gaussian beams, the mode function (Eq. 1.1.12) takes the form:[59]

$$\mathcal{E}(k, \boldsymbol{r}, w_0) = \frac{1}{\sqrt{\pi/2}} \frac{w_0}{q} e^{-\frac{x^2+y^2}{q} + ikz}. \tag{1.2.6}$$

Here, w_0 is the beam waist and

$$q = w_0^2 + 2iz/k. \tag{1.2.7}$$

If all fields have the same confocal parameter $b = 2z_{\text{R}}$ and there is negligible walkoff (no double refraction of the pump beam), the mode overlap for a

Gaussian beam $\mathcal{O}_{\text{Gaussian}}$ (Eq. 1.1.23) is proportional to the *Boyd-Kleinman* factor:[59,174]

$$\left|\mathcal{O}_{\text{Gaussian}}(\omega_s, \omega_i)\right|^2 \propto h(\sigma, \xi, \mu) = \frac{1}{4\xi}\left|\int_{-\xi(1-\mu)}^{\xi(1+\mu)} \mathrm{d}\tau \, \frac{e^{i\sigma\tau}}{1+i\tau}\right|^2. \tag{1.2.8}$$

Here, the *focussing parameter*

$$\xi = l/b \tag{1.2.9}$$

is the ratio of crystal length l to the confocal parameter b, $\sigma = \Delta k\, b/2$ and the *focus position parameter* μ is defined by:

$$\mu = 1 - 2z_f/l, \tag{1.2.10}$$

where z_f is the distance between the focus and the crystal's front facet.

1.2.1 | Spectral features and focussing parameter

For a monochromatic pump, the spectral density of the signal photons is proportional to the Boyd-Kleinman factor:

$$\left|\psi_s(\omega_s)\right|^2 \propto h(\sigma(\omega_s, \omega_i), \xi, \mu) = h(\Delta k(\omega_s, \omega_p - \omega_s), l, \xi, \mu). \tag{1.2.11}$$

The integral appearing in Eq. 1.2.8 cannot be solved analytically. This section subsequently shows that in the limit of small values of ξ the Boyd-Kleinman factor converges to the sinc^2 shape known from the interaction of plane waves (Eq. 1.1.30). For very tight focussing, i.e. larger values of ξ, the maximum of the spectral density shifts to larger values of Δkl as expected.

Weakly focussed pump. For weakly focussed pump beams (small values of ξ), h is proportional to the familiar[59] $\text{sinc}^2\left(\Delta kl/2\right)$ term (Eq. 1.1.11), as can be shown

by a variable substitution ($\tau \longrightarrow \xi(t+\mu)$) and Taylor expansion:

$$h(\sigma,\xi,\mu) = h(\Delta k, l, \xi, \mu) = \frac{1}{4\xi}\left|\int_{-\xi(1-\mu)}^{\xi(1+\mu)} \mathrm{d}\tau\, \frac{e^{i\sigma\tau}}{1+i\tau}\right|^2 \tag{1.2.12}$$

$$= \frac{1}{4}\left|\int_{-1}^{1} \mathrm{d}t\, \frac{e^{i\sigma\xi t + i\xi\mu}}{1+i\xi t + i\xi\mu}\sqrt{\xi}\right|^2 \tag{1.2.13}$$

$$\overset{\xi\ll 1}{\approx} \frac{1}{4}\left|\int_{-1}^{1} \mathrm{d}t\, e^{i\Delta k l t/2}\sqrt{\xi}\right|^2 \tag{1.2.14}$$

$$= \frac{\xi}{4}\,\mathrm{sinc}^2\left(\Delta k l/2\right) \tag{1.2.15}$$

As expected for small values of ξ, the conversion efficiency is independent of the focus position μ and is proportional to the pump intensity I,[196] since

$$\xi \propto 1/z_\mathrm{R} \propto I. \tag{1.2.16}$$

Since $\xi = l/b$, Eq. 1.2.15 shows that for weakly focussed pump beams the photon-pair generation rate is proportional to the length of the nonlinear crystal.

Strongly focussed pump. As discussed earlier, for larger values of ξ, h reaches its maximum value only for a phase mismatch $\Delta k > 0$, resulting in a focus-dependent wavelength shift of the generated signal and idler photons.[197] The spectrum of the generated photons also deviates from the sinc^2 shape and becomes more and more skewed for larger values of ξ. The Boyd-Kleinman factor is shown for different values of ξ in Fig. 1.7.

The largest value of parametric gain envelope $h(\xi,\sigma,\mu)$ is found for $\xi_\mathrm{max} \approx 2.838$ and $\sigma_\mathrm{max} \approx 0.576$:[174]

$$h_\mathrm{max} = h(\xi_\mathrm{max}, \sigma_\mathrm{max}, 0) \approx 1.06. \tag{1.2.17}$$

For larger values $\xi > \xi_\mathrm{max}$, the maximum of the gain envelope decreases. But, with increasing values of ξ, the gain bandwidth increases due to the decreased effective length of phase-matched parametric interaction.

The overall photon-pair generation rate summed over all frequencies increases monotonically with ξ up to $\xi \approx 10$: The generation rate is proportional to $\arctan(\xi)$ to good approximation.[59]

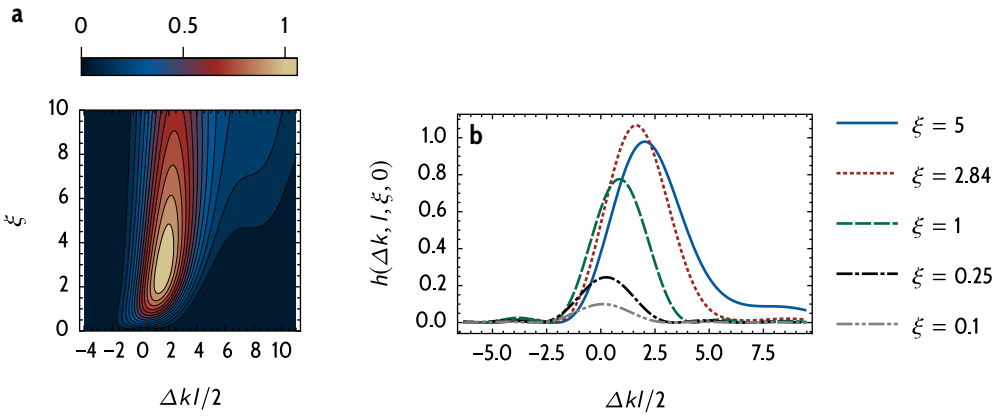

Figure 1.7 | Boyd-Kleinman factor. **a**, For different values of the focussing parameter ξ the Boyd-Kleinman factor $h(\Delta k l, \xi, 0)$ (Eq. 1.2.12) is plotted as a function of the (dimensionless) phase mismatch $\Delta k l$. The maximum shifts to $\Delta k > 0$ as ξ increases. The global maximum is found at $\xi = 2.84$. While the spectral distribution is almost symmetric for small values of ξ, it becomes increasingly skewed and broader for $\xi > 1$. **b**, Sections through **a** for different values of ξ (indicated in the plot). For small values of ξ, h is proportional to $\mathrm{sinc}^2(\Delta k l/2)$. Although the maximum over all values of $\Delta k l$ of h decreases for values $\xi > 2.838$, the overall brightness (which is proportional to the area under the curve) is still monotonically increasing if the pump is focussed more strongly.[59] If the focus of the pump is not in the center of the nonlinear crystal ($\mu \neq 0$), the spectrum shows qualitatively the same behavior, but $h(\Delta k, l, \xi, \mu)$ is always smaller than $h(\Delta k, l, \xi, 0)$.[174]

If the photon-pair generation rate summed over all frequencies is the main figure of merit the pump focus should be as small as possible. If, on the other hand, the aim is a large number of photons generated into a specific spectral mode of a cavity-enhanced source, the Boyd-Kleinman factor of the cavity should be maximized for optimum performance. But, this kind of brightness optimization could affect the heralding ratio of the photon-pair source. We will discuss this reduction in heralding ratio in section 1.2.4.

1.2.2 | Gouy phase inside a resonator

The spectral properties of photon pairs generated by spontaneous parametric down-conversion in a triply-resonant cavity are affected by the relative phase acquired between the nonlinear crystal and the first mirror (see section 1.1.4). For the interaction of Gaussian beams, the additional Gouy phase has to be taken into account to estimate this relative phase. If there are, besides the nonlinear crystal, additional elements (e.g. compensation crystals) placed inside the cavity, the expression for the optical phase at any point and the resonance conditions become more involved. The Gouy phase at any point in the cavity

depends on the position of each optical element and the radii of curvature of the mirrors. Here, we will provide an expression for the position-dependent confocal parameter. With the help of this expression, the total Gouy phase acquired in a single pass through the cavity and the Gouy phase at any point can be calculated. In the literature, comparable expressions can commonly be found for empty cavities.[198–200] In contrast to this, in this section, we will discuss the case of a linear cavity consisting of an arbitrary number of optical elements and an arbitrary position of the nonlinear crystal.

Confocal parameter and effective cavity length. The confocal parameter $b(z)$ of a beam matched to the fundamental Gaussian mode of the cavity, depends on the refractive index $n(z)$ inside the resonator. For a cavity with mirror radii of curvature R_1 and R_2, it is:[198]

$$\begin{aligned} b(z) = 2z_\mathrm{R} &= 2n(z)l_\mathrm{eff}\frac{\sqrt{g_1g_2\left[1-g_1g_2\right]}}{\left|g_1+g_2-2g_1g_2\right|}, \quad \text{with } g_{1/2} = 1 - l_\mathrm{eff}/R_{1/2} \\ &= \begin{cases} n(z)\sqrt{l_\mathrm{eff}\left[2R - l_\mathrm{eff}\right]}, & \text{spherical cavity } (R_1 = R_2 = R) \\ 2n(z)\sqrt{l_\mathrm{eff}\left[R - l_\mathrm{eff}\right]}, & \text{hemispherical cavity } (R_1 = \infty, R_2 = R). \end{cases} \end{aligned} \tag{1.2.18}$$

If the resonator consists of m elements of length l_i and refractive index n_i (see Fig. 1.8a), the effective length l_eff in Eq. 1.2.18 is:

$$l_\mathrm{eff} = \sum_{i=1}^{m} l_i/n_i. \tag{1.2.19}$$

The effective cavity length is smaller than the distance of the mirrors.[200]

Total Gouy phase and resonance condition. Assuming the two mirrors are placed at positions z_1 and z_2, the total Gouy phase acquired in a single pass through the cavity is:[199]

$$\begin{aligned} \Phi_\mathrm{Gouy} &= \phi_\mathrm{Gouy}(z_2) - \phi_\mathrm{Gouy}(z_1) = \arccos\left(\sqrt{g_1g_2}\right) \\ &= \begin{cases} \arccos\left(\left|1 - \frac{l_\mathrm{eff}}{R}\right|\right), & \text{spherical cavity } (R_1 = R_2 = R) \\ \arcsin\left(\sqrt{\frac{l_\mathrm{eff}}{R}}\right), & \text{hemispherical cavity } (R_1 = \infty, R_2 = R). \end{cases} \end{aligned} \tag{1.2.20}$$

The resonance condition given in Eq. 1.1.80 now can be extended to:

$$\phi_\mathrm{rt}(\omega_q) = 2\pi q, \quad q \in \mathbb{N}, \tag{1.2.21}$$

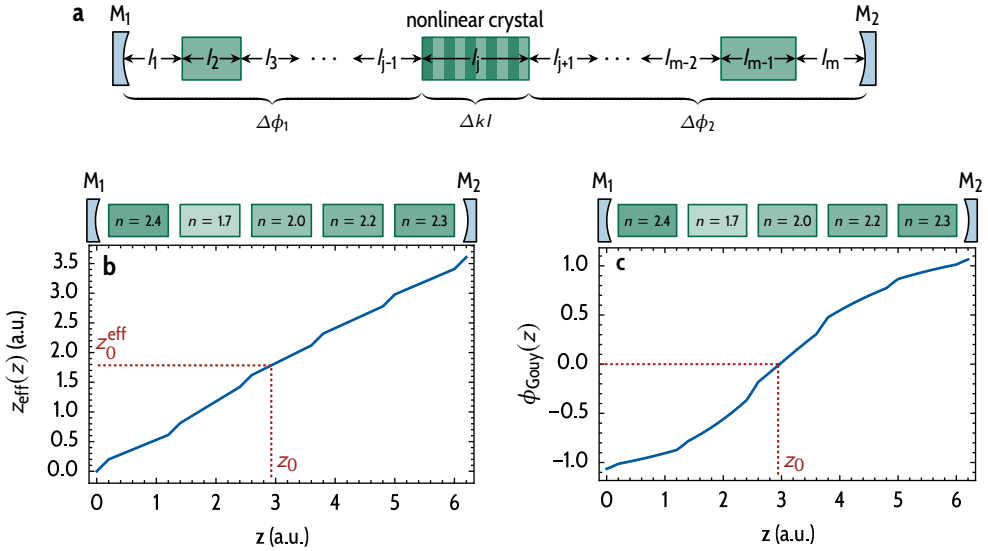

Figure 1.8 | Linear resonator with arbitrary number of optical elements. **a**, Here, a linear resonator with m elements (e.g. free space or compensation crystals) of length l_i and refractive index n_i is shown. The nonlinear crystal with refractive index n_j is placed at position j. The focus position as well as the Gouy phase at each point in the resonator depend on the mirror radii of curvature, as well as the position and ordering of the optical elements. **b**, For a cavity with five crystals (each with an arbitrarily chosen refractive index), the effective position $z_{\text{eff}}(z)$ (Eq. 1.2.26) is shown. Above the plot, the position and refractive index of each crystal is indicated. The effective position is needed to find an expression for the Gouy phase $\phi_{\text{Gouy}}(z)$ at any point in the cavity, which is shown in **c**. The position of the focus z_0 and the effective focal position z_0^{eff} are indicated with dotted lines.

where the round-trip phase is given by:

$$\phi_{\mathrm{rt}}(\omega) = 2\frac{\omega}{c}\sum_{i=1}^{m} l_i n_i + \delta_1 + \delta_2 - 2\Phi_{\mathrm{Gouy}} + \frac{4\pi l_j}{\Lambda}. \tag{1.2.22}$$

Here, for completeness, the poling period Λ (Eq. 1.1.8) must be included. The corresponding resonance frequencies are:

$$\omega_q = c\frac{2\pi q - \delta_1 - \delta_2 + 2\Phi_{\mathrm{Gouy}} - \frac{4\pi l_j}{\Lambda}}{2\sum_{i=1}^{m} l_i n_i}. \tag{1.2.23}$$

Position dependent Gouy phase. If the first mirror is placed at position $z_1 = 0$, the effective position z_0^{eff} of the focal point is given by:[198]

$$\begin{aligned} z_0^{\mathrm{eff}} &= l_{\mathrm{eff}}\frac{g_2\left[1-g_1\right]}{g_1+g_2-2g_1g_2} \\ &= \begin{cases} l_{\mathrm{eff}}/2, & \text{spherical cavity } (R_1 = R_2 = R) \\ 0, & \text{hemispherical cavity } (R_1 = \infty, R_2 = R). \end{cases} \end{aligned} \tag{1.2.24}$$

To compute the Gouy phase at any point in the cavity, Eq. 1.2.1 needs to be modified:

$$\phi_{\mathrm{Gouy}}(z) = \arctan\left(\frac{z_{\mathrm{eff}}(z) - z_0^{\mathrm{eff}}}{z_{\mathrm{R}}}\right), \tag{1.2.25}$$

where the effective position $z_{\mathrm{eff}}(z)$ is given by:

$$z_{\mathrm{eff}}(z) = \mathrm{Lin}\left(\{L\}, \{L_{\mathrm{eff}}\}, z\right). \tag{1.2.26}$$

The function $\mathrm{Lin}\left(\{L\}, \{L_{\mathrm{eff}}\}, z\right)$ is the linear interpolation between the points:

$$(L_0, L_{0,\mathrm{eff}}),\ (L_1, L_{1,\mathrm{eff}}),\ \ldots,\ (L_m, L_{m,\mathrm{eff}}) \tag{1.2.27}$$

evaluated at the position z, where the following accumulated lengths are introduced:

$$\begin{aligned} L_\nu &= \sum_{i=1}^{\nu} l_i, \quad \text{with} \quad L_0 = 0, \\ L_{\nu,\mathrm{eff}} &= \sum_{i=1}^{\nu} \frac{l_i}{n_i}, \quad \text{with} \quad L_{0,\mathrm{eff}} = 0. \end{aligned} \tag{1.2.28}$$

The effective position $z_{\text{eff}}(z)$ can also be expressed as an integral:

$$z_{\text{eff}}(z) = \text{Lin}\left(\{L\}, \{L_{\text{eff}}\}, z\right) = \int_0^z \mathrm{d}z' \, \frac{1}{n(z')}, \tag{1.2.29}$$

where $n(z)$ is the refractive index at position z in the cavity. The effective position $z_{\text{eff}}(z)$ and the Gouy phase $\phi_{\text{Gouy}}(z)$ are shown in Fig. 1.8 for an exemplary cavity.

The position z_0 of the focal point measured from the first mirror can be found by:

$$z_0 = \text{Lin}\left(\{L_{\text{eff}}\}, \{L\}, z_0^{\text{eff}}\right). \tag{1.2.30}$$

Boyd-Kleinman factor with arbitrary focus position. If the focal position lies outside of the nonlinear crystal, the focus position parameter (Eq. 1.2.10) in the Boyd-Kleinman integral (Eq. 1.2.8) has to be modified to take into account the different refractive indices outside the crystal. After some algebra, one finds:

$$\mu_{\text{eff}} = 1 - 2\frac{n_j}{l_j}\left[z_0^{\text{eff}} - z_{\text{eff}}(L_j)\right]. \tag{1.2.31}$$

If the focal position is inside the nonlinear crystal, $\mu_{\text{eff}} = \mu$. If it is outside, $|\mu_{\text{eff}}| > 1$.

1.2.3 | Triply-resonant cavity with Gaussian beams

Gaussian mode functions. For the cavity depicted in Fig. 1.8 with m elements of length l_i and refractive index n_i, the mode function for photons generated in the forward direction is:

$$\mathcal{E}^{\text{fw}}(\omega, \boldsymbol{r}) = \frac{\mathcal{T}(\omega)}{\sqrt{\pi/2}} \frac{w_0}{q_{\text{eff}}(z)} e^{-\frac{x^2+y^2}{q_{\text{eff}}(z)}} e^{i\phi_{\text{opt}}(\omega,z)}, \tag{1.2.32}$$

where $\mathcal{T}(\omega)$, the cavity transmission function defined in Eq. 1.1.61, now depends on the round-trip phase given in Eq. 1.2.22. The spatial phase factor is:

$$\phi_{\text{opt}}(\omega, z) = \frac{\omega}{c}\text{Lin}\left(\{L\}, \{L_{\text{opt}}\}, z\right) \tag{1.2.33}$$

where the accumulated optical path lengths are:

$$L_{\nu,\text{opt}} = \sum_{i=1}^{\nu} l_i n_i, \quad \text{with } L_{0,\text{opt}} = 0. \tag{1.2.34}$$

This definition implies that the first mirror M_1 is placed at the position $z_1 = 0$. Then, the beam parameter $q_{\text{eff}}(z)$ is given by Eq. 1.2.7, modified according to Eq. 1.2.25:

$$q_{\text{eff}}(z) = w_0^2 + \frac{2i\left[z_{\text{eff}}(z) - z_0^{\text{eff}}\right]}{k}. \tag{1.2.35}$$

The mode function for photons generated in the backward direction is given by:

$$\mathcal{E}^{\text{bw}}(\omega, \boldsymbol{r}) = \frac{\mathcal{T}(\omega)}{\sqrt{\pi/2}} \frac{w_0}{q_{\text{eff}}^*(z)} e^{-\frac{x^2+y^2}{q_{\text{eff}}^*(z)}} e^{-i\phi_{\text{opt}}(\omega,z)}. \tag{1.2.36}$$

Phase-balancing factor. Now, the steps leading to the derivation of state $|\psi_{\text{cavity}}\rangle$ (Eqs. 1.1.72 and 1.1.79) can be repeated with the Gaussian mode functions. The only difference is the spatial phase-factor ϕ_{opt} and that the overlap integral $\left|\mathcal{O}(\omega_{\text{s}}, \omega_{\text{i}})\right|^2$ has to be replaced by the Boyd-Kleinman factor:

$$\left|\mathcal{O}_{\text{Gaussian}}(\omega_{\text{s}}, \omega_{\text{i}})\right|^2 \propto h(\sigma(\omega_{\text{s}}, \omega_{\text{i}}), \xi, \mu_{\text{eff}}), \tag{1.2.37}$$

where μ_{eff} is given by Eq. 1.2.31. We will discuss the proportionality constant in Eq. 1.2.37 in section 1.3.

Utilizing the resonance condition (Eq. 1.2.21), we find the phase-balancing amplitude (see Eq. 1.1.73) to be:

$$p_{\text{Gaussian}}(\omega_{\text{s}}, \omega_{\text{i}}) = 1 + r_{1\text{p}} r_{2\text{s}} r_{2\text{i}} t_{\text{sp,p}} t_{\text{sp,s}} t_{\text{sp,i}} e^{i[\Delta k_{\text{qpm}} l + \Delta\Phi_{\text{Gaussian}}]}, \tag{1.2.38}$$

where Δk_{qpm} is the phase mismatch including the quasi-phase-matching term:

$$\Delta k_{\text{qpm}} = \Delta k + \frac{2\pi l_j}{\Lambda}. \tag{1.2.39}$$

The relative phase $\Delta\Phi_{\text{Gaussian}}$ is given by:

$$\Delta\Phi_{\text{Gaussian}} = \Delta\delta_1 - 2\Delta\phi_{\text{Gouy}}^{\text{eff}} + 2\sum_{i=1}^{j-1} \Delta k_i l_i, \tag{1.2.40}$$

where $\Delta\phi_{\text{Gouy}}^{\text{eff}}$ is the relative Gouy phase acquired between the center of the nonlinear crystal at position z_{c} and the first mirror at position z_1:

$$\Delta\phi_{\text{Gouy}}^{\text{eff}} = \Delta\phi_{\text{Gouy}}(z_{\text{c}}) - \Delta\phi_{\text{Gouy}}(z_1). \tag{1.2.41}$$

We will discuss the expression for joint spectral density for Gaussian beams in section 1.3.1.

1.2.4 | Heralding ratio

If the photon-pair source is used as a source of heralded single photons, the *heralding ratio*[59,195] is an important figure of merit. It is defined by:

$$\eta_{\text{herald}} = \frac{P_{\text{si}}}{P_{\text{i}}}, \tag{1.2.42}$$

where P_{si} is the probability to detect both photons from a pair and P_{i} is the probability to detect just the (heralding) idler photon. If both signal and idler photons are collected into Gaussian modes, Bennink[59] showed that the heralding ratio decreases with increasing values of ξ. This decrease in the heralding ratio was verified by Guerreiro et al.[201] and Dixon et al.[195] It is caused by the spatial entanglement of the photons in a photon pair. The detection of the heralding idler photon in a specific Gaussian collection mode (e.g. an optical fiber) projects the signal photon into a superposition of Laguerre-Gaussian modes which has a reduced overlap with a Gaussian collection mode. This results in a reduction of the signal photon collection efficiency of up to 25 % for $\xi \gtrsim 1$.

To the best of the author's knowledge, it has not been studied in the literature whether this phenomenon also applies to cavity-enhanced parametric down-conversion. At least for a cavity with a low finesse it still must apply. But, for a higher finesse, the presence of a cavity should suppress the emission into non-Gaussian modes since the higher-order Laguerre-Gaussian modes have different resonance frequencies than the fundamental mode and are therefore suppressed. The experiments performed within the scope of this thesis were using a cavity with a small value of $\xi \approx 0.2$, where Bennink's theory predicts only a small reduction in the heralding ratio. Therefore, a quantitative experimental evaluation of the impact of the cavity on the heralding rate is not within the scope of this thesis.

If the photon-pair generation rate is the most important figure of merit, the Boyd-Kleinman factor needs to be optimized. In a triply-resonant cavity, the spatial modes of all three fields are determined by the cavity geometry and cannot be optimized independently. This constraint will be discussed in the following.

1.2.5 | Boyd-Kleinman-theory for unequal confocal parameters

Since, in a triply-resonant cavity, the confocal parameters of the three interacting fields cannot be chosen independently (Fig. 1.9), the Boyd-Kleinman factor has to be modified to account for unequal confocal parameters.

For this case, Bennink[59] introduced the *effective confocal parameter* $\bar{b}$, which is defined by:

$$\bar{b} = \frac{\alpha}{\beta}\frac{b_p}{b_s b_i}, \tag{1.2.43}$$

with

$$\alpha = \frac{k_s b_i b_p + k_i b_s b_p + k_p b_s b_i}{b_s b_i b_p} \quad \text{and} \tag{1.2.44}$$

$$\beta = \frac{b_s\left[k_i - k_p\right] + b_i\left[k_p - k_s\right] + b_p\left[k_s + k_i\right]}{b_p k_p}. \tag{1.2.45}$$

Bennink showed that, for unequal confocal parameters, the Boyd-Kleinman factor has to be modified:

$$h(\sigma, \xi, 0) \rightarrow \bar{h}(\bar{\sigma}, \bar{\xi}, 0) = \frac{4}{\alpha\beta} h(\bar{\sigma}, \bar{\xi}, 0). \tag{1.2.46}$$

The effective Boyd-Kleinman factor $\bar{h}$ can be expressed in terms of the conventional Boyd-Kleinman factor h and effective parameters $\bar{\xi} = l/\bar{b}$ and $\bar{\sigma} = \Delta k\, \bar{b}/2$.

Boyd and Kleinman[174] also derived an expression for $\bar{h}$. Although they have different definitions for $\bar{b}$, α and β due to different approximations, numerically the values of the effective Boyd-Kleinman factor agree within the range of a few percent with the values obtained based on Bennink's theory.

Fig. 1.9 uses a practical example to illustrate how the geometry of the cavity affects the Boyd-Kleinman factor. The confocal parameter of a resonating field is determined by the geometry of the cavity, i.e. the radii of curvature of the mirrors and the effective length (Eq. 1.2.18). In a triply-resonant cavity, the confocal parameter of the three fields therefore cannot be independently chosen. There is a large mismatch between the pump and the signal/idler confocal parameter for small values of the mirrors' radii of curvature. Compared to the case where all fields share the same confocal parameter, the maximum of the effective Boyd-Kleinman factor is shifted to a considerably larger pump beam waist.

Focus position. If the position of the focus defined by $\mu_{\text{eff}} \neq 0$ (Eq. 1.2.10) is identical for all three fields, one can extend Eq. 1.2.46 after some algebra to:

$$\bar{h}(\bar{\sigma}, \bar{\xi}, \mu_{\text{eff}}) = \frac{4}{\alpha\beta} h(\bar{\sigma}, \bar{\xi}, \mu_{\text{eff}}), \tag{1.2.47}$$

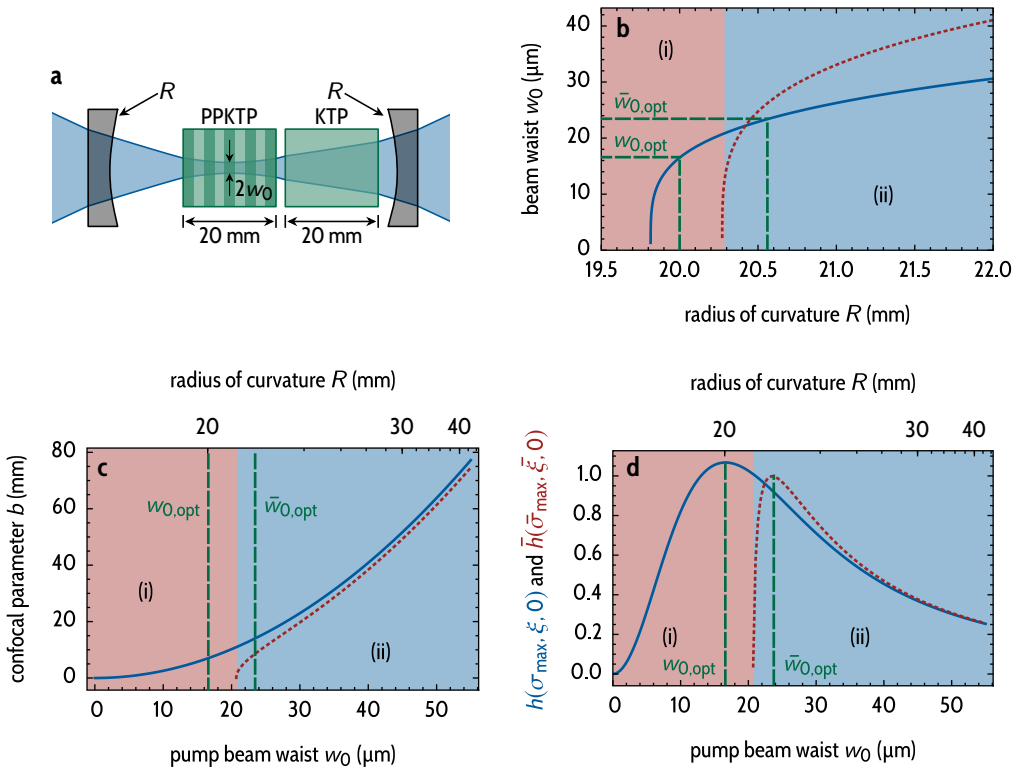

Figure 1.9 | Boyd-Kleinman factor with unequal confocal parameters. **a**, Exemplary setup[128] of a cavity with a $l = 20$ mm long periodically poled KTP conversion crystal and an additional compensation crystal: For a spherical cavity with $R_1 = R_2 = R$, the position of the focus does not depend on the mirrors' radii of curvature (see Eqs. 1.2.24 and 1.2.30). It is determined solely by the refractive indices and the spacing between mirrors and crystals. Here, the spacing is chosen so that the focus is placed at the center of the nonlinear crystal. For a fixed crystal spacing, the beam waist w_0 can be adjusted by changing R. The pump beam profile (—) is simulated using the ABCD-matrix formalism.[196] **b**, Beam waist w_0 for pump (—) and signal/idler (----) fields depending on the mirrors' radii of curvature R: Due to the chromatic dispersion of the crystals, there is a region (i) in which only the pump field can oscillate inside the cavity. If the radius of curvature R is large enough (region (ii)), the cavity is also stable[196] for signal and idler fields. **c**, Confocal parameter of pump (—) and signal/idler (----) fields as a function of the pump beam waist which is defined by R: Close to the boundary between region (i) and (ii), there is a large mismatch between the confocal parameters. For larger values of R, the ratio $b_p / b_{s/i}$ approaches unity. **d**, Effect of unequal confocal parameters on the Boyd-Kleinman factor: Here, the maximum over all values of σ, $h(\sigma_{max}, \xi, 0)$, is shown (—) and compared to the effective Boyd-Kleinman factor $\bar{h}(\bar{\sigma}_{max}, \bar{\xi}, 0)$ (----). The maximum of $\bar{h}$ at $\bar{w}_{0,opt}$ is shifted to considerably larger pump beam waists compared to $w_{0,opt}$. The values of $\bar{w}_{0,opt}$ and $w_{0,opt}$ are also indicated in **b** and **c**. The maximum of the Boyd-Kleinman factor is reduced by ~15 % compared to the case where all fields have the same confocal parameter. For larger values of w_0, there is no difference. This is to be expected since the confocal parameters inside the cavity differ only for tight focussing (see).

where μ_{eff} is given by Eq. 1.2.31. This extension is straightforward if one follows the derivation of $\bar{h}$ in Ref. [174] and performs a substitution of variables similar to Eq. 1.2.12.

The assumption that the focus position is identical for all three fields is valid to good approximation for a linear triply-resonant cavity. This is shown for an exemplary cavity in Fig. 1.10.

1.2.6 | Discussion and Outlook

Most theoretical studies on cavity-enhanced parametric down-conversion treat the interacting fields as plane waves. The theory of the parametric interaction of Gaussian beams, as shown in this section, is more involved but offers a more accurate description of effects which can be observed in experiments: The Boyd-Kleinman factor is directly related to the brightness of a photon-pair source based on cavity-enhanced parametric down-conversion, as we will show in section 1.3.4. Thus, with the expressions found in this section, the geometry of the cavity can be optimized to obtain maximum brightness.

The phase-balancing amplitude (Eq. 1.2.38) depends on the Gouy phase. This dependency has not been discussed in detail in the literature. The theory of an optical parametric oscillator with resonant pump and signal laid out by Schiller and coworkers[202] also finds an expression for the effective nonlinearity which depends on the Gouy phase. But, their work is not directly applicable to photon-pair generation and does not address triply-resonant cavities. We will show in section 2.3.6 that the Gouy phase directly influences the spectral characteristics of the generated photon pairs which can be measured in an experiment.

In conventional (non-resonant) spontaneous parametric down-conversion, the heralding ratio is reduced if the pump is focussed tightly.[59] To the author's knowledge, this phenomenon has not been studied in the literature in the context of cavity-enhanced parametric down-conversion. One can assume that a cavity with sufficiently high finesse suppresses the generation of photon pair into non-Gaussian spatial modes. Under this assumption, such a suppression would result in a spatial single-mode emission[203] and thus a negligible reduction of the heralding ratio. Further theoretical and experimental studies are required to verify this assumption.

In the following section, we will derive an expression for the joint spectral density of the generated photon pairs. By utilizing the theory of parametric interaction of Gaussian beams developed in this section, it is possible to calculate *absolute* photon-pair generation rates. Since the expression found in this section

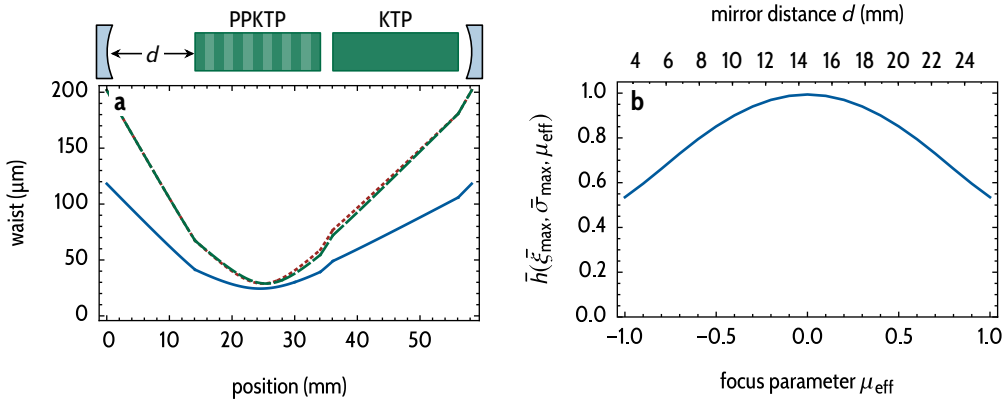

Figure 1.10 | Boyd-Kleinman factor and the position of the focus. **a**, Beam profile for pump (——), signal (----), and idler (– –) fields for the cavity discussed in Fig. 1.9. The upper part indicates the position of the two crystals and the mirrors. We choose the distance d between the first mirror and the PPKTP crystal such that the pump beam waist is located at the center of the PPKTP crystal. The radius of curvature is chosen such that the Boyd-Kleinman factor $\bar{h}$ is maximum ($R = 20.6$ mm, Fig. 1.9d). For this configuration, the pump confocal parameter is considerably larger than the signal/idler confocal parameter (Fig. 1.9c). Nevertheless, the position of the focus is nearly identical for all three fields. **b**, By changing the mirror distance d, the position of the focus of the three fields can be shifted to either side of the PPKTP crystal. Therefore, the focus position parameter μ_{eff} directly depends on d. Here, we plot the maximum of the Boyd-Kleinman factor $\bar{h}$ over all values of $\bar{\xi}$ and $\bar{\sigma}$ depending on the mirror distance d (or μ_{eff}, respectively).

applies for arbitrary cavity geometries, we can derive the joint spectral density and the generation rate for cavities with and cavities without compensation crystals.

1.3 | Cavity enhancement and brightness

From an experimentalist's perspective, the brightness is for most experiments, besides the spectral characteristics, the most important property of a photon-pair source. Of course, a high brightness at a low pump power is desired. Therefore, the figure of merit is the photon-pair generation rate per mW of pump power $\mathcal{R}$.

For continuous wave pumping, the joint spectral density $\left|\psi_{\text{cavity}}(\omega_s, \omega_i)\right|^2$ (see Eq. 1.1.78) is the expected number of the photon pairs emitted per signal/idler bandwidth per unit time Δt for a given pump power P_p (see section 1.1.2).

Therefore, the photon-pair generation rate per pump power $\mathcal{R}$ is:

$$\mathcal{R} = \frac{1}{P_\mathrm{p}\Delta t}\int_0^\infty \mathrm{d}\omega_\mathrm{s}\,\mathrm{d}\omega_\mathrm{i}\left|\psi_\mathrm{cavity}(\omega_\mathrm{s},\omega_\mathrm{i})\right|^2. \tag{1.3.1}$$

This section provides an expression for the joint spectral density in the case of the nonlinear interaction of Gaussian beams. Based on this expression, we will discuss how the finesse and the extraction efficiency of the resonator enhance or decrease the brightness of the photon-pair source. Finally, we will derive an expression for the absolute photon-pair generation rate $\mathcal{R}$. Similar expressions have been reported earlier[161] (for plane-wave interactions) even with numerical predictions for specific cavity configurations.[162] But, the expression we will derive here has the distinct advantage that it is directly given in terms of experimentally accessible parameters. The expression is furthermore applicable to an arbitrary cavity geometry and especially to triply-resonant cavities which were not covered by prior studies. However, the theory presented here does not cover pulsed pumping since all experiments discussed in this thesis utilize continuous wave pumping.

We will benchmark the expression for the absolute photon-pair generation rate by comparing numerical values with measured values reported in the literature for several different sources. The last part of this section utilizes the theory to optimize the geometry of cavity-enhanced photon-pair sources.

1.3.1 | Joint spectral density

In the previous sections, we defined the joint spectral density of a cavity-enhanced source in terms of the single-pass joint spectral density $\left|\psi_\mathrm{sp}(\omega_\mathrm{s},\omega_\mathrm{i})\right|^2$ (Eq. 1.1.78):

$$\left|\psi_\mathrm{cavity}(\omega_\mathrm{s},\omega_\mathrm{i})\right|^2 = \left|\psi_\mathrm{sp}(\omega_\mathrm{s},\omega_\mathrm{i})\right|^2 P(\omega_\mathrm{s},\omega_\mathrm{i},\Delta\Phi)\mathcal{A}_\mathrm{p}(\omega_\mathrm{s}+\omega_\mathrm{i})\mathcal{A}_\mathrm{s}(\omega_\mathrm{s})\mathcal{A}_\mathrm{i}(\omega_\mathrm{i}). \tag{1.3.2}$$

In the case of the interaction of Gaussian beams, the phase-balancing factor $P(\omega_\mathrm{s},\omega_\mathrm{i},\Delta\Phi)$ is defined as the modulus squared of Eq. 1.2.38. Here, we explicitly address the relative phase $\Delta\Phi$, given by Eq. 1.2.40, since it is an important experimentally tunable parameter, as we will discuss in chapter 2.

Furthermore, utilizing Bennink's[59] theory, an explicit expression for the single-pass joint spectral density in terms of experimentally accessible parameters can be given. This expression has been verified[195] with excellent agreement between theory and experiment.

Bennink showed that $\left|\psi_{\mathrm{sp}}(\omega_\mathrm{s},\omega_\mathrm{i})\right|^2$ is proportional to the mean number of pump photons N_p arriving at the nonlinear crystal per unit time Δt. The mean number of pump photons can be related to the pump power for a continuous wave pump by:

$$P_\mathrm{p} = \frac{N_\mathrm{p}\hbar\omega_\mathrm{p}}{\Delta t}. \tag{1.3.3}$$

Single-pass joint spectral density. With this definition of the pump power, the single-pass joint spectral density is:[59]

$$\left|\psi_{\mathrm{sp}}(\omega_\mathrm{s},\omega_\mathrm{i})\right|^2 = \kappa l \Delta t P_\mathrm{p} \bar{h}(\bar{\sigma}(\omega_\mathrm{s},\omega_\mathrm{i}),\bar{\xi},\mu_\mathrm{eff})\left|s(\omega_\mathrm{s}+\omega_\mathrm{i})\right|^2, \tag{1.3.4}$$

where $s(\omega)$ is the pump spectral amplitude distribution (Eq. 1.1.17) and the coupling constant κ is given by:[59,195]

$$\kappa = \frac{16\pi^2\lambda_\mathrm{p}}{\epsilon_0 n_\mathrm{p}^2 c}\left[\frac{d_\mathrm{eff}}{\lambda_\mathrm{s}\lambda_\mathrm{i}}\right]^2. \tag{1.3.5}$$

Plugging Eqs. 1.3.4 and 1.3.5 into Eq. 1.3.1, results in:

$$\begin{aligned}\mathcal{R} = \kappa l \int_0^\infty \mathrm{d}\omega_\mathrm{s}\,\mathrm{d}\omega_\mathrm{i}\,\bar{h}(\bar{\sigma}(\omega_\mathrm{s},\omega_\mathrm{i}),\bar{\xi},\mu_\mathrm{eff})\left|s(\omega_\mathrm{s}+\omega_\mathrm{i})\right|^2 P(\omega_\mathrm{s},\omega_\mathrm{i},\Delta\Phi) \\ \times \mathcal{A}_\mathrm{p}(\omega_\mathrm{s}+\omega_\mathrm{i})\mathcal{A}_\mathrm{s}(\omega_\mathrm{s})\mathcal{A}_\mathrm{i}(\omega_\mathrm{i}).\end{aligned} \tag{1.3.6}$$

In the case of monochromatic pumping, the integral over ω_i can easily be evaluated utilizing $s(\omega) = \delta(\omega-\omega_\mathrm{p})$ (Eq. 1.1.19). The generation rate can then be expressed in terms of the signal spectral density $\left|\psi_{\mathrm{cavity}}(\omega_\mathrm{s})\right|^2$:

$$\mathcal{R} = \kappa l \int_0^\infty \mathrm{d}\omega_\mathrm{s}\left|\psi_{\mathrm{cavity}}(\omega_\mathrm{s})\right|^2, \tag{1.3.7}$$

where

$$\begin{aligned}\left|\psi_{\mathrm{cavity}}(\omega_\mathrm{s})\right|^2 = \bar{h}(\bar{\sigma}(\omega_\mathrm{s},\omega_\mathrm{p}-\omega_\mathrm{s}),\bar{\xi},\mu_\mathrm{eff})P(\omega_\mathrm{s},\omega_\mathrm{p}-\omega_\mathrm{s},\Delta\Phi) \\ \times \mathcal{A}_\mathrm{p}(\omega_\mathrm{p})\mathcal{A}_\mathrm{s}(\omega_\mathrm{s})\mathcal{A}_\mathrm{i}(\omega_\mathrm{p}-\omega_\mathrm{s}).\end{aligned} \tag{1.3.8}$$

With Eq. 1.3.6, we can calculate the pair generation rate for a wide range of experimental parameters. In general, the integral over ω_s in Eq. 1.3.6 must be evaluated numerically. Although absolute values for the generation rate can

be computed with Eq. 1.3.6, this expression does not provide direct insights into how $\mathcal{R}$ depends on various experimentally tunable parameters, e.g. on the finesse of the resonator. We can obtain these insights by normalizing the signal spectral density as will be shown in the following. With this normalization, we can pull the factors which do not depend on ω_s out of the integral in Eq. 1.3.6.

The next section begins with normalizing the Airy functions $\mathcal{A}(\omega)$ in Eq. 1.3.6 to gain a more intuitive understanding of the enhancement effect of the cavity.

1.3.2 | Cavity enhancement and finesse

The Airy functions can be expressed in terms of the real-valued reflection and transmission coefficients $R_n = r_n^2$ and $T_n = t_n^2$. In the following, the wavelength dependence of $R_n = R_n(\omega)$ and $T_n = T_n(\omega)$ will be omitted. The non-normalized Airy function $\mathcal{A}(\omega)$ (Eq. 1.1.76) can be written as the product of an enhancement factor $F_{\text{enh}}(\omega)$ and a normalized Airy function $\text{Airy}(\mathcal{F}, \omega)$:

$$\begin{aligned}\mathcal{A}(\omega) &= \left|\frac{t_2}{1 - r_1 r_2 t_{\text{sp}} e^{i\phi_{\text{rt}}(\omega)}}\right|^2 = \left|\frac{\sqrt{1-R_2}}{1 - \sqrt{R_1 R_2 T_{\text{sp}}^2}\, e^{i\phi_{\text{rt}}(\omega)}}\right|^2 \\ &= F_{\text{enh}}(\omega)\text{Airy}(\mathcal{F}, \omega),\end{aligned} \tag{1.3.9}$$

where

$$F_{\text{enh}}(\omega) = \frac{1 - R_2}{\left[1 - \sqrt{R_1 R_2 T_{\text{sp}}^2}\right]^2} \tag{1.3.10}$$

and

$$\text{Airy}(\mathcal{F}, \omega) = \frac{1}{1 + \frac{4}{\pi^2}\mathcal{F}^2 \sin^2\left(\phi_{\text{rt}}(\omega)/2\right)}. \tag{1.3.11}$$

Cavity finesse. Here, $\mathcal{F}$ is the *finesse* of the cavity:

$$\mathcal{F} = \frac{\pi \left[R_1 R_2 T_{\text{sp}}^2\right]^{1/4}}{1 - \sqrt{R_1 R_2 T_{\text{sp}}^2}}. \tag{1.3.12}$$

The finesse is defined such that it is proportional to the ratio of free spectral range (FSR) and cavity decay rate Γ:[204]

$$\mathcal{F} = \frac{2\pi\,\mathrm{FSR}}{\Gamma}. \tag{1.3.13}$$

The free spectral range is the separation of two resonances in frequency space. With Eq. 1.2.23:

$$\mathrm{FSR} = \frac{\omega_{q+1} - \omega_q}{2\pi}. \tag{1.3.14}$$

It can be approximated by:

$$\mathrm{FSR} \approx \frac{c}{2L_{\mathrm{opt}}}, \tag{1.3.15}$$

where L_{opt} is the optical path length of the cavity. The single-pass transmission of a crystal of length l is wavelength-dependent and can be expressed as:

$$T_{\mathrm{sp}} = T_{\mathrm{facet}}^2 e^{-\alpha l}, \tag{1.3.16}$$

where T_{facet} is the transmission of each of the two crystal facets and $\alpha = \alpha(\omega)$ is the absorption coefficient.

Given that the factor $1 - \sqrt{R_1 R_2 T_{\mathrm{sp}}^2}$ appears in the denominator of both $\mathcal{F}$ (Eq. 1.3.12) and F_{enh} (Eq. 1.3.9), one can show that these two quantities are closely related. This relationship will be analyzed in the following.

Enhancement and finesse. The enhancement factor F_{enh} can be approximated for $\mathcal{F} \gtrsim 10$ in the form:

$$F_{\mathrm{enh}} = \frac{1 - R_2}{\left[1 - \sqrt{R_1 R_2 T_{\mathrm{sp}}^2}\right]^2} \tag{1.3.17}$$

$$\approx \frac{\left[R_1 R_2 T_{\mathrm{sp}}^2\right]^{2/4}}{\left[1 - \sqrt{R_1 R_2 T_{\mathrm{sp}}^2}\right]^2} \frac{2(1 - \sqrt{R_2})}{R_2^{1/4}}, \tag{1.3.18}$$

which results in:

$$F_{\mathrm{enh}} \approx \frac{2}{\pi} \frac{\mathcal{F}^2}{\mathcal{F}_0}, \tag{1.3.19}$$

where the *cold cavity* finesse $\mathcal{F}_0$ is the finesse of an empty cavity with the same value of R_2 but without losses ($R_1 = T_{sp} = 1$). The approximation in Eq. 1.3.18 appears rather arbitrary at first glance, but it is inspired by the seminal work of Ou and Lu[111] on cavity-enhanced parametric down-conversion and is in excellent agreement with Eq. 1.3.10 (see Fig. 1.11a). Since the finesse of the cold cavity is always larger than the finesse of the corresponding lossy cavity, the enhancement factor is always smaller than the finesse:

$$F_{enh} \approx \frac{2}{\pi}\frac{\mathcal{F}}{\mathcal{F}_0} \times \mathcal{F} < \mathcal{F}, \tag{1.3.20}$$

As will be shown in the following, the factor $\mathcal{F}/\mathcal{F}_0$ is approximately the extraction efficiency of the cavity.

1.3.3 | Extraction efficiency

The extraction efficiency is the probability that a photon created inside the cavity leaves the cavity through the outcoupling mirror M_2. The extraction efficiency can be calculated to be:[136]

$$\eta(\omega) = \frac{1 - R_2}{1 - R_1 R_2 T_{sp}^2}. \tag{1.3.21}$$

This expression shows a strong resemblance with the enhancement factor (Eq. 1.3.10). Hence, one can perform an approximation similar to Eq. 1.3.19 in excellent agreement with the full form (see Fig. 1.11b):

$$F_{enh} \approx \frac{2}{\pi}\eta\mathcal{F}. \tag{1.3.22}$$

By comparison of Eq. 1.3.22 and Eq. 1.3.19, the extraction efficiency can be written as the ratio of finesse to cold-cavity finesse:

$$\eta \approx \frac{\mathcal{F}}{\mathcal{F}_0}. \tag{1.3.23}$$

Finesse dependence of the extraction efficiency. If a crystal is placed into a cavity, the extraction efficiency is a function of the length of the crystal, the absorption coefficient α, the transmission of the crystal's facets T_{facet} and the reflectivities of the mirrors. Often, the losses by absorption inside the crystal are negligible compared to losses caused by imperfect anti-reflection coatings or transmission

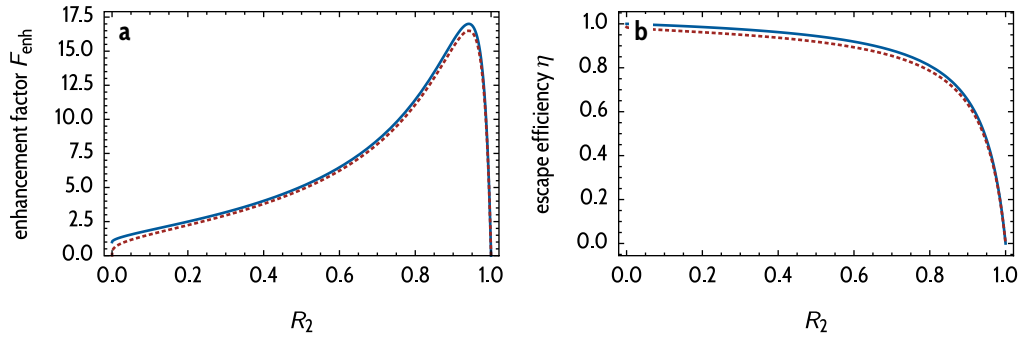

Figure 1.11 | Enhancement factor and extraction efficiency. **a**, Comparison of the enhancement factor F_{enh} (—) defined in Eq. 1.3.10 with the approximation $F_{enh} \approx 2\mathcal{F}^2[\pi\mathcal{F}_0]^{-1}$ (Eq. 1.3.19) (----) for $R_1 = T_{sp} = 98\,\%$. The largest enhancement is found for an impedance-matched cavity with $R_2 = R_1 T_{sp}^2$. The deviation between Eq. 1.3.10 and the approximation becomes even smaller for larger values of R_2 or T_{sp}. **b**, The extraction efficiency η defined in Eq. 1.3.21 is, in good approximation, equal to the ratio $\mathcal{F}/\mathcal{F}_0$ of finesse to cold cavity finesse. Here, η (—) and the approximation $\mathcal{F}/\mathcal{F}_0$ (----) are shown as a function of R_2 for $R_1 = T_{sp} = 98\,\%$. As in **a**, the deviation between the approximation and the full form becomes smaller for larger values of R_2 or T_{sp}.

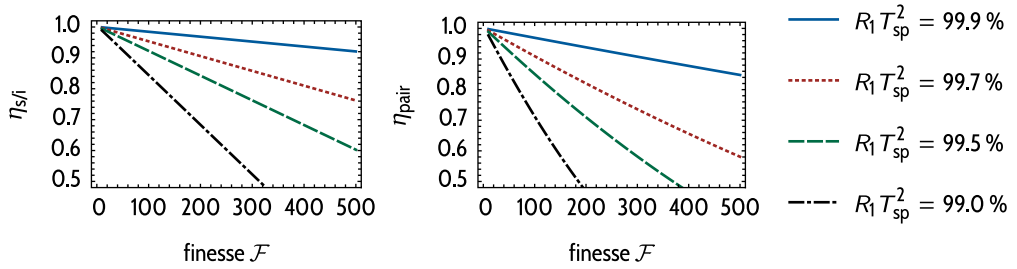

Figure 1.12 | Extraction efficiency depending on the finesse. If the losses by absorption inside the crystal are negligible, the extraction efficiency does not depend on the length but only on the finesse of the cavity. Here, the signal/idler extraction efficiency $\eta_{s/i}$ and the pair extraction efficiency $\eta_{pair} = \eta_s \eta_i$ are shown as a function of the cavity finesse for different values of the round-trip transmission $R_1 T_{sp}^2$. This plot emphasises that a compromise between cavity enhancement (requires a large finesse) and extraction efficiency (requires a low finesse) has to be made.

of the photons through the first mirror M_1. In this case, the extraction efficiency is no longer a function of the crystal length and thus depends only on the finesse of the cavity.

In Fig. 1.12, the signal/idler extraction efficiency $\eta_{s/i}$ is plotted as a function of the finesse for different values of the round-trip transmission $R_1 T_{sp}^2$. For a fixed round-trip transmission, the extraction efficiency depends only on the reflectivity of the outcoupling mirror R_2 which in turn can be expressed as a function of the finesse. Here, it is assumed that the single-pass transmission is of the form $T_{sp} = T_{facet}^2$ or $T_{sp} = T_{facet}^4$ (no absorption inside the crystal) for a cavity with one or two crystals, respectively. To obtain high extraction efficiencies ($\eta_{s/i} > 95\,\%$), for a cavity with a moderately high finesse $\mathcal{F} \sim 100$, the round-trip transmission $R_1 T_{sp}^2$ must be larger than 99.7 %. Note that $\eta_{s/i} \approx 95\,\%$ corresponds to a pair extraction efficiency of just $\eta_{pair} = \eta_s \eta_i \approx 90\,\%$.

Although it is feasible to produce a mirror M_1 with $R_1 \gg 99.7\,\%$, the anti-reflection coating of the crystals poses a significant challenge as illustrated with the following example: Consider a single-crystal source with a finesse of $\mathcal{F} = 100$, negligible absorption and ideal reflectivity $R_1 = 1$ of the first mirror. To obtain a pair extraction efficiency of $\eta_{pair} > 90\,\%$, a transmission of the crystal's facets $T_{facet} > 99.8\,\%$ would be required. This already is a demanding specification for the anti-reflection coating. For a two crystal cavity configuration with four anti-reflection coated surfaces, a transmission of $T_{facet} > 99.92\,\%$ per surface would be required. This is currently technologically extremely challenging, especially if the crystal should also be anti-reflection coated at the pump wavelength.

Impedance matching. The enhancement factor F_{enh} can also be related to the field enhancement which a mode-matched laser entering the cavity through the second mirror would experience. From Eq. 1.1.66 one can show that F_{enh} is the exact same factor by which the circulating power P_{circ} is larger than the input power P_{in}:

$$F_{enh} = \frac{P_{circ}}{P_{in}}. \tag{1.3.24}$$

Therefore, to obtain the maximum brightness of a cavity-enhanced parametric down-conversion source, the reflectivity of the first mirror must be as high as possible and the reflectivity R_2 of the outcoupling mirror must be *impedance matched*[196] to the round-trip transmission of the cavity:

$$R_2^{opt} = R_1 T_{sp}^2. \tag{1.3.25}$$

Eq. 1.3.24 is less important from a practical perspective in determining the

brightness of a cavity-enhanced source than Eq. 1.3.19 or Eq. 1.3.22. However, it provides an intuitive insight into the nature of the enhancement process.

Discussion. Fig. 1.12 highlights that even small imperfections of the cavity mirrors or the anti-reflection coatings result in high losses for high finesse cavities. For the same reason it is challenging to build cavity-enhanced photon-pair sources with high extraction efficiency based on nonlinear waveguides.[136,173] Therefore, monolithic cavities made of bulk crystals[130,162] are the most promising configurations to date to obtain high brightness sources with low losses. Monolithic designs have the advantage that no anti-reflection coating is required and the mirror distance of the cavity is intrinsically stable with respect to vibrations.

1.3.4 | Generation rate

At this point, all tools are at hand to find a simplified expression for the photon-pair generation rate $\mathcal{R}$ (Eq. 1.3.6) for a triply-resonant cavity pumped by a Gaussian beam. The aim of this section is to derive an expression which contains only experimentally accessible parameters and can be readily compared with measurement results (see section 1.3.5) or can be used e.g. to optimize the geometry of a photon-pair source (see section 1.3.6).

The expression found in this section is functionally equivalent to Eq. 1.3.6 for cavities with a finesse $\mathcal{F}_{s/i} \gtrsim 10$ and it is applicable to cavities with and without compensation crystals. It will be derived by utilizing the normalized Airy functions found in the previous section. Additionally, the parametric gain envelope will also be normalized, introducing the normalized signal spectral density. Finally, it will be shown that the generation rate is proportional to the effective number of spectral modes as pointed out by Ou and Lu.[111]

Enhancement factors and cavity finesse. If the resonator is locked to a pump resonance ($\mathrm{Airy}_p(\omega_p) = 1 \implies \mathcal{A}_p(\omega_p) = F^p_{enh}$), the photon-pair generation rate (Eq. 1.3.6) can be written as:

$$\mathcal{R} = \kappa l F^p_{enh} \int_0^\infty \mathrm{d}\omega\, h(\omega, \xi, \mu) P(\omega, \Delta\Phi) \mathcal{A}_s(\omega) \mathcal{A}_i(\omega_p - \omega), \tag{1.3.26}$$

where the short-hand notations:

$$P(\omega, \Delta\Phi) \equiv P(\omega, \omega_p - \omega, \Delta\Phi) \tag{1.3.27}$$

and

$$h(\omega, \xi, \mu) \equiv \bar{h}(\bar{\sigma}(\omega, \omega_p - \omega), \bar{\xi}, \mu_{\text{eff}}) \tag{1.3.28}$$

are used. With Eq. 1.3.9, the enhancement factors can be pulled out of the integral:

$$\mathcal{R} = \kappa l F^{\text{p}}_{\text{enh}} F^{\text{s}}_{\text{enh}} F^{\text{i}}_{\text{enh}} \int_0^\infty \mathrm{d}\omega\, h(\omega, \xi, \mu) P(\omega, \Delta\Phi) \text{Airy}_{\text{s}}(\omega) \text{Airy}_{\text{i}}(\omega_{\text{p}} - \omega) \tag{1.3.29}$$

and with Eq. 1.3.22, the generation rate can be expressed in terms of the signal/idler finesse and the extraction efficiencies:

$$\mathcal{R} = \kappa l F^{\text{p}}_{\text{enh}} \eta_{\text{s}} \eta_{\text{i}} \mathcal{F}_{\text{s}} \mathcal{F}_{\text{i}} \frac{4}{\pi^2} \int_0^\infty \mathrm{d}\omega\, h(\omega, \xi, \mu) P(\omega, \Delta\Phi) \text{Airy}_{\text{s}}(\omega) \text{Airy}_{\text{i}}(\omega_{\text{p}} - \omega). \tag{1.3.30}$$

The proportionality $\mathcal{R} \propto \eta_{\text{s}} \eta_{\text{i}} \mathcal{F}_{\text{s}} \mathcal{F}_{\text{i}}$ has been found earlier.[111,136,137] Note, that $\mathcal{R}$ is the rate of *pairs* of photons emitted by the cavity. In an experiment without photon losses after the cavity and ideal single-photon detectors, $\mathcal{R}$ corresponds to the coincidence rate between the signal and idler photon detectors. Since the losses of signal or idler photons inside the cavity are independent of each other, the single-photon generation rates measured on ideal signal/idler detectors are:

$$\mathcal{R}_{\text{s/i}} = \frac{\mathcal{R}}{\eta_{\text{i/s}}}. \tag{1.3.31}$$

In the following, the integral in Eq. 1.3.30 is simplified by normalizing the parametric gain envelope.

Parametric gain envelope. The parametric gain envelope $h(\omega, \xi, \mu) P(\omega, \Delta\Phi)$ typically varies much slower with ω than the term $\text{Airy}_{\text{s}}(\omega)\text{Airy}_{\text{i}}(\omega_{\text{p}} - \omega)$, which is called the *joint resonance function* in the following. The gain envelope can be normalized to unity by introducing the *envelope factor* $\text{Gain}_{\max}(\xi, \mu, \Delta\Phi)$:

$$\text{Gain}_{\max}(\xi, \mu, \Delta\Phi) = \max_{\omega} h(\omega, \xi, \mu) P(\omega, \Delta\Phi). \tag{1.3.32}$$

The photon-pair generation rate now becomes:

$$\mathcal{R} = \kappa l F^{\text{p}}_{\text{enh}} \eta_{\text{s}} \eta_{\text{i}} \mathcal{F}_{\text{s}} \mathcal{F}_{\text{i}} \frac{4}{\pi^2} \text{Gain}_{\max}(\xi, \mu, \Delta\Phi) \int_0^\infty \mathrm{d}\omega_{\text{s}} \left| \tilde{\psi}(\omega_{\text{s}}) \right|^2, \tag{1.3.33}$$

where the normalized signal spectral density is given by:

$$\left|\tilde{\psi}(\omega_\mathrm{s})\right|^2 = \mathrm{Gain}(\omega_\mathrm{s}, \xi, \mu, \Delta\Phi)\mathrm{Airy}_\mathrm{s}(\omega_\mathrm{s})\mathrm{Airy}_\mathrm{i}(\omega_\mathrm{p} - \omega_\mathrm{s}), \tag{1.3.34}$$

and the normalized parametric gain envelope is:

$$\mathrm{Gain}(\omega, \xi, \mu, \Delta\Phi) = \frac{h(\omega, \xi, \mu)P(\omega, \Delta\Phi)}{\mathrm{Gain}_\mathrm{max}(\xi, \mu, \Delta\Phi)}. \tag{1.3.35}$$

Eq. 1.3.33 is a significant improvement upon Eq. 1.3.6, as now the enhancement factor as well as the extraction efficiencies and the enhancement by double-pass pumping are addressed explicitly. The normalized signal spectral density is depicted in Fig. 1.13 for cavities with and without compensation crystal.

We can simplify the integral over the normalized signal spectral density for cavities with a compensation crystal and a (moderately) high finesse, as will be discussed in the following.

Effective number of modes. For $\mathcal{F} \gtrsim 10$, we can write the Airy functions in good approximation as an infinite series of Lorentzian resonances:[161]

$$\mathrm{Airy}(\mathcal{F}, \omega) = \frac{1}{1 + \frac{4}{\pi^2}\mathcal{F}^2 \sin^2\left(\phi_\mathrm{rt}(\omega)/2\right)} \tag{1.3.36}$$

$$\approx \sum_{j=-\infty}^{\infty} \frac{\Gamma^2}{\Gamma^2 + 4\left[\omega - \omega_j\right]^2}, \tag{1.3.37}$$

where the cavity decay rate Γ (the full width at half maximum of the resonances) is given by Eq. 1.3.13 and the resonance frequencies ω_j are defined with the help of Eq. 1.2.23 by:

$$\phi_\mathrm{rt}(\omega_j) = 2j\pi, \qquad j \in \mathbb{N}. \tag{1.3.38}$$

With Eq. 1.3.37, the joint resonance function is given by:

$$\mathrm{Airy}_\mathrm{s}(\omega_\mathrm{s})\mathrm{Airy}_\mathrm{i}(\omega_\mathrm{p} - \omega_\mathrm{s}) = \sum_{j=-\infty}^{\infty}\sum_{k=-\infty}^{\infty} \frac{\Gamma_\mathrm{s}^2\Gamma_\mathrm{i}^2}{\left[\Gamma_\mathrm{s}^2 + 4\left[\omega_\mathrm{s} - \omega_{\mathrm{s},j}\right]^2\right]\left[\Gamma_\mathrm{i}^2 + 4\left[\omega_\mathrm{s} - \omega_\mathrm{p} - \omega_{\mathrm{s},k}\right]^2\right]}. \tag{1.3.39}$$

Cavity with compensation crystal. If a compensation crystal is placed into the cavity and the signal/idler free spectral range is identical, the signal and idler resonances can be tuned (e.g. by changing the crystals' temperatures or orientations) such that they perfectly coincide in frequency. Then, for each value of j a value

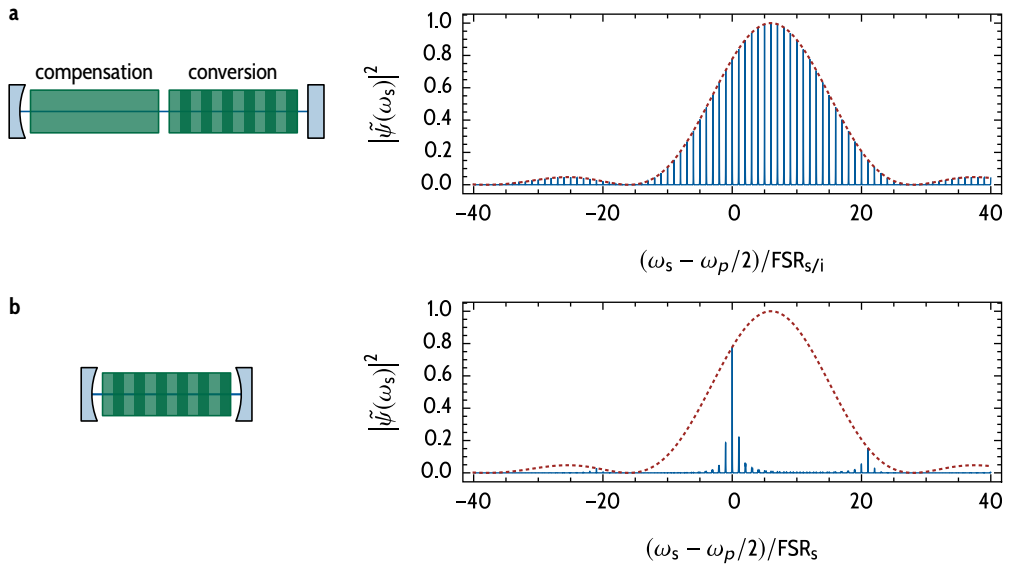

Figure 1.13 | Normalized signal spectral density with and without compensation crystal. The normalized signal spectral density $\left|\tilde{\psi}(\omega_s)\right|^2$ (——) and the corresponding parametric gain envelope $\mathrm{Gain}(\omega_s, \xi, \mu, \Delta\Phi)$ (----) are shown for two cavity configurations. In both cases, the finesse is $\mathcal{F} = 20$ and a small value of ξ is assumed for which the gain envelope has a sinc^2 shape. For simplicity, the relative phase is set to $\Delta\Phi = 0$. The photon-pair source is tuned close to degeneracy. In both cases, one particular mode is tuned to perfect degeneracy with $\omega_s = \omega_i = \omega_p/2$. **a**, For a cavity with compensation crystal, the free spectral ranges of signal and idler fields are identical. Therefore, all signal and idler resonances overlap and the joint resonance function given by $\mathrm{Airy}_s(\omega_s)\mathrm{Airy}_i(\omega_p - \omega_s)$ forms a comb of equally spaced peaks. The effective number of modes N_{modes} lies typically between 40 and 50 in a realistic configuration where the length of the cavity is not much longer than the combined length of the crystals. **b**, For a cavity without compensation crystal, the effective number of modes is drastically reduced due to the cluster effect[188] (see Fig. 1.4). Typically 2 to 3 clusters lie within the parametric gain envelope.[188] The number of modes per cluster approaches unity for high finesse cavities with a double-pass pump.[136,162]

of k can be found for which $\omega_\mathrm{p} - \omega_{\mathrm{s},k} = \omega_{\mathrm{s},j}$. Then, Eq. 1.3.39 can be written as a single sum over pairs of coinciding resonances:

$$\begin{aligned}&\mathrm{Airy}_\mathrm{s}(\omega_\mathrm{s})\mathrm{Airy}_\mathrm{i}(\omega_\mathrm{p} - \omega_\mathrm{s}) = \\ &\sum_{j=-\infty}^{\infty} \frac{\Gamma_\mathrm{s}^2\Gamma_\mathrm{i}^2}{\left[\Gamma_\mathrm{s}^2 + 4\left[\omega_\mathrm{s} - \omega_{\mathrm{s},j}\right]^2\right]\left[\Gamma_\mathrm{i}^2 + 4\left[\omega_\mathrm{s} - \omega_{\mathrm{s},j}\right]^2\right]}.\end{aligned} \tag{1.3.40}$$

These coinciding resonances are commonly called the (spectral) *modes* of the photon-pair source.[111,161] Since the spectral width of the modes is typically much smaller than the parametric gain bandwidth (the width of the parametric gain envelope) and each mode has the same spectral shape, the integral over the signal spectral density in Eq. 1.3.33 can be approximated by:

$$\begin{aligned}\int_0^\infty \mathrm{d}\omega_\mathrm{s} \left|\tilde{\psi}(\omega_\mathrm{s})\right|^2 &= \int_0^\infty \mathrm{d}\omega_\mathrm{s}\, \mathrm{Gain}(\omega_\mathrm{s}, \xi, \mu, \Delta\Phi)\mathrm{Airy}_\mathrm{s}(\omega_\mathrm{s})\mathrm{Airy}_\mathrm{i}(\omega_\mathrm{p} - \omega_\mathrm{s}) \\ &\approx \sum_{j=-\infty}^{\infty} \mathrm{Gain}(\omega_{\mathrm{s},j}, \xi, \mu, \Delta\Phi) \int_{-\infty}^{\infty} \mathrm{d}\omega_\mathrm{s}\, \frac{\Gamma_\mathrm{s}^2\Gamma_\mathrm{i}^2}{\left[\Gamma_\mathrm{s}^2 + 4\omega_\mathrm{s}^2\right]\left[\Gamma_\mathrm{i}^2 + 4\omega_\mathrm{s}^2\right]} \\ &= \frac{\pi\Gamma_\mathrm{s}\Gamma_\mathrm{i}}{\Gamma_\mathrm{s} + \Gamma_\mathrm{i}} \sum_{j=-\infty}^{\infty} \mathrm{Gain}(\omega_{\mathrm{s},j}, \xi, \mu, \Delta\Phi).\end{aligned} \tag{1.3.41}$$

The contribution of each mode at frequency $\omega_{\mathrm{s},j}$ is scaled by the value of the parametric gain envelope at the center of each resonance $\mathrm{Gain}(\omega_{\mathrm{s},j}, \xi, \mu, \Delta\Phi)$. Since the parametric gain envelope has been normalized (Eq. 1.3.35) and the free spectral range is typically much smaller than the gain bandwidth, there is always a resonance frequency $\omega_{\mathrm{s},k}$ for which $\mathrm{Gain}(\omega_{\mathrm{s},k}, \xi, \mu, \Delta\Phi) \approx 1$. Therefore, the sum over the scaling factors in Eq. 1.3.41 is the *effective number of modes* N_modes:

$$N_\mathrm{modes} = \sum_{j=-\infty}^{\infty} \mathrm{Gain}(\omega_{\mathrm{s},j}, \xi, \mu, \Delta\Phi). \tag{1.3.42}$$

The effective number of modes typically lies in the range $40 \leq N_\mathrm{modes} \leq 50$ (Fig. 1.13) for a photon-pair source with compensation crystal.[128,205] Although, if the length of the cavity is much longer than the combined length of the crystals, the number of modes can be considerably higher due to the small free spectral range.[53,126]

Main finding of this chapter. The pair generation rate (Eq. 1.3.33) can now be written as:

$$\mathcal{R} = \kappa l F_{\mathrm{enh}}^{\mathrm{p}} \eta_{\mathrm{s}} \eta_{\mathrm{i}} \mathcal{F}_{\mathrm{s}} \mathcal{F}_{\mathrm{i}} \frac{4}{\pi^2} \mathrm{Gain}_{\mathrm{max}}(\xi, \mu, \Delta\Phi) \frac{\pi \Gamma_{\mathrm{s}} \Gamma_{\mathrm{i}}}{\Gamma_{\mathrm{s}} + \Gamma_{\mathrm{i}}} N_{\mathrm{modes}}. \tag{1.3.43}$$

This expression is the main finding of this chapter. We express the photon-pair generation rate solely in terms of parameters which are directly accessible to an experimenter wanting to design a photon-pair source with a specific wavelength combination of the three fields and a specific geometrical configuration. Eq. 1.3.43 also confirms that the brightness is proportional to the number of modes, as highlighted by Ou and Lu.[111]

Cavity without compensation crystal. Eq. 1.3.43 is valid even for a cavity without compensation crystal. But, the effective number of modes can no longer be calculated with the help of Eq. 1.3.42. Instead, the number of modes can be found by plugging Eq. 1.3.42 into Eq. 1.3.41 and solving for N_{modes}:

$$\begin{aligned} N_{\mathrm{modes}} &= \frac{\int_0^\infty \mathrm{d}\omega_{\mathrm{s}} \left|\tilde{\psi}(\omega_{\mathrm{s}})\right|^2}{\int_{-\infty}^{\infty} \mathrm{d}\omega_{\mathrm{s}} \frac{\Gamma_{\mathrm{s}}^2 \Gamma_{\mathrm{i}}^2}{\left[\Gamma_{\mathrm{s}}^2 + 4\omega_{\mathrm{s}}^2\right]\left[\Gamma_{\mathrm{i}} + 4\omega_{\mathrm{s}}^2\right]}} \\ &= \frac{\Gamma_{\mathrm{s}} + \Gamma_{\mathrm{i}}}{\pi \Gamma_{\mathrm{s}} \Gamma_{\mathrm{i}}} \int_0^\infty \mathrm{d}\omega_{\mathrm{s}} \left|\tilde{\psi}(\omega_{\mathrm{s}})\right|^2. \end{aligned} \tag{1.3.44}$$

The integral over the signal spectral density in Eq. 1.3.44 must be evaluated numerically, in general. The number of modes for a cavity without a compensation crystal is typically $N_{\mathrm{modes}} < 10$ for medium or low finesse cavities. In a double-pass pump (or triply-resonant) configuration with a very high finesse, it can be brought down to $N_{\mathrm{modes}} \approx 1$[130,136,162] (see Fig. 1.13). Of course, such a single-mode source of photon pairs is advantageous for many applications since no external spectral filtering is required to isolate the desired mode.

Discussion. The model for the photon-pair generation rate $\mathcal{R}$ (Eq. 1.3.43) applies not only to triply-resonant cavities. By setting the reflectivity of the first mirror at the pump wavelength to $R_{1,\mathrm{p}} = 0$, it can also be used for a double-pass pumping scheme. Similarly, it can be used for cavity configurations where either signal or idler fields are non-resonant.[206] In the limit of vanishing mirror reflectivities, Eq. 1.3.6 (the starting point of the discussion in this section) converges to the model of Bennink.[59]

When designing a photon-pair source with fixed cavity decay rates $\Gamma_{s/i}$, the parameters appearing in Eq. 1.3.43 cannot be chosen independently. They are interrelated by the properties of the crystals and the geometry of the cavity (especially the length of the nonlinear crystal and the total length of the cavity). Therefore, the dependence of the photon-pair generation rate on the length of the nonlinear crystal is not obvious. We study this dependency in detail in section 1.3.6.

Throughout this section, we assume a continuous wave pump. To also cover pulsed pumping, the spectral structure of the pump field has to be taken into account. In this case, Eq. 1.3.6 cannot be simplified in general and we need to perform a numerical evaluation of the integral. The impact of the pump spectral bandwidth on the generation rate is discussed by Jeronimo-Moreno and colleagues.[129] Note, that a pulsed pump can be used to generate spectrally pure single photons by cavity-enhanced SPDC, as discussed in section 1.4.

1.3.5 | Comparison of theory vs. experiment

With the model from the previous section, *absolute* values of the photon-pair generation rate can be estimated. To evaluate the accuracy of the model, it is therefore mandatory to compare the theoretical prediction with values measured in experiments.

Therefore, in table 1.1, the photon-pair generation rate $\mathcal{R}$ calculated with Eq. 1.3.43 is compared with measured values $\mathcal{R}^{\text{exp}}$ for four different cavity configurations.

Cavity configurations. The photon-pair sources discussed in this section are shown above table 1.1. Two of these sources were built for this thesis and will be discussed in detail in chapter 2. Since these two sources employ a low-finesse cavity, they are contrasted with two high-finesse cavities. The high-finesse photon-pair source reported by Scholz and colleagues[128] consists of a spherical cavity with an additional compensation crystal. In the following this source is abbreviated with the label (HF-C).

The low-finesse sources (LF-C)[205] (with compensation crystal) and (LF-NC)[138] (without compensation crystal) share the same set of mirrors which form a hemispherical cavity. All the aforementioned cavities are triply resonant.

In contrast, the monolithic high-finesse cavity (HF-M) presented by Chuu and Harris[130] is not resonant for the pump beam. Instead, the photon-pair source is pumped in a double-pass configuration.

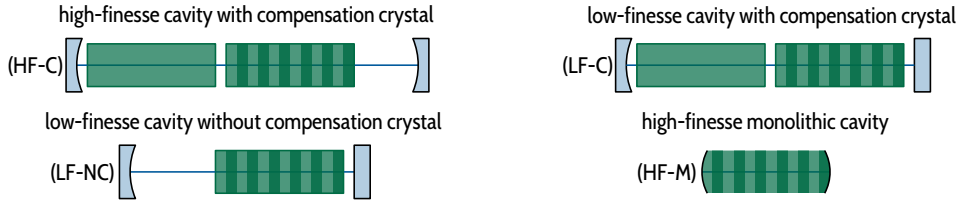

source	(HF-C)[128]	(LF-C)[205]	(LF-NC)[138]	(HF-M)[130]
λ_p (nm)	447	447	447	532
l (mm)	20	20	20	10
L (mm)	66	47.5	39	10
ξ	0.2	0.2	0.2	0.6
μ	0	1	1	0
R_{1p} (%)	50 ± 5	60 ± 5	60 ± 5	0
R_{2p} (%)	99.7 ± 0.2	99.7 ± 0.2	99.7 ± 0.2	99.7 ± 0.2
$T_{coat,p}$ (%)	99.65 ± 0.05	99.65 ± 0.05	99.65 ± 0.05	–
$R_{1s/i}$ (%)	99.95 ± 0.01	99.5 ± 0.2	99.5 ± 0.2	99.54 ± 0.10
$R_{2s/i}$ (%)	98.7 ± 0.5	69 ± 5	69 ± 5	99.54 ± 0.10
$T_{coat,s/i}$ (%)	99.88 ± 0.05	99.88 ± 0.05	99.88 ± 0.05	–
$\mathrm{FSR}_s/(2\pi)$ (GHz)	1.52	1.84	2.7	8.32
$\Gamma_p^{exp}/(2\pi)$ (MHz)	360	340	333	–
$\Gamma_s^{exp}/(2\pi)$ (MHz)	5.66	120	165	12.6
$\mathcal{F}_p$	4.7 ± 0.4	5.5 ± 0.4	8.0 ± 0.9	–
$\mathcal{F}_p^{exp}$	3.8	4.5 ± 1.0	8.0 ± 1.0	–
F_{enh}^p	2.19 ± 0.08	2.18 ± 0.01	3.87 ± 0.02	1
$\mathcal{F}_{s/i}$	270 ± 60	16 ± 3	16 ± 3	660 ± 90
$\mathcal{F}_{s/i}^{exp}$	270	15 ± 1	16 ± 1	660
$F_{enh}^{s/i}$	97 ± 19	10.1 ± 1.8	10.3 ± 1.9	210 ± 40
N_{modes}	49 ± 6	39 ± 6	4.3 ± 0.2	1.002 ± 0.002
η_s (%)	56 ± 11	96.9 ± 0.9	97.5 ± 0.8	49 ± 6
$\mathcal{R}$ (kHz/mW)	5100 ± 1800	900 ± 300	320 ± 110	450 ± 160
$\mathcal{R}^{exp}$ (kHz/mW)	3800	600 ± 100	400 ± 100	110
$\mathcal{R}_{center}$ (kHz/mW)	100 ± 40	22 ± 7	80 ± 30	450 ± 160
$\mathcal{R}_{center}^{exp}$ (kHz/mW)	60	16 ± 5	60 ± 20	–

Table 1.1 | Photon-pair generation rates – theory and experiments. Comparison of measured photon-pair generation rates and theoretical predictions. For details see the main text.

Mirror reflectivities and crystal properties. The values for the mirror reflectivities of sources (HF-C) and (HF-M) were not given in the corresponding publications. Therefore, fitting values were calculated from the measured values of the finesse

$\mathcal{F}^{\text{exp}}$ and the cavity decay rates Γ_n^{exp}. It was further assumed for source (HF-M) that both mirrors had the same reflectivity at the signal wavelength. The error margins for the mirror reflectivities of sources (HF-C) and (HF-M) are estimated values. For sources (LF-C) and (LF-NC), the reflectivities of the mirrors $R_{1/2,n}$ and the transmission of the crystals' anti-reflection coatings $T_{\text{coat},n}$ were measured in the experiment. Since the crystals of source (HF-C) where built by the same manufacturer, we assume that the anti-reflection coatings had the same properties. For the absorption inside the crystal, absorption coefficients of $\alpha_{s/i} = 0.01\,\%/\text{cm}$ and $\alpha_{\text{p}} = 3.5\,\%/\text{cm}$ are assumed.[138,207]

All photon-pair sources analyzed in this section use a periodically poled KTP crystal and are phase-matched for degenerated type-II parametric down-conversion. For the effective nonlinear coefficient, the value $d_{\text{eff}} = 1.8(2)\,\text{pm/V}$ reported by Dixon and coworkers[195] was used which lies within the range of values published by other groups.[208,209] Note, that the uncertainty in d_{eff} is a mayor contribution to the overall uncertainties in $\mathcal{R}$ and $\mathcal{R}_{\text{center}}$.

Parameters. In table 1.1, l denotes the length of the crystals and L is the distance between the two mirrors. λ_{p} is the pump wavelength, ξ is the focussing parameter and μ is the focus position parameter. The following values were calculated from the cavity geometry, the mirror reflectivities and the transmission of the crystals: the free spectral range $\text{FSR}_{\text{s/i}}$, the values of the cavity finesse $\mathcal{F}_n$, the enhancement factors F_{enh}^n, the number of modes N_{modes} and the pair extraction efficiency η_{pair}. The photon-pair generation rate of the central mode $\mathcal{R}_{\text{center}}$ was calculated by:

$$\mathcal{R}_{\text{center}} = \frac{\mathcal{R}}{N_{\text{modes}}}. \tag{1.3.45}$$

The reported values for the photon-pair generation rate (without spectral filtering) $\mathcal{R}^{\text{exp}}$ where corrected for all experimental photon losses and for the detection efficiency of the single-photon counters, but not for the extraction efficiencies. The corresponding error margin therefore includes the uncertainties in the measurement of the different photon loss factors. The corresponding values $\mathcal{R}_{\text{center}}^{\text{exp}}$ for sources (HF-C), (LF-C) and (LF-NC) where measured by selecting only photons from the central mode with spectral filters. The values given in table 1.1 are corrected for the additional losses of the spectral filters. For the monolithic source (HF-M), the absolute photon-pair generation rate should be equal to the photon-pair generation rate of the central mode since this source is essentially single-mode due to its high finesse and the double-pass pump configuration.

Mirror phase shift and resonance frequencies. For simplicity, a relative phase of $\Delta\Phi = 0$ (see Eq. 1.2.40) was assumed. For the photon-pair generation rate, this is a

best-case scenario and corresponds to vanishing mirror phase shifts ($\Delta\delta_1 \approx 0$) and relative Gouy phases ($\Delta\phi^{\text{eff}}_{\text{Gouy}} \approx 0$). At least for cavities (HF-C) and (LF-C) with compensation crystals, this assumption was verified experimentally by measuring the spectral shape of the parametric gain envelope (see section 2.3.3)

For cavities (LF-NC) and (HF-M) without compensation crystals, if was further assumed that a cluster was located at the center of the parametric gain envelope. For source (LF-NC) this was not always the case (see section 2.3.6). For source (HF-M) this could have been achieved by fine-tuning the wavelength of the pump, but such a fine-tuning was not discussed in the publication.

Discussion. For sources (HF-C), (LF-C), and (LF-NC), a good agreement between the theoretical model (Eq. 1.3.43) and the measured values of the photon-pair generation rate is found. Due to the various uncertainties (mainly in the reflectivities of the mirrors and the effective nonlinear coefficient), the theoretical values have an uncertainty of about 30 %. The measured values all lie within this uncertainty range, except for source (HF-M) where a significant deviation is observed.

The deviation for source (HF-M) may have the following causes: The pump beam might have been improperly aligned or improperly mode-matched to the cavity, reducing the effective focussing parameter ξ. Additionally, the extraction efficiency was not reported for this source and might be lower than the theoretical value. The extraction efficiency strongly depends on the losses in the cavity (see section 1.3.3). Losses not covered by the theoretical model might be caused by scattering on the spherically polished end facets of the monolithic cavity, for example.

Note, that the assumption $R_{1,\text{s/i}} = R_{2,\text{s/i}}$ for source (HF-M) might not be justified since the coatings of the cavity's facets must at least differ at the pump wavelength. A more reasonable choice for the reflectivities (e.g. $R_{1,\text{s/i}} = 99.9\,\%$ and $R_{2,\text{s/i}} = 99.1\,\%$) would result in the same value for the finesse but a much higher extraction efficiency of 90(10) %. The corresponding theoretical value of the generation rate of $\mathcal{R} = 1.5(6)\,\text{MHz/mW}$ would even be an order of magnitude larger than the measured value of $\mathcal{R}^{\text{exp}} = 110\,\text{kHz/mW}$.

Conclusion. In conclusion, the theoretical model developed in this section could experimentally be confirmed, given that the properties of the cavity mirrors are known with low uncertainty. Especially for high-finesse cavities, all losses inside the cavity must also be known precisely to provide a reasonable estimate of the generation rates. To further improve the accuracy of the predicted photon-pair generation rate, a more accurate value of the effective nonlinear coefficient d_{eff} would be required. In general, this can only be achieved by directly measuring

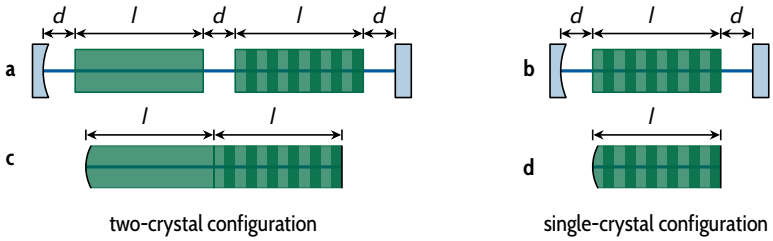

Figure 1.14 | Length optimization for cavity-enhanced photon-pair sources. In Fig. 1.15, the photon-pair generation rate for different cavity configurations are calculated as a function of the length l of the nonlinear crystal. There are two-crystal configurations and corresponding single-crystal configurations. Configurations **a** and **b** are conventional cavities with a fixed spacing between crystals and mirrors of $d = 1\,\text{mm}$. The two monolithic configurations **c** and **d** do not have any anti-reflection coated surfaces. Their end faces are polished and a highly reflective coating is applied to them. For configuration **c**, the nonlinear crystal and (rotated) compensation crystal have to be optically bonded e.g. by diffusion bonding.[211,212] All cavities are hemispherical and the radius of curvature of the concave mirror is chosen such that the focussing parameter is $\xi = 0.2$ for each length l of the crystals. The reflectivity of the mirrors at the pump wavelength is matched to the losses inside the cavity to obtain an optimum enhancement of the pump field. At the signal and idler wavelength, the reflectivity is chosen for every length l such that the signal and idler photon have a spectral width of $\Delta\nu_{s/i} = \sqrt{\sqrt{2}-1} \times \Gamma_{s/i}/(2\pi) = 100\,\text{MHz}$.[161]

d_{eff} of the crystal in use since the effective nonlinear coefficient is affected by the growth process of the crystal and imperfections in the periodic poling.[210]

1.3.6 | Optimization of the cavity length

One of the main objectives of this thesis is to design a cavity-enhanced photon-pair source with a spectral bandwidth of the signal and idler photons of $\Delta\nu_{s/i} \approx 100\,\text{MHz}$ to produce photons which are indistinguishable from photons generated by quantum dots[169,213] and can be stored in quantum memories based on neutral atoms.[110,163,166]

The spectral bandwidth of the photons is related to the cavity decay rate by:[161,162]

$$\Delta\nu_{s/i} = \sqrt{\sqrt{2}-1}\,\frac{\Gamma_{s/i}}{2\pi}. \tag{1.3.46}$$

Therefore, for a given length of the nonlinear crystal and the corresponding free spectral range of the cavity, it is straightforward to compute the required finesse via Eq. 1.3.13. But, it is not obvious whether the maximum generation rate per pump power is achieved with a shorter or a longer nonlinear crystal since there are several competing mechanisms: At least for small values of the focussing parameter ξ, the generation rate is proportional to the length of the nonlinear

crystal l (see Eq. 1.2.15). This favors longer crystals. For smaller values of l, the free spectral range is larger and therefore a higher finesse is needed to obtain the same linewidth. On the one hand, a higher finesse leads to a stronger enhancement inside the cavity (see Eq. 1.3.29). On the other hand, this results in a lower extraction efficiency due to higher losses (see Fig. 1.12).

One important loss factor is absorption inside the crystal. The loss by absorption increases exponentially with the length of the crystal. Signal and idler photons typically are emitted in the near infrared region where losses by absorption are much smaller than losses by imperfect anti-reflection coatings, for example. But, at the pump wavelength, losses by absorption can have a strong impact on the brightness especially for long ($l > 1\,\mathrm{cm}$) crystals where the pump enhancement factor is typically limited to values $F_{\mathrm{enh}}^{\mathrm{p}} < 5$.[128,138]

To evaluate the influence of these different enhancement and loss mechanisms on the photon-pair generation rate, the theoretical model previously developed in this section (Eq. 1.3.43) is utilized. The generation rate $\mathcal{R}$ and the rate of photon pairs generated into the central mode $\mathcal{R}_{\mathrm{center}}$ is calculated depending on the length l of the crystals for different cavity configurations. In this way, the optimum crystal length of a photon-pair source with a bandwidth of $\Delta\nu_{\mathrm{s/i}} = 100\,\mathrm{MHz}$ is found for the different cavity configurations. The following paragraph describes in detail the cavity configurations used in this simulation.

Cavity configurations. The generation rates as functions of the crystal length l are calculated for the four different cavity configurations shown in Fig. 1.14. The results are shown in Fig. 1.15 for crystal lengths between $l = 1\,\mathrm{mm}$ and $l = 20\,\mathrm{mm}$. Two-crystal configurations are compared with single-crystal configurations and conventional cavities are compared with monolithic cavities. An important aim of this comparison is to evaluate the influence of the number of (anti-reflection coated) surfaces on the generation rate.

For conventional cavities, the spacing d between the crystals is an important parameter since it cannot be chosen arbitrarily small to avoid direct contact of the different surfaces. The spacing d also defines an upper bound for the free spectral range and therefore the finesse of cavity. Here, the spacing is fixed to $d = 1\,\mathrm{mm}$ for both conventional cavities and for all values of l. These conventional cavities are contrasted with monolithic cavities where $d = 0\,\mathrm{mm}$. Of course, a monolithic two-crystal configuration is an exotic design which would require that nonlinear and compensation crystals are optically bonded.[212,214]

In Fig. 1.15, it is assumed that periodically poled KTP crystals phase-matched for degenerate type-II parametric down-conversion pumped at 447 nm are used. The losses at the crystals' facets are $1 - T_{\mathrm{coat,s/i/p}} = 0.2\,\%$[215] for all three fields. Note, that for the pump wavelength, the losses at the facets measured

in the experiment were substantially higher.[138] The following reflectivities are fixed: $R_{1,s/i} = R_{2,p} = 99.9\,\%$. This enables maximum pump enhancement and maximum signal/idler extraction efficiency through the second mirror. For the absorption inside the crystal, absorption coefficients of $\alpha_{s/i} = 0.01\,\%/\text{cm}$ and $\alpha_p = 3.5\,\%/\text{cm}$ are assumed.[138,207] The reflectivity at the pump wavelength of the first mirror $R_{1,p}$ is always impedance matched to the losses to obtain an optimum enhancement of the pump field (see Eq. 1.3.25). Only for cavities with short crystals (low losses), the reflectivity $R_{1,p}$ is chosen such that the pump cavity decay rate stays above $\Gamma_p = 2\pi \cdot 1\,\text{GHz}$ to enable the generation of pure single photons (see section 1.4). The reflectivity $R_{2,s/i}$ is chosen such that the linewidth $\Delta\nu_{s/i}$ is 100 MHz for all cavity lengths.

The radius of curvature of the concave mirror is chosen such that the focussing parameter is $\xi = 0.2$ for all values of the cavity length. For this value of ξ, the Boyd-Kleinman factor drops to about 20 % of its maximum value (see Fig. 1.7). The position of the focus with respect to the center of the nonlinear crystal is no longer a critical parameter as the Boyd-Kleinman factor varies very slowly with the focus position parameter μ (Eqs. 1.2.8 and 1.2.10) for $\xi = 0.2$. A symmetrical cavity with two concave mirrors ($\mu = 0$) and $\xi = 0.2$ would have nearly the same Boyd-Kleinman factor.

Results. Fig. 1.15 shows that for a fixed bandwidth $\Delta\nu_{s/i} = 100\,\text{MHz}$ the generation rate $\mathcal{R}$ and the central mode generation rate $\mathcal{R}_{\text{center}}$ increase monotonically for decreasing values of the crystal length l. The cavity enhancement overbalances the losses at higher values of the finesse. Compared to conventional cavities, monolithic cavities are brighter due to lower losses. The increase in generation rate for shorter crystals is also much stronger for monolithic cavities: While from $l = 20\,\text{mm}$ to $l = 1\,\text{mm}$ the rates $\mathcal{R}$ and $\mathcal{R}_{\text{center}}$ are increased by about a factor of 10 for conventional cavities, for monolithic cavities there is an increase of more than two orders of magnitude. An important contribution to the increase in brightness is the increase in the pump enhancement factor F^p_{enh} for short cavities. The advantage of triply-resonant configurations over double-pass pumping schemes can be quantified by comparing Fig. 1.15 with Fig. 1.16.

The two-crystal configurations have a higher absolute photon-pair generation rate than the corresponding single-crystal configurations caused by a higher number of effective modes N_{modes}. Conversely, the central mode generation rate $\mathcal{R}_{\text{center}}$ is nearly an order of magnitude higher for the single-crystal configurations than for the corresponding two-crystal configurations due to a higher signal/idler finesse, a higher pump enhancement and a considerably higher extraction efficiency $\eta_{s/i}$.

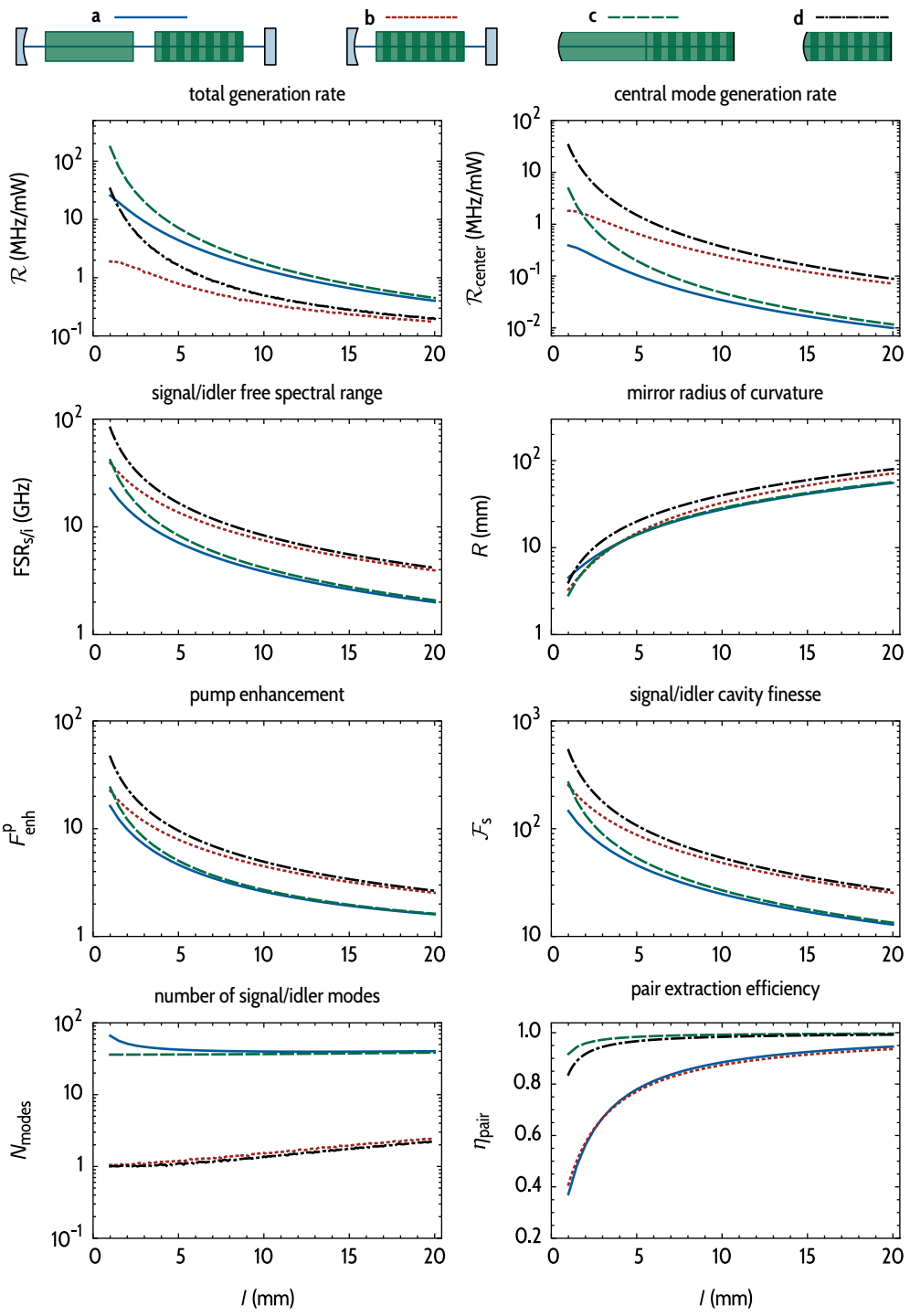

Figure 1.15 | Optimization of the cavity length. For details see the main text and Fig. 1.14.

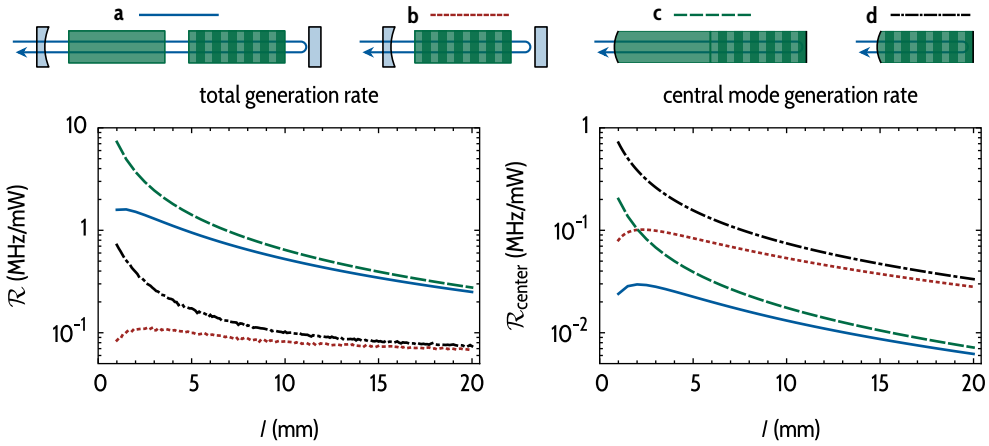

Figure 1.16 | Photon-pair generation rates without pump resonance. Here, the generation rates $\mathcal{R}$ and $\mathcal{R}_{\text{center}}$ are shown for the same cavity configuration as in Fig. 1.15. Instead of resonant pumping, a double-pass pumping scheme is simulated. This corresponds to setting $F^{\text{p}}_{\text{enh}} = 1$ in Eq. 1.3.43. Compared to Fig. 1.15, the generation rates for the conventional cavities are nearly constant for all values of the crystal length l. For $l \lesssim 3$ mm, the generation rates are even decreasing with decreasing values of l due to low values of the extraction efficiencies. For monolithic cavities, the generation rates are also nearly constant. Only for crystal lengths below $l \approx 3$ mm, where the signal/idler finesse is very large, a significant increase is expected.

The monolithic cavities have a very high extraction efficiency ($\eta_{\text{s/i}} > 95\,\%$) for all crystal lengths down to $l \approx 2\,\text{mm}$. Conventional cavities with short crystals ($l < 15\,\text{mm}$), in contrast, have an extraction efficiency which is too low ($\eta_{\text{pair}} < 90\,\%$) for experiments which rely on efficient heralding of single photons.

The strong increase in the generation rate for shorter cavities is mainly caused by pump enhancement. This is illustrated in Fig. 1.16 where the generation rates for the same cavities operated with a double-pass pump configuration are shown. In the model (Eq. 1.3.43), this corresponds to setting $F^{\text{p}}_{\text{enh}} = 1$. Without pump resonance, the generation rates for the conventional cavities are nearly constant for all values of the crystal length l. For small values of l, the generation rate does no longer increase due to the low values of the extraction efficiency. The generation rate for the monolithic cavities is increased significantly only for crystal lengths l below ~3 mm.

Discussion. Considering just the generation rates, cavities with short crystals are favorable due to the higher values of the finesse. Short cavities also have the advantage of a larger free spectral range which facilitates the filtering of individual spectral modes. But, short cavities with a high finesse also have disadvantages: They require a more elaborate alignment and a more precise mode-matching to reduce unwanted resonances of higher order transverse

modes. Additionally, a higher finesse also causes higher losses of signal and idler photons especially for conventional cavities.

Shorter crystals also have the disadvantage that low values of the mirror radius of curvature are required to attain the same Boyd-Kleinman factor. For $l < 5$ mm the radius of curvature must lie below 20 mm to obtain a focussing parameter $\xi > 0.2$ such that off-the-shelf components for the conclusion mirrors can no longer be used. The fabrication of monolithic cavities with a length of 1 mm and a radius of curvature of $R \approx 3$ mm is certainly challenging. Cavities in the form of a sphere or a spherical disk ($R = l/2$) may be more viable.

In terms of the generation rate per mW of pump power, monolithic cavities are superior to conventional cavities. Of course, monolithic cavities have the advantage that they are not susceptible to acoustic noise or vibrations and therefore require no active stabilization of the crystal lengths. The resonance conditions are determined by the temperature of the crystals. Therefore, the resonance frequencies of the three fields can in general not be tuned independently.

Alternative cavity designs. If perfect signal/idler frequency degeneracy in the central mode is required, the resonance frequencies of all three fields must be tuned appropriately.[118,125] For conventional cavities, triple resonance with degenerate signal/idler resonances can be achieved by tuning the temperature and orientation of the crystals.[138,185,216] For monolithic cavities, the crystal can no longer be tilted with respect to the optical axis. Therefore, triple-resonance with degenerate signal and idler photons cannot be achieved at an arbitrary pump wavelength for the monolithic single-crystal configuration unless alternative tuning mechanisms are utilized.

To overcome this limitation of monolithic cavities, in Fig. 1.17 a modified cavity configuration is proposed, inspired by the recent work on doubly-resonant second-harmonic generation and squeezed light generation of Zielińska and colleagues.[152,217] The modified cavity consists of a single KTP crystal which is periodically poled only in the central region of length l. There are three heating elements placed beneath the crystal such that the three regions have different temperatures T_1, T_2 and T_3. The resonance frequencies of the three fields can be tuned by setting these temperatures. An additional tuning parameter is strain applied onto the crystal with a piezo-electric transducer. The expected central-mode generation rate is identical to the monolithic two-crystal configuration **c** discussed above. A slight disadvantage of this configuration is that the effective number of modes is $N_{\text{modes}} \approx 4$ even for small values of the cavity length and high values of the signal/idler finesse. There are always multiple clusters of modes within the parametric gain bandwidth. A detailed analysis of this setup is required to evaluate whether the tuning mechanisms discussed here are

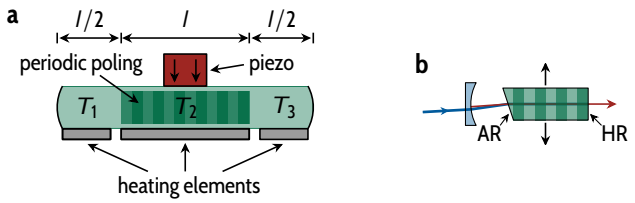

Figure 1.17 | Alternative cavity configurations with tuning capabilities. **a**, Design proposal for a triply-resonant cavity which can be tuned to perfect signal/idler degeneracy for an arbitrary pump wavelength inspired by the work on resonant second-harmonic generation and squeezed light generation by Zielińska[152,217] and coworkers: The cavity consists of a single nonlinear crystal which is periodically poled only in the central region. The different regions in the crystal can be brought to temperatures T_1, T_2 and T_3 via heating elements. The resonance frequencies of the three fields can be tuned by changing these temperatures. Additionally, mechanical strain can be applied by a piezo-electric transducer to shift the resonance frequencies. The thermo-optic and elasto-optic coefficients are different for pump and signal/idler wavelength.[217] An additional piezo-electric transducer acting on the other axis perpendicular to the optical axis could provide another tuning degree of freedom. Changing temperatures T_1 and T_3 should also allow for a tuning of the relative phase $\Delta\Phi$ of the phase-balancing factor (Eq. 1.2.40). The central mode generation rate $\mathcal{R}_{\text{center}}$ of this photon-pair source should be identical to the monolithic two-crystal configuration **c** (Figs. 1.14 and 1.15). Further studies are required to analyze how temperature gradients affect the brightness of this setup – especially for short cavities. **b**, To reduce the number of surfaces inside the cavity, a semi-monolithic configuration can be used. The configuration shown here is inspired by earlier works on semi-monolithic cavities,[111,123] combined with the idea to use a wedged crystal.[218,219] To achieve triple resonance, the crystal can no longer be tilted since otherwise the alignment of the cavity would be lost. But, it can be translated perpendicularly to the optical axis instead. Due to the small wedge of the crystal, the effective optical path length is changed. On the wedged side of the crystal an anti-reflection coating (AR) is applied. On the other side a highly reflective (HR) coating is applied, acting as the outcoupling mirror for the signal and idler photons. The brightness and extraction efficiency of this source should be between configurations **b** and **d**, which were shown in Fig. 1.15.

sufficient to achieve triple resonance for all wavelength combinations. Possibly, additional strain tuning on the other crystal axis is required to tune signal and idler resonances independently.

Another option to reduce the losses is shown in Fig. 1.17b. In this case, a semi-monolithic cavity with a wedged crystal is used to reduce the number of surfaces inside the cavity. The wedge on the crystal can be utilized to tune the resonance frequencies by translating the crystal perpendicularly to the optical axis. This configuration has a brightness and extraction efficiency between sources **b** and **d**, which have been discussed in Fig. 1.15. It would still need an active stabilization of the cavity length via a piezo-electric transducer.

1.4 | Purity

If the photon-pair source is used as a source of heralded single photons, the *purity* $\mathcal{P}_s$ of the heralded signal photons is an important figure of merit for many experiments in quantum optics and for applications like quantum computation based on linear optics[66] or quantum information processing.[220] The great importance of purity in quantum optics experiments is illustrated by the example of the well known Hong-Ou-Mandel effect.[33] The visibility of the Hong-Ou-Mandel interference can only reach unity if the two interaction photons are spectrally indistinguishable and if both photons are in a pure state.[221,222] Conceptually important experiments like quantum teleportation[34,92] or entanglement swapping[35,223] also require pure states.

Often, narrowband spectral filtering in employed to obtain pure single photons from parametric down-conversion sources.[34,35,85,223,224] But, spectral filtering of conventional down-conversion sources always results in a reduced heralding efficiency.[68,69]

The spectral correlations of signal and idler photons in parametric down-conversion can be eliminated by various methods without spectral filtering,[225–227] e.g. by group velocity matching[71] or Gaussian phase matching conditions.[228,229] A detailed discussion how to use and optimize these methods in practical experiments can be found in the recent publication by Graffitti and colleagues.[230]

This section shows that triply-resonant cavity-enhanced parametric down-conversion can also produce photons in a pure state. For this, a pulsed pump and spectral filtering to isolate a single spectral mode are required. For cavity-enhanced photon sources, the spectral filtering does not degrade the heralding efficiency for signal photons emitted into the selected spectral mode.

In the following, the concept of the spectral purity of a single photon state will be introduced. It will be shown how Schmidt decomposition can be used to calculate the purity of a heralded single photons generated by spontaneous parametric down-conversion. Subsequently, the purity of photons generated in a triply-resonant cavity is analyzed quantitatively. Spectrally pure photons can only be generated if the spectral bandwidth of the pump and the linewidth of the cavity at the pump wavelength are much larger than the cavity decay rate of the signal and idler fields. Additionally, the linewidth of the pump resonance must be large enough. Otherwise, the pump-pulse would be (partially) reflected by the cavity.

1.4.1 | Purity and Schmidt decomposition

If the down-conversion source is used as a heralded single-photon source, the two-photon wave function (Eq. 1.1.28) can be written as:

$$\left|\psi\right\rangle = \int_0^\infty \mathrm{d}\omega_\mathrm{s}\,\mathrm{d}\omega_\mathrm{i}\,\psi(\omega_\mathrm{s},\omega_\mathrm{i})\hat{a}_\mathrm{s}^\dagger(\omega_\mathrm{s})\hat{a}_\mathrm{i}^\dagger(\omega_\mathrm{i})\left|0,0\right\rangle, \tag{1.4.1}$$

where the vacuum contribution is discarded due to the heralding process. Now, a basis of orthogonal *Schmidt modes* $\psi_n(\omega_\mathrm{s})$ and $\phi_n(\omega_\mathrm{i})$ with creation operators[226,231]

$$\begin{aligned}\hat{b}_n^\dagger &= \int_0^\infty \mathrm{d}\omega_\mathrm{s}\,\psi_n(\omega_\mathrm{s})\hat{a}_\mathrm{s}^\dagger(\omega_\mathrm{s})\\ \hat{c}_n^\dagger &= \int_0^\infty \mathrm{d}\omega_\mathrm{i}\,\phi_n(\omega_\mathrm{i})\hat{a}_\mathrm{i}^\dagger(\omega_\mathrm{i})\end{aligned} \tag{1.4.2}$$

can be introduced. Note, that in general the analytic form of ψ_n and ϕ_n cannot be found and must be approximated numerically.[221,231] The two-photon state can now be expressed as a (possibly) infinite sum:

$$\begin{aligned}\left|\psi\right\rangle &= \sum_n \sqrt{\lambda_n}\hat{b}_n^\dagger\hat{c}_n^\dagger\left|0,0\right\rangle\\ &= \sum_n \sqrt{\lambda_n}\left|b_n\right\rangle\left|c_n\right\rangle,\end{aligned} \tag{1.4.3}$$

where the so-called *Schmidt coefficients* λ_n are sorted in descending order of magnitude and fulfil $\sum_n \lambda_n = 1$. The joint spectral amplitude now is of the

form:[225,231]

$$\psi(\omega_s, \omega_i) = \sum_n \sqrt{\lambda_n}\psi_n(\omega_s)\phi_n(\omega_i). \tag{1.4.4}$$

Assume that the idler photon is used to herald the presence of a signal photon: If the idler photon is detected by a single-photon detector which does not discriminate the different Schmidt modes, the state after measurement is:[228]

$$\rho_s = \sum_n \lambda_n \, |b_n\rangle\langle b_n| \tag{1.4.5}$$

This is a mixed state in general and a pure state if and only if $\lambda_1 = 1$ and $\lambda_n = 0$ for all $n > 1$. With Eq. 1.4.4, this implies that the heralded signal photon is in a pure state if and only if the joint spectral amplitude is separable:

$$\psi(\omega_s, \omega_i) = \psi_1(\omega_s)\phi_1(\omega_i). \tag{1.4.6}$$

Purity. The *purity* $\mathcal{P}_s$ of the heralded signal photon can be derived from the density operator of the two-photon state:[221]

$$\rho = \left|\tilde{\psi}\right\rangle\left\langle\tilde{\psi}\right|, \tag{1.4.7}$$

by taking the partial trace:

$$\rho_s = \mathrm{Tr}_i(\rho) = \sum_n \langle c_n|\rho|c_n\rangle \, . \tag{1.4.8}$$

Accordingly, the purity of the heralded photons is defined as:

$$\mathcal{P}_s = \mathrm{Tr}_s(\rho_s^2) = \sum_n \langle b_n|\rho_s^2|b_n\rangle = \sum_n \lambda_n^2. \tag{1.4.9}$$

Schmidt decomposition. The purity can be calculated numerically[71] by constructing a complex matrix Ψ with matrix elements:

$$\Psi_{jk} = \psi(\omega_{s,j}, \omega_{i,k}), \tag{1.4.10}$$

where $\omega_{s,j}$ and $\omega_{i,k}$ are discrete sampling points laid out in a rectangular or square grid. The sampling points need to lie sufficiently close to each other to sample all structural features of the joint spectral amplitude. Now, the singular values[232] d_n of the matrix (Ψ_{jk}) can be computed.[227] In the limit

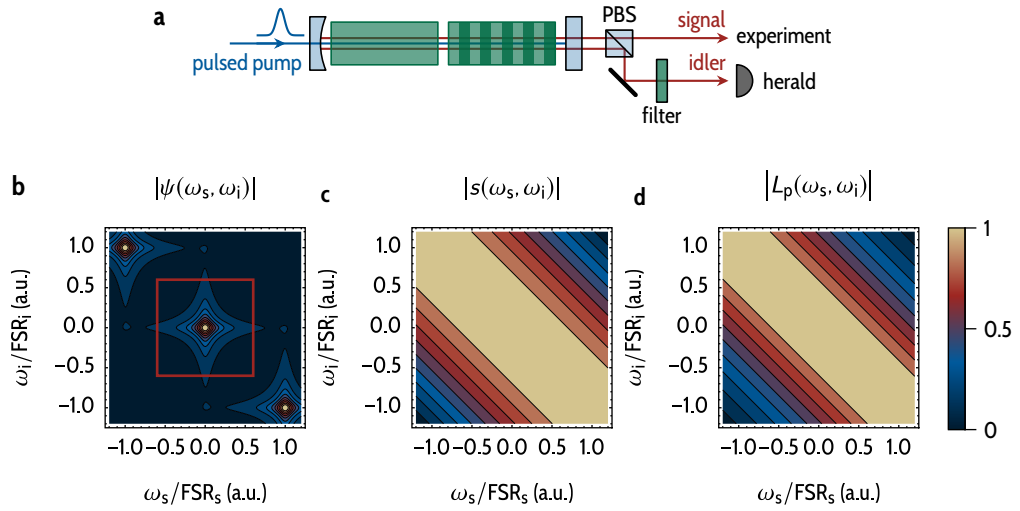

Figure 1.18 | Generation of pure single photons. **a**, A photon-pair source based on triply-resonant cavity-enhanced SPDC can herald spectrally pure photons in the signal arm if two conditions are fulfilled: The photon-pair source is operated with a pulsed pump of sufficient bandwidth and the spectral linewidth of the pump resonances is much broader than the signal/idler resonance line widths. Signal and idler photons are split at a polarizing beam splitter. In the idler arm, a narrow spectral filter selects only a single spectral mode. A click at the idler single-photon detector then heralds the presence of a signal photon in a spectrally pure state. **b**, The joint spectral amplitude $|\psi(\omega_s, \omega_i)|$ is plotted for a photon-pair source with compensation crystal pumped by a pulsed pump. The corresponding pump spectral amplitude $|s(\omega_s, \omega_i)|$ and Lorentzian contribution of the pump resonance $|L_p(\omega_s, \omega_i)|$ (Eq. 1.4.14) are shown in panel **c** and **d**, respectively. The pump resonance linewidth is much larger than the signal/idler linewidth ($\Gamma_p \gg \Gamma_{s/i}$). A Gaussian pulse with a spectral width σ_p much larger than the signal/idler cavity decay rate $\Gamma_{s/i}$ is simulated. The pump spectral amplitude has a diagonal structure since $s(\omega_p) = s(\omega_s + \omega_i)$. The central region marked in **b** indicates the frequencies which are transmitted by the spectral filter shown in **a**. Though only the idler photons are directly spectrally filtered, the frequency of the corresponding heralded photons in the signal arm is also fixed due to energy conservation.

$|\omega_{s/i,j} - \omega_{s/i,j+1}| \to 0$, the normalized singular values d_n correspond to the Schmidt coefficients:[71]

$$d_n \to \sqrt{\lambda_n}. \tag{1.4.11}$$

Using Eq. 1.4.9, the purity can numerically be approximated by:

$$\mathcal{P}_s = \sum_n d_n^4. \tag{1.4.12}$$

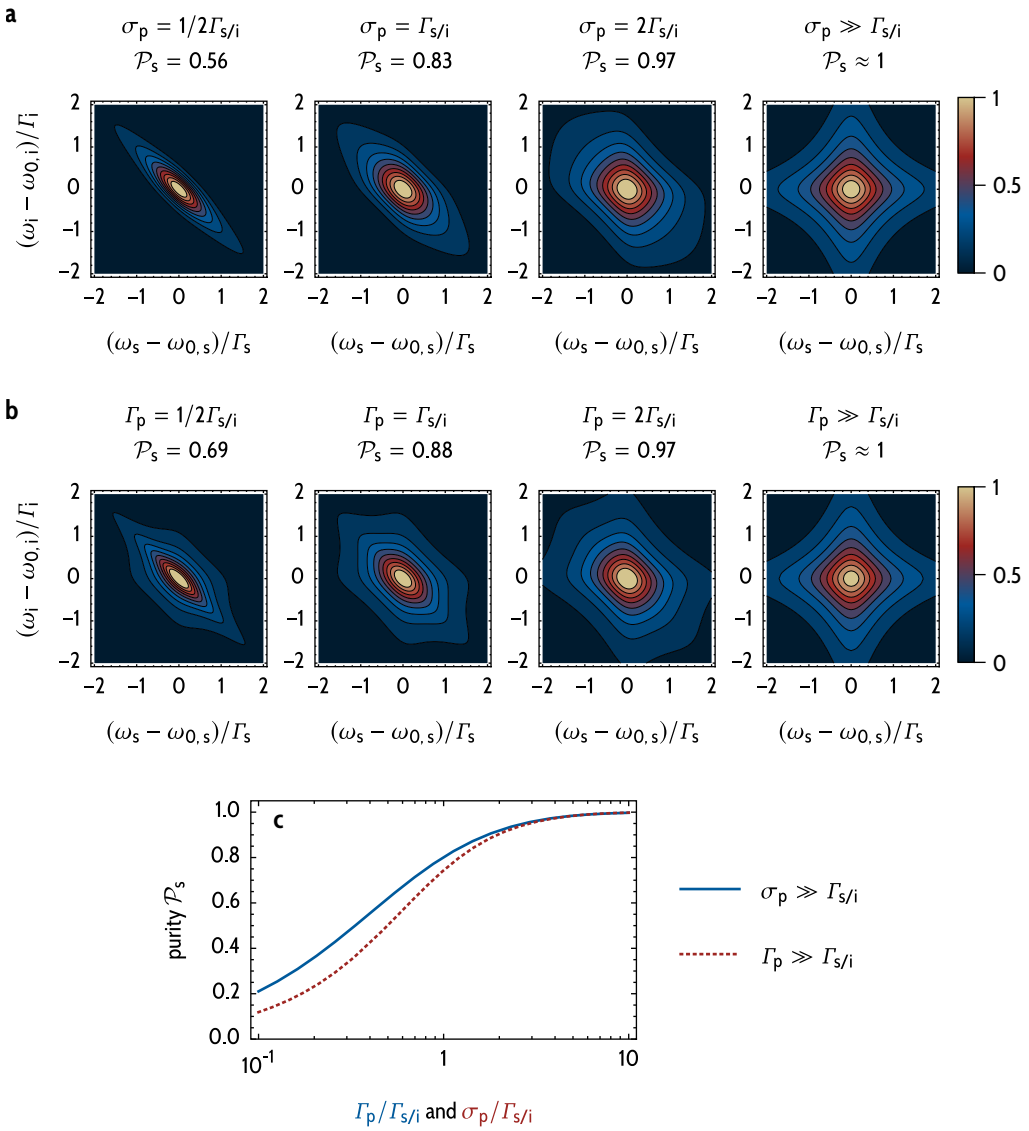

Figure 1.19 | Joint spectral amplitude and spectral purity depending on pump spectral bandwidth and pump cavity linewidth. **a**, Joint spectral amplitude $|\psi(\omega_s, \omega_i)|$ for large pump cavity decay rate ($\Gamma_p \gg \Gamma_{si}$) for different values of the pump spectral bandwidth σ_p. If the pump spectral bandwidth is smaller than the signal/idler cavity decay rate, strong spectral correlations between signal and idler photons can be observed. The spectral correlations result in a symmetric joint spectral amplitude which cannot be factored into a signal and an idler part. Only if both $\Gamma_p \gg \Gamma_{s/i}$ and $\sigma_p \gg \Gamma_{s/i}$ are fulfilled, the spectral purity of the generated photons approaches unity and the joint spectral amplitude is symmetric. Here, it is assumed that the heralding idler photons are spectrally filtered as shown in Fig. 1.18b. **b**, Joint spectral amplitude for a broadband pump ($\sigma_p \gg \Gamma_{s/i}$) for different values of the cavity decay rate at the pump wavelength Γ_p. **c**, Purity $\mathcal{P}_s$ as a function of either $\Gamma_p/\Gamma_{s/i}$ or $\sigma_p/\Gamma_{s/i}$. For a continuous wave pump or a very narrow pump resonance, signal and idler photons are highly correlated and the signal photon purity approaches $\mathcal{P}_s \approx 0$. If $s(\omega_s, \omega_i)$ and $L_p(\omega_s, \omega_i)$ are nearly constant over the length scale of the signal/idler cavity decay rate, the signal photon purity approaches $\mathcal{P}_s \approx 1$ (see Fig. 1.18).

1.4.2 | Triply-resonant cavity-enhanced parametric down-conversion

The purity of a cavity-enhanced source with single-pass pumping has been analyzed quantitatively by Brecht and coworkers.[137] They found that spectrally pure photons can be heralded given that a pulsed pump with a pulse bandwidth σ_p much larger than the signal/idler cavity decay rates $\Gamma_{\mathrm{s/i}}$ is used. Zhang et al.[107] came to the same conclusion and verified the purity with a Hong-Ou-Mandel type experiment using a cavity with a single-pass pump. Qualitatively, the relation between pulse bandwidth and purity had already been discussed by Jeronimo-Moreno and colleagues.[129] Jeronimo-Moreno also pointed out that for a triply-resonant cavity, the pump resonance also induces spectral correlations between signal and idler photons. They argued that to herald spectrally uncorrelated photons, the cavity decay of the pump field must also be much larger than the signal/idler cavity decay rates. This section confirms their findings quantitatively by studying the purity of heralded single photons generated in a triply-resonant cavity.

In the following, we consider the case where only the central mode of the full triply-resonant down-conversion spectrum is spectrally selected with a filter, as shown in Fig. 1.18. Here, the joint spectral amplitude can be factored into Lorentzian contributions L_n from the pump, signal and idler resonances (see Eq. 1.3.40), and the pump spectral amplitude distribution $s(\omega_\mathrm{p}) = s(\omega_\mathrm{s} + \omega_\mathrm{i})$ introduced in (1.1.17):

$$\psi(\omega_\mathrm{s}, \omega_\mathrm{i}) \propto s(\omega_\mathrm{s} + \omega_\mathrm{i}) L(\Gamma_\mathrm{p}, \omega_\mathrm{s} + \omega_\mathrm{i}) L(\Gamma_\mathrm{s}, \omega_\mathrm{s}) L(\Gamma_\mathrm{i}, \omega_\mathrm{i}), \tag{1.4.13}$$

with

$$L(\Gamma_n, \omega_n) = \frac{1}{\Gamma_n/2 + i\left[\omega_n - \omega_{0,n}\right]}, \tag{1.4.14}$$

where $\omega_{n,0}$ is the resonance frequency of the selected mode and Γ_n is the cavity decay rate. It is assumed that $\omega_\mathrm{p} = \omega_{0,\mathrm{p}}$ and $\omega_{0,\mathrm{s}} = \omega_\mathrm{p} - \omega_{0,\mathrm{i}}$, i.e., the triple-resonance condition is fulfilled. The parametric gain bandwidth is typically much larger than the linewidth of the selected spectral mode. Therefore, the parametric gain envelope is a constant and does not enter in Eq. 1.4.13.

Monochromatic pumping. For a monochromatic continuous wave pump beam, the pump spectral amplitude can be approximated by a delta distribution:

$$\begin{aligned} s_\mathrm{cw}(\omega) &= \delta(\omega - \omega_\mathrm{p}) \\ \Rightarrow s_\mathrm{cw}(\omega_\mathrm{s} + \omega_\mathrm{i}) &= \delta(\omega_\mathrm{p} - \omega_\mathrm{s} - \omega_\mathrm{i}). \end{aligned} \tag{1.4.15}$$

Therefore, the joint spectral amplitude is highly anti-correlated and $\psi(\omega_s, \omega_i)$ is not factorable in the form of Eq. 1.4.6:

$$\begin{aligned}\psi(\omega_s, \omega_i) &= \psi(\omega_s, \omega_p - \omega_s) \\ &= L_p(\omega_p) L_s(\omega_s) L_i(\omega_p - \omega_s)\end{aligned} \tag{1.4.16}$$

Pulsed pumping. In the following, we assume that a pulsed pump[233] with bandwidth σ_p and a Gaussian spectral amplitude distribution

$$s_{\text{pulse}}(\omega) = \left(\frac{\log(16)}{\pi\sigma_p^2}\right)^{1/4} e^{-2\log(2)\frac{\omega^2}{\sigma_p^2}} \tag{1.4.17}$$

is used. In Figs. 1.19a and 1.19b, the joint spectral amplitude is plotted for various values of the ratios of $\Gamma_p/\Gamma_{s/i}$ and $\sigma_p/\Gamma_{s/i}$. If either σ_p or Γ_p are of the order of $\Gamma_{s/i}$ or smaller, strong spectral correlations between signal and idler photons indicated by an asymmetric joint spectral amplitude can be observed. By computing the singular values and using Eq. 1.4.12, the purity $\mathcal{P}_s$ as a function of the ratios $\Gamma_p/\Gamma_{s/i}$ and $\sigma_p/\Gamma_{s/i}$ were computed. The results are shown in Fig. 1.19c.

Discussion. Fig. 1.19 quantitatively confirms the findings of Jeronimo-Moreno and coworkers. The pulse spectral amplitude $s(\omega_s, \omega_i)$ and the pump resonance function $L_p(\omega_s, \omega_i)$ must be nearly constant over the scale of the signal/idler cavity decay rate $\Gamma_{s/i}$ to herald signal photons with purity $\mathcal{P} \approx 1$. These two functions can then be pulled out of the integral in Eq. 1.4.1 as a constant factor and the joint spectral density takes the factorable form:

$$\psi(\omega_s, \omega_i) \approx L_s(\omega_s) L_i(\omega_i). \tag{1.4.18}$$

While both $\sigma_p \gg \Gamma_{s/i}$ and $\Gamma_p \gg \Gamma_{s/i}$ are required for high purity, the pump decay rate should also be larger than the pulse bandwidth ($\Gamma_p \gtrsim \sigma_p$) to avoid that the pump pulse is partially reflected by the cavity.[129] Note, that the photon-pair generation rate decreases with increasing values of σ_p and Γ_p since the values of $s(\omega_{0,s}, \omega_{0,i})$ and $L_p(\omega_{0,s}, \omega_{0,i})$ decrease.[234] Therefore, a compromise between purity and the required pump power has to be found.

In principle, the purity of the signal photons can also be increased by temporal filtering.[132] But, temporal filtering always results in losses of photons and therefore a reduced heralding efficiency. Only if the detection of the heralding idler photon approximates a single-mode measurement, this degradation in heralding efficiency can be circumvented.[235]

So far, the higher-order multi-pair contributions of parametric down-conversion were not discussed in this section. These also limit the purity of the generated state.[236] This further emphasises that a compromise between generation rate and purity has to be found since large values of the generation rate correspond to higher multi-pair contributions due to the thermal photon statistics of spontaneous parametric down-conversion.

2 Experiments

In this chapter, we present the design and characterization of a cavity-enhanced photon-pair source based on SPDC. We present the experiments performed within the scope of this thesis.

The main goal of this thesis is to design a cavity-enhanced photon-pair source with degenerate signal and idler photons resonant to the cesium D_1. The experimental setup is based on the design of Scholz and coworkers.[128,237,238] While Scholz's work focusses on a narrow linewidth (3–4 MHz) cavity, here, the target signal-idler bandwidth is >100 MHz. As discussed below, the design of the new photon-pair source therefore differs from the design proposal by Scholz and coworkers in many aspects.

In this chapter, we show that for many experiments it is beneficial not to use a compensation crystal inside the cavity. Although tuning the cavity to perfect degeneracy is more involved without compensation crystal, to achieve the design goal (high-brightness source with large spectral bandwidth of signal and idler photons) a single-crystal configuration is advantageous.

Filter cavities. Both the two-crystal and the single-crystal cavity emit spectrally multi-mode signal and idler photons. Therefore, spectral filtering of the central, degenerate mode is required. Section 2.1 presents a novel implementation of temperature-tuned monolithic Fabry-Pérot filter cavities. We refine the experimental proposal of Palittapongarnpim and colleagues.[239] With an optimized mounting of the cavity, we eliminate birefringence. Thereby, we achieve polarization-independent operation which is crucial in many applications and for several experiments presented in this thesis. By cascading two filter cavities with differing free spectral ranges, we build a high-resolution spectrometer.

Photon-pair source and digital locking electronics. Section 2.2 presents the experimental details of the newly developed photon-pair source including the mechanical design and a characterization of the fluorescence background generated inside the nonlinear crystal. We conclude the description and characterization of the experimental tools and the down-conversion setup by presenting the various feedback control systems required to operate the cavity-enhanced source. To stabilize the distance of the two cavity mirrors, we use a specialized digital

locking scheme. This micro-controller based feedback loop enables automatic re-locking and, thus, nearly unlimited measurement duration without manual intervention.

Signal/Idler spectrum. The theory developed in chapter 1 predicts the spectral structure of signal and idler photons. In section 2.3 we measure the signal/idler spectral density both with a conventional grating spectrometer as well as with the high-resolution cascaded filter-cavity scheme. We confirm the theory not only for the static case, but also for temperature tuning of the nonlinear crystal. We further analyze the impact of the mirror-spacing on the spectral properties for a cavity without compensation.

Signal/Idler correlation. The joint spectral amplitude determines not only the spectral properties and correlations between signal and idler photons. As we will show in section 2.4, the joint spectral amplitude is also directly connected to the temporal correlation of the two photons of one pair. We measure this correlation via the second-order signal-idler correlation function. The main contribution of this section is the focus on the impact of both pump resonance and spectral filtering on the correlation function.

Hong-Ou-Mandel effect. The photon-pair source is designed to generate signal and idler photons which are indistinguishable in all degrees of freedom (except for their polarization). In section 2.5, we verify that both the (spectrally filtered) two-crystal configuration and the single-crystal configuration produce indistinguishable photons by measuring the Hong-Ou-Mandel effect. Additionally, we theoretically analyze two-photon interference of photons generated by cavity-enhanced SPDC. Again, the joint spectral amplitude leads us to the conclusion that the Hong-Ou-Mandel signal also sensitively depends on the relative phase of pump, signal and idler fields inside the triply-resonant cavity. We verify this theory by measuring the Hong-Ou-Mandel dip with the (unfiltered) two-crystal cavity where we can tune this phase by changing the compensation-crystal temperature. We conclude chapter 2 by providing evidence that we can use the cavity-enhanced photon pair source to generate polarization-entangle photons.

2.1 | Filter cavity

Current experiments in quantum optics employ a variety of photon sources, such as single atoms and ions,[240–242] defect centers in diamond,[243] quantum

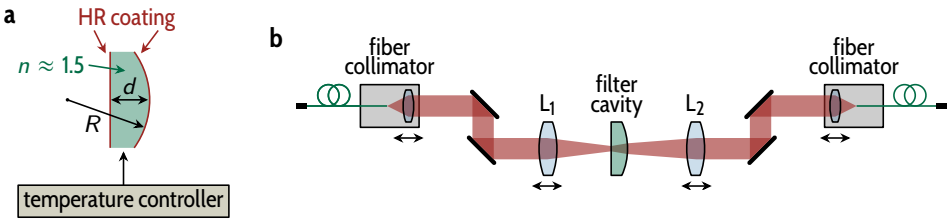

Figure 2.1 | Monolithic Fabry-Pérot cavity with single-mode fiber coupling. **a**, As in the proposal of Palittapongarnpim and colleagues,[239] the cavity is built of an of-the-shelf plano-convex lens with center thickness d and radius of curvature R. Onto both sides, a highly reflective coating is applied. The resonance frequencies of the resonator can be tuned by changing the substrate temperature. Any high-transmission substrate can be used. But, substrates with larger values of the thermal expansion and thermo-optic coefficients (e.g. BK7) are favored due to their higher tuning rate upon temperature changes. **b**, Mode matching: The filter cavity is mode-matched to signle-mode fibers with two telescopes. These consist of fiber collimators with movable lenses (Schäfer+Kirchhoff 60FC) and additional mode-matching lenses L_1 and L_2. By translating $L_{1/2}$, the focus can be positioned at the flat mirror of the filter cavity. The beam waist can be matched to the fundamental mode of the cavity by adjusting the position of the lenses inside the fiber collimators.

dots,[244,245] or spontaneous parametric down-conversion.[246] These sources typically have limited count rates, and can be spectrally multimode or have relatively large linewidths. For certain experiments, only a single spectral mode might be necessary, and the linewidth of the emission needs to be tailored to a specific value. In more complex architectures, including multiple sources, photons might need to be filtered to have identical spectral properties.[168] Traditional two-mirror configurations of Fabry-Pérot etalons can be difficult to stabilize or set up. They are often operated with additional stabilization laser beams which can introduce noise photons into the experimental setup or require a mechanical chopper which reduces the duty cycle of the experiment.[127,247–249]

Cascaded monolithic filter cavities. We present a filtering setup that relies on cascading of two monolithic Fabry-Pérot cavities to achieve fully customizable narrow linewidth transmission. In 2012, Palittapongarnpim, MacRae, and Lvovsky,[239] proposed to use monolithic Fabry-Pérot cavities based on of-the-shelf lens substrates. Based on their proposal, here, we present a modification of both cavity design and mounting. In contrast to the original manuscript, this modification permits simultaneous filtering of photons with orthogonal polarizations at the same frequency. By cascading two filter cavities with different free spectral ranges, we extend the (effective) free spectral range (FSR) of the filtering system to hundreds of GHz. Parts of this section have been published in Ref. [205] and have been discussed in Ref. [250].

For all experiments discussed in this chapter, we use two different filter cavities. Filter cavity FC_1 has high-reflectivity coatings with a finesse of $\mathcal{F}_1 = 175$. The substrate has a center thickness of $d = 2.6\,\mathrm{mm}$ and free spectral range

of 37.8 GHz. This corresponds to a linewidth of $\Gamma_1 = 2\pi \cdot 192\,\mathrm{MHz}$. Filter cavity FC_2 has a low finesse of $\mathcal{F}_2 = 32$, a center thickness of 3.6 mm, a FSR of 28.8 GHz, and a linewidth of $\Gamma_2 = 2\pi \cdot 885\,\mathrm{MHz}$. For both cavities, high quality, of-the-shelf lenses with a surface figure of $\lambda/10$ (Laser Components PLCX-25.4/64.4C and PLCX-25.4/38.6C) were used as substrates.

2.1.1 | Cavity mounting and characterization

Monolithic Design. The use of monolithic Fabry-Pérot interferometers as frequency filters has several distinct advantages: They offer high transmission at the resonance frequency while maintaining high suppression of unwanted frequencies. They preserve the Gaussian mode profile of the incoming beam. Finally, they do not need sophisticated locking schemes,[127,128] since the resonance frequency can be adjusted by temperature tuning of the cavity material. Nevertheless, the accessible free spectral range is limited. For a large FSR, a very small cavity thickness is required, which results either in a large beam waist or a very small radius of curvature of the cavity. For a narrow linewidth, a cavity with a large FSR requires a high finesse, which often results in poor transmission since high-finesse cavities are more susceptible to losses caused by small imperfections on the surfaces or by absorption inside the resonator (see section 1.3.3).

Stress-free mounting and birefringence. Fig. 2.2 shows the prototype and improved design of the cavity mount. The cavity described by Palittapongarnpim and colleagues[239] suffers from birefringence in the cavity substrate resulting in a splitting of the cavity resonances. Therefore, special care has been taken to eliminate mechanical stress acting on the cavity substrate. The cavity substrate is inserted into a commercial 1 inch lens holder with an internal thread and is held in place by a retaining ring. The pressure exerted by the retaining ring onto the substrate is finely tuned by monitoring the stress-induced birefringence (see Fig. 2.3).

If a large torque is applied to the retaining ring, birefringence is introduce into the lens material and the cavity resonance splits up. The torque is reduced until this splitting can no longer be observed. But, the torque is still strong enough such that the cavity is held in place and the position relative to the laser beam does not change over time. To be able to eliminate birefringence is an important improvement over the setup of Palittapongarnpim and coworkers. This improvement allows for simultaneous filtering of two perpendicularly polarized signals at the same frequency (see section 2.5).

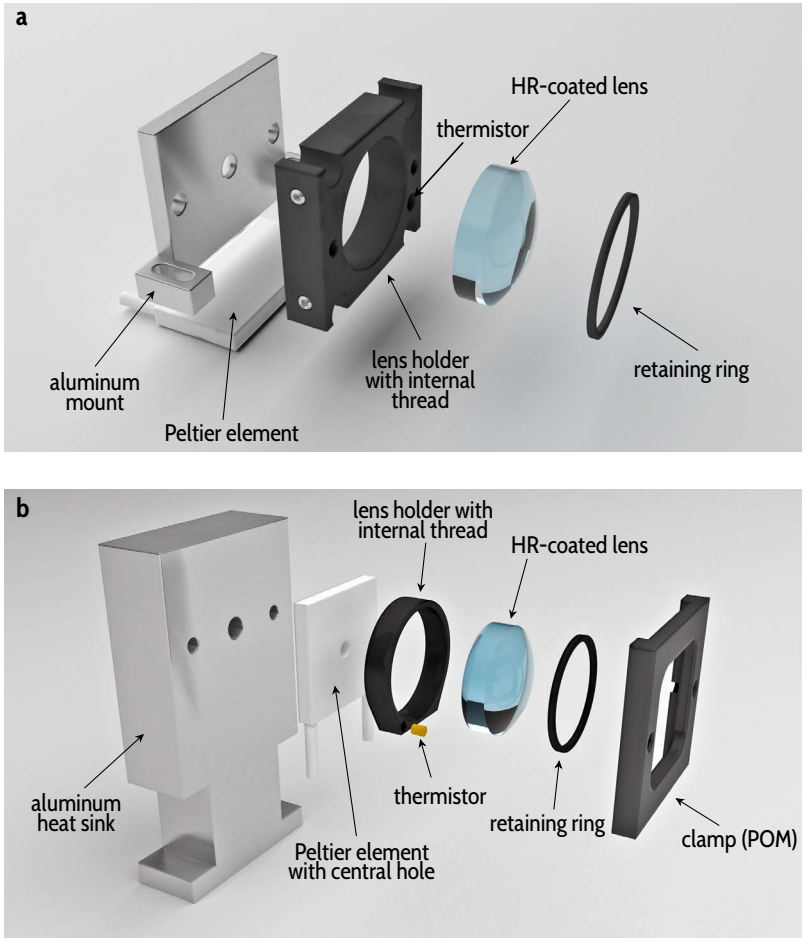

Figure 2.2 | Stress-free mounting of the monolithic filter cavity. **a**, Prototype of the cavity mount: The lens with high-reflection (HR) coatings is placed into a commercial lens holder with internal thread. The lens holder is screwed onto an aluminum mount which in turn is pressed onto a Peltier element under an angle of 90° with respect to the optical axis. Due to the large thermal mass of the assembly, the temperature of the cavity can only be tuned slowly. For temperature stabilization, a 10 kΩ thermistor is glued into the lens holder. By untightening the retaining ring, mechanical stress-induced birefringence of the cavity material can be reduced (see Fig. 2.3). **b**, Improved design of the cavity mount: The flat side of the high-reflection coated plano-convex lens is directly attached to a Peltier element with a central hole for optical access. In contrast to the prototype, the thermal mass of the lens holder is reduced, resulting in a much faster thermal relaxation time (see Fig. 2.5). The lens holder and the Peltier element are clamped to an aluminum heat sink. The clamp is made of Polyoxymethylene (POM).

Temperature-dependence of the transmission. Since the lens mount is also attached to the Peltier element, it is affected by deformation due to temperature changes as well. We suspect that our mounting concept also reduces transmission losses due to misalignment and mode mismatch caused by these deformations. We measured a loss of the transmission at the resonance frequency of less than 10 % for a temperature change of 15 K. This temperature change corresponds to a detuning of more than a free spectral range. In contrast, Palittapongarnpim and colleagues observed a reduction of transmission by more than 30 % for a 15 K temperature change.

Absolute calibration of the resonance frequency. To evaluate the response of the filter cavities to temperature changes, we have to measure the resonance frequency relative to an absolute frequency reference. We use the four well-known hyperfine transitions of the cesium D_1-line at 894 nm for this purpose. In the following, the frequency ω_0 corresponds to the $F = 4$ to $F' = 3$ transition.[251] The measurement setup is depicted in Fig. 2.4. The laser frequency is scanned repeatedly over the absorption lines. Simultaneously, we record the filter cavity transmission spectrum with a photodiode. With this method, we can calibrate the absolute values of the resonance frequencies depending on the substrate temperature of the filter cavity. We measure a tuning rate of $\mathrm{d}\omega/\mathrm{d}T = 2\pi \cdot 2.7\,\mathrm{GHz/K}$. A similar value has been found by Palittapongarnpim and coworkers for the same cavity substrate.[239] Additionally, we can measure the impact of the design of the cavity mounting on the tuning speed and thermal relaxation times with this measurement scheme.

Tuning speed. Fig. 2.5 compares the tuning speed and the thermal relaxation time of the prototype and the improved cavity design. The improved cavity mounting utilizes a Peltier element with a central hole to reduce the thermal mass of the mounting assembly. The direct contact between Peltier element and cavity substrate allows for a much faster tuning speed of the cavity resonance frequency. While, for the prototype, we measure a tuning rate of 50 MHz/s, for the improved design a tuning rate of $> 300\,\mathrm{MHz/s}$ can be achieved. These tuning rates are obtained for temperature-controller settings which are optimized for minimum settling time and minimum overshoot. If we apply the maximum Peltier current of 1.5 A, we measure a tuning rate of 2 GHz/s for the improved design.

Thermal relaxation and resonance frequency estimation. Besides the increase in tuning speed, with the improved mounting design we reduce the thermal relaxation time from over 100 s for the prototype to below 30 s for the improved design. Additionally, we also reduce the delay between a measured change in temperature and a measured drift of the resonance frequency for the improved design.

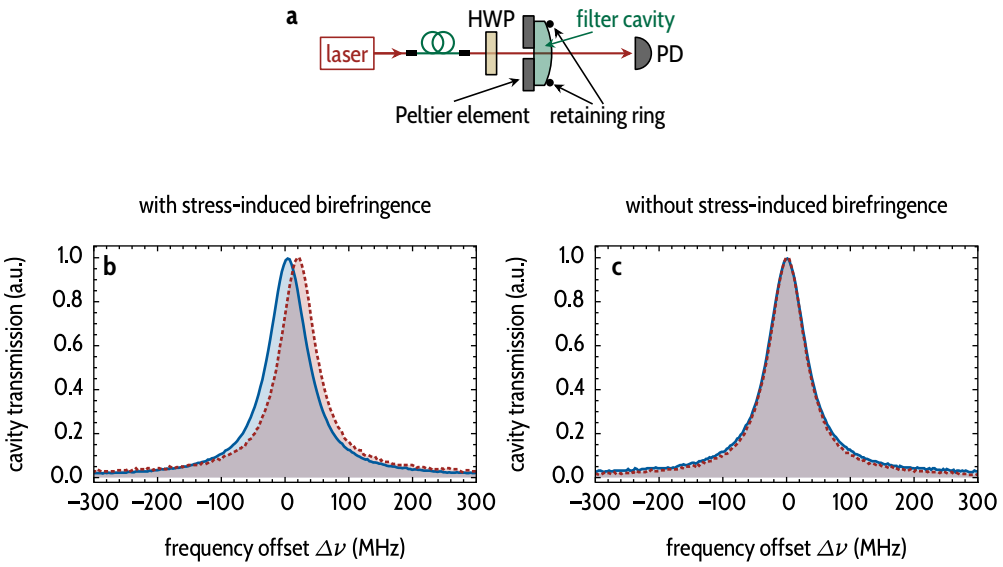

Figure 2.3 | Measurement of the stress-induced birefringence inside a filter cavity. **a**, The frequency of the laser is swept over a resonance of the cavity. The polarization of the laser is aligned with a half-wave plate (HWP) either along the ordinary axis or the extraordinary axis of the cavity substrate. The transmitted power is recorded with a photodiode (PD). **b**, If a large torque is applied to the retaining ring, we observe stress-induced birefringence. The resonance frequency of the ordinary polarization (——) is shifted with respect to the extraordinary polarization (----) by up to 20 % of the cavity linewidth. Similar results have been found by Palittapongarnpim and coworkers.[239] **c**, By choosing a lower torque for the retaining ring, the stress-induced birefringence can be eliminated. Therefore, the resonance frequency for the two perpendicular polarization directions is identical within the measurement uncertainty.

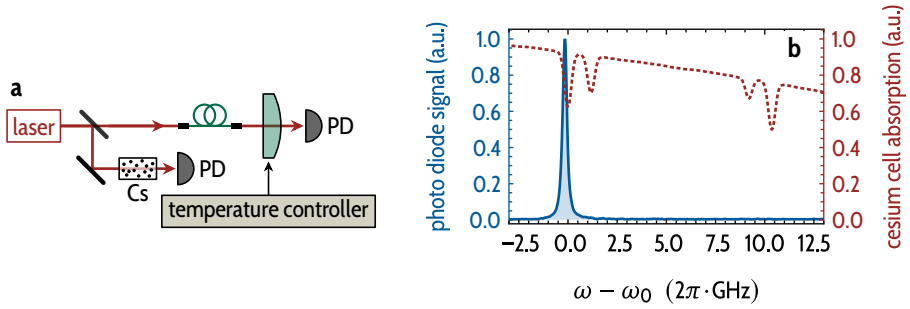

Figure 2.4 | Filter cavity calibration. **a**, Setup for the characterisation and calibration of the filter cavities: The frequency of an external cavity diode laser (Toptica TA pro with a mode-hop free tuning range of ∼30 GHz) is repeatedly scanned over a resonance of the filter cavity. The power transmitted through the cavity is monitored with a photodiode (PD). Simultaneously, we record the transmission of the laser through a cesium vapor cell. Subsequently, we utilize the well-known positions of the cesium D_1-line hyperfine transitions to calibrate the absolute frequencies of the transmission spectra. **b**, Filter cavity transmission (——) and Doppler-broadened hyperfine absorption lines of the cesium D_1 line (----). Here, we scan the frequency of the laser ω relative to the $F = 4$ to $F' = 3$ hyperfine transition of the cesium D_1-line at frequency ω_0. The accuracy of the calibration method is limited by nonlinearities between the applied voltage to the piezo-electric tranducer attached to the grating of the laser and the frequency variations of the laser. These nonlinearities are especially hard to detect for frequencies not in the vicinity of an absorption line. A Doppler-free measurement setup therefore did not improve the accuracy of the calibration.

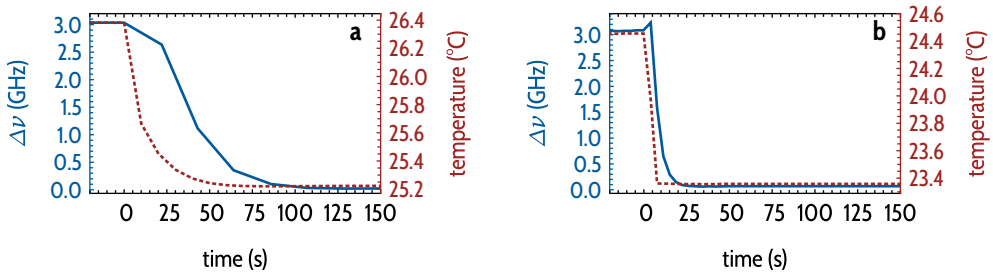

Figure 2.5 | Filter cavity tuning speed and relaxation time. At time $t = 0$ the set point of the temperature controller is reduced by ≈1 K, resulting in a drift of the resonance frequency of about $\Delta\nu = 3$ GHz. The measurement setup is depicted in Fig. 2.4. **a**, For the prototype (Fig. 2.2a), a tuning rate of about 50 MHz/s was measured. Due to the large thermal mass of the cavity mount, the thermal relaxation time is well above 120 s. **b**, With the improved cavity mount (Fig. 2.2b), the tuning rate is increased to more than 300 MHz/s and the relaxation time is reduced to less than 30 s. The temporal lag between the measured values of the temperature and the resonance frequency is also reduced. With a reduced lag, the resonance frequency can be inferred from a temperature measurement with increased accuracy.

This lag plays an important role if the filter is used as a scanning Fabry-Pérot filter where we measure the transmission of a signal while we slowly scan the temperature of the cavity: Note, that we cannot monitor the actual resonance frequency at any point in time without side effects if we use the cavity to filter weak signals at the single-photon level. In principle, we could introduce an additional read-out laser to measure the actual resonance frequency. But, any additional light will either degrade the transmission of the filtering system, as additional spectral filters to block the read-out laser are required, or the additional read-out laser will reduce the signal-to-noise ratio of the measured signal.

Therefore, a small delay between changes in temperature and resonance frequency is important. For the improved mounting design, we obtain a more precise estimate of the actual resonance frequency at every point in time during the scan from the measured temperature. Thus, we do not require an additional read-out laser to monitor the cavity resonance frequency even if we scan the temperature.

Transmission and impedance matching. For cavities with a low finesse of $\mathcal{F}_1 = 32$, we measure a maximum transmission at the resonance frequency of 85–90 %. For the high-finesse cavities ($\mathcal{F}_2 = 175$), we obtain a filter transmission of 50(4) %. This value is significantly lower than the maximum transmission of 60 % measured by Palittapongarnpim and coworkers for a cavity with an even higher finesse of $\mathcal{F} = 275$.

On resonance, the high-finesse cavity FC_2 reflects up to 35 % of the incident light. The surface quality of the substrates of cavities FC_1 and FC_2 is comparable to the cavity of Palittapongarnpim and coworkers. In combination with the low transmission, we therefore attribute the poor transmission performance to an imperfect impedance matching of the two high-reflectivity coatings. With commercial-grade coatings, we would expect a significant improvement of the maximum transmission.

Stability. As shown in Fig. 2.6, the filter cavities feature an excellent stability of the resonance frequency. If enclosed in a plastic box to shield the setup from turbulences and temperature fluctuations in the surrounding air, the root-mean-square (RMS) resonance-frequency drift over a measurement duration of 15 h is less than 2 % of the cavity linewidth. With the tuning rate of 2.7 GHz/K, this corresponds to a RMS temperature stability of better than 1.5 mK.

On a time scale of several days, we observe a fluctuation of the resonance frequency of about 50 MHz. On a time scale of months, the resonance frequency

is stable within 75 MHz. The cause of these long-term drifts cannot be identified, but they might be attributed to strong variations of the air humidity in the laboratory, for example. Measurements with an additional high-precision temperature sensor mounted into the lens mount did not find a correlated drift of the cavity temperature which could have attributed the long-term drifts to imperfections of the temperature controller.

Hysteresis. Besides stability, repeatability is of great importance for experiments which rely on an *absolute* calibration of the resonance frequency of a filter cavity. To analyze the repeatability, we periodically vary the set point of the temperature controller, alternating between three different temperatures (see Fig. 2.7). While the two outermost points show excellent repeatability, for the inner point we observe a significant hysteresis. Depending on the direction of the temperature change, the system settles on two different resonance frequencies. The deviation between these two points stretches up to 40 MHz, depending on the temperature difference of the end points of each step.

We cannot identify the cause of the hysteresis. We attach an additional temperature to the lens mount. But, we do not observe a significant hysteresis of the temperature of the lens. Therefore, the temperature controller can be excluded as the source of the observed hysteresis of the resonance frequency. The hysteresis might be caused by thermal deformations due to the differing thermal expansion coefficients of the cavity substrate and the aluminum lens mount.

For most applications of the filter cavity, the hysteresis is not a limiting factor. For the low-finesse cavity FC_2, the offset caused by the hysteresis is much smaller than the cavity linewidth. For the high-finesse cavity, we take the hysteresis into account in the calibration procedure. The resonance frequency of the cavity can be reliably brought to any desired value by always approaching the target temperature from the same direction.

2.1.2 | Application: Spectral analysis of quantum dot resonance fluorescence

The monolithic Fabry-Pérot cavities can be used as high-resolution spectrum analyzers. Fig. 2.8 shows an experiment where we use the high-finesse filter cavity (FC_1) to analyze the spectral properties of single photons generated by resonantly excited quantum dots.[252]

As shown in Fig. 2.8, a sample of self-assembled InGaAs/GaAs quantum dots[258] is placed into a helium flow cryostat. A continuous wave pump laser with a power of about 700 nW is used to resonantly drive the two-level system of the

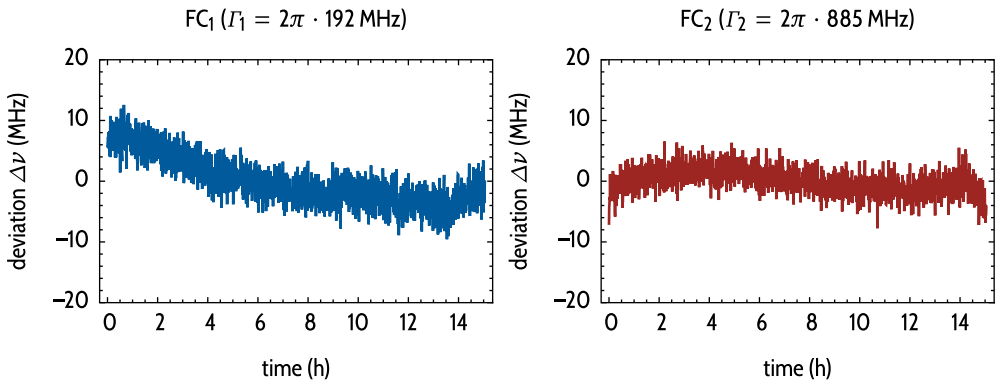

Figure 2.6 | Filter cavity stability. Stability of the resonance frequency of filter cavities FC_1 (—) and FC_2 (—) over a measurement duration of 15 h. For FC_1 (FC_2) a root mean square (RMS) deviation of 4.0 MHz (2.1 MHz) was measured. This corresponds to a fraction of 2 % (0.2 %) of the cavity linewidth. With a tuning rate of 2.7 GHz/K, a long-term RMS temperature stability of better than 1.5 mK can be inferred. This level of stability can only be attained by enclosing the whole cavity mount assembly in a plastic box to shield it from turbulences in the surrounding air.

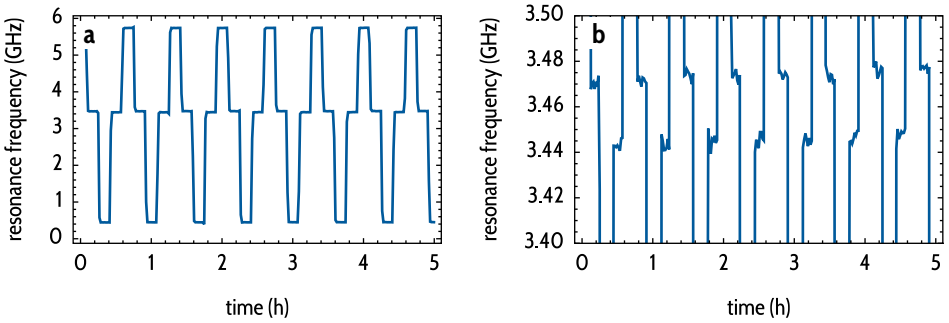

Figure 2.7 | Filter cavity hysteresis. Measurement of the hysteresis of the filter resonance frequency upon repeated changes of the substrate temperature. The measurement setup shown in Fig. 2.4 is used. **a**, The set point of the temperature controller is repeatedly set to three different values shifting the resonance frequency of the filter cavity by about 2.5 GHz in each step. The outermost points show an excellent repeatability over time with a stability similar to the measurement shown in Fig. 2.6. **b**, Detail of the data shown in **a**: A significant hysteresis is observed. Depending on the direction of the temperature change, the resonance frequency stabilizes on two different values. A deviation of up to 40 MHz was observed depending on the difference between initial and final temperature.

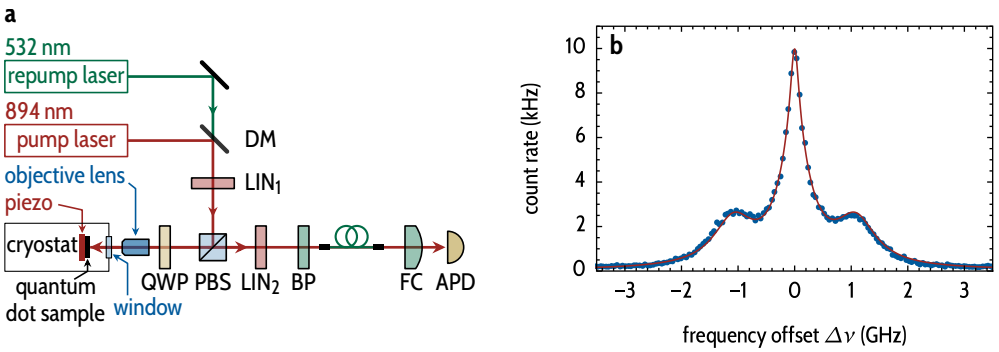

Figure 2.8 | Quantum dot resonance fluorescence. **a**, The quantum dot sample is placed into a helium flow cryostat at a temperature of about 4 K. A continuous wave 894 nm pump laser (Toptica TA pro) is tuned in resonance with the exciton transition of the quantum dot. The polarization of the pump laser is purified by a high-quality linear polarizer (LIN_1). The resonance fluorescence is collected with a high-numerical-aperture objective lens and coupled into a single-mode fiber. The quarter-wave plate (QWP) in front of the objective compensates for slight polarization rotations caused by the window of the cryostat. The polarizing beam splitter (PBS) and an additional linear polarizer (LIN_2) block the reflected pump light with a suppression by a factor larger than 10^8.[253] To record the spectrum, the resonance frequency of the filter cavity is scanned over the laser wavelength and the transmission of the photons is monitored with an avalanche photodiode (APD). A non-resonant repump laser with a power of ∼2 nW at 532 nm is used to stabilize the charge carriers inside the quantum dot and, thus, enhance the emission at resonant wavelength.[254,255] The reflected repump light is blocked with a band-pass filter (BP). **b**, Mollow-triplet[256] of the quantum dot resonance fluorescence with a Rabi frequency of ∼1.2 GHz. The measured APD count rate (●) as a function of the filter cavity detuning $\Delta\nu$ from the pump laser frequency is in good agreement with the theory given by Astafiev and colleagues.[257] For the fit (—), we have to take into account residual photons from the pump laser transmitted though the crossed polarizers. The measurement was performed and the data shown here was kindly provided by Tim Kroh and Christian Pugatschow.[252]

quantum dot exciton transition. The resonance fluorescence is collected into a signle-mode fiber. The transmission through the filter cavity is monitored with an avalanche photodiode. To block the reflected pump light, a crossed-polarizer scheme[253] was utilized.

The measured spectrum (Fig. 2.8b) shows the familiar features of a *Mollow triplet*.[256,257] Due to the calibration (see Fig. 2.4) of the filter cavity, with the monolithic design, the *absolute* emission wavelength of the quantum dot can be measured. Another advantage over Fabry-Pérot cavities tuned with a piezo-electric transducer is that the monolithic cavity can be used as a long-term stable monochromator for the generated photons. Cavities tuned with a piezo-electric transducer are often more susceptible to acoustic noise. Therefore, there is a lower bound for their tuning rate since the resonance frequency is stable only over short periods of time. The inherent stability of the monolithic filter cavity allows for very low tuning rates (<1 MHz/s). For the measurement shown here, this allows for a longer integration period for each data point and an increased signal-to-noise ratio compared to a scan with a piezo-tuned cavity.

2.1.3 | Cascaded filtering system

As discussed in Fig. 2.8, the filter cavities are ideally suited for spectral analysis. But, in case of a single filter cavity, only signals can be analyzed for which the spectral width is not larger than the free spectral range of the cavity. To increase the (effective) free spectral range, two filter cavities with differing central thickness can be combined.

Fig. 2.9a shows such a cascaded filter system. Here, filters FC_1 with a FSR of 39 GHz and FC_2 with a FSR of 29 GHz are connected with a polarization-maintaining fiber. The resulting filter system has a linewidth comparable to the high-finesse cavity FC_1. Since the adjacent resonances of the two filter cavities do not overlap (Fig. 2.9b), we extend the effective free spectral range to nearly 500 GHz (Fig. 2.9c).

Synchronous tuning. The transmission wavelength of the combined system can be tuned over a wide range of frequencies (much larger than the free spectral range of each filter). While tuning the combined system, we can restrict the tuning range of each filter to one FSR (see Fig. 2.9d). A prerequisite for this long-range tuning scheme is that the free spectral ranges of the filter cavities must be known with high accuracy to precisely reset the temperature of the filter by one FSR after each step.

High-precision measurement of the free spectral range. To measure the FSR, we create sidebands in the spectrum of a continuous wave laser with a variable-frequency phase modulator (EOSPACE). We monitor the transmission of the laser through the cavity with a photodiode, while we scan the laser frequency. For a modulation frequency of FSR/2, the sidebands transmitted by adjacent cavity resonances overlap. Since we know the modulation frequency with a low uncertainty, the precision (relative to the full FSR) of this measurement method is better than 10^{-4}. We measure the filters' FSR with a precision below 2 MHz, which is much smaller than the linewidth. In 1999, Araya and colleagues[259] independently proposed a similar measurement scheme.

Cascaded filter transmission. If we tune both filter cavities into resonance with a continuous-wave laser, we measure a fiber-to-fiber transmission of about 15 %. In a comparable setup with *two* low-finesse cavities ($\mathcal{F} = 32$), we obtain a transmission of about 50 %. We can reduce the transmission losses further by using anti-reflection coated fibers (~4 % loss per surface in our setup) and by optimizing the fiber incoupling efficiency (~70 % in our setup). In principle, a free-space connection between the filter cavities could be set up. But, the advantage of a fiber coupling between the cavities is that we can align and use the filters independently.

The transmission of each filter is given by the Airy function (see Eq. 1.1.85):

$$\mathcal{A}_{\text{filter}}(\omega) = \left|t_1 t_2 t_{\text{sp}} \mathcal{T}(\omega)\right|^2 \tag{2.1.1}$$

$$= \frac{T_1 T_2 T_{\text{sp}}^2}{\left[1 - \sqrt{R_1 R_2 T_{\text{sp}}^2}\right]^2} \text{Airy}(\mathcal{F}, \omega), \tag{2.1.2}$$

where $T_{1/2}$ ($R_{1/2}$) is the transmission (reflectivity) of the two mirrors and T_{sp} is the single-pass transmission of the cavity substrate. The normalized Airy function $\text{Airy}(\mathcal{F}, \omega)$ is given by Eq. 1.3.11. For a signal with a bandwidth much smaller than the filter linewidths, the transmission through the filter system $\mathcal{A}_{\text{system}}(\omega)$ is the product of the individual transmission functions:

$$\mathcal{A}_{\text{system}}(\omega) = \mathcal{A}_{\text{filter},1}(\omega)\mathcal{A}_{\text{filter},2}(\omega). \tag{2.1.3}$$

Cascaded filter suppression. To evaluate the tuning behaviour of the combined system and to verify Eq. 2.1.3, we measure the transmission of a continuous-wave laser through the cascaded filter (see Fig. 2.10). Since we can attain a maximum suppression of more than 10^6, we use a mechanical chopper and a lock-in amplifier to increase the signal-to-noise ratio of the measurement. We lock the laser frequency to a cesium hyperfine transition and tune the frequency

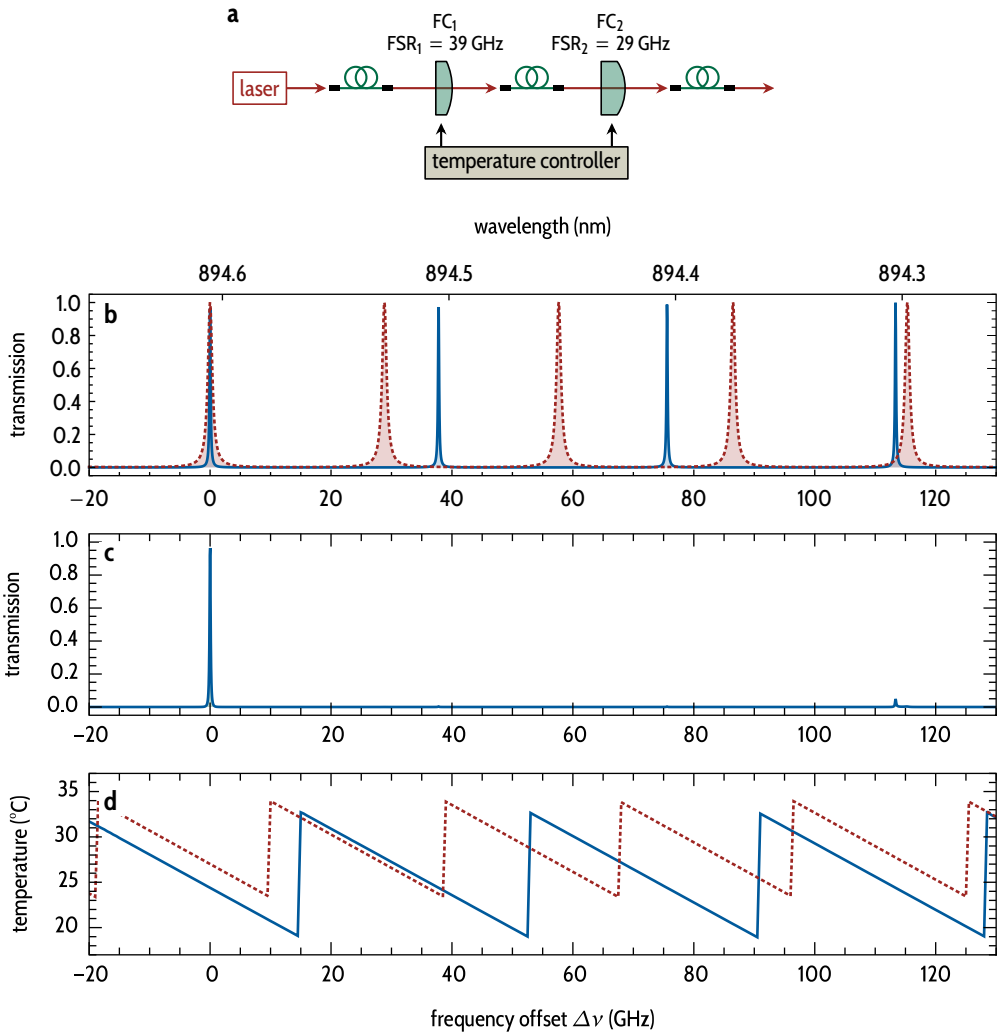

Figure 2.9 | Cascaded filter cavities and long-range tuning. **a**, We connect two filter cavities with differing free spectral ranges with a single-mode fiber. The combined filter system has an effective FSR of more than 1 nm (500 GHz) and a transmission on resonance exceeding 15 %, including all fiber coupling losses. **b**, The resonance frequencies of the two filter cavities can be brought in coincidence only for a specific wavelength. Due to the differing FSR, adjacent resonances do not overlap over a large range of frequencies. **c**, The transmission of the combined filter system is the product of the two transmission profiles. Therefore, the cascaded filter system has a similar linewidth as the high-finesse cavity. The spurious transmission at the detuning $\Delta\nu \approx 110$ GHz could be avoided by combining two high-finesse cavities, albeit thereby reducing the transmission. **d**, To use the cascaded filter system as high-resolution spectrum analyzer, we need to tune the two cavities in parallel such that the same pair of resonances always coincides. The maximum temperature difference attainable with the Peltier element limits the tuning range of each filter. However, we still can tune the combined system over a wide range of frequencies. For this, we scan each filter over one free spectral range and then set back the temperature to its initial value. Here, we plot the temperature profiles for a long-range scan for filter cavities FC_1 (——) and FC_2 (----). Figure replicated from Ref. [205].

offset $\Delta\nu$ between laser frequency and transmission frequency of the filter system over 500 GHz by temperature tuning of the cavities.

Fig. 2.10b shows a good agreement between the measured transmission and the theory. At a suppression of 60 dB, we reach the noise floor of the measurement system. Additional measurements with a higher incident power reveal a good agreement with the theory even for detuning with a suppression larger than 60 dB. But, for those measurements, the transmission at $\Delta\nu = 0$ saturates the photodiode. The small peaks around $\Delta\nu = 0$, which are not covered by the theory (Eq. 2.1.3), can be attributed to non-Gaussian higher-order modes caused by imperfect alignment or mode matching of the input beam with respect to the cavities.

In the range of $\Delta\nu = -20$ GHz to $\Delta\nu = 500$ GHz as plotted in Fig. 2.10b, 73 % of the transmitted power lies between a frequency offset $\Delta\nu$ of -10 GHz and 10 GHz. At the first major peak between 480 GHz and 500 GHz, 13 % of the transmitted power is located. The minor peak between 100 GHz and 120 GHz contributes only 5 % of the transmitted signal.

Discussion and Conclusion. In conclusion, we have shown that the excellent long-term stability of monolithic Fabry-Pérot cavities can be used to build polarization-independent fiber-coupled frequency filters which also can be used as high-resolution monochromators. Polarization-independent filters are of great interest in many applications, in particular in quantum optics, whenever filtering of high-quality photon pairs[260] of polarization-entangled photons[261] is crucial.

To further optimize the monolithic filter cavities, we can explore several routes in the future. On the one hand, it might be beneficial to select smaller cavity substrates. Instead of standard 1-inch lenses, we can evaluate the performance of 1/2-inch or even smaller substrates. A much larger tuning speed and shorter thermal settling times are the main advantages of smaller cavity substrates. Larger tuning speed and shorter settling times will largely decrease the time needed for calibration of the filter cavities. But, a smaller thermal mass might also require a more elaborate thermal shielding against environmental influences of the setup.

We use the (cascaded) filter cavities in multiple experiments with cavity-enhanced photon-pair sources, as will be discussed in the subsequent sections. Here, the long-term stability and polarization-independent operation of the filter cavities are the key performance parameters.

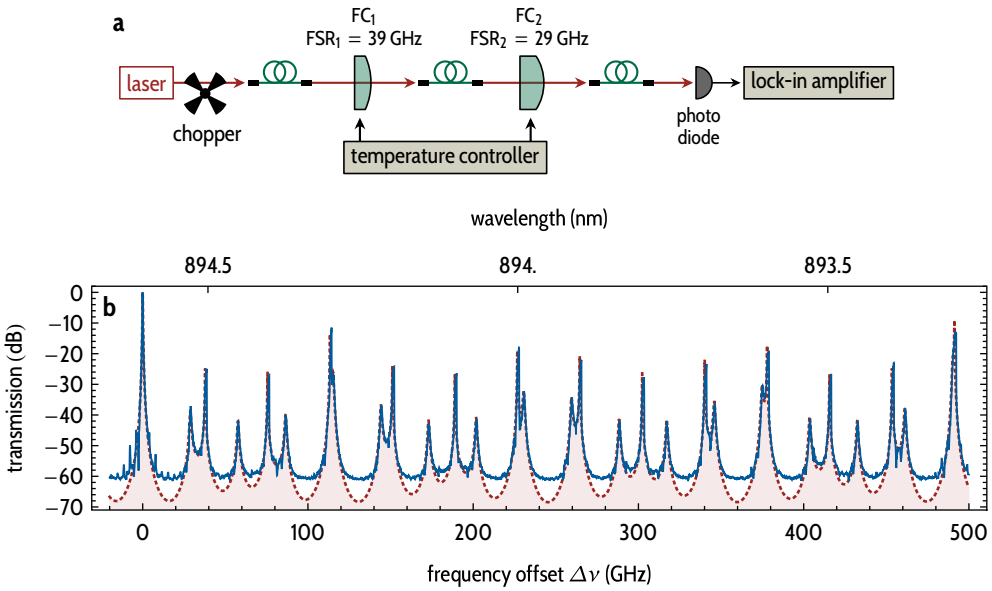

Figure 2.10 | Filter cavity suppression. **a**,A diode laser is stabilized to a D_1-line hyperfine transition of atomic cesium at 894.3 nm and periodically blocked by a mechanical chopper. The transmission wavelength of the combined system is tuned (see Fig. 2.9d) over 500 GHz (1.3 nm). The transmission trough the combined filter system is measured with a photodiode and a lock-in amplifier. **b**,The measurement results (——) are in good agreement with theory (----) as given by Eq. 2.1.3. At a suppression of 60 dB, the noise floor of the measurement setup is reached. Figure replicated from Ref. [205].

2.2 | Cavity-enhanced photon-pair source

This section presents the experimental realization of the triply-resonant cavity-enhance photon-pair source. The source fulfills all requirements outlined in the introduction to chapter 1: We designed a low-finesse OPO cavity to obtain a bandwidth of about 100 MHz, which is compatible to the linewidth of quantum dots[169,262] or quantum memories based on atomic vapors.[163]

In the design phase of the photon-pair source, the theory in section 1.3.4, (especially Eq. 1.3.30), had not been derived yet. Therefore, two design principles introduced by Scholz and colleagues[237] where not changed for the new cavity design: On the one hand, we adopted the design decision to use a comparatively long crystal ($l = 20\,\mathrm{mm}$). On the other hand, we did not optimize the focussing parameter ξ of the cavity.

Long-crystal cavity. Since the direct dependence of the generation rate $\mathcal{R}$ on the crystal length was not easily accessible, the design goal was to optimize the single-pass generation rate. For small values of the focussing parameter ξ, the single-pass photon-pair generation rate increases with the length of the crystal (see Eq. 1.2.15). Therefore, the crystal length was thought to be required to be be as long a possible (see Ref. [237]). Since there is significant pump absorption at 477 nm, $l = 20\,\mathrm{mm}$ is a compromise between pump enhancement (see Fig. 1.15) and single-pass gain.

Weakly focussed pump beam. There are several reasons not to optimize the focussing parameter ξ: To achieve the maximum conversion efficiency, for a 20 mm PPKTP crystal, the optimum pump beam waist is $\bar{w}_{\mathrm{opt}} = 24\,\mu\mathrm{m}$ (see Fig. 1.9). The optimum pump beam waist requires to specify the mirror radius of curvature with an accuracy of less than 1 mm. Additionally, one needs to match the spacing of the mirrors precisely to the mirror radius of curvature.

A very tight focus also results in a more laborious alignment procedure of the cavity. The large beam width of the signal and idler fields at the second surface of the compensation crystal (see Fig. 1.10a) requires a thick compensation crystal to avoid vignetting and photon-pair loss. The larger cross section of the fields at the crystals' facets results in higher losses due to scattering at surface imperfections.

In contrast to this, a focussing parameter in the range of $\xi = 0.2$, which corresponds to a pump beam waist of 50 µm, is easily accessible. For a spherical cavity, this value results in a reduction of the pair-generation rate by a factor of 3 compared to an optimized pump beam profile. Fig. 2.11 compares the spherical cavity configuration with a hemispherical configuration. Fig. 2.11c

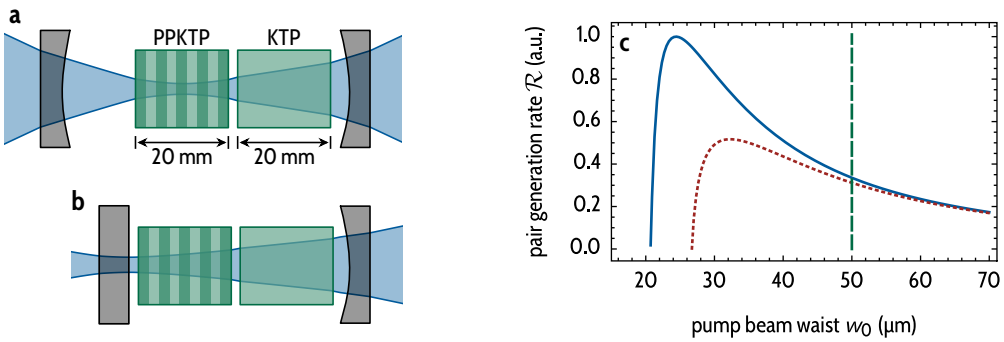

Figure 2.11 | Comparison between a spherical and a hemispherical cavity. **a**, Spherical cavity with two convex mirrors. The focus of the pump beam profile (—) is placed at the center of the nonlinear crystal. **b**, Pump beam profile (—) for a hemispherical cavity where the nonlinear crystal is placed close to the focus of the pump beam at the flat mirror. **c**, Comparison of the photon-pair generation rate $\mathcal{R}$ of a spherical cavity (—) and a hemispherical cavity (----) as a function of the pump beam waist w_0. At the optimum pump waist, the generation rate of the spherical cavity is a factor of 2 larger than the generation rate of the hemispherical cavity. But, for the design value of the focussing parameter $\xi = 0.2$ ($w_0 = 50$ µm) there is no difference in brightness between the spherical and the hemispherical cavity. Against this background, the hemispherical cavity was chosen since it features a lager free spectral range and the cavity alignment is less involved.[263]

shows the pair-generation rate for the two configurations as a function of the pump beam waist. For $\xi = 0.2$, the position of the focus with respect to the center of the crystal is no longer relevant for the brightness.

Hemispherical cavity. For the new cavity design, we therefore chose the hemispherical design. For a hemispherical cavity, the pump focus is no longer located at the center of the crystal but at the surface of the flat mirror. The hemispherical cavity has several advantages over a spherical cavity. Since the focus in not at the center of the nonlinear crystal, no section without any crystal is required. Therefore, the hemispherical cavity has a larger free spectral range. A larger FSR enables us to an use a higher signal/idler finesse for a fixed cavity decay rate. Additionally, narrow-band spectral filtering of single spectral modes is more convenient for a larger FSR.

Another important reason to use a hemispherical cavity is that the alignment of the cavity is much simpler.[263] The flat mirror can be fixed and does not need to be aligned. Furthermore, a hemispherical cavity allows for a tuning of the cavity length by moving the convex mirror. For a spherical cavity, this would always require a rearrangement of the mode-matching optics. Since the pump-focus position is not affected by the spacing of the mirrors for a hemispherical cavity, moving of the convex mirror does not require major adjustments to the mode-matching lenses. In section 2.3.6, we present an experiment where the mirror spacing of the cavity is adjusted to change the spectral features of the

generated signal and idler photons.

2.2.1 | Experimental setup

Fig. 2.12 shows the complete setup to operate and stabilize the cavity-enhanced photon pair source:

Master laser and pump. We lock a grating stabilized diode laser at $\lambda_{\text{laser}} = 894\,\text{nm}$ to a hyperfine transition of the cesium D_1-line by modulation-transfer spectroscopy.[264] The pump light at $\lambda_{\text{pump}} = 447\,\text{nm}$ is generated by second harmonic generation (SHG) inside a high-finesse ring cavity. We collect the pump light into a polarization-maintaining signle-mode fiber. After the fiber collimator, the pump beam mode is matched to the cavity mode with the help of a telescope. The polarization of the pump beam is aligned with the y-axis of the PPKTP crystal by use of a half-wave plate (HWP) for maximum conversion efficiency.

Cavity configuration and geometry. The hemispherical cavity consists of a concave mirror (M_1) with radius of curvature $R = 5\,\text{cm}$ and a flat mirror (M_2) on the other side of the nonlinear crystal. Similar to down-conversion source presented in ref. [265], the cavity is mounted into a monolithic U-shaped aluminum box to enhance the mechanical stability. Fig. 2.13 shows the mechanical design of the cavity and the mounting of the crystals.

Cavity housing. The down-conversion cavity is placed into a hermetically sealed box. For mechanical stability, we choose a monolithic design for the main frame. We mount the concave mirror into a kinematic mirror mount which can be aligned with three fine-thread screws. The flat mirror is glued onto a piezo-electric transducer which is fixed to the side of the main frame.

The two crystals can be aligned with custom-made 5-axis tip-tilt aligners. All fine-thread screws are accessible from the outside such that the cavity and the crystals can be aligned without opening the box and disturbing the crystals' temperature stabilization. The sides with the crystal tip-tilt aligners can be detached from the box. After reinsertion, the position and orientation of the crystals does not need to be realigned. This modular design eases the alignment of the whole cavity since the crystals can be aligned independently from each other.

Temperature stabilization. As will be discussed in section 2.2.2, long-term operation of the photon-pair source requires a temperature stability of the crystals in the mK range. To meet this requirement, the temperature of the cavity main frame in actively stabilized with Peltier elements. These Peltier elements are

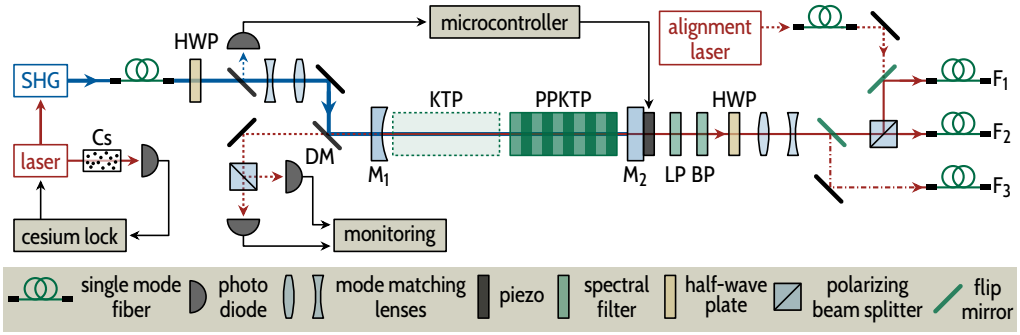

Figure 2.12 | Experimental setup of the cavity-enhanced photon-pair source. The frequency of the master laser is locked to a cesium resonance. After frequency doubling by second-harmonic generation, the pump beam is collected into a single-mode fiber and mode matched to the down-conversion cavity. The length of the cavity is stabilized to a resonance of the pump beam with a fast microcontroller acting on a piezo-electric transducer attached to the flat mirror (M_2). The generated signal and idler photons can either be split up into two fibers (F_1 and F_2) or be collected simultaneously into a single fiber (⇢ F_3). A longpass (LP) filter (transmission 98 % at 894 nm) blocks remaining pump photons. A narrow bandpass (BP) filter (1 nm bandwidth, transmission > 95 %) suppresses broadband, non-phase-matched fluorescence photons generated inside the crystals. We discuss more details and, e.g., the alignment beam (⇢) in the main text.

placed beneath the monolithic main frame. The base plate which is attached to the optical table acts a heat sink.

Additionally, to protect the cavity from turbulences and temperature variations in the air optical windows (anti-reflection coated) and an air-tight cover (not shown in Fig. 2.13a) are used. This cover also shields the cavity against acoustic noise.

The two crystals are placed into brass mounts with a high thermal conductivity. The temperature of the crystal can be individually tuned and stabilized via Peltier elements which are attached to the tip-tilt aligners (see Fig. 2.13b).

Mirror coating and cavity finesse. Mirror M_1 has a reflectivity $R_{1p} \approx 50\,\%$ at the pump wavelength and $R_{1s/i} = 99.7\,\%$ at the signal/idler wavelength. Mirror M_2 has a reflectivity of $R_{2p} = 99.7\,\%$ and $R_{1s/i} \approx 70\,\%$.

At the pump wavelength, this corresponds to a finesse of $\mathcal{F}_p \approx 5$ when both crystals are inserted into the cavity, and a finesse of about $\mathcal{F}_p = 8$ when only the down-conversion crystal is placed into the cavity. The pump finesse is not limited by absorption inside the crystals but by an imperfect anti-reflection coating with a residual reflectivity of about 3.5 % at the pump wavelength. At the signal/idler wavelength, we measure a cavity finesse of $\mathcal{F}_{s/i} = 16(3)$.

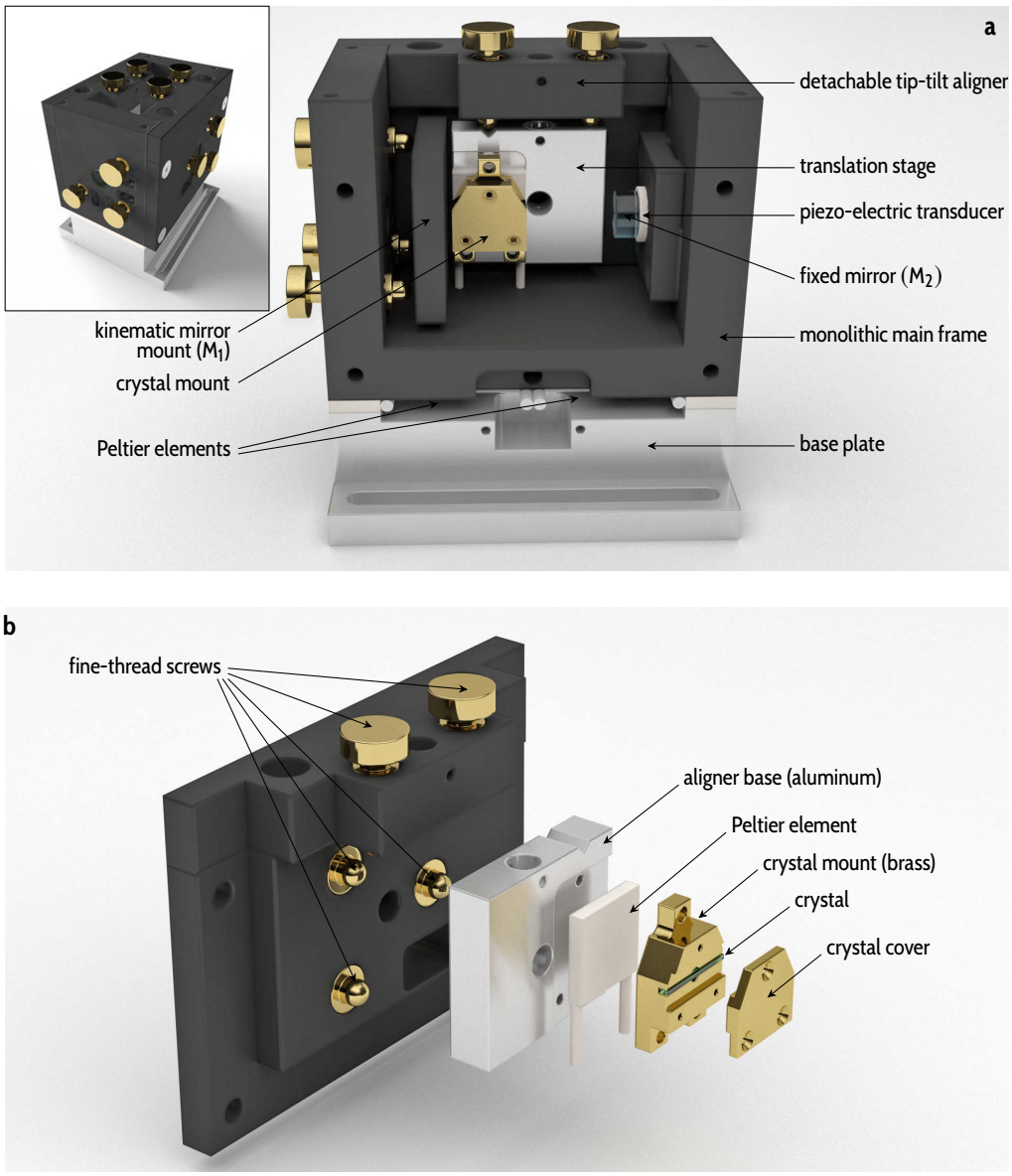

Figure 2.13 | Mechanical design of the cavity. **a**, The cavity is mounted into a monolithic U-shaped aluminum main frame. The concave mirror (M_1) is placed into a custom-made kinematic mirror mount. The flat mirror (M_2) is glued onto a piezo-electric transducer which in turn is glued onto an aluminum plate. This plate is attached to the main frame by four screws such that the mirror-piezo assembly can easily be replaced. The temperature of the main frame is stabilized with two Peltier elements to (partly) compensate long-term drifts of the cavity length. The base plate is screwed to the optical table. **b**, Custom-made tip-tilt aligner for the crystals: The aligner base is pressed by two springs (not shown) against five fine-thread screws. The crystal can be rotated about three axes and can be translated along both directions perpendicular to the pump beam. The crystal is placed into a brass crystal mount which is temperature-stabilized by a Peltier element. The aligner base acts as the heat sink. Special care in the design of the crystal mount has been taken to avoid stress on the crystal to avoid accidental breaking. The two crystal mount assemblies are screwed onto the sides of the monolithic main frame (see inset of **a**).

Cavity length stabilization. Part of the pump light reflected by the cavity is directed to a photodiode by a beam sampler (reflectivity ~4 %). A fast microcontroller utilizes this signal to provide feedback to the piezo-electric transducer which is attached to the flat outcoupling mirror (M_2) to lock the cavity to a resonance of the pump beam. We discuss this locking scheme in detail in section 2.2.2.

Fiber coupling of photon pairs. The spatial mode of signal and idler photons is matched to signle-mode fibers with a telescope. Signal and idler photons can either be split at a polarizing beam splitter and directed to individual single-mode fibers (F_1 and F_2 in Fig. 2.12). Alternatively, we can utilize a flip mirror to collect signal and idler photons simultaneously into the same single-mode fiber (F_3).

Cavity alignment and tuning. To align the orientation of the cavity mirror with respect to each other and to measure the resonance frequencies of the cavity, the setup is operated in reverse: We feed part of the master laser as an alignment laser over a flip mirror into the down-conversion cavity through mirror M_2. We detect the signal transmitted through the cavity and through the dichroic mirror (DM) with a polarizing beam splitter and two photodiodes. Simultaneously, we scan the voltage applied to the piezo-electric transducer attached to the flat mirror.

This signal on the three photodiodes is used to monitor the alignment of the cavity and to estimate the resonance frequencies of signal and idler fields. If we detect unwanted higher-order Laguerre-Gaussian modes, we align the mirror (M_1) with the fine-thread screws. Additionally, we optimize the position of the mode-matching lenses until all higher-order modes are eliminated.

The resonance frequency for the three fields can be tuned by changing the crystals' temperatures and orientations with respect to the optical axis. During photon-pair generation in the experiments, we block the alignment beam.

Background fluorescence. A narrow bandpass (BP) filter (1 nm bandwidth, transmission > 95 %) suppresses broadband, non-phase-matched fluorescence photons generated inside the crystals. Fig. 2.14 shows the more than 100 nm wide spectrum of this background fluorescence. Background fluorescence is generated in both compensation and down-conversion crystals and the generated intensity is independent of the pump polarization. Hedge and coworkers analyzed the infrared fluorescence of KTP crystals.[266] They observed comparable spectral characteristics with a peak in fluorescence at about 850 nm. They attribute the fluorescence to the presence of titanium Ti^{3+} complexes at the normal Ti^{4+} cites in KTP crystals.

Without spectral filtering, more than 50 % of the photons detected with an avalanche photodiode behind the cavity can be attributed to background fluorescence. The bandpass filter reduces the ratio of detected background photons to detected down-conversion photons to less than 5 %. The 1 nm (385 GHz at 894 nm) transmission band of the filter is larger than the bandwidth of the photons generated by type-II cavity-enhanced SPDC with a 2 cm long crystal (<250 GHz). We tune the transmission wavelength to maximize the transmission of the photon pairs by slightly rotating the bandpass filter. A larger incidence angle shifts the transmission to larger wavelengths.

2.2.2 | Cavity-length stabilization via fast microcontrollers

The experimental setup to generated photon-pairs via cavity-enhanced SPDC shown in Fig. 2.12 comprises various interrelated feedback loops. Fig. 2.15 depicts the feedback control systems employed in each subsystem of the experiment. For many experiments with the photon-pair source, long-term stability of the complete experimental setup is required. In earlier experiments,[57,128,237] feedback-loops based on analog circuits were employed. Analog electronics often has favorable properties im terms of noise and control bandwidth, compared to digital equivalents. But, inspired by the article of Huang and colleagues,[267] a microcontroller-based digital locking scheme was developed for this thesis to stabilize the cavity length of the down-conversion and the second-harmonic generation cavity.

The main advantages of digital feedback loops are, on the one hand, that they can easily be programmed to include re-locking logic. On the other hand, their use simplifies the experimental setup. Neither additional optical elements, as for a Hänsch-Coulliaud[128,268] locking scheme, nor fast electro-optical modulators used with the Pound-Drever-Hall[135,269,270] technique or additional locking lasers with optical choppers are needed.[121,125,126,133] We also use a similar digital locking scheme with re-locking logic to stabilize the SHG ring cavity.

Master laser. The master laser requires active stabilization of the temperature and current through the laser diode for longterm operation. We utilize a digital feedback controller (Toptica DigiLock 110) based on a field-programmable gate array (FPGA) to stabilize the laser frequency via modulation-transfer spectroscopy by modulating the laser diode current. Since the digital locking electronics can be monitored remotely with a computer, a convenient relocking scheme can be employed to stabilize the master-laser frequency over days without manual intervention.

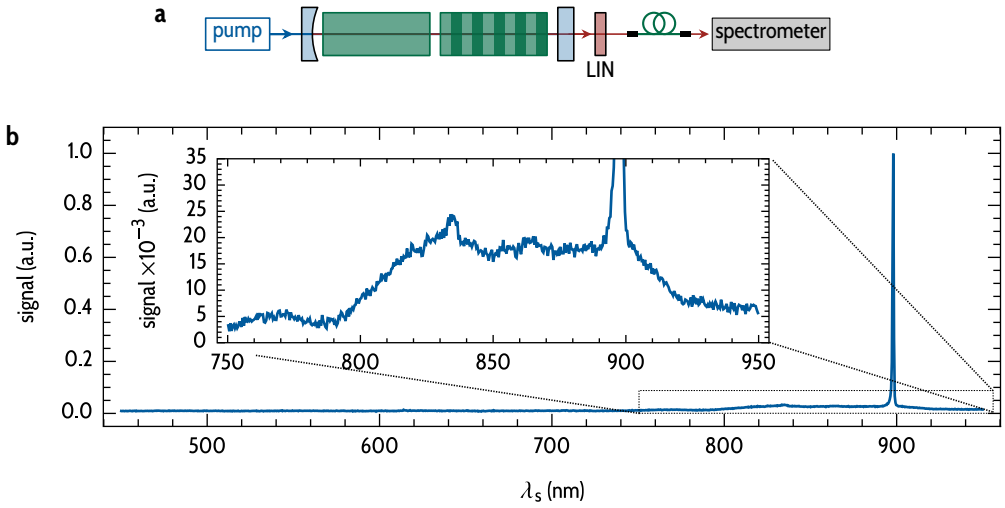

Figure 2.14 | Non-phase-matched background fluoresence. **a**, Only signal photons are selected with a linear polarizer (LIN) and sent to a grating spectrometer. **b**, The signal photons are generated at about 900 nm at a crystal temperature of 20 °C. The broadband background fluorescence stretches over a range of more than 100 nm and amounts to about 50 % of the generated photons. The inset shows the same data. Background photons are generated in the compensation and the down-conversion crystals with nearly identical spectra. This has been verified by removing one crystal from the cavity at a time.

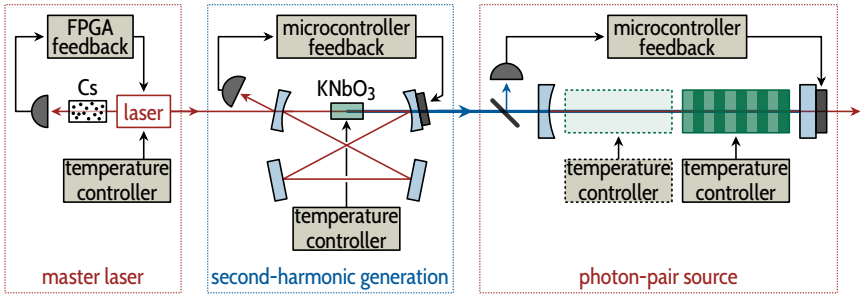

Figure 2.15 | Feedback control system required for photon-pair generation. Photon-pair generation requires the stable operation of a cascaded system of feedback control loops. First, the frequency of the master laser is locked to a hyperfine transition of cesium using commercial digital locking electronics based on a field-programmable gate array (FPGA). Subsequently, the cavities for second harmonic and photon-pair generation are locked with fast microcontrollers,[267] implementing digital bottom-of-fringe locking schemes. Besides these three fast controllers, temperature controllers are required for the laser diode, the nonlinear crystal inside the SHG cavity (potassium niobate, $KNbO_3$), and the crystals inside the down-conversion cavity.

Microcontroller cavity lock. Once the master-laser frequency is locked to a hyperfine transition of cesium, the second harmonic cavity can be locked to the master laser. Subsequently, the down-conversion cavity is locked to a resonance of the blue pump light (see Fig. 2.15). The locking of the two cavities is done with the help of a fast microcontroller (STMicroelectronics STM32F3) with on-chip 12-bit analog-to-digital (ADC) and digital-to-analog (DAC) converters. As proposed by Huang et al.,[267] the microcontroller measures the voltage on a photodiode which monitors the beam that is reflected by the cavity. The DAC applies feedback to a piezo-electric transducer attached to one of the cavity mirrors. The same locking scheme is used to stabilize the cavity length of the photon-pair source as depicted in Fig. 2.16.

The following algorithm for a bottom-of-fringe lock is used: We increment the piezo voltage in steps until the intensity of the reflected beam reaches its minimum and we find the cavity resonance. Whenever, after a step, we detect a sign-flip in the change in intensity, we invert the direction of the voltage steps. In contrast to the algorithm proposed by Huang and colleagues,[267] the step size depends on the magnitude of the change in intensity at the last step. This decreases the settling time and improves the stability of the locking system. For details, see the discussion in Ref. [271].

Digital noise. Compared to the purely analog control systems used in earlier experiments,[128] the microcontroller-based locking systems introduce higher electronic noise levels into the system. This electronic noise acts directly on the voltage applied to the piezo-electric transducer. The RMS noise of the piezo voltages is increased by a factor of 1.5–2 compared to the analog locking system. Further investigations reveal that the additional noise is caused by insufficient isolation of the analog and digital parts of the circuit boards of the microcontroller-based locking scheme. Huang and coworkers showed that their digital locking scheme performs on par with a conventional analog locking scheme in terms of electronic noise levels.

For the experiments discussed in this thesis, the additional noise has no detrimental effects: For the SHG cavity, the additional noise decreased the maximum attainable power at 447 nm by no more than 5 %. For the photon-pair source, we do not observe any difference in performance between the digital and the anlog locking schemes. In principle, a higher noise floor at the piezo voltage results in a frequency modulation and, thus, a linewidth broadening of the generated photon pairs. Due to the low finesse of the cavity and the broad cavity linewidth at both the pump and the signal/idler wavelengths, this effect is too small to be measurable. For a cavity with a higher finesse and smaller signal/idler linewidths, the noise level would have to be reduced.

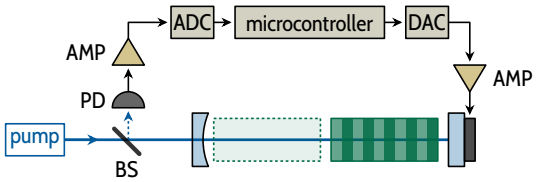

Figure 2.16 | Microcontroller-based locking. Part of the pump light reflected by the cavity is split with a beam sampler (BS, reflectivity 4 %) and directed to a photodiode (PD). The signal is amplified (AMP) to cover the full range (0–3 V) of the analog-to-digital converter (ADC). In each step of the locking algorithm, the microcontroller reads the current value of the ADC and computes the new value for the digital-to-analog converter (DAC). The DAC voltage is amplified to cover the range of 0–150 V applied to the piezo-electric transducer.

Automatic re-locking. The main advantage of a digital locking scheme over an analog one is that we can implement a sophisticated re-locking logic. For example, the microcontroller can keep track of whether the down-conversion cavity is locked to an appropriate resonance of the pump beam: When scanning the piezo voltage, there are twice as many resonances at the pump frequency ω_p than at the signal and idler frequency $\omega_{\mathrm{s/i}} \approx \omega_\mathrm{p}/2$. The photon-pair source can only produce signal and idler photons which are indistinguishable in frequency in the central mode if we lock the cavity to a pump resonance for which the signal/idler resonance frequencies are $\omega_{\mathrm{s/i}} = \omega_\mathrm{p}/2 \pm 2\pi n \cdot \mathrm{FSR}_{\mathrm{s/i}}$, with $n \in \mathbb{N}$. Otherwise the signal/idler resonance frequencies would be at $\omega_{\mathrm{s/i}} = \omega_\mathrm{p}/2 \pm 2\pi[n + 1/2] \cdot \mathrm{FSR}_{\mathrm{s/i}}$ and, due to energy conservation, no frequency-degenerate photons would be generated.

As shown in Fig. 2.17, the microcontroller can detect whether the system is in a locked state. For this identification, the variance of the preceding step sizes is evaluated. The algorithm always stores the last value of the piezo voltage for which a locked state was detected. An external disturbance can cause the cavity to be locked to a neighboring pump resonance with a different piezo voltage. Once the microcontroller detects a locked state with a new value of the piezo voltage, the microcontroller tries to re-lock the system in the vicinity of the stored value of the piezo voltage. Similarly, the digital locking system can detect whether one of the limits of the piezo tuning range is reached. In this case, the microcontroller executes a shift of the piezo-voltage by two resonances to maintain continuous operation.

Long-term stability. A similar re-locking logic is used for the SHG cavity, which is much more susceptible to acoustic noise than the down-conversion cavity. The analog locking scheme used in earlier experiments requires a manual re-locking of the SHG cavity about once every two hours. When both cavities are locked with a microcontroller, the photon-pair source can be operated over days without manual intervention. Fig. 2.18 shows the signal/idler count rates as

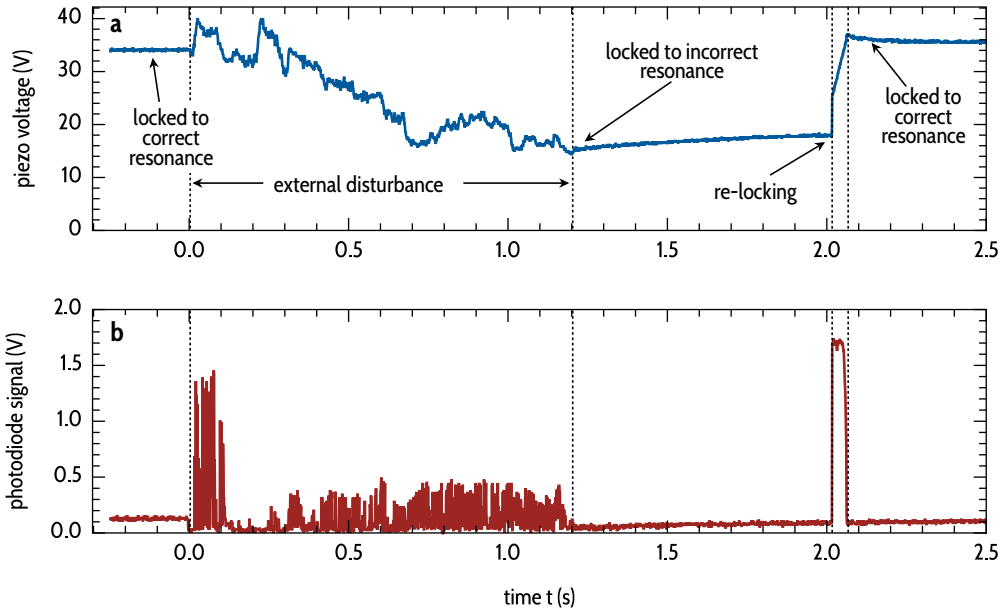

Figure 2.17 | Automatic re-locking of the down-conversion cavity. **a**, A sophisticated re-locking logic can be programmed into the microcontroller. Here, the response of the locking system to a manually generated disturbance is shown. A screw driver is scratched vigorously over the optical table for ~1 s starting at $t = 0$. This forces the system to lock the cavity to a neighboring resonance of the pump field. Since the piezo voltage (—) of the correct resonance (for time $t < 0$) is stored as a reference value in the microcontroller, the incorrect piezo voltage is identified. Therefore, a re-locking to the correct pump resonance is initialized. While the time constant for the identification of a stable locked state is deliberately chosen larger than 1 s to avoid false positives, the relocking process takes less than 50 ms. **b**, Signal of the photodiode (—) for the same process. The external disturbance introduces strong fluctuations in the mirror position which can no longer be compensated by the feedback loop. Note, that not only the down-conversion cavity but also the master laser and the second-harmonic-generation cavity are affected by the disturbances.

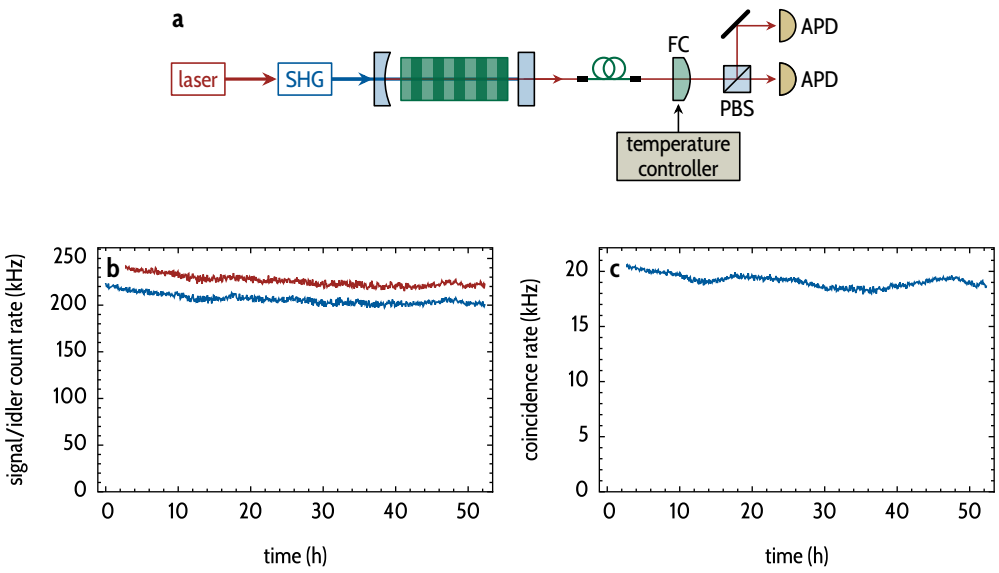

Figure 2.18 | Longterm stability of the photon-pair source. **a**, The photon-pair source is stabilized with the feedback control system depicted in Fig. 2.15. The down-conversion cavity is tuned such than in the central mode frequency-degenerate signal and idler photons are generated. After collection into a fiber, signal and idler photons are spectrally filtered with a monolithic filter cavity (FC) which is tuned in resonance with the central mode. Signal and idler photons are split with a polarizing beam splitter (PBS) and detected with avalanche photodiodes (APD). **b**, The signal (—) and idler (—) count rates are stable over more than 50 h. Over the measurement duration, both the SHG as well as the down-conversion cavity were automatically re-locked several times. Due to the short re-locking time, the default period was very short. From detailed detection and measurements of individual re-locking events, we infer a stable operation for more than 99.8 % of the whole measurement duration. **c**, The coincidence rate (—) also shows excellent stability over the whole measurement period. The spectral filtering verifies that the system was locked to the correct pump resonance all the time. The fluctuations in the coincidence rate are mainly caused by fluctuations in the pump power as well as slow drifts in the temperature of the nonlinear crystal. Fluctuations in the resonance frequency of the filter cavity are negligible (see section 2.1).

well as the coincidence rate over a measurement period of more than 50 h.

2.3 | Spectral properties of photons generated by cavity-enhanced parametric down-conversion

In this section we discuss the measurements of the spectral properties of the photons generated by cavity-enhanced SPDC. First, we provide a broad overview of the spectral features of the photons generated inside a single-crystal cavity recorded with a conventional grating spectrometer. We identify the spectral

mode clusters and their relative position to the parametric gain profile. Subsequently, we verify this measurement by measuring the signal spectral density with the cascaded filtering setup discussed in section 2.1.3. With this high-resolution measurement scheme, we can fully resolve the mode structure within the clusters.

For the down-conversion cavity with compensation crystal, we repeat this measurement and find the complete comb of spectral modes. Additionally, we verify that the central, degenerate mode coincides with the frequency of the master laser which is locked to a cesium resonance by performing an absorption spectroscopy with generated signal photons.

We then return to the single-crystal cavity and analyze the spectral tuning behaviour upon temperature changes of the nonlinear crystal. We explain theoretically why, for a triply-resonant cavity, the relative position of the frequency clusters with respect to the center of the parametric gain envelope does not depend on the temperature. The temperature tuning is also measured with a grating spectrometer and the cascaded filter-cavity setup. Finally, we evaluate the impact of the mirror spacing on the signal spectral density for the single-crystal cavity. Interestingly, we find a dependency of the relative Gouy phase and the effective reflectivity $\bar{r}$ on the mirror spacing.

2.3.1 | Single-crystal cavity – signal-photon spectrum

To study the spectral characteristics of the generated photons we use a conventional grating spectrometer to gain a first overview of the spectral features. In the following, we present the measurement of the signal spectral density for the single-crystal photon-pair source. We discuss the measurement results and compare them with the theoretical expectations detailed in chapter 1.

Theory. According to Eq. 1.3.34, the signal photon spectral density is proportional to:

$$\left|\psi(\omega_s)\right|^2 \propto \mathrm{Gain}(\omega_s, \xi, \mu, \Delta\Phi)\mathrm{Airy}_s(\mathcal{F}_s, \omega_s)\mathrm{Airy}_i(\mathcal{F}_i, \omega_p - \omega_s), \tag{2.3.1}$$

where the normalized Airy functions are defined by Eq. 1.3.11. Since the focussing parameter is small ($\xi \approx 0.2$, see section 1.2.1), for all experiments discussed in the following, the parametric gain envelope does not depend on the focussing parameter ξ and the focus position parameter μ and can be approximated by:

$$\mathrm{Gain}(\omega_s, \xi, \mu, \Delta\Phi) \approx \mathrm{sinc}^2\big(\Delta kl/2\big)P(\omega_s, \Delta\Phi). \tag{2.3.2}$$

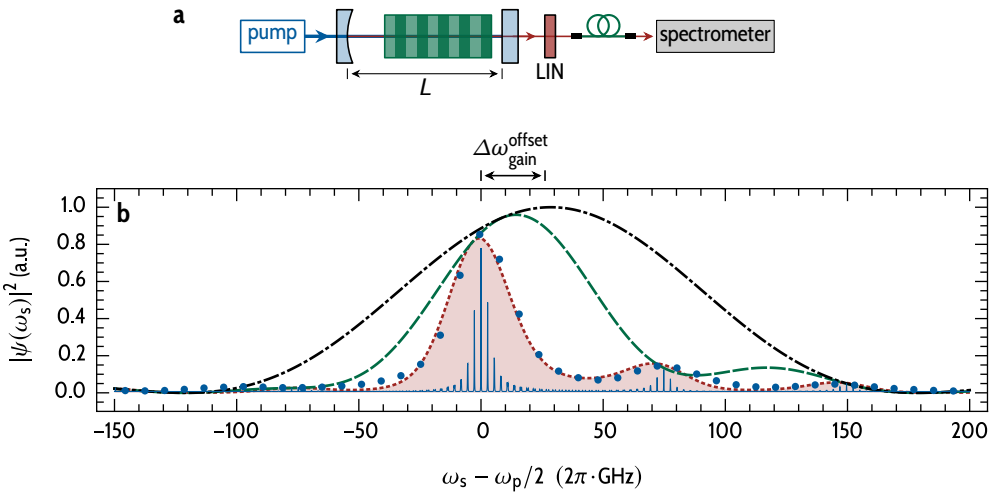

Figure 2.19 | Single crystal cavity – spectrometer measurement. **a**, The spectrum of the signal photons generated in the single-crystal cavity with a total length $L = 38$ mm is recorded with a conventional grating spectrometer. A linear polarizer (LIN) blocks the idler photons. The spectrometer has a resolution of $\Delta\omega_{\text{spec}} = 2\pi \cdot 25$ GHz. **b**, Utilizing the alignment beam (see Fig. 2.12), the cavity is tuned to perfect triple resonance such that a mode is located at $\omega_{s/i} = \omega_p/2$. The spectrometer measurement (•) reveals two clusters separated by about 75 GHz. The fit (----) to Eq. 2.3.6 shows good agreement. The plots of the deconvoluted signal spectral density $\left|\psi(\omega_s)\right|^2$ defined by Eq. 2.3.1 (——), the parametric gain envelope given by Eq. 2.3.2 (– –) and the single-pass gain $\text{sinc}\left(\Delta k l/2\right)$ (–·–) serve as a guide to the eye. As indicated in the plot, the gain envelope has an offset of $\Delta\omega_{\text{gain}}^{\text{offset}} = 2\pi \cdot 27$ GHz from perfect degeneracy.

If the cavity is locked to a pump resonance, the phase-balancing factor is the modulus squared of Eq. 1.2.38:

$$\begin{aligned} P(\omega_s, \Delta\Phi) &= 1 + \bar{r}^2 + 2\bar{r}\cos(\Delta k l + \Delta\Phi) \\ &= [1+\bar{r}]^2 \left[1 - \frac{4\bar{r}}{[1+\bar{r}]^2} \sin^2\left(\Delta k l/2 + \Delta\Phi/2\right)\right], \end{aligned} \tag{2.3.3}$$

where the relative phase $\Delta\Phi$ is defined by Eq. 1.2.40:

$$\Delta\Phi = \Delta\delta_1 - 2\Delta\phi_{\text{Gouy}}^{\text{eff}}. \tag{2.3.4}$$

Measurement. Fig. 2.19 shows the signal spectral density measured with a conventional grating spectrometer. The signal spectrum is dominated by a single cluster accompanied by a second minor cluster which is separated by about 75 GHz. Due to the low spectral resolution, we cannot analyze the mode structure within the clusters with this measurement.

We measure the instrument response function of the spectrometer with the master laser (linewidth 100 kHz). The IRF is, to good approximation, a Gaussian

distribution:

$$\mathrm{IRF}_{\mathrm{spec}}(\omega) = \exp\left(-4\ln(2)\frac{\omega^2}{\Delta\omega_{\mathrm{spec}}^2}\right) \tag{2.3.5}$$

with a FWHM of $\Delta\omega_{\mathrm{spec}} = 2\pi \cdot 25\,\mathrm{GHz}$. The measurement signal is the convolution of the IRF with the signal spectral density:

$$\left|\psi(\omega_{\mathrm{s}})\right|^2_{\mathrm{exp}} = a\,(\mathrm{IRF}_{\mathrm{spec}} * \left|\psi\right|^2)(\omega_{\mathrm{s}}) + c, \tag{2.3.6}$$

where the amplitude a and the offset c are left as fit parameters.

Fit. The fit of Eq. 2.3.6 to the measured data points has, besides the overall amplitude a and the offset c, only the following free parameters: the relative phase $\Delta\phi = 0.8(2)$, the parameter $\bar{r} = 0.43(5)$ in Eq. 1.1.8 and an offset from perfect degeneracy of $\Delta\omega_{\mathrm{gain}}^{\mathrm{offset}} = 2\pi \cdot 27(3)\,\mathrm{GHz}$ of the sinc-function in Eq. 2.3.2. This offset accounts for the temperature and orientation of the nonlinear crystal and is indicated in Fig. 2.19.

We estimate all further parameters required to fully define Eq. 2.3.1 from other measurements: The temperature-dependent KTP Sellmeier equations where taken from Emanueli and Arie.[272] The signal idler finesse $\mathcal{F}_{\mathrm{s/i}} = 16(3)$ (see table 1.1) is calculated from the mirror-reflectivity values supplied by the manufacturer. The mirror distance and the length of the nonlinear crystal are estimated with a caliper gauge. We adjust the temperature and orientation of the nonlinear crystal with the alignment beam (see Fig. 2.12) such that there is a degenerate spectral mode with $\omega_{\mathrm{s}} = \omega_{\mathrm{i}} = \omega_{\mathrm{p}}/2$ at the center of the dominant cluster. The alignment procedure is detailed by D'Auria and coworkers.[216]

Discussion. The fit shows excellent agreement with the measurement. Fig. 2.19b highlights how the second cluster is suppressed by the pump-resonant cavity configuration. For a cavity with a single-pass pump, the second cluster would have the same amplitude as the dominant cluster. Nevertheless, the fit value of $\bar{r} = 0.43(5)$ does not coincide with the value obtained with Eq. 1.1.75. With the values of the mirror reflectivities supplied by the mirror manufacturer and the measured absorption coefficient of the nonlinear crystal, a value of $\bar{r}_{\mathrm{theo}} \approx 0.9$ would be expected. This discrepancy will be discussed in section 2.3.6.

Using the cascaded filtering system presented in section 2.1.3 as a high-resolution spectrum analyzer, in the next section, we can resolve the fine structure within the clusters and the grating-spectrometer measurement, which has been discussed above, can be verified.

2.3.2 | Single-crystal cavity – high-resolution spectroscopy

The cascaded filtering system based on the monolithic cavities discussed in section 2.1.3 has an effective free spectral range of well above 1 nm. Therefore, this setup is suitable to measure the spectrum shown in Fig. 2.19 in much greater detail. Compared to the grating spectrometer, the resolution is increased by a factor of more than 200 and the mode structure within the clusters can be resolved.

Measurement. The measurement setup is depicted in Fig. 2.20. The cavity configuration (especially the total length of the cavity) is identical to the grating-spectrometer measurement (Fig. 2.19a). Since only a small fraction ($\sim$120 GHz $\widehat{=}$ $\sim$0.3 nm) of the spectrum was recorded, a 1 nm bandpass filter could be used to enhance the signal-to-noise ratio by suppressing background fluorescences (see section 2.2.1). The signal photons were collected into a single-mode fiber and directed to the cascaded filtering system. A linear polarizer blocked the idler photons and the signal photons were detected with an avalanche photodiode.

Fit. In Figs. 2.20b, 2.20d and 2.20e, the measured signal spectral density is shown. To fit the data points, we use a simplified model. Instead of a convolution with the full system transmission function $\mathcal{A}_{\text{system}}(\omega)$ (Eq. 2.1.3):

$$\left|\psi(\omega_\text{s})\right|^2_\text{exp} = c + a\left[\mathcal{A}_\text{system} * \left|\psi\right|^2\right](\omega_\text{s}), \tag{2.3.7}$$

the product of two Lorentzian distributions with the linewidths of the two cavities is used for the convolution:

$$\left|\psi(\omega_\text{s})\right|^2_\text{exp} = c + a\int_{-\infty}^{\infty} \mathrm{d}\omega' \left|\psi(\omega_\text{s}-\omega')\right|^2 \mathcal{L}(\Gamma_1,\omega')\mathcal{L}(\Gamma_2,\omega'), \tag{2.3.8}$$

where the Lorentzian distribution is defined by:

$$\mathcal{L}(\Gamma,\omega) = \frac{\Gamma/(2\pi)}{\Gamma^2/4+\omega^2}, \tag{2.3.9}$$

and the linewidths of the two filter cavities are $\Gamma_1 = 2\pi\cdot 192\,\text{MHz}$ and $\Gamma_2 = 2\pi\cdot 885\,\text{MHz}$. The simplification was mainly performed to speed up the computationally intensive fitting routine. Some of the small deviations between measurement and theory in the range $2\pi\cdot 80\,\text{GHz} < \omega_\text{s} - \omega_\text{p}/2 < 2\pi\cdot 100\,\text{GHz}$ in Fig. 2.20b can be attributed to this simplification.

For the fit of Eq. 2.3.8 to the measured data, we use the offset c and the amplitude a as fitting parameters. Furthermore, the mirror distance L and a small offset of the center of the signal Airy function in Eq. 2.3.1 from perfect degeneracy are additional fitting parameters. The spectrometer measurement shown in Fig. 2.19 is used to determine the values of $\bar{r}$ and $\Delta\Phi$ as well as the width of the parametric gain profile $\Delta\omega_{\text{gain}}$.

Discussion. Qualitatively, there is a good agreement between the measurement and Eq. 2.3.8. The overall position of the modes and the center of the clusters were fit with good accuracy. The original fit shown in Ref. [138], could not replicate the position of the modes in the second cluster. This is caused by the assumption in the original manuscript that the free spectral range of the signal and idler field is constant over the whole frequency range. The fit shown here, however, takes the dispersion into account and utilizes the KTP Sellmeier equations to calculate the resonance frequencies with higher accuracy.

Due to nonlinearities in the scanning of the filtering system, the exact position of modes is shifted in some parts of the spectrum by up to 300 MHz compared to the theoretical curve. These deviations are caused by the measurement procedure: The resonance frequency of the monolithic filter cavities is inferred from the readings of the temperature sensor at each point in time. In the second half of each temperature ramp (see Fig. 2.9), the deviations between actual resonance frequency and inferred resonance frequency are especially pronounced.

Another imperfection is that the two transmitting resonances of the filter cavities do not always coincide perfectly. Especially for values $\omega_s < \omega_p/2$ in Fig. 2.20b, this issue reduces the amplitude of the modes. The deviation between the resonance frequencies of the two filter cavities can be attributed to an imperfect calibration which is performed with the four cesium resonances at frequencies $\omega_s \geq \omega_p/2$.

Fig. 2.20 highlights the potential as well as the deficiencies of the cascaded filtering system used as a spectrum analyzer. While most of the spectral features can be replicated with high fidelity, absolute values for peak heights and peak positions are not reliable. Therefore, the spectrum analyzer can be used to verify a known model, as it is shown with the above-described measurement. But, the filtering system is not suited to *quantitatively* analyze the spectrum of an unknown source over a broad range of frequencies.

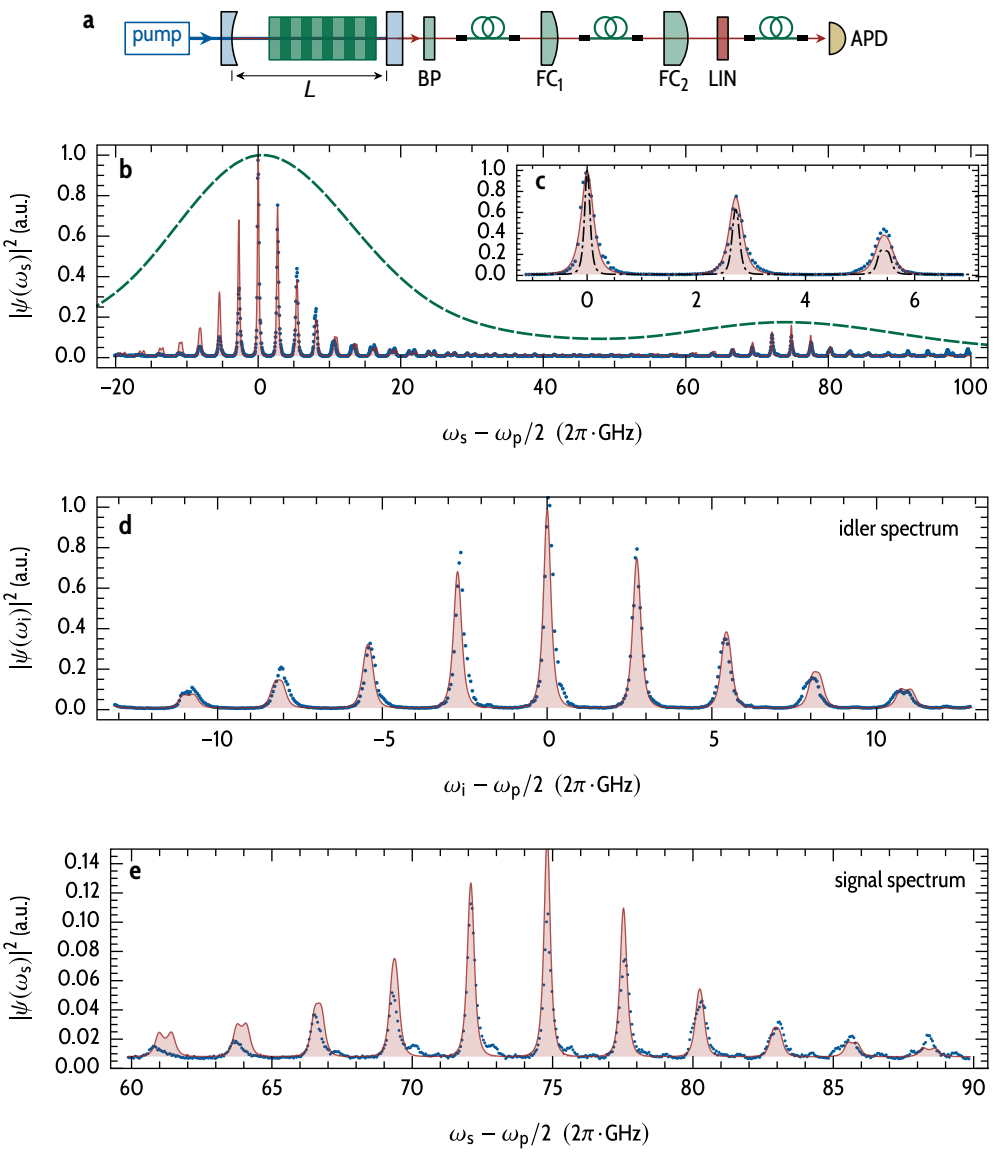

Figure 2.20 | Single-crystal cavity high-resolution spectrum. **a**, Photons generated in the single-crystal cavity are collected into a fiber and spectrally analyzed with the cascaded filtering system. The transmission frequency of the combined filtering system is scanned over the two clusters (see Fig. 2.9). Either idler or signal photons are blocked with a linear polarizer (LIN). The transmitted photons are counted with an avalanche photodiode (APD). A 1-nm bandpass filter is used to suppress background fluorescence. **b**, Measured signal-photon count rate (•) as a function of the filter-system detuning. Qualitatively, there is a good agreement to the model (—) given by Eq. 2.3.8. For comparison, the spectrometer measurement (– –) from Fig. 2.19 is shown. **c**, Zoom into the first three peaks of the data shown in **b**. The unconvoluted signal spectral density in shown for reference (–·–). **d**, Detail for the central cluster of the idler spectral density. **e**, Detail for the second cluster of the signal spectral density. Figure replicated in part from Ref. [138].

2.3.3 | Two-crystal configuration – high-resolution spectroscopy

For the two-crystal configuration, we perform the same measurement as discussed in Fig. 2.20.[205] Fig. 2.21 shows the measurement results. As for the single-crystal configuration, qualitatively, a good agreement between the model (Eq. 2.3.8) and the measurement is found. Compared to the single-crystal cavity measurement, we choose a lower tuning speed of the filtering system. Therefore, the accuracy of the measurement is higher for positive detuning from degeneracy $\omega_s \geq \omega_p/2$. For negative detuning, the same imperfections in the calibration of the filter cavities cause an underestimation of the peak heights.

Fit. The same model (Eq. 2.3.8) is used for the fit. Of course, the Airy functions have to be modified to account for the compensation crystal, resulting in equal free spectral ranges for the signal and idler fields. The same fitting parameters are used as for the fit of the single-crystal data discussed in section 2.3.2. The fit yields a total cavity length of 47.5(1) mm with two 20 mm long crystals. These values are in excellent agreement with the mechanical design of the cavity (see Fig. 2.13). We estimate a finesse of $\mathcal{F}_{s/i} = 15(1)$ from the fit. Within the measurement uncertainty, this value cannot be distinguished from the signal/idler finesse measured for the single-crystal cavity. Since the losses by the crystals' anti-reflection coatings are much smaller than the photons losses through the outcoupling mirror M_2, the additional crystal surfaces do not significantly contribute to the cavity finesse.

All in all, the fit is in good agreement with the measured values. In contrast to the fit presented in the publication,[205] the fit shown here covers a much broader wavelength range. This is possible since, here, the wavelength-dependent Sellmeier equations are used to define the Airy functions.

But, especially for negative detuning $\omega_s < \omega_p/2$ we observe significant deviations between theoretical expectation and measurement. These deviations can be attributed to an imperfect calibration of the filter cavities. The calibration procedure was optimized for positive detuning. For negative detuning, the filter-cavity resonance frequencies are interpolated with only four data points given by the four hyperfine lines of the cesium D_1 transition.

Discussion. In contrast to the single-crystal configuration, for the two-crystal cavity the fit value $\bar{r} = 0.9(2)$ coincided with the theoretical value of $\bar{r}_{\text{theo}} = 0.89$ calculated from the mirror reflectivity and the absorption of the crystals at the pump wavelengths. This indicates that, compared to the measurement with the single-crystal cavity, the pump beam is better superimposed with the signal and idler fields. Therefore, there is only a negligible spatial walk-off between photons generated in the forward direction and photons generated in the backward

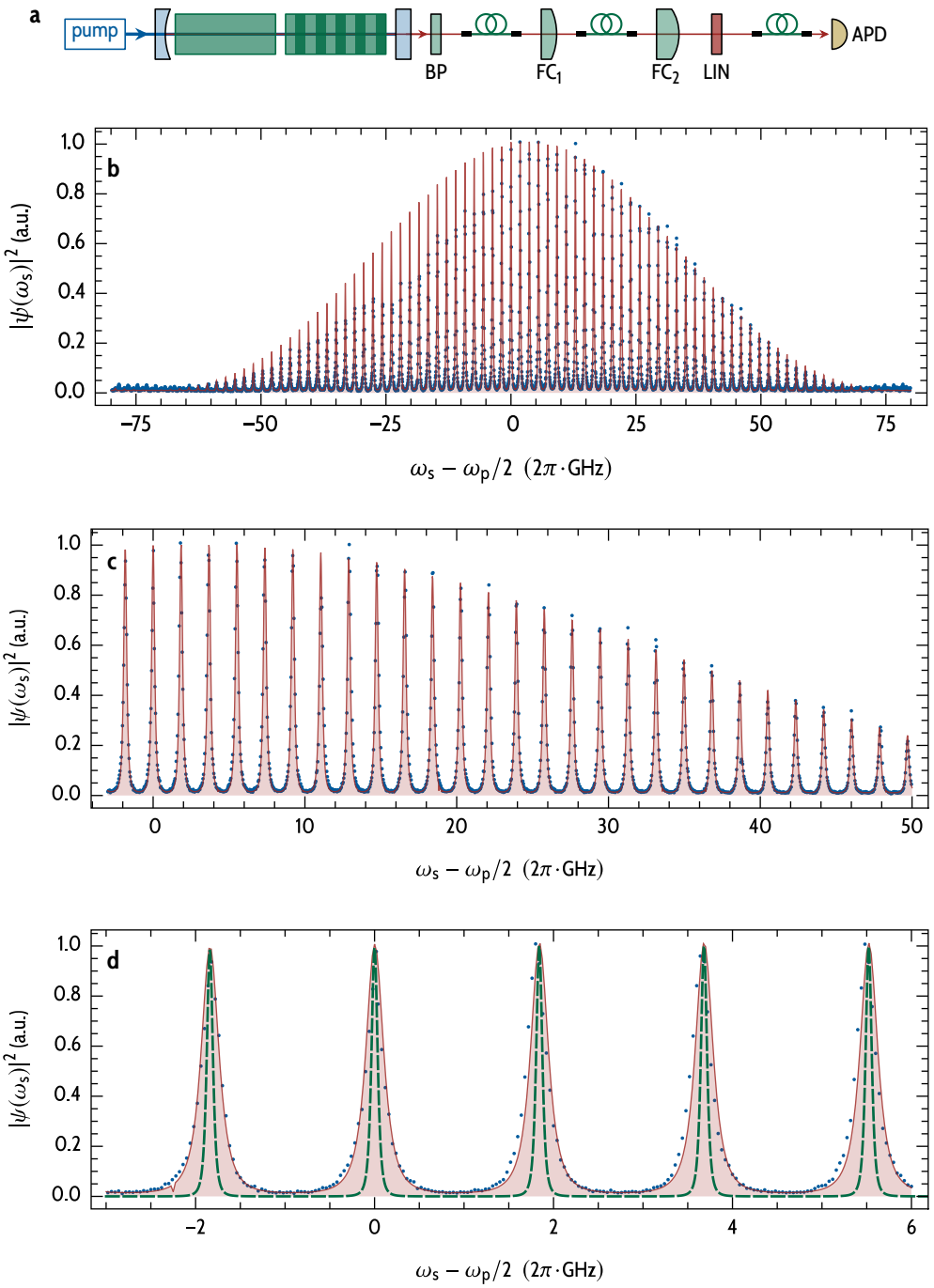

Figure 2.21 | Signal spectral density for the two-crystal configuration. **a**, The measurement setup shown here is identical to Fig. 2.20a. **b**, The measured values (•), are in good agreement with the theory (—) for values $\nu_s > \nu_p/2$. For negative values, the filtering system was not properly calibrated resulting in an underestimation of the peak heights. **c**, Detail for positive detuning. **d**, Further detail to evaluate the quality of the fit. The deconvoluted spectrum (Eq. 2.3.1) is shown for reference (– –). Figures replicated in part from Ref. [138].

direction. Compared to a single-pass down-conversion source, the width of the parametric gain envelope is reduced by a factor of about 2.[205] Scholz and coworkers[238] measured (with a grating spectrometer) the same width of 60 GHz for their triply-resonant two-crystal cavity.

To the best of the author's knowledge, the measurements presented in Figs. 2.20 and 2.21 were able to resolve the mode structure of the full spectrum of a cavity-enhanced parametric down-conversion source for the first time. Pomarico et al.[132,173] as well as Monteiro and coworkers[273] verified the cluster structure of the spectrum, but could not resolve the modes within the clusters. Rieländer and colleagues[50,149] also resolved the mode structure within a cluster, but with a much lower signal to noise ratio since only a single filter cavity was used. Luo and coworkers[136,141] verified with a scanning Fabry-Pérot interferometer that their monolithic photon-pair source features only a single mode per cluster.

2.3.4 | Frequency locking of the photon-pair source

The cascaded filter system can also be used to perform an absorption spectroscopy with the generated signal photons. Fig. 2.22 depicts the measurement principle. A cesium vapor cell is placed into the signal photon beam path. Then, the measurement presented in Fig. 2.21 is repeated. The spectrum of the signal photons transmitted by the cesium cell is recorded with the cascaded filter system.

Results. The master laser (see Fig. 2.12) at frequency $\omega_p/2$ is locked to the $F = 4$ to $F' = 3$ transition of the cesium D_1 line.[251] Therefore, signal photons generated into the central mode at the degenerate frequency of $\omega_s = \omega_p/2$ are strongly absorbed by the cesium vapor. Coincidentally, one mode is also in resonance with the weaker $F = 3$ to $F' = 3$ transition. Photons generated into this mode are also partially absorbed by the cesium vapor.

Discussion. As will be discussed in section 2.5, a Hong-Ou-Mandel[33] type experiment can verify that the signal and idler photons generated into the central mode with $\omega_s = \omega_i = \omega_p/2$ are indistinguishable in frequency. Wolfgram and coworkers[143] used a similar photon-pair source based on (non-pump-resonant) cavity-enhanced parametric down-conversion[126] to generate atom-resonant NOON-states.[142] These NOON-states were used for entanglement-enhanced sensing.[144]

The ability to generate heralded single photons at a specific wavelength with a well-defined spectral bandwidth has been utilized in various experiments published in the literature.[65,146,155,274] Zhang and coworkers[107] presented the

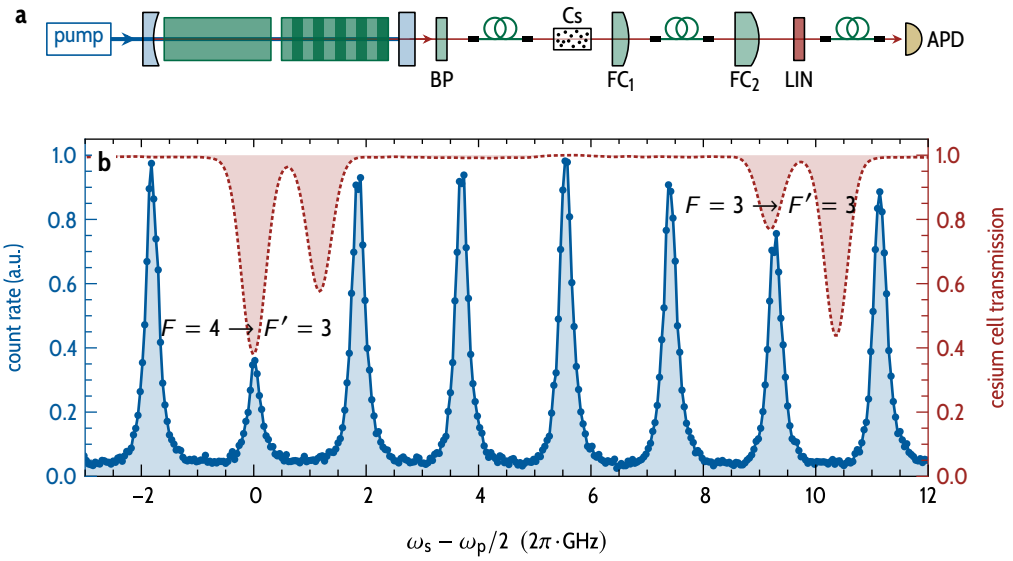

Figure 2.22 | Frequency locking of the photon-pair source. **a**, To verify that the central mode is located at pump-laser frequency ω_p, a cesium spectroscopy is performed with the generated signal photons. The measurement setup and measurement procedure is identical to the one presented in Fig. 2.21. The only difference is the cesium vapor cell (Cs) which is placed in front of the spectrum analyzer. **b**, Signal-photon count rate as function of the detuning of the filter-cavity transmission frequency (–●–). Doppler-broadened absorption lines of the cesium D_1-line measured with master laser in frequency-scanning mode (----). Figure replicated from Ref. [205].

storage of entangled frequency-uncorrelated heralded single photons with a bandwidth of 5 MHz in a quantum memory based on ultracold atoms. Their cavity-enhanced photon-pair source utilizes an additional (shorter) tuning crystal to achieve the desired degeneracy of signal and idler resonances. A birefringent tuning crystal can additionally be used to reduce the number of modes per cluster to one.[151]

Rieländer and colleagues[145] reported the storage of heralded single photons with a bandwidth of 2 MHz in a Pr^{3+} doped Y_2SiO_5 crystal with non-degenerated cavity-enhanced SPDC. The experiment presented by Piro et al.[275] also showed an atom-resonant source of entangled photons. But, since their photon-pair source is not cavity-enhanced, the coincidence rate is much lower than in the case of the aforementioned cavity-enhanced sources.

2.3.5 | Temperature Tuning

A cavity-enhanced photon-pair source can be tuned by changing the crystals' orientation and temperature,[216] utilizing the electro-optic effect by applying a voltage across the nonlinear crystal,[276] or by applying strain to the crystal.[152,217] Changing the temperature does not only change the refractive index of the crystal, it also affects the crystal by thermal expansion. Applying a voltage also induces the piezo-electric effect.[188]

Fig. 2.23 simulates the tuning behaviour of the signal-photon spectral density upon a temperature change of the nonlinear crystal. For a cavity which is not in resonance with the pump beam, the position of the centers of the clusters relative to the center of the parametric gain envelope can arbitrarily be chosen by temperature tuning of the nonlinear crystal. This is no longer possible for a cavity which is in resonance with the pump field. For such a pump-resonant cavity, the clusters are shifted at the same rate as the gain envelope. Temperature tuning affects only the mode structure within a cluster.

In the following, we analyze the temperature tuning characteristics theoretically and subsequently verify the findings by a spectrometer measurement. Additionally, we analyze the temperature dependence of the mode structure within the clusters and compare it to a measurement performed with the cascaded filtering system for different temperatures of the nonlinear crystal.

In this section, we cover only triply-resonant single-crystal cavities. The phenomena discussed here are relevant both in the case of temperature tuning as well as for rotations of the nonlinear crystals. The theory which describes the influence of crystal rotations on the spectral properties of the generated photons

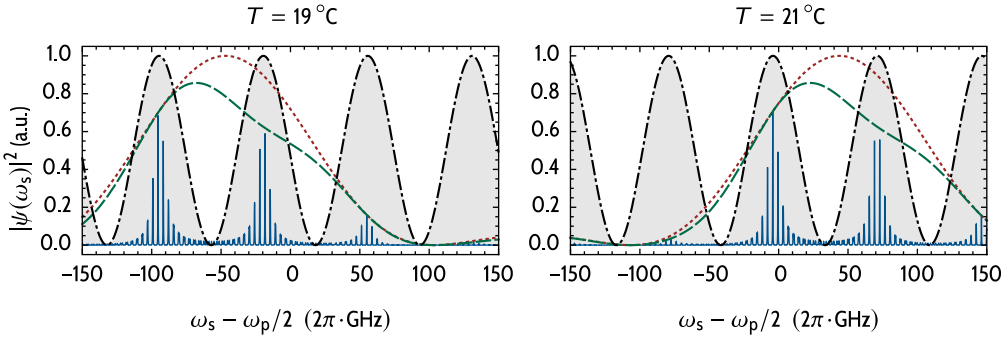

Figure 2.23 | Temperature tuning – single-crystal cavity. Simulation of the signal spectral density $|\psi(\omega_s)|^2$ (—) for two different temperatures of the nonlinear crystal for a single-crystal cavity. The single-pass parametric gain envelope (----) and the triply-resonant gain envelope (– –) have the same tuning speed as the cluster phase ϕ_{cluster}. Here, $\cos^2\left(\phi_{\text{cluster}}(\omega_s)/2\right)$ is plotted (–·–) to illustrate Eq. 2.3.15. The center of the clusters are located a frequencies where $\cos^2\left(\phi_{\text{cluster}}(\omega_s)/2\right) = 1$. While the location of the modes within a cluster can be finely tuned by changing the crystal's temperature, temperature changes do not affect the relative height and the position of the clusters within the gain envelope. In the simulation, the parameter $\bar{r}$ in Eq. 2.3.3 is set to $\bar{r} = 0.09$ to match the measured data. Fig. 2.24 shows a spectrometer measurement which confirms this simulation.

is closely related to the theory discussed in this section. However, for the sake of brevity, we do not discuss the effects of rotations of the crystal in detail.

Gain envelope. The phase mismatch Δk can be adjusted by changing the temperature T or the orientation of the nonlinear crystal with respect to the optical axis.[216] A change in Δk results in a shift of the center of the parametric gain envelope. The relative phase $\Delta\Phi$ (Eq. 2.3.4) does not depend on the temperature or orientation of the crystal (the change of $\Delta\phi^{\text{eff}}_{\text{Gouy}}$ is negligible). Therefore, the single-pass gain $\text{sinc}^2\left(\Delta kl/2\right)$ and the phase-balancing factor $P(\omega_s)$ share the same dependency on Δkl: Upon change of the temperature or the orientation of the nonlinear crystal, these two functions are shifted synchronously without changing the shape of the gain envelope (see Eq. 2.3.2). In the following, we will show that the position of the clusters relative to the center of the gain envelope also does not depend on the temperature or orientation of the nonlinear crystal.

Clusters as mode beating. As we will show in the following, for the signal spectral density (Eq. 2.3.1), the product of Airy functions:

$$\text{Airy}_s(\omega_s)\text{Airy}_i(\omega_p - \omega_s) \tag{2.3.10}$$

resembles a beat of two oscillations. For the signal and idler fields the cavity resonances can be found at frequencies where the round-trip phase is a multiple

of 2π:

$$\begin{aligned} \phi_{\mathrm{rt,s}}(\omega_\mathrm{s}) &\stackrel{!}{=} 2\pi q, \quad \text{with } q \in \mathbb{N} \\ \phi_{\mathrm{rt,i}}(\omega_\mathrm{p} - \omega_\mathrm{s}) &\stackrel{!}{=} 2\pi q', \quad \text{with } q' \in \mathbb{N}. \end{aligned} \tag{2.3.11}$$

For a single-crystal cavity, the round-trip phase (Eq. 1.2.22) is:

$$\phi_{\mathrm{rt},n}(\omega_n) = 2k_n l + \delta_{1,n} + \delta_{2,n} - 2\Phi_{\mathrm{Gouy},n} + 2\,\omega_n/c\,[L - l], \tag{2.3.12}$$

where k_n is the k-vector inside the nonlinear crystal, δ_i are the mirror phase shifts, Φ_{Gouy} is the total Gouy phase shift and L is the distance between the two mirrors.

The analogy to a beat of two oscillations becomes apparent if Eq. 2.3.11 is written as:

$$\begin{aligned} \cos^2\left(\phi_{\mathrm{rt,s}}(\omega_\mathrm{s})/2\right) &\stackrel{!}{=} 1 \\ \cos^2\Big(\phi_{\mathrm{rt,i}}(\omega_\mathrm{p} - \omega_\mathrm{s})/2\Big) &\stackrel{!}{=} 1. \end{aligned} \tag{2.3.13}$$

Instead of Eq. 2.3.10, we analyze the product:

$$\cos^2\left(\phi_{\mathrm{rt,s}}(\omega_\mathrm{s})/2\right)\cos^2\Big(\phi_{\mathrm{rt,i}}(\omega_\mathrm{p} - \omega_\mathrm{s})/2\Big). \tag{2.3.14}$$

The centers of the clusters are at the anti nodes of the beat of these two $\cos^2$-functions.

Cluster phase. The positions of the centers of the clusters are at frequencies for which:

$$\cos^2\left(\phi_{\mathrm{cluster}}(\omega_\mathrm{s})/2\right) \stackrel{!}{=} 1, \tag{2.3.15}$$

where we define the *cluster phase* $\phi_{\mathrm{cluster}}(\omega_\mathrm{s})$ as:

$$\phi_{\mathrm{cluster}} = \phi_{\mathrm{rt,s}}(\omega_\mathrm{s}) + \phi_{\mathrm{rt,i}}(\omega_\mathrm{p} - \omega_\mathrm{s}). \tag{2.3.16}$$

Eq. 2.3.15 is illustrated in Fig. 2.23.

If the cavity is locked to a pump resonance, the pump round-trip phase is also a multiple of 2π: $\phi_{\mathrm{rt,p}} = 2q''\pi$, with $q'' \in \mathbb{N}$. Therefore, without changing the condition stated in Eq. 2.3.15, the cluster phase can also be written as:

$$\phi_{\mathrm{cluster}} = \phi_{\mathrm{rt,p}}(\omega_\mathrm{p}) - \phi_{\mathrm{rt,s}}(\omega_\mathrm{s}) - \phi_{\mathrm{rt,i}}(\omega_\mathrm{p} - \omega_\mathrm{s}). \tag{2.3.17}$$

Temperature dependence. Thus, the centers of the clusters of a pump-resonant single-crystal cavity can be found at frequencies for which:

$$\cos^2\left(\Delta kl + \Delta\delta_1/2 + \Delta\delta_2/2 - \Delta\Phi_{\text{Gouy}}\right) \stackrel{!}{=} 1. \tag{2.3.18}$$

The temperature dependence of the relative Gouy phase $\Delta\Phi_{\text{Gouy}}$ is negligible compared to Δkl. Additionally, the phase shifts δ_1 and δ_2 do not depend on the crystal temperature. Therefore, from this equation, it is obvious that the center of the clusters in shifted with the same rate as the parametric gain envelope (Eq. 2.3.2) upon temperature tuning of the nonlinear crystal.

Gouy phase and cavity length. Note, that Eq. 2.3.18 does not directly depend on the total distance L of the two mirrors due to energy conservation ($[\omega_\text{p} - \omega_s - \omega_\text{i}]L = 0$). Therefore, the relative Gouy phase $\Delta\Phi_{\text{Gouy}}$ is the only term in Eq. 2.3.18 which depends on L, as will be discussed in section 2.3.6. Thus, the only degree of freedom which can be utilized to shift the centers of the clusters with respect to the center of the phase-matching envelope is the distance of the mirrors.

Low-resolution measurement. In Fig. 2.24, the signal an idler spectrum measured with a grating spectrometer is shown for different temperatures of the down-conversion crystal. As expected, the cluster structure is not affected by temperature tuning: With this measurement, we verify the simulation shown in Fig. 2.23.

High-resolution spectrum with temperature tuning. Since we cannot resolve the mode structure within the cluster with the grating spectrometer (Fig. 2.24), we repeat the high-resolution measurement shown in figure Fig. 2.20 for different crystal temperatures. The results are shown in Fig. 2.25.

In contrast to the previous measurement (Fig. 2.15), we operate the down-conversion source close to perfect degeneracy. The simulation of Eq. 2.3.8 (Fig. 2.25b) shows that in order to keep the amplitude of the central mode within 90 % of its maximum value, the temperature of the nonlinear crystal must be stabilized with an accuracy of better than 50 mK. The measurement presented in Fig. 2.18 confirms that this level of stability could be attained over many hours.

2.3.6 | Cavity-length tuning

For the single-crystal cavity used in the experiments discussed in this thesis, there is only one degree of freedom which allows to modify the cluster structure (i.e. the relative height of the clusters) within the parametric gain envelope:

Changing the distance of the two mirrors results in a modified relative round-trip Gouy phase $\Delta\Phi_{\text{Gouy}}$ and therefore a change in the relative phase $\Delta\Phi$ in Eq. 2.3.2. To study this effect, we vary the distance d between the concave mirror and the nonlinear crystal. For each value of d we record the signal spectral density with a grating spectrometer. The measurement results are presented in Fig. 2.26.

Gouy phase shift. For the cavity used in the experiments with a mirror radius of curvature of 50 mm, the confocal parameter is nearly identical for all three fields (see Fig. 1.9c). Therefore, the relative Gouy phase $\Delta\Phi_{\text{Gouy}}$ in Eq. 2.3.18 can be approximated by the signal round-trip Gouy phase $\Phi_{\text{Gouy,s}}$:

$$\Delta\Phi_{\text{Gouy}} = \Phi_{\text{Gouy,p}} - \Phi_{\text{Gouy,s}} - \Phi_{\text{Gouy,i}} \approx -\Phi_{\text{Gouy,s}}. \tag{2.3.19}$$

The same is true for the effective relative Gouy phase in Eq. 2.3.4:

$$\Delta\phi^{\text{eff}}_{\text{Gouy}} \approx -\phi^{\text{eff}}_{\text{Gouy,s}}. \tag{2.3.20}$$

In the experiment, the distance d between the concave mirror and the crystal is varied between 0.5 mm and 18.0 mm (see Fig. 2.26a). Using Eqs. 1.2.25 and 1.2.41, the effective relative Gouy phase should vary almost linearly between $\Delta\phi^{\text{eff}}_{\text{Gouy}} = 0.15$ rad and $\Delta\phi^{\text{eff}}_{\text{Gouy}} = 0.45$ rad. Thus, a linear increase of the relative phase $\Delta\Phi$ in Eq. 2.3.4 of about 0.6 rad is expected.

Measurement. However, in the experiment, we observe a much stronger dependence of the relative phase $\Delta\Phi$ on the mirror distance d (see Figs. 2.26b and 2.27c). This strong deviation from the theoretical expectation might be caused, in part, by imperfect alignment of the cavity.

Whenever we vary the mirror distance, the cavity has to be realigned. Especially for short cavities, the three fields are not properly collinearly aligned. Therefore, photon pairs generated in the forward direction are not exactly superimposed with the photon pairs generated in the backward direction. But, the theory developed for a triply resonant cavity in section 1.1.4 does not account for a misalignment of the three beams. Heuristically, one can assume that small misalignments result in a reduced value of the parameter $\bar{r}$ in Eq. 2.3.3. Further studies are required to analyze to what extent a misalignment also affects the relative phase $\Delta\Phi$ and the positions of the clusters relative to the center of the gain envelope.

Fit. We use a simplified model of Eq. 2.3.6 to fit the data. Since the mode structure within the clusters cannot be resolved with the grating spectrometer, the clusters (convoluted with the spectrometer's IRF) are approximated by

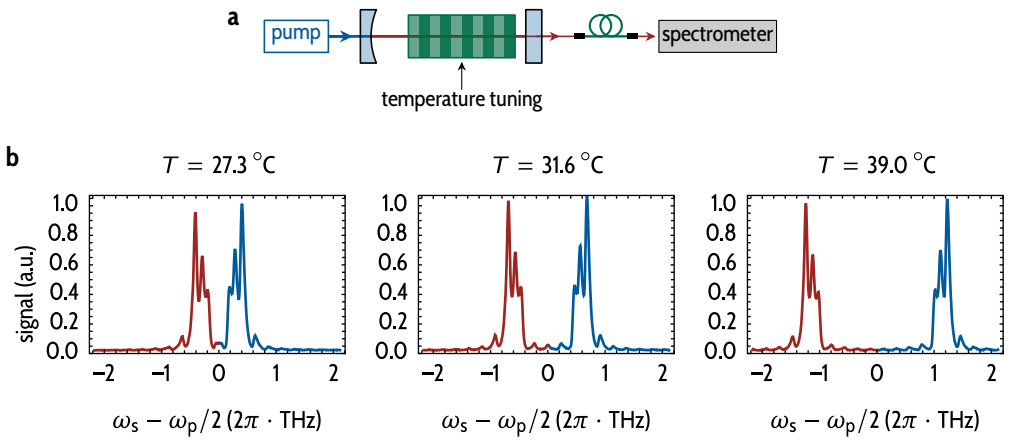

Figure 2.24 | Temperature tuning of a single-crystal photon-pair source. **a**, The spectrum of signal and idler photons is recorded with a grating spectrometer for different temperatures of the down-conversion crystal. To distinguish the signal and idler signals, the down-conversion source is operated far from degeneracy. **b**, Within the down-conversion gain envelope, three clusters of the signal (—) and idler (—) spectrum can be identified. As simulated in Fig. 2.23, the relative height of the clusters within the parametric gain envelope is independent of the temperature of the nonlinear crystal. With the spectrometer, the position of the modes within the clusters cannot be resolved.

equally-spaced Gaussian peaks of width $\Delta\omega_{\text{peak}}$. A fit function with amplitude a of the form:

$$\begin{aligned}\left|\psi(\omega_s)\right|^2 = a\,\text{sinc}^2\left(\Delta k(\omega_s)l/2 - \phi_0\right) \\ \times\left[1 + \bar{r}^2 + 2\bar{r}\cos\left(\Delta k(\omega_s)l - 2\phi_0 - \Delta\Phi\right)\right] \\ \times\sum_{n=-\infty}^{\infty}\exp\left(\frac{\left[\omega_s - \omega_0 - n\Delta\omega_{\text{cluster}}\right]^2}{\Delta\omega_{\text{peak}}^2}\right)\end{aligned} \tag{2.3.21}$$

is used. Here, ϕ_0 accounts for small deviations of the center of the gain envelope from degeneracy caused by temperature fluctuations or small tilts of the nonlinear crystals during each realignment procedure. The position of the cluster relative to the center of the gain envelope is specified via the parameter ω_0. The parameter $\bar{r}$ is used as a fitting parameter. The width of the gain profile given by Δkl and the cluster spacing $\Delta\omega_{\text{cluster}}$ are taken as constants over all fits.

Discussion. In the fit, the relative phase $\Delta\Phi$ and the position of the cluster defined by ω_0 were chosen independently. From Eqs. 2.3.3 and 2.3.18 a strong correlation would be expected between these two quantities since $\Delta\Phi_{\text{Gouy}}$ and

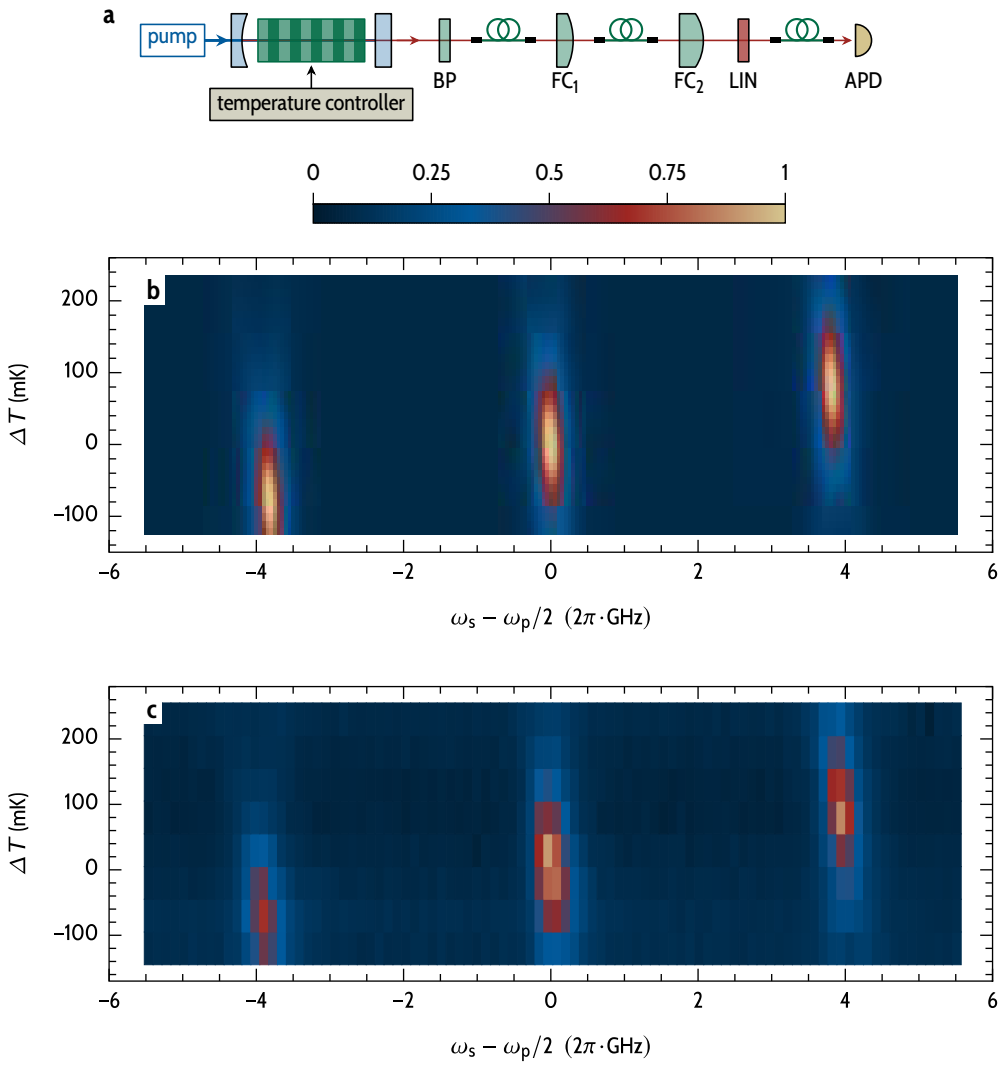

Figure 2.25 | Temperature tuning to achieve perfect indistinguishability. **a**, High-resolution spectroscopy of the mode structure within a cluster as a function of the crystal temperature. The same experimental setup, utilizing the monolithic filter cavities as in Fig. 2.20, is used. **b**, Simulated tuning behaviour of the signal spectral density given by Eq. 2.3.8 as a function of the crystal temperature. We use the temperature-dependent KTP Sellmeier equations published by Emanueli and Arie[272] to predict the temperature-tuning rates. **c**, Measurement results: We scan the filter cavities over the central part of the signal spectrum for 8 different temperatures of the nonlinear crystal. The data is in good agreement with the simulation shown above. In order to stabilize the amplitude of the degenerate mode within 90 % of its maximum value, the nonlinear crystal must be temperature-stabilized with an accuracy better than 50 mK.

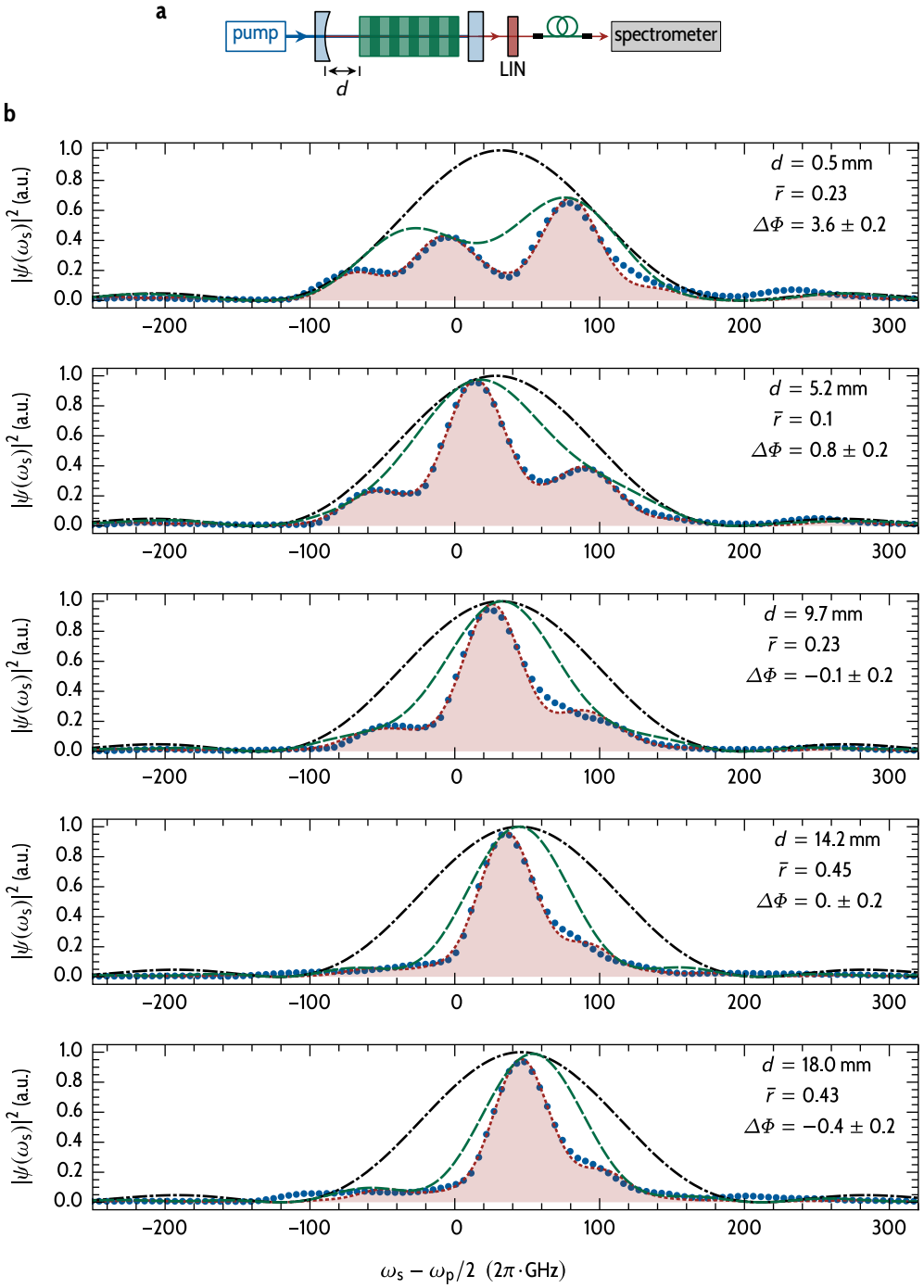

Figure 2.26 | Spectral changes upon cavity-length tuning. **a**, The spectrum of the signal photons is measured with a grating spectrometer (resolution ∼50 GHz) for different values of the distance d between concave mirror a nonlinear crystal. The idler photons are blocked with a linear polarizer (LIN). **b**, The measurement (•) is in good agreement with the simplified model (----) given by Eq. 2.3.21. As a guide to the eye, the plot also shows the single-pass gain envelope (– –) and the triply-resonant gain envelope (–·–).

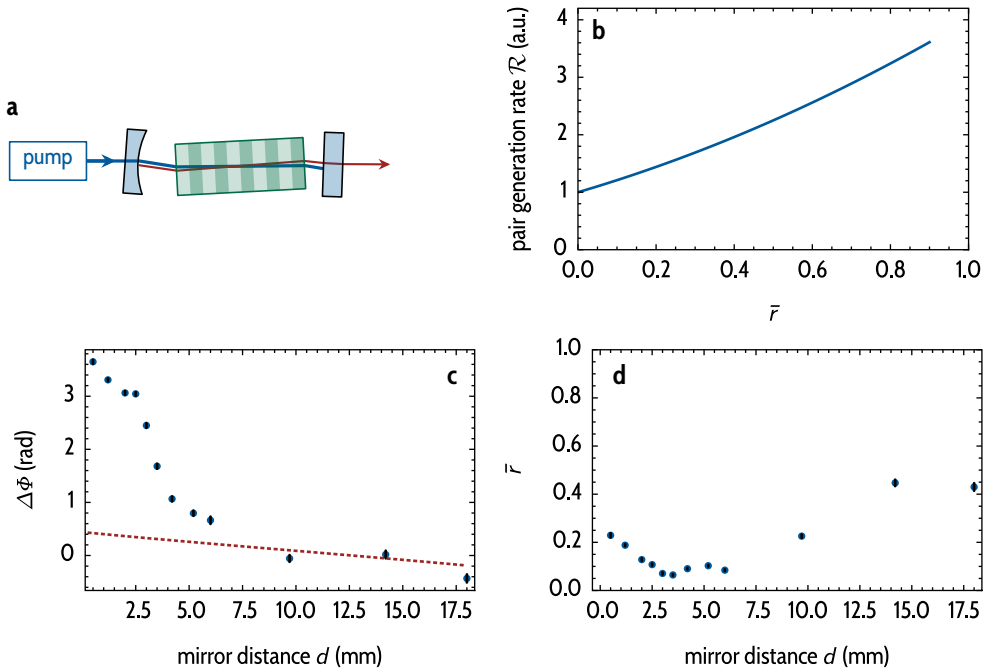

Figure 2.27 | Cavity-length tuning. **a**, Exaggerated depiction of a misaligned cavity where the three fields are superimposed only partially. Here, photon pairs generated in the forward direction interfere only partially with photon pairs generated in the backward direction. Imperfect alignment results in a reduced value of the parameter $\bar{r}$. **b**, The photon-pair generation rate $\mathcal{R}$ (——) of a triply-resonant cavity is proportional to $[1 + \bar{r}]^2$. A well-aligned cavity with $\bar{r} \approx 0.9$ is brighter by a factor of more than 3 compared to an improperly aligned cavity. **c**, Fit values (●) of the relative phase $\Delta\Phi$ in Eq. 2.3.21. Selected measurements are presented in Fig. 2.26. A strong deviation from the expected trend given by Eq. 2.3.4 (----) is observed. **d**, These deviations might, in part, be attributed to an imperfect alignment of the three fields inside the cavity. The fit shows relatively small values for the parameter $\bar{r}$, especially for small distances d between the concave mirror and the nonlinear crystal.

$\Delta\phi^{\text{eff}}_{\text{Gouy}}$ share the same dependence on the mirror distance d. Due to the alignment problems, we do not observe these correlations.

The photon-pair generation rate $\mathcal{R}$ also depends on the alignment of the three fields. Eqs. 1.3.43 and 2.3.3 show that the pair-generation rate scales as $\mathcal{R} \propto [1 + \bar{r}]^2$ (see Fig. 2.27b).

2.4 | Signal-idler correlation function

The joint spectral amplitude of the two-photon state expresses the strong spectral correlation of signal and idler photons generated by SPDC. But, the two photons of a pair are also correlated in time. This temporal correlation is experimentally accessible by measuring the *second-order signal-idler correlation function*.

Theoretically, this correlation function is (via the phase-matching function) closely linked to the joint spectral amplitude. We show that for monochromatic pumping the second-order signal-idler correlation function is modulus squared of the Fourier transform of the phase-matching function introduced in Eq. 1.1.29.

In section 2.4.1, we derive a phase-matching function for photons generated by cavity-enhanced SPDC. With this expression we can discuss and explain the comb-like structure of the signal-idler correlation function and compare our results to theoretical expressions found in the literature.

In section 2.4.2, we discuss the measurement principle, especially how spectral filtering and the timing resolution of the measurement setup affect the measured correlation function. Using these results, we compare the measured correlation function for a cavity-enhanced photon-pair source with compensation crystal with the theoretical predictions (section 2.4.3).

To the best of the author's knowledge, the effect of the pump resonance on the correlation function has not been studied in the literature. In section 2.4.4, we therefore theoretically evaluate the impact of the relative phase $\Delta\Phi$ and the effective reflectivity $\bar{r}$ on the correlation function. Unfortunately, the timing jitter of state-of-the-art single-photon detectors is to large to resolve this impact.

The structure of the signal-idler correlation function for a single-crystal cavity-enhanced photon-pair source is more complicated as in the case of a cavity with compensation crystal. Sections 2.4.5 and 2.4.6 discuss the temporal structure of the two-photon wave packet and compare a measurement with theoretical predictions. As in the case of the cavity with compensation crystal, we find excellent agreement between measurement and theory.

Cavity-enhanced photon-pair sources usually are spectrally multi-mode. But, many experiments require a single-mode operation. By narrow-band spectral filtering, we can eliminate unwanted spectral modes to achieve single-mode operation. In section 2.4.7, we evaluate the impact of (moderate) narrow-band filtering on the signal-idler correlation function both theoretically as well as experimentally. We find that a single low-finesse cavity is not sufficient to operate our single-crystal photon-pair source in the single-mode regime. Finally, we show that a cascaded filtering system is most efficient to reach this regime even with low-finesse cavities.

Second-order signal-idler correlation function. The second-order signal-idler correlation function $G^{(2)}_{\mathrm{s/i}}(\tau)$ for a two-photon state $\left|\psi\right\rangle$ is given by the following expectation value:[119,206]

$$G^{(2)}_{\mathrm{s/i}}(\tau) = \left\langle \psi \middle| \widehat{E}^{(-)}_{\mathrm{i}}(z,t)\widehat{E}^{(-)}_{\mathrm{s}}(z,t+\tau)\widehat{E}^{(+)}_{\mathrm{s}}(z,t+\tau)\widehat{E}^{(+)}_{\mathrm{i}}(z,t) \middle| \psi \right\rangle, \tag{2.4.1}$$

where the electric field operators are defined by Eq. 1.1.13:

$$\widehat{E}^{(+)}_{\mathrm{s/i}}(z,t) \propto \int_{-\infty}^{\infty} \mathrm{d}\omega\, \hat{a}_{\mathrm{s/i}}(\omega) e^{-i[\omega t - kz]}. \tag{2.4.2}$$

In contrast to Eq. 1.1.13, we extend the lower limit of the integral in Eq. 2.4.2 to $-\infty$. This approximation is valid since the bandwidth of the generated photons is much smaller than the central frequency.[206]

In the remainder of this section, the vacuum contribution (see Eq. 1.1.28) of the two-photon state is discarded, as it does not contribute to the correlation function. Therefore, the two-photon state is:

$$\left|\psi\right\rangle = \int_{-\infty}^{\infty} \mathrm{d}\omega_{\mathrm{s}} \int_{-\infty}^{\infty} \mathrm{d}\omega_{\mathrm{i}}\, \psi(\omega_{\mathrm{s}},\omega_{\mathrm{i}}) \hat{a}^{\dagger}_{\mathrm{s}}(\omega_{\mathrm{s}}) \hat{a}^{\dagger}_{\mathrm{i}}(\omega_{\mathrm{i}}) \left|0,0\right\rangle. \tag{2.4.3}$$

Signal-idler correlation function for a monochromatic pump. In principle, we can compute the signal-idler correlation function for any state $\left|\psi\right\rangle$ numerically by plugging Eqs. 2.4.2 and 2.4.3 into Eq. 2.4.1. But, for a monochromatic pump, the integrals in Eq. 2.4.1 can be simplified significantly, as we will show in the following.

For a monochromatic pump, we can write the joint spectral amplitude in Eq. 2.4.3 in terms of the phase-matching function $f(\omega_{\mathrm{s}},\omega_{\mathrm{i}})$ and a delta distribution (see Eq. 1.1.29):

$$\psi(\omega_{\mathrm{s}},\omega_{\mathrm{i}}) = s(\omega_{\mathrm{s}}+\omega_{\mathrm{i}}) f(\omega_{\mathrm{s}},\omega_{\mathrm{i}}) = \delta(\omega_{\mathrm{p}}-\omega_{\mathrm{s}}-\omega_{\mathrm{i}}) f(\omega_{\mathrm{s}},\omega_{\mathrm{i}}). \tag{2.4.4}$$

As pointed out by Herzog and colleagues,[206] Eq. 2.4.1 can be simplified to:

$$G^{(2)}_{\mathrm{s/i}}(\tau) = \left\| \widehat{E}^{(+)}_{\mathrm{s}}(z, t+\tau)\widehat{E}^{(+)}_{\mathrm{i}}(z,t)\left|\psi\right\rangle \right\|^2 . \tag{2.4.5}$$

With Eqs. 2.4.2 to 2.4.4, we obtain:

$$\begin{aligned} G^{(2)}_{\mathrm{s/i}}(\tau) \propto \Bigg\| \int_{-\infty}^{\infty} \mathrm{d}\omega_{\mathrm{s}} \int_{-\infty}^{\infty} \mathrm{d}\omega_{\mathrm{i}} \int_{-\infty}^{\infty} \mathrm{d}\omega'_{\mathrm{s}} \int_{-\infty}^{\infty} \mathrm{d}\omega'_{\mathrm{i}} \\ \times \exp\left(-i\left[\omega_{\mathrm{s}}\left[t+\tau\right] + \omega_{\mathrm{i}} t - \left[\omega'_{\mathrm{s}}/c + \omega'_{\mathrm{i}}/c\right] z\right]\right) \\ \times \delta(\omega_{\mathrm{p}} - \omega'_{\mathrm{s}} - \omega'_{\mathrm{i}}) f(\omega'_{\mathrm{s}}, \omega'_{\mathrm{i}}) \\ \times \hat{a}_{\mathrm{s}}(\omega_{\mathrm{s}})\hat{a}_{\mathrm{i}}(\omega_{\mathrm{i}})\hat{a}^{\dagger}_{\mathrm{s}}(\omega'_{\mathrm{s}})\hat{a}^{\dagger}_{\mathrm{i}}(\omega'_{\mathrm{i}})\left|0,0\right\rangle \Bigg\|^2 . \end{aligned} \tag{2.4.6}$$

Now, the commutator relations for the creation and annihilation operators can be utilize to simplify Eq. 2.4.5:

$$\left[\hat{a}_{\mathrm{s/i}}(\omega_{\mathrm{s/i}}), \hat{a}^{\dagger}_{\mathrm{s/i}}(\omega'_{\mathrm{s/i}})\right] = \delta(\omega_{\mathrm{s/i}} - \omega'_{\mathrm{s/i}}), \tag{2.4.7}$$

from which follows:[206]

$$\hat{a}(\omega_{\mathrm{s/i}})\hat{a}^{\dagger}_{\mathrm{s/i}}(\omega'_{\mathrm{s/i}})\left|0\right\rangle = \delta(\omega_{\mathrm{s/i}} - \omega'_{\mathrm{s/i}})\left|0\right\rangle . \tag{2.4.8}$$

Using these relations, we find a simple expression for the second-order signal-idler correlation function:

$$G^{(2)}_{\mathrm{s/i}}(\tau) = \left\| \int_{-\infty}^{\infty} \mathrm{d}\omega_{\mathrm{s}}\, f(\omega_{\mathrm{s}}, \omega_{\mathrm{p}} - \omega_{\mathrm{s}}) e^{-i\omega_{\mathrm{s}}\tau} \right\|^2 . \tag{2.4.9}$$

In the case of monochromatic pumping, the signal-idler correlation function is the modulus squared of the Fourier transform of the phase-matching function. For pulsed pumping, the integrals appearing in Eq. 2.4.6 cannot be straightforwardly simplified and need to be evaluated numerically, in general.

Discussion. Eq. 2.4.9 is the central theoretical expression of this section. Although it is a concise and very useful expression, it is not widely used in the literature. An exception is the article by Lu, Campbell and Ou,[119] in which they derived the corresponding relation for non-resonant type-I SPDC. Kuklewicz[122]

also uses Eq. 2.4.9, but does not provide any derivation or a detailed discussion thereof.

In contrast to other expressions[121,162,206,277] reported for $G^{(2)}_{s/i}(\tau)$, Eq. 2.4.9 can easily be used to simulate the signal/idler correlation function for cavities with unequal free spectral ranges of the signal and idler fields (see section 2.4.6). In principle, the expression found by Scholz and colleagues[161] is also valid for unequal free spectral ranges. But, as discussed in the following section, their expression is computationally expensive and converges only slowly. In contrast to this, Eq. 2.4.9 can be efficiently computed, e.g., by fast Fourier transformation.[278,279]

Another advantage over expressions previously used in the literature is that Eq. 2.4.9 can also be used to analyze the signal-idler correlation function for double-pass pumping or pump-resonant configurations. As it turns out, the impact of double-pass pumping on the correlation function can typically not be resolved in an experiment (see section 2.4.4).

2.4.1 | Signal-idler correlation function of a cavity-enhanced photon-pair source

To compare Eq. 2.4.9 with the experimental results discussed in this section, we need to provide an expression for the phase-matching function $f(\omega_s, \omega_p - \omega_s)$. According to Eq. 1.1.72, the joint spectral amplitude for a triply-resonant cavity pumped by a monochromatic pump is proportional to:

$$\psi(\omega_s, \omega_p - \omega_s) \propto \psi_{sp}(\omega_s, \omega_p - \omega_s) p(\omega_s) \mathcal{T}_p(\omega_p) \mathcal{T}_s(\omega_s) \mathcal{T}_i(\omega_p - \omega_s). \quad (2.4.10)$$

where the phase-balancing factor (Eq. 1.2.38) is given by:

$$p(\omega_s) = 1 + \bar{r} e^{i[\Delta k(\omega_s) l + \Delta\Phi]}. \quad (2.4.11)$$

The single-pass joint spectral amplitude for a monochromatic pump can be approximated by (see Eq. 1.1.30):

$$\psi_{sp}(\omega_s, \omega_p - \omega_s) \propto \operatorname{sinc}\big(\Delta k(\omega_s) l/2\big) e^{i\Delta k(\omega_s) l/2} \delta(\omega_p - \omega_s - \omega_i). \quad (2.4.12)$$

This approximation is valid for all experiments discussed in this section, since the focussing parameter is small ($\xi \approx 0.2$, see section 1.2.1). Using Eq. 2.4.4, the phase-matching function for a pump-resonant cavity-enhanced photon-pair source with $\mathcal{T}_p(\omega_p) = 1$ is:

$$f(\omega_s, \omega_p - \omega_s) = \operatorname{sinc}\big(\Delta k(\omega_s) l/2\big) e^{i\Delta k(\omega_s) l/2} p(\omega_s) \mathcal{T}_s(\omega_s) \mathcal{T}_i(\omega_p - \omega_s). \quad (2.4.13)$$

Closed-form solution. For a cavity with a single-pass pump, (i.e. $\bar{r} = 0$), a closed-form solution of Eq. 2.4.9 has been found[161,206] and experimentally verified:[53,133,143]

$$G^{(2)}_{\mathrm{s/i,\,sp}}(\tau) \propto \left| \sum_{m_\mathrm{s},m_\mathrm{i}=-\infty}^{\infty} \frac{1}{\tilde{\Gamma}_\mathrm{s} + \tilde{\Gamma}_\mathrm{i}} \begin{cases} e^{-\tilde{\Gamma}_\mathrm{s}\left[\tau-\frac{\tau_0}{2}\right]} \operatorname{sinc}\left(i\frac{\tau_0}{2}\tilde{\Gamma}_\mathrm{s}\right), & \tau \geq \frac{\tau_0}{2} \\ e^{\tilde{\Gamma}_\mathrm{i}\left[\tau-\frac{\tau_0}{2}\right]} \operatorname{sinc}\left(i\frac{\tau_0}{2}\tilde{\Gamma}_\mathrm{i}\right), & \tau < \frac{\tau_0}{2} \end{cases} \right|^2, \tag{2.4.14}$$

with

$$\tilde{\Gamma}_\mathrm{s/i} = \frac{\Gamma_\mathrm{s/i}}{2} + i m_\mathrm{s/i}\, 2\pi \mathrm{FSR}_\mathrm{s/i}. \tag{2.4.15}$$

The constant τ_0 in Eq. 2.4.14 is given by

$$\tau_0 = \frac{l\Delta n}{c}, \tag{2.4.16}$$

where

$$\Delta n = n_\mathrm{s} + \omega_\mathrm{s} \left.\frac{\partial n_\mathrm{s}}{\partial \omega}\right|_{\omega=\omega_\mathrm{s}} - n_\mathrm{i} - \omega_\mathrm{i} \left.\frac{\partial n_\mathrm{i}}{\partial \omega}\right|_{\omega=\omega_\mathrm{i}}. \tag{2.4.17}$$

The constant τ_0 represents the propagation delay between signal and idler photons inside the nonlinear crystal. For a 2 cm long PPKTP crystal pumped at 447 nm, τ_0 is on the order of 6.6 ps.

Two-crystal cavity. For a cavity with a compensation crystal and equal free spectral ranges $\mathrm{FSR_s} = \mathrm{FSR_i}$, the limit $m_\mathrm{s/i} \to \pm\infty$ can be evaluated, and the sum in Eq. 2.4.14 converges to:[206]

$$G^{(2)}_{\mathrm{s/i,\,sp}}(\tau) \propto \begin{cases} \sum_{m_\mathrm{s}=1}^{\infty} e^{-\Gamma_\mathrm{s}\left[\frac{m_\mathrm{s}}{\mathrm{FSR_s}}-\frac{\tau_0}{2}\right]} \operatorname{rect}\left(\left[\tau - \frac{m_\mathrm{s}}{\mathrm{FSR_s}} - \frac{\tau_0}{2}\right]\frac{1}{\tau_0}\right), & \tau \geq \frac{\tau_0}{2} \\ \sum_{m_\mathrm{i}=0}^{\infty} e^{-\Gamma_\mathrm{i}\left[\frac{m_\mathrm{i}}{\mathrm{FSR_i}}-\frac{\tau_0}{2}\right]} \operatorname{rect}\left(\left[\tau + \frac{m_\mathrm{i}}{\mathrm{FSR_i}} - \frac{\tau_0}{2}\right]\frac{1}{\tau_0}\right), & \tau < \frac{\tau_0}{2} \end{cases} \tag{2.4.18}$$

where the rectangular function is defined by:

$$\operatorname{rect}(\tau) = 1, \quad \text{for } |\tau| \leq 1/2 \text{ and 0 elsewhere.} \tag{2.4.19}$$

The signal-idler correlation function for a two-crystal cavity therefore is a series of rectangular peaks separated by the cavity round-trip time $\Delta t_\mathrm{rt} = 1/\mathrm{FSR}$ of the generated photons. The amplitude of the peaks decreases exponentially for $|\tau| > 0$. The decay constant is the cavity decay rate $\Gamma_\mathrm{s/i}$.

Structure of the signal-idler correlation function. The comb-like temporal structure of the second-order correlation function is depicted in Fig. 2.28 and can than be understood as follows: Detection of either photon from a pair projects the other photon from the pair to a wave packet bouncing back and forth inside the cavity. The second photon can then only be detected with a delay of integer multiples of the cavity's round-trip time t_{rt}. The probability to detect the second photon after a certain delay τ scales exponentially with the cavity decay rate.

Gibbs-Wilbraham phenomenon. Fig. 2.29 compares the central peak of Fig. 2.28 simulated with Eq. 2.4.14 and Eq. 2.4.18. Here, Eq. 2.4.14 is simulated with a large number of terms in the sums. Nevertheless, strong oscillations at the plateau of the correlation function can be observed. These oscillations are closely related to the Gibbs-Wilbraham phenomenon[280] which can be observed for truncated Fourier series. As discussed earlier, the signal-idler correlation function is related to the Fourier transformation of the phase-matching function. Therefore, it is not surprising to observe oscillations for the truncated sums simulated in Fig. 2.29.

2.4.2 | Measurement of the signal-idler correlation function

The signal-idler correlation function $G^{(2)}_{\mathrm{s/i}}(\tau)$ can be probed with time-correlated single-photon counting (TCSPC). Signal and idler photons are split up on a polarizing beam splitter and detected by single-photon counters (see Fig. 2.30a). The TCSPC electronics measures time stamps for the arrival times of photons at each detector. The histogram of the temporal delays between the signal time stamps and the idler time stamps is proportional to the second order signal-idler correlation function.

For low count rates and a small fraction of multi-pair events, a start-stop histogram is sufficient. In this case, a click on the signal detector is the start event and a click on the idler detector is the stop event. Only the delays between start and stop events are recorded in the histogram. Of course, the delay can also have a negative sign if the idler photon is detected before the signal photon. For all measurements discussed in this thesis, start-stop histograms where sufficient to measure the correlation functions.

Spectral filtering. Experiments analyzing photon-pair sources based on spontaneous parametric down-conversion typically deploy some form of spectral filtering of signal and idler photons. This spectral filtering might be necessary e.g. to obtain heralded photons in a pure quantum state (see section 1.4) or to suppress spurious background fluorescence (see section 2.2.1). If no direct

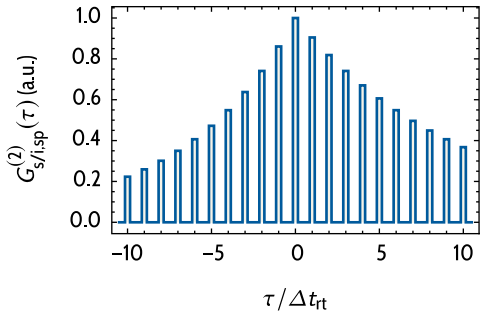

Figure 2.28 | Signal-idler correlation function for a two-crystal cavity with single-pass pump. For a cavity with equal signal/idler free spectral ranges, the second-order signal-idler correlation function is a series of square peaks with a spacing corresponding to the cavity round-trip time Δt_{rt} of the photons (Eq. 2.4.18). The signal/idler cavity decay rates can differ, e.g., if the reflectivity of the mirror coating is polarization-dependent. This results in an asymmetric shape of the two exponential decays.

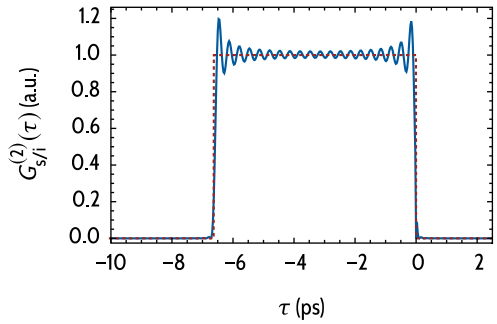

Figure 2.29 | Analytic solutions for the signal-idler correlation function. The central peak for the second-order signal-idler correlation function for a two-crystal cavity (with single-pass pump) according to Eq. 2.4.14 is plotted (——). Here, the sums over m_s and m_i were taken from -50 to 50. The oscillations observed here are closely related to the Gibbs-Wilbraham phenomenon[280] encountered for truncated Fourier series. The oscillations are less pronounced if the upper limits of the sums are increased. If the limits are extended to infinity, Eq. 2.4.14 converges to the simplified model given by Eq. 2.4.18 (----).

spectral filtering is present, the single-photon detectors also act as a spectral bandpass filter due to their finite spectral acceptance bandwidth. Spectral filtering modifies the joint-spectral amplitude of the pair-photon state and therefore the measured correlation function as follows:

The joint spectral amplitude after spectral filtering is:[69,281]

$$\psi_{\text{filtered}}(\omega_s, \omega_i) = \psi(\omega_s, \omega_i)\sqrt{\mathfrak{F}_s(\omega_s)}\sqrt{\mathfrak{F}_i(\omega_i)}, \tag{2.4.20}$$

where $\mathfrak{F}_{s/i}(\omega_{s/i})$ is the spectral intensity transmission function of the filter at the signal/idler frequency $\omega_{s/i}$. For a monochromatic pump, the phase-matching function after filtering therefore is:

$$f_{\text{filtered}}(\omega_s, \omega_p - \omega_s) = f(\omega_s, \omega_p - \omega_s)\sqrt{\mathfrak{F}_s(\omega_s)}\sqrt{\mathfrak{F}_i(\omega_p - \omega_s)}, \tag{2.4.21}$$

with $f(\omega_s, \omega_p - \omega_s)$ given by Eq. 2.4.13.

As discussed earlier, the second-order correlation function and the phase-matching function are related to each other by Fourier transformation (see Eq. 2.4.9). Therefore, spectral bandpass filtering corresponds to temporal broadening of the correlation function. In Fig. 2.30, this broadening is simulated for single-pass pump SPDC.

Correlation measurements and the instrument response function. Due to the large bandwidth of the phase-matching function (typically ranging from ~100 GHz to multiple THz, see Fig. 2.30c), the signal-idler correlation function exhibits very narrow features in the time domain on the order of picoseconds or shorter (see Fig. 2.30b). These features can often not be resolved in experiments. The timing resolution of the measurements is limited by the width of the instrument response function of the TCSPC setup. Even with state-of-the-art superconducting single-photon detectors, the width of the IRF is on the order of ~100 ps.

The measured start-stop time-delay histograms are proportional to the second-order signal-idler correlation function convoluted with the IRF of the TCSPC setup. In all experiments discussed below, the following convolution has been used as fit function:

$$G^{(2)}_{s/i,\text{exp}}(\tau) = c + a\left[\text{IRF} * G^{(2)}_{s/i}\right](\tau). \tag{2.4.22}$$

Here, the constant c accounts for accidental coincidences caused by uncorrelated background photons or detector dark counts. The amplitude a is proportional to the measurement duration and inversely proportional to the width of the time bins of the histogram. In Eq. 2.4.22, we use Eq. 2.4.9 for $G^{(2)}_{s/i}(\tau)$ and Eq. 2.4.21 for the phase-matching function.

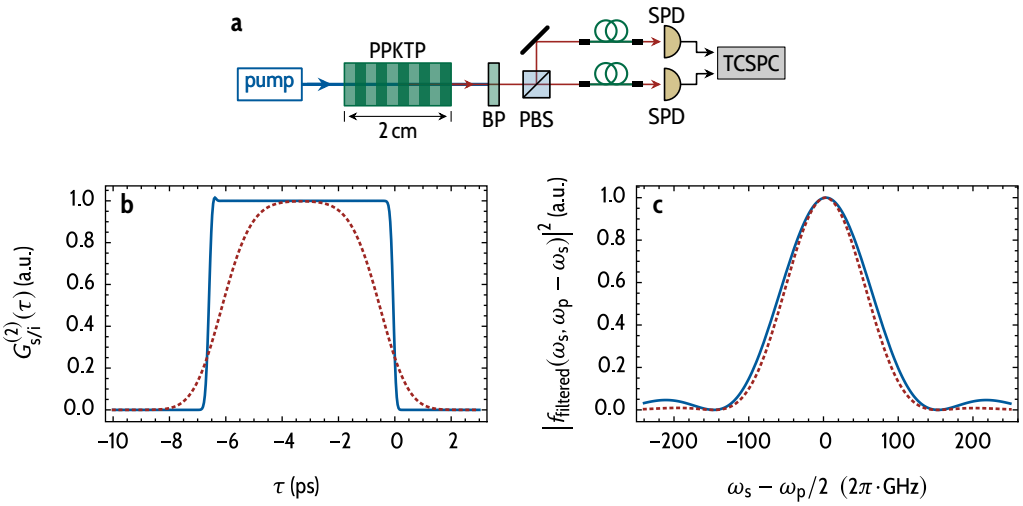

Figure 2.30 | Correlation function with spectral filtering. **a**, Measurement setup for a signal-idler correlation measurement: Signal and idler photons are split up at a polarizing beam splitter, collected into fibers and directed to single-photon detectors (SPD). The correlation function can be probed by recording a start-stop time-delay histogram by time-correlated single-photon counting (TCSPC). If the signal and idler photons are spectrally filtered with a bandpass (BP) filter, a temporal broadening of the correlation function can be observed. **b**, The correlation function is simulated for signal and idler photons generated in a 2 cm long PPKTP crystal without a cavity as shown in **a**. We simulate $G^{(2)}_{s/i}(\tau)$ utilizing Eq. 2.4.9 for a Gaussian bandpass filter with a bandwidth of 10 nm (——) and 1 nm (----). The corresponding modulus squared of the filtered phase-matching functions (Eq. 2.4.21) is shown in **c**. For a 2 cm long PPKTP crystal, the signal and idler photons have a spectral bandwidth of about 150 GHz. The corresponding correlation time (see Eq. 2.4.16) is $\tau_0 = 6.6$ ps.

To good approximation, the instrument response function can be expressed as a Gaussian distribution with a FWHM of $\Delta\tau_{\mathrm{IRF}}$:

$$\mathrm{IRF}(\tau) = \exp\left(-4\ln(2)\frac{\tau^2}{\Delta\tau_{\mathrm{IRF}}^2}\right). \tag{2.4.23}$$

For the experiments discussed in the following, the width of the IRF is mainly determined by the timing resolution of the single-photon detectors. The timing resolution of the TCSPC electronics (PicoHarp 300) is much smaller (~12 ps) than the timing jitter of the single-photon detectors and therefore does not contribute significantly to the width of the IRF.

2.4.3 | Signal-idler correlation function for two-crystal cavities

The signal-idler correlation function for a cavity-enhanced photon-pair source has been measured in various experiments.[53,121,126,128,277] Generally, a good agreement between theory and experiments is found. In contrast to earlier experiments, in this section the measured signal/idler spectral density (Fig. 2.21) can be used to verify the tight connection between spectral and temporal properties of the photons as expressed by Eq. 2.4.9.

In Fig. 2.31 we present the measurement of the second-order signal-idler correlation function for a two-crystal cavity. Due to the compensation crystal, the signal and idler free spectral ranges are nearly identical. Therefore, signal and idler photons also feature nearly identical cavity round-trip times.

Fit. For the fit of Eq. 2.4.22 to the measured correlation function, most of the parameters where taken from the fit to the two-crystal cavity spectrum (see Fig. 2.21). The values for the cavity length of 47.5(5) mm and the cavity finesse of $\mathcal{F}_{\mathrm{s/i}} = 15(1)$ taken from the fit to the spectrum are in excellent agreement with the measured signal/idler correlation function. The measured cavity round-trip time of 540(10) ps corresponds to a signal/idler free spectral range of $\mathrm{FSR}_{\mathrm{s/i}} = 1.840(30)$ GHz. The measurement therefore verifies the cavity decay rate of $\Gamma_{\mathrm{s/i}} = 2\pi \cdot \mathrm{FSR}_{\mathrm{s/i}}/\mathcal{F}_{\mathrm{s/i}} = 2\pi \cdot 122(2)$ MHz (see table 1.1).

Discussion. All in all, the measurement is in good agreement with the model given by Eq. 2.4.22. Note, that the only free parameters of the fit are the overall amplitude a, the constant offset c, and the width of the IRF $\Delta\omega_{\mathrm{IRF}}$. These three parameters are not determined by the properties of the photon-pair source, but are mainly given by the measurement duration and the properties of the measurement equipment. All other parameters, namely the length of the crystals

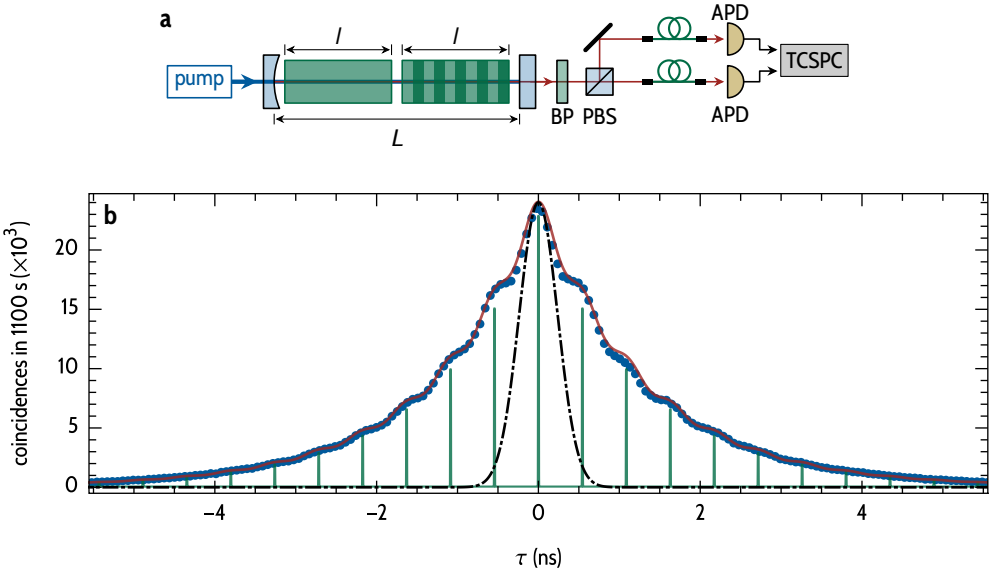

Figure 2.31 | Signal-idler correlation function – two-crystal cavity. **a**, The second-order signal-idler correlation function for the two-crystal cavity is measured with two APDs by time-correlated single-photon counting (TCSPC, PicoHarp 300). The signal and idler photons are split by a polarizing beam splitter and are collected into fibers which direct the photons to the single-photon detectors. A 1 nm bandpass (BP) filter suppresses unwanted background fluorescence. **b**, With a pump power of 200 µW the signal-idler coincidences are integrated over 1100 s (•) with a bin width of ~60 ps. As expected, the correlation function exhibits two exponential decays with nearly identical time constants. The combined jitter of the APDs results in a temporal width of the IRF (–··–) of $\Delta\tau_{\mathrm{IRF}} = 560$ ps which is nearly identical to the signal/idler round-trip time $\Delta t_{\mathrm{rt,s/i}} = 1/\mathrm{FSR_{s/i}}$. Therefore, the peak structure caused by the cavity round trips can only just be resolved. The fit (—) of the convoluted model (Eq. 2.4.22) is in good agreement with the measurement. For comparison, the non-convoluted model (Eq. 2.4.9) is shown (—).

l, the total length of the cavity L, the finesse of the cavity $\mathcal{F}_{s/i}$, and the parameter $\bar{r}$ were taken from the measurement of the spectral density (section 2.3.3).

In principle, the length of both the crystals and the cavity can be measured with higher precision using the spectral measurement as the spacing of the spectral modes can be resolved with high resolution. In contrast, the uncertainty of the measured cavity decay rate and, thus, the uncertainty of the measured finesse is lower for the measurement of the correlation function. For the spectral measurement, the accuracy of the cavity decay rate is limited by the spectral resolution of the monochromator. Based on a correlation measurement, the cavity decay rate can be inferred with high precision from the exponential decline of the peak heights.

Although Eq. 2.4.22 has been used as the fit function, the measured correlation function closely resembles Eq. 2.4.18, simulated in Fig. 2.28. Eq. 2.4.18 is a good approximation, although it was derived for a single-pass pumping scheme and, in principle, is not valid for double-pass pumping or pump-resonant photon-pair sources. But, the difference between a convoluted version of Eq. 2.4.18 and the complete model Eq. 2.4.22 cannot be resolved with this measurement.

For a pump-resonant cavity, photon pairs can be generated in both directions. The impact of the pump resonance on the signal-idler correlation function is discussed in the subsequent section.

2.4.4 | Double-pass pumping and triple resonance

The measurement discussed in Fig. 2.31 cannot distinguish between a single-pass and a pump-resonant photon pair source. In this section, we show that between these two different types of sources the second-order signal-idler correlation function differs with respect to the fine structure of the narrow peaks. The global structure is not affected by the pumping scheme but depends only on the properties of the cavity at the signal and idler wavelength.

Non-resonant double-pass parametric down-conversion. Before we discuss triply-resonant cavities, we first analyze non-resonant double-pass parametric down-conversion to highlight the effect of double-pass pumping on the shape of the correlation function.

The signal-idler correlation function for (non-resonant) double-pass pumping is shown in Fig. 2.32 for various parameter combinations. To derive an expression for the phase-matching function for double-pass parametric interaction, the effective reflectivity $\bar{r} = r_{2p} r_{1s} r_{1i}$ and the relative phase $\Delta\Phi$ of the three fields have to be taken into account (section 1.1.3).

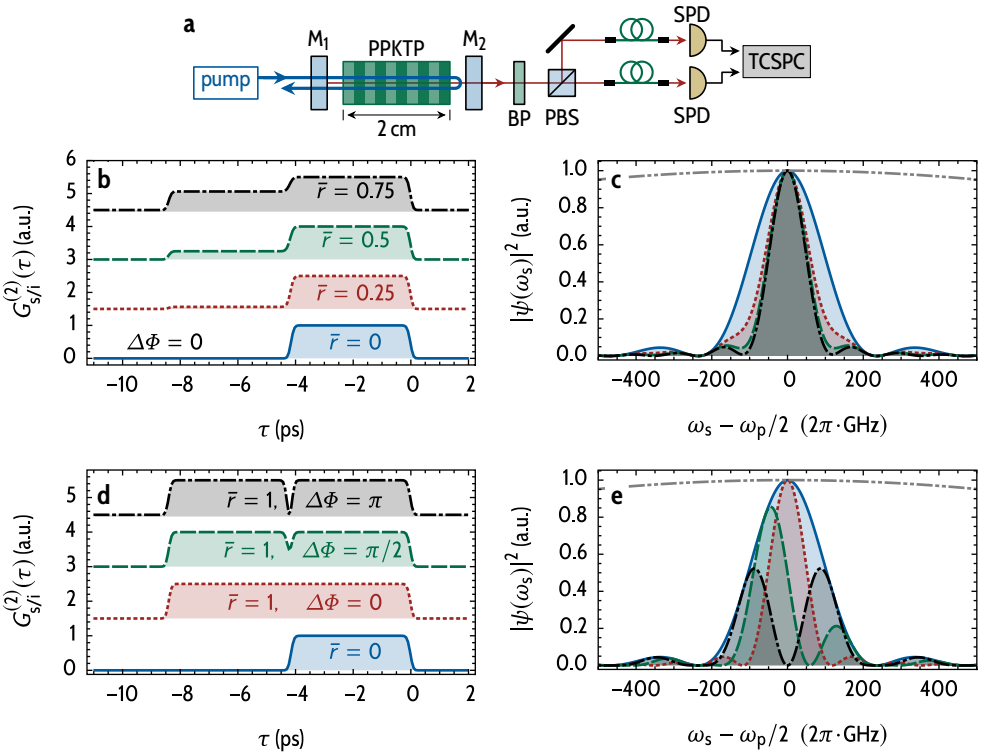

Figure 2.32 | Signal-idler correlation function for double-pass pumping. **a**, Signal-idler correlation measurement with a (non-resonant) double-pass pumping scheme: The pump beam is reflected by mirror M_2 such that signal and idler photons are generated in both directions. Mirror M_1 reflects the photon pairs while M_2 transmits the photon pairs. Bandpass (BP) filtering and detection is identical to the setup shown in Fig. 2.30. **b**, Signal-idler correlation function (Eq. 2.4.9) for different values of $\bar{r}$ and a constant value of the relative phase $\Delta\Phi = 0$. The correlation function is simulated for a 10 nm bandpass with a Gaussian filter transmission function. **c**, Normalized signal spectral density for the parameter combinations indicated in **b**. For reference, the Gaussian filter transmission function $\mathfrak{F}(\omega_{s/i})$ is also plotted (····). **d**, The signal-idler correlation function is simulated for different values of the relative phase $\Delta\Phi$ and $\bar{r}$. The same 10 nm bandpass filter as in **b** is applied. The dip at the center of the correlation function for $\bar{r} > 0$ and $\Delta\phi > 0$ can be related to destructive interference between photons generated in the forward direction and photons generated in the backward direction (see Fig. 1.2). **e**,The signal spectral density is plotted for the different parameter combinations indicated in **d**.

Effective reflectivity. As shown in Fig. 2.32b, for increasing values of $\bar{r}$, the signal-idler correlation function approaches a shape which is identical to the case of $\bar{r} = 0$, but with twice the width. This can be rationalized as follows: For $\bar{r} = 1$, the interaction length is doubled (see section 1.1.3). Therefore, the width of the phase matching envelope is reduced (see Fig. 2.32c) and the temporal width of the correlation function is increased by a factor of 2, respectively.

For intermediate values $1 > \bar{r} > 0$, only the first interaction between pump beam and nonlinear crystal contributes fully to the correlation function. The second pass contributes with a reduced amplitude due to losses at the mirrors and inside the crystal.

Relative phase. Fig. 2.32d shows a simulation of the signal-idler correlation function for different values of the relative phase $\Delta\Phi$ with $\bar{r} = 1$. For $\Delta\phi = \pi$, there is a time-delay τ directly at the center of the correlation function for which no signal and idler photons are detected simultaneously. Correspondingly, for $\Delta\Phi = \pi$, we also find a dip at the center of the signal/idler spectral density (see Fig. 2.32e). As discussed in Fig. 1.2, this phenomenon can be related to destructive interference between photons generated in the forward direction and photons generated in the backward direction. For intermediate values of $0 < \Delta\Phi < \pi$, this interference effect is less pronounced.

Triple resonance. Fig. 2.33 compares the signal-idler correlation function between a triply resonant two-crystal cavity ($\bar{r} = 1$) and a two-crystal cavity which is not resonant at the pump wavelength ($\bar{r} = 0$): The global comb-like structure of the correlation function only depends on the properties of the cavity at the signal and idler wavelength. The properties of the cavity at the pump wavelength only affect the fine structure of the peaks. This fine structure is identical for all peaks. Only the height of the peaks scales exponentially with the time delay τ. We will discuss the shape of the correlation function in the subsequent section.

For a typical crystal length of 2 cm, the peaks of the signal-idler correlation function have a width of approximately 6 ps. Even if the width of these peaks would be doubled by double-pass parametric interaction, the fine structure within the peaks could not be resolved by time-correlated single-photon counting due to the limited temporal resolution (typically >50 ps) of the single-photon detectors. Therefore, single-pass and double-pass interaction cannot be distinguished with the measurement scheme discussed in this section.

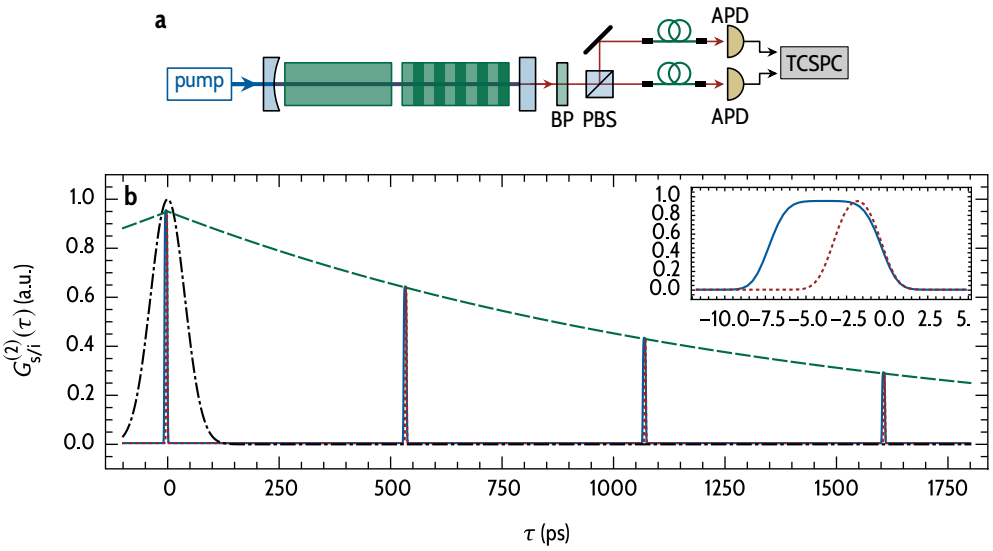

Figure 2.33 | Signal-idler correlation function for a triply-resonant cavity with compensation crystal. **a**, The same experimental setup as discussed in Fig. 2.31 is shown. A triply-resonant two-crystal cavity produces photon pairs which are filtered with a 1 nm bandpass filter and are analyzed by time-correlated single-photon counting. **b**, Comparison of the signal-idler correlation function for an effective reflectivity $\bar{r} = 1$ (——) and $\bar{r} = 0$ (----), respectively. The global comb-like structure of the correlation function only depends on the properties of the cavity at the signal and idler wavelength. The fine structure of the peaks differs between a pump-resonant source ($\bar{r} = 1$) and a source with single-pass pumping ($\bar{r} = 0$). The fine structure of each peak (see inset) is identical and has been discussed in Fig. 2.32. The height of the peaks scales exponentially (– –) and is proportional to $\exp\left(-|\tau|\Gamma_{s/i}\right)$, where $\Gamma_{s/i}$ is the signal/idler cavity decay rate (see Eq. 2.4.18). The width of the peaks is on a time scale of several picoseconds. Therefore, the fine structure cannot be resolved by time-correlated single-photon counting. For reference, we plot a typical Gaussian instrument response function with a temporal width on the order of 100 ps (–·–).

2.4.5 | Signal-idler correlation function for single-crystal cavities

In the following, we present a simplified model to explain the signal-idler correlation function of cavity-enhanced SPDC with and without compensation crystals. This simplified model assumes that the temporal width of the individual peaks of the signal-idler correlation function is so small that the peaks can be treated as delta distributions.

The signal-idler correlation function can be rationalized as follows: A pair of signal and idler photons is created at time $t = 0$. The signal photons perform n round trips and the idler photons perform m round trips until they leave the cavity and are detected. The photons are detected at times $t_\mathrm{s} = t_{0,\mathrm{s}} + n \cdot \Delta t_{\mathrm{rt,s}}$ and $t_\mathrm{i} = t_{0,\mathrm{i}} + m \cdot \Delta t_{\mathrm{rt,i}}$, respectively. Here, $t_{0,\mathrm{s/i}}$ is the time it takes the signal/idler photon to propagate form the cavity to the detector. The signal/idler round-trip time is:

$$\Delta t_{\mathrm{rt,s/i}} = \frac{1}{\mathrm{FSR_{s/i}}}. \tag{2.4.24}$$

The time delay τ which is recorded in the start-stop histogram is given by:

$$\tau = t_\mathrm{s} - t_\mathrm{i} - (t_{0,\mathrm{s}} - t_{0,\mathrm{i}}). \tag{2.4.25}$$

Cavity with compensation crystal. We discuss the case of a cavity with compensation crystal and equal signal/idler cavity round-trip times. The center peak of the signal-idler correlation function at $\tau = 0$ comprises all events for which the signal and idler photons from one pair perform the same number of round trips in the cavity ($n = m$). The first peak at a delay $\tau > 0$ is comprised of all events for which the signal photon performs one round trip more than the idler photon ($n = m + 1$). The subsequent peak corresponds to two more round trips for the signal photons than for the idler photons, and so forth ($n = m + q, q \geq 2$). The peaks detected for delays $\tau < 0$ correspond to events for which the idler photon performs more round trips than the signal photon.

Since the cavity round-trip time for the signal and idler photons is identical for a cavity with a compensation crystal, the measured time delay τ does not depend on the absolute values of n and m but only on the difference $n - m$. Therefore, a comb with equally-spaced peaks is detected (see Figs. 2.31 and 2.33).

Cavity without compensation crystal. This is no longer true for a single-crystal cavity for which $\Delta t_{\mathrm{rt,s}} \neq \Delta t_{\mathrm{rt,i}}$. Even for the same number of round trips, the measured time delay τ depends on the absolute value of $n = m$. For a cavity with unequal signal/idler round-trip times, the peaks of the signal-idler correlation split up into a series of sub peaks with a temporal spacing of $\Delta t_{\mathrm{rt,s}} - \Delta t_{\mathrm{rt,i}}$. The amplitude

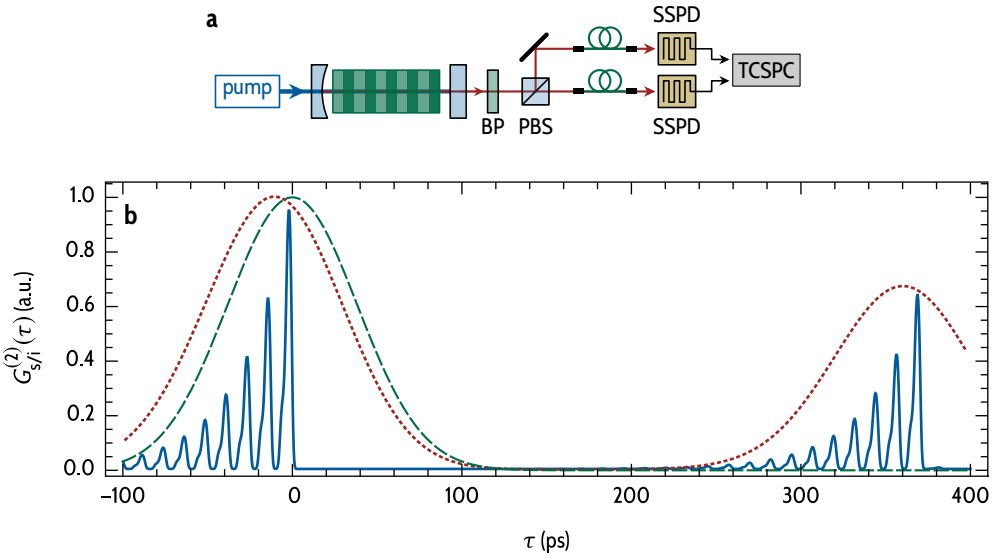

Figure 2.34 | Signal-idler correlation function for a triply-resonant single-crystal cavity. **a**, Measurement of the signal-idler correlation function for a single-crystal cavity. The measurement setup is identical to Fig. 2.30. Here, we assume the usage of superconducting single-photon detectors (SSPD) with a low timing jitter of ∼50 ps. **b**, Simulation of the signal-idler correlation function for a single-crystal cavity with $\Delta\Phi = 0$ and $\bar{r} = 0.5$ (——). Each of the two peaks of the correlation function is split up into a series of sub peaks with decreasing amplitude due to the differing signal/idler cavity round-trip times. Even with state-of-the-art single-photon detectors, the temporal substructure of the peaks cannot be resolved. Therefore, to simulate the experiment, we simulate (----) the signal-idler correlation function convoluted with a typical Gaussian instrument response function (– –) with a FWHM of $\Delta\tau_{\mathrm{IRF}} = 90$ ps. The shape of the convoluted correlation is nearly Gaussian for each peak. But, the presence of the substructure of the peaks could be inferred by measuring the shift the center of the peak at $\tau = 0$ compared to the peak of non-resonant photon-pair source.

of these sub peaks is increasing or decreasing with τ, depending on whether the signal round-trip time is larger or lower than the idler round-trip time. This splitting for the correlation peaks into multiple sub peaks has been studied theoretically by Kuklewicz.[122]

In Fig. 2.34, the signal-idler correlation function is simulated for a triply-resonant single-crystal cavity using Eqs. 2.4.9, 2.4.21 and 2.4.22. All parameters were taken from the measurement which we discuss in the next section. Here, only the peaks with $n = m$ and $n = m + 1$ are shown. In contrast to Fig. 2.33, each peak is split up into a series of sub peaks. But, again, each of these sub peaks shares the same fine structure. It is the same fine structure which has been discussed in Fig. 2.32.

2.4.6 | Signal-idler correlation function for the single-crystal cavity

Fig. 2.35 shows the measured signal-idler correlation function for the triply-resonant cavity. The measurement is in excellent agreement with the theoretical model given by Eq. 2.4.22. Due to the low timing jitter of the superconducting single-photon detectors, the individual peaks of the correlation function could be resolved. But, both the separation of each peak into the sub peaks, as discussed in the previous section, as well as the fine structure of these sub peaks cannot be resolved. To resolve such a fine structure, single-photon detectors with a much lower timing jitter would be required.[282]

Fit. For the fit of Eq. 2.4.22 to the data, the free parameters are an arbitrary shift τ_0 of the correlation function with respect to the data, the distance of the mirrors, the finesse of the cavity for the signal and idler field, the width $\Delta\tau_{\mathrm{IRF}}$ of the instrument response function, as well as the offset c, and the amplitude a. The fit values of the finesse ($\mathcal{F}_{\mathrm{s}} = 15$ and $\mathcal{F}_{\mathrm{i}} = 16$) are in good agreement with the value found for the fit to the measured signal spectral density (Fig. 2.20). Since the distance of the mirrors and the orientation of the nonlinear crystal was slightly altered between the measurement presented in Figs. 2.20 and 2.35, the fit values also differ by about 10 %.

The superconducting single-photon detectors feature a very low dark-count rate and the bandpass filter blocks most of the spurious background fluorescence generated inside the nonlinear crystal. Therefore, only a small fraction of the detected signal can be attributed to uncorrelated background events. The fit value of the offset is $c = 22$. In relation to the maximum of 7400 detected events in the central bin at $\tau = 0$, this corresponds to a remarkable signal-to-noise ratio of 300:1.

Detection of the substructure of the peaks. The fit value of the width of the IRF yields $\Delta\tau_{\mathrm{IRF}} = 90(1)$ ps. Note, that the shape of the peaks is still Gaussian to good approximation. The underlying substructure of the peaks is asymmetric. Fig. 2.36 compares the fit function with $\Delta_{\mathrm{IRF}} = 90$ ps with a Gaussian peak with FWHM of 96 ps. Within the uncertainty of the measurement, the experimental data does not significantly deviate from the simple Gaussian peak. But, the Gaussian peak is shifted by about 20 ps from $\tau = 0$ (see also Fig. 2.34b). Therefore, the presence of the underlying substructure of the peaks can, in principle, be identified as follows:

Expanding on the experiment shown in Fig. 2.35, we can measure the signal-idler correlation function for a non-resonant photon-pair source with the same combination of polarizing beam splitter and single-photon detectors. The non-resonant source features a signal peak without substructure centered at $\tau = 0$.

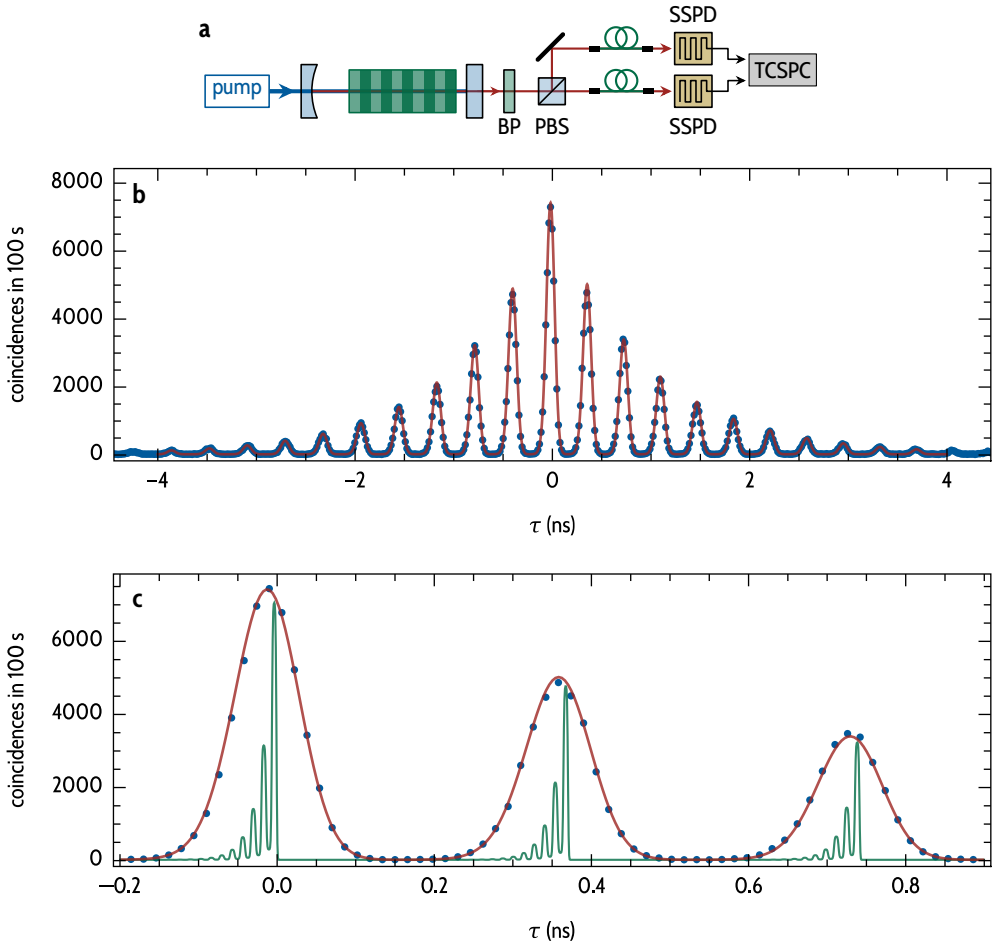

Figure 2.35 | Measurement of the signal-idler correlation function for the single-crystal cavity. **a**, The single-crystal setup discussed, e.g., in Fig. 2.20 is analyzed by time-correlated single photon-counting (TCSPC). Signal and idler photons are split at a polarizing beam splitter (PBS) and detected with superconducting single-photon detectors (SSPDs). A 1 nm bandpass filter is used to block background fluorescence. **b**, The second-order signal-idler correlation function is measured (•) as a start-stop histogram for time delays τ between the detection of signal and idler photons. The measurement is in excellent agreement with the theoretical model (—) given by Eq. 2.4.22. **c**, Zoom into the first three peaks shown in **b**: The deconvoluted signal-idler correlation function (—) is asymmetric due to the differing signal/idler round-trip times $\Delta t_{\mathrm{rt,s}} \neq \Delta t_{\mathrm{rt,i}}$. Nevertheless, the peaks after convolution with the instrument response function exhibit a shape close to a Gaussian distribution. The fine structure within the peaks cannot be resolved.

For this peak, the width $\Delta\tau_{\mathrm{IRF}}$ can be measured. A shift of the central peak of the signal-idler correlation function of the cavity-enhanced source then indicates the presence of the substructure of the peaks.

Discussion. Similar measurements for single-crystal cavities have been performed by other groups.[130,133,136,149,273,274] The experimental results published by Fekete and colleagues[133] indicate a splitting of the peaks into sub peaks due to the differing signal/idler cavity round-trip times. Their analysis utilizes Eq. 2.4.14. But, for the simulation of the correlation function, they assume identical round-trip times for signal and idler photons. Therefore, the asymmetry of the individual peaks is not explained by the authors.

Luo and colleagues[141] derived an alternative expression for the second-order signal-idler correlation function and verified their findings for a short (waveguide) cavity experimentally. Other groups also were not able to resolve the substructure of the peaks of the correlation function since they used short cavities with a very short round-trip time.[130,273,274] Rieländer and coworkers[149,274] did not resolve the peak structure of the correlation function due to subsequent narrowband spectral filtering of the signal and idler photons.

Compared to the measurements shown in Fig. 2.31 which were performed with avalanche photodiodes, the measurements presented in Fig. 2.35 clearly highlight the advantage of using superconducting single-photon detectors. The superior timing resolution of these state-of-the-art detectors allows for a high-fidelity measurement of the temporal structure of the correlation function. The experiment presented in Fig. 2.35 led to further investigations[283] into the possibility of shaping the wave packet of single photons via a fast amplitude modulator. These experiments will be discussed in chapter 3 of this thesis.

2.4.7 | Narrowband spectral filtering

Narrowband spectral filtering is often used to isolate a single spectral mode of the photons generated by cavity-enhanced SPDC.[128,133,136,143,145,149] The absence of the periodic peak structure in the signal-idler correlation function is typically associated with a (spectral) single-mode operation of a cavity-enhanced photon-pair source.[128,130] An ideal photon-pair source with a single (Lorentzian) spectral mode has a signal-idler correlation function with two exponential slopes and no further internal structure.

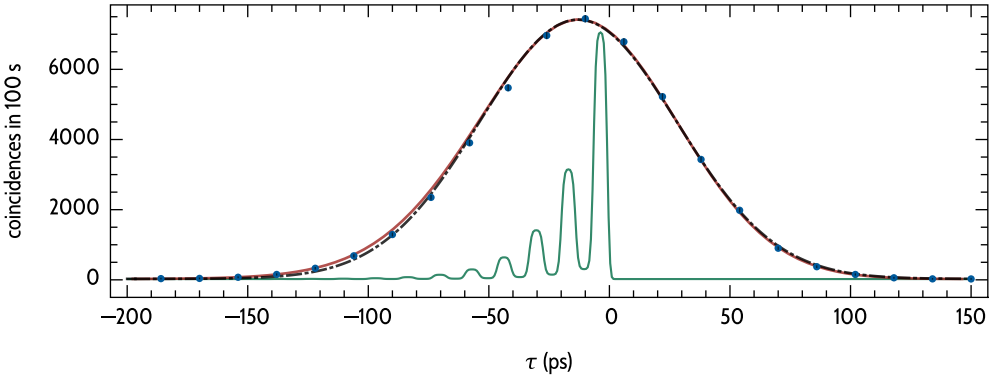

Figure 2.36 | Detail of the signal-idler correlation measurement. Measurement (♦), deconvoluted theory (—), convoluted theory (—) with IRF width of 90(1) ps, Gaussian (– · –) with IRF width of 96(1) ps and a shift of 20 ps.

Near single-mode operation. Scholz and colleagues[128] showed how a cascaded narrowband filtering system completely eliminates the peak structure of the correlation function. In this section, we evaluate the impact of narrowband filtering with a *single* low-finesse cavity on the second-order signal-idler correlation function. The aim of the chosen filtering system is to achieve near single-mode operation in conjunction with high brightness and minimum loss of photon-pairs.

In the case of the single low-finesse filter cavity, a single spectral mode dominates the spectral density of signal and idler photons. But, the filter cavity also partially transmits the adjacent spectral modes. This results in a correlation function which still features a peaked structure, but exhibits a reduced visibility.

Experimental setup. Fig. 2.37a shows the experimental setup. Signal and idler photons generated inside the single-crystal cavity are coupled into a single-mode fiber. Subsequently, they are transmitted through a monolithic filter cavity with a linewidth of 885 MHz (much larger than the linewidth of the central mode) and a free spectral range of 28.8 GHz (see section 2.1). A resonance of the filter cavity is tuned to the degenerate mode ($\omega_s = \omega_i = \omega_p/2$) at the center of the central cluster. The filter cavity suppresses the two adjacent modes of the central cluster by a factor of about 15. All further peaks of the central cluster are suppressed by more than two orders of magnitude. The splitting of signal and idler photons, as well as the experimental setup used to measure the correlation function, is identical to the setup shown in Fig. 2.35.

The filter cavity has an on-resonance transmission of more than 90 % and a fiber-to-fiber coupling efficiency of more than 50 %. Therefore, the losses induced by

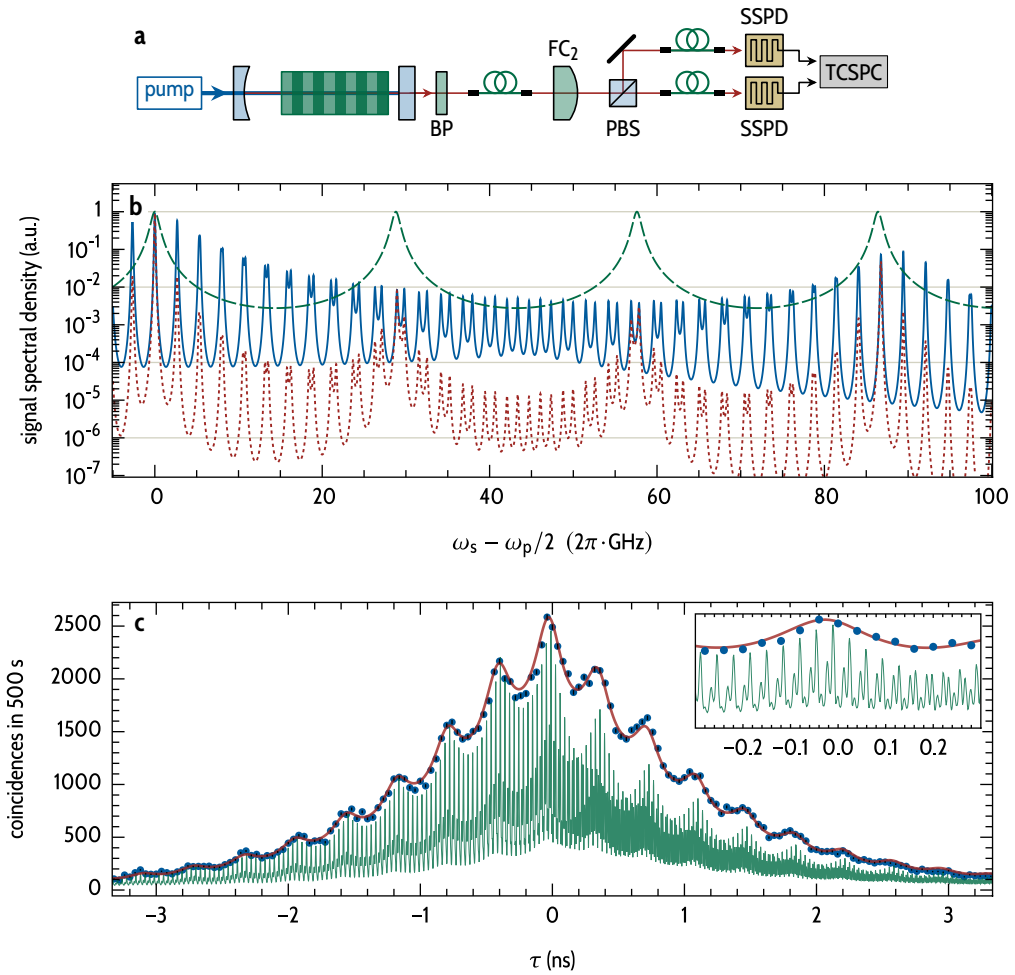

Figure 2.37 | Signal-idler correlation function with spectral filtering. **a**, Signal and idler photons generated inside a single-crystal cavity are spectrally filtered with a monolithic filter cavity (FC_2, see section 2.1) with a linewidth of 885 MHz and a free spectral range of 28.8 GHz. Subsequently, the signal-idler correlation function is recorded by time-correlated single-photon counting (see Fig. 2.35). **b**, Signal spectral density without spectral filtering (——) as discussed in Fig. 2.20. A filter-cavity resonance is tuned to the central peak ($\omega_s = \omega_{p/2}$) of the central cluster. Most of the other spectral modes are suppressed by the filter cavity transmission function (– –). The filtered signal spectral density (----) is dominated by a single spectral mode. But, the two adjacent modes are suppressed by a factor of only 15. Additionally, one spectral mode at $\omega_s - \omega_p/2 \approx 2\pi \cdot 85$ GHz is partially transmitted by the filter cavity. **c**, The measured signal-idler correlation function (♦) is in good agreement with the theoretical model (——) given by Eq. 2.4.22. The unconvoluted signal/idler correlation function (——) features a complicated internal structure caused by the bouncing of the signal and idler wave packets inside the filter cavity. The inset is a zoom into the central part of the plot.

the single-cavity spectral filtering are considerably lower than the losses of a cascaded filtering system.

Spectral filtering. Fig. 2.37b compares the signal-photon spectral density before and after filtering. In the second cluster, one of the modes coincides with a filter-cavity resonance. Photons generated into this mode are transmitted with high (>50 %) probability. The filter-cavity transmission spectrum is symmetrical about the degeneracy frequency $\omega_{s/i} = \omega_p/2$. If a signal photon is transmitted at the frequency $\omega_s = \omega_p/2 + \Delta\omega$, the corresponding idler photon of the pair at frequency $\omega_i = \omega_p/2 - \Delta\omega$ is also transmitted by the filter cavity.

Mode structure after filtering. The spectral density of the filtered signal and idler photons is dominated by the degenerate mode at $\omega_{s/i} = \omega_p/2$. Nevertheless, the photon-pair source does not operate with a single spectral mode. The partial multi-mode characteristic manifests itself in the measurement of the signal-idler correlation function.

Experimental results – broadening of the peak structure. Fig. 2.37c shows the experimental data which was also presented in Ref. [138]. The measured signal-idler correlation function still features a comb structure instead of a single exponential decay. But, the filter cavity broadens the peak structure of the correlation function. This broadening reduces the visibility of the individual peaks.

Ref. [138] approximates this broadening by noting that the narrowband filtering corresponds to an increase in the effective width of the instrument response function of the detection system. The spectral filtering increases the width of the IRF from $\Delta\tau_{IRF} = 90(1)$ ps to the effective width $\Delta\tau_{IRF,\,eff} = 340(10)$ ps.

Fit. But, with Eqs. 2.4.21 and 2.4.22, the theoretical signal-idler correlation function can be simulated more thoroughly and without introducing an effective width of the IRF. Again, the theoretical curve (Fig. 2.37c) is in good agreement with the measurement data. As it turns out, the shape of the correlation function is extremely sensitive to the mirror spacing and the free spectral range of the filter cavity.

This can be rationalized as follows: After leaving the down-conversion cavity, the signal and idler wave packets are localized in discrete time slots indicated by the peaks of the signal-idler correlation function (see Fig. 2.35b). Once these localized wave packets enter the filter cavity, they bounce back and forth inside the cavity until they exit after several round trips. The signal-idler correlation function accounts for all combinations of the number of round trips of both photons in either cavity.

Therefore, the ratio of the round-trip times of signal and idler photons inside the conversion and the filter cavity gives rise to a complicated pattern of the deconvoluted correlation function (see Fig. 2.37c). The mirror spacings of the down-conversion cavity and the free spectral range of the filter cavity, thus, determine the exact time delays with which signal and idler photons can be detected after leaving the filter cavity. Even slight changes in either parameter drastically change the structure of the correlation function.

Discussion – efficient single-mode filtering. The experimental results presented in this section show that one can achieve single-mode operation of the single-crystal photon-pair source only partially with a single low-finesse filter cavity. A filter-cavity with a finesse of $\mathcal{F} = 30$ broadens the peak structure of the correlation function, but does not completely eliminate this structure.

Fig. 2.38a evaluates whether a filter cavity with a higher finesse could obtain single-mode operation of the down-conversion source. The signal-idler correlation function (convoluted with the IRF of the detection system, Eq. 2.4.22) is plotted for different values of the filter-cavity finesse. For this simulation, we fix the free spectral range of the filter cavity to 28.8 GHz. The FWHM of the filter-cavity resonances is reduced from 960 MHz ($\mathcal{F} = 30$) to 380 MHz ($\mathcal{F} = 75$) and approaches the signal/idler cavity decay rate.

Therefore, for larger values of the filter-cavity finesse, the transmission of the selected spectral mode is reduced. For $\mathcal{F} = 75$, less than 80 % of signal and idler photons of the selected spectral mode are transmitted by the filter cavity. The probability to detect both photons from one pair is, thus, reduced by about 40 % after filtering.

Although the filtering losses are comparably high for $\mathcal{F} = 75$, we can still observe the peak-structure of the signal-idler correlation function. Thus, to achieve single-mode operation we require an even higher finesse. To circumvent the filtering losses, one could use a filter cavity with a larger free spectral range to obtain a larger FWHM of the cavity resonances. But, as has been discussed in section 2.1, high-finesse monolithic filter cavities also suffer from poor transmission due to losses inside the cavity. Therefore, to achieve high transmission, other filter-cavity configurations or alternative spectral filter technologies need to be used.

Cascaded filtering. Instead of a single filtering cavity, we can use cascaded filter cavities with differing free spectral ranges.[128] This offers the possibility to obtain single-mode operation whilst using low-finesse cavities with high transmission.

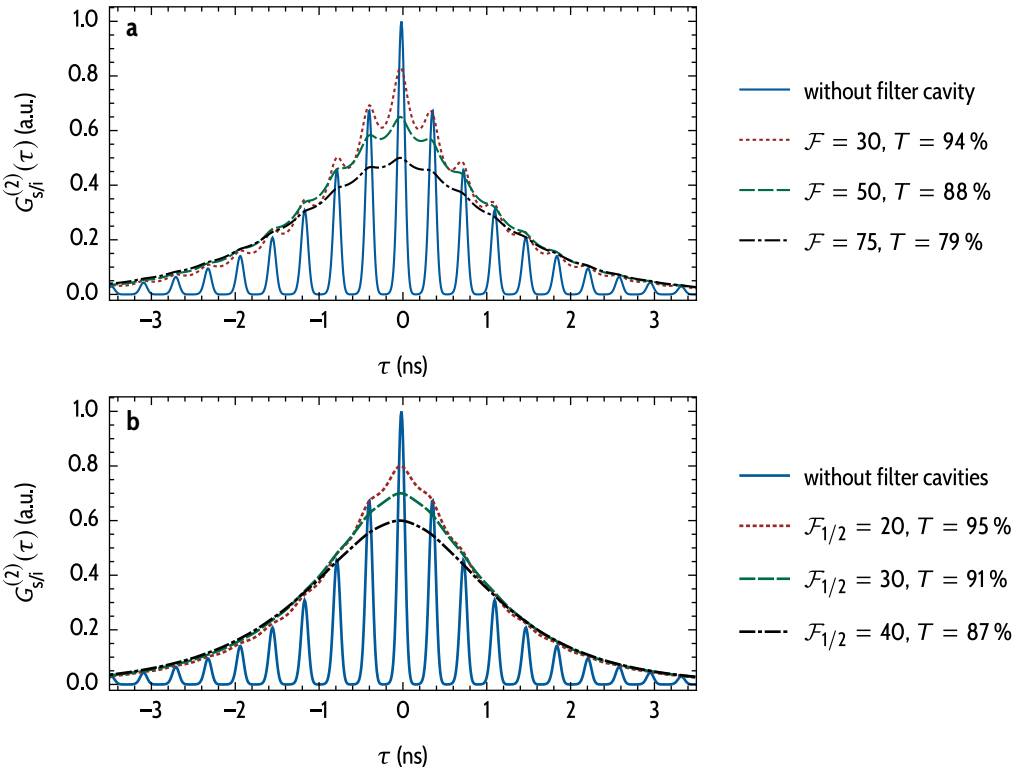

Figure 2.38 | Signal-idler correlation function with narrowband filtering. **a**, The correlation function $G^{(2)}_{s/i}(\tau)$ is shown for different values of the filter-cavity finesse and a free spectral range of 28 GHz. Even for a moderately high finesse of $\mathcal{F} = 75$, the filter cavity does not fully eliminate the peak structure of the correlation function. Additionally, at $\mathcal{F} = 75$, the transmission of the central spectral mode through the filter cavity is only $T = 79\,\%$. **b**, A cascaded filter-cavity system is much more efficient in spectrally selecting only the central mode. The correlation function is shown for different values of the filter-cavity finesse. Here, both filter cavities share the same finesse. For two cascaded filter cavities with a finesse of $\mathcal{F} = 50$ and free spectral ranges of 28 GHz and 35 GHz, the peak structure is fully eliminated whilst the transmission is still high ($T = 87\,\%$).

Fig. 2.38b compares the signal-idler correlation functions for different cascaded filter-cavity systems. For all curves, the two filter cavities have free spectral ranges of 28 GHz and 35 GHz and both filters share the same finesse $\mathcal{F}_{1/2}$. The correlation function for two cavities with $\mathcal{F}_{1/2} = 20$ is qualitatively comparable to the case of a single filter cavity with $\mathcal{F} = 75$ shown in Fig. 2.38a. In both cases, we observe slight modulations superimposed on the exponential slopes. But, the losses by spectral filtering are much lower (≈5 %) for the cascaded filter system when compared to the single-cavity filtering scheme ($T = 79\,\%$).

The application of cascaded filters with a finesse of just $\mathcal{F}_{1/2} = 40$ completely eliminates the peak structure of correlation function. In this case, the transmission ($T = 87\,\%$) is comparable to a single filter cavity with $\mathcal{F} = 50$.

2.5 | Hong-Ou-Mandel effect – photon indistinguishability

The so-called Hong-Ou-Mandel[32] (HOM) effect is *the* main textbook example for the non-classical interaction of single photons. It dramatically highlights the bosonic nature[284] of single photons.

Upon coalescence of two single photon states on a beam splitter, the photons exhibit a bunching behavior which cannot be observed for classical particles: The two photons always exit the beam splitter through the same output port. But, this photon bunching on a beam splitter can only be observed for photons indistinguishable in all (spectral, temporal, spatial, polarization) degrees of freedom. The HOM effect has been studied extensively in the literature.[285–289] Assuming that the reader is familiar with the HOM effect, we do not present the theoretical foundation here in greater depth.

Hong-Ou-Mandel dip. The HOM effect is typically observed by measuring the coincidence rate of photons leaving the beam splitter through either output port. If the arrival of either photon is delayed by a time delay τ with respect to the other, the coincidence rate typically features a dip in the coincidence rate $R_{\mathrm{coin}}(\tau)$ at $\tau = 0$. For indistinguishable photons, the shape of this *Hong-Ou-Mandel dip* can be related to a self convolution of the temporal wave function.[290]

Non-resonant Hong-Ou-Mandel effect. Before we discuss the Hong-Ou-Mandel effect measured with the cavity-enhanced photon pair sources, we present a simple experiment based on non-resonant SPDC. Although all results obtained in this non-resonant experiment have already been published in the literature,[290] the experiment is nevertheless instructive. The non-resonant experiment gives valuable insights into the shape of the Hong-Ou-Mandel dip for type-II SPDC.

Furthermore, the limitations of the experimental setup are highlighted. The measured HOM visibility serves as an upper bound for the visibility measured for the cavity-enhanced photon-pair source since the visibility is mainly limited by the experimental setup and not by the properties of the photon-pair source.

Cavity-enhanced photon-pair source. The Hong-Ou-Mandel effect for photons generated by degenerate cavity-enhanced SPDC has already been discussed in the literature: Photon-pair sources based on degenerate type-II SPDC can be utilized as sources of polarization-entangled photons.[121,122,125] But, for the generation of high-fidelity entangled states, a high degree of spectral indistinguishability between signal and idler photons is required. The Hong-Ou-Mandel effect provides as versatile tool to evaluate the distinguishability of photons. Photon pairs generated by cavity-enhanced SPDC have been analyzed with a HOM interferometer.[126] Indistinguishable photons generated by cavity-enhanced SPDC can also be utilized to generate so-called *NOON-states*.[142,144]

Another focus of research lies on the so-called *revival* of the HOM dip for photon pairs generated inside a cavity.[36,117,119,150] For a cavity with equal free spectral ranges for signal and idler fields, additional HOM dips separated by multiples of half the cavity round-trip time t_{rt} can be observed. The revival of the HOM dip will be discussed in a latter part of this section.

Hong-Ou-Mandel effect for triply-resonant cavity-enhanced SPDC. This section focusses on the shape of the central HOM dip depending on the relative phase $\Delta\Phi$ of the three interacting fields inside the down-conversion cavity. To the best of the author's knowledge, this topic has not been discussed in the literature. As we have analyzed before, the relative phase $\Delta\Phi$ has a fundamental impact on the spectral features of the generated photon pairs (see section 2.3). The impact on the signal-idler second-order correlation function is also apparent (e.g. from Fig. 2.32), but is not experimentally accessible with the timing jitter of state-of-the-art single-photon detectors. In this section, we show that the two-crystal configuration with a compensation crystal is especially suited to analyze the impact of the relative phase on the HOM dip. By detuning the compensation-crystal temperature, not only can one adjust the degree of distinguishability of the signal and idler photons. It is also possible to fine-tune the relative phase $\Delta\Phi$ to arbitrary values. The measured HOM-dip shapes are in excellent agreement with the theoretical predictions developed in this thesis.

Single-mode spectral filtering. In section 2.4.7, we discussed how single-mode operation of a cavity-enhanced photon-pair source can be achieve by narrowband spectral filtering. Here, we use the same setup to generate spectrally indistinguishable signal and idler photons. These filtered photon pairs show high-visibility Hong-Ou-Mandel interference with high coincidence rates at the

single-photon detectors. The evaluate theoretically how the finesse of the filter cavity affects the shape of the Hong-Ou-Mandel dip.

Generation of polarization-entangled photons. With a conventional non-polarizing beam splitter, degenerate type-II SPDC can be used to generate polarization-entangled photons. Since we show that after single-mode spectral filtering the photons are spectrally nearly indistinguishable, it becomes apparent that we can use our cavity-enhanced photon-pair source to generate entangled photons. We conclude this section by measuring the bell-state fidelity of this polarization-entangled two-photon state.

2.5.1 | Non-resonant Hong-Ou-Mandel effect

As an introduction to the discussion of the Hong-Ou-Mandel effect in the context of cavity-enhanced photon-pair sources, we briefly discuss the non-resonant case in the following. The experimental setup[291] is depicted in Fig. 2.39. The Hong-Ou-Mandel effect is measured for signal and idler photons generated inside a periodically poled KTP crystal by non-resonant SPDC. The pump laser is tightly focussed with lens L_1, locating the beam waist at the center of the nonlinear crystal. The generated photon pairs are collimated via lens L_2 and the pump light is blocked by a 50 nm bandpass (BP) filter centered at signal and idler wavelength of 894 nm. A half-wave plate (HWP) precisely aligns the polarization axes of signal and idler photons with the mechanical axes of a polarizing beam splitter.

Hong-Ou-Mandel interferometer. The idler photons are directly coupled into a fiber and directed to a 50/50 non-polarizing beam splitter. The signal photons are directed to a monolithic retroreflector which is mounted onto a translation stage. After this variable delay, the polarization of the signal photons is rotated by a half-wave plate to coincide with the idler photon polarization. Subsequently, the signal photons are fiber coupled and directed to the second input port of the beam splitter. The path-length variation Δl, adjusted by the retroreflector position,[33] precisely defines the temporal delay τ between signal and idler photons at the beam splitter. We detect photons exiting the beam splitter on either side with two avalanche photon diodes. A TCSPC electronics measures the rate at which photons are detected in coincidence.

Indistinguishability. The experimental setup depicted in Fig. 2.39 aims to render signal and idler photons indistinguishable in all degrees of freedom:

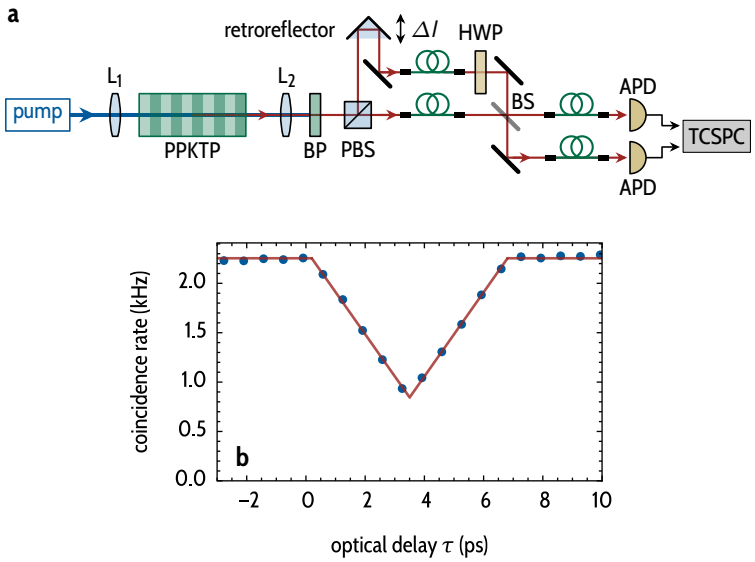

Figure 2.39 | Hong-Ou-Mandel effect without spectral filtering. **a**, Signal and idler photons generated (non-resonantly) inside the PPKTP crystal are split up at a polarizing beam splitter (PBS). The PBS directs the signal photons directly to a 50/50 non-polarizing beam splitter (BS). A retroreflector mounted on a translation stage delays the arrival time of the idler at second input port of the beam splitter. Two fiber-coupled avalanche photodiodes measure the coincidence rate at which the photons from one pair leave the beam splitter at either side. **b**, For a time delay $\tau \approx 3.3$ ps, we detect a strong reduction of the coincidence rate. This coincidence-rate reduction can be attributed to an increase of events in which both photons exit the beam splitter through the same output port. The V-shape of the so-called *Hong-Ou-Mandel dip* is in excellent agreement with the theory presented by Sergienko and coworkers[290] for photon pairs generated by type-II SPDC. The visibility of 45.4(5) % of the HOM dip is limited by imperfections in the measurement setup (see main text).

- The temperature of the PPKTP crystal is chosen as close as possible to the degeneracy point where the signal spectral density coincides with the idler spectral density.
- The difference in group velocity of signal and idler photons inside the crystal is compensated by the variable delay line.
- By rotating the signal-photon polarization, the photons are indistinguishable in polarization.
- Signal and idler photons are coupled into single-mode fibers before and after the beam splitter. Therefore, their spatial mode is nearly Gaussian. The spatial mode overlap at the beam splitter is optimized by monitoring the classical interference visibility, which exceeds 95 %.

Measurement results. For a time delay $\tau \approx 3.3\,\mathrm{ps}$, we detect a strong reduction of the coincidence rate (see Fig. 2.39b). This time delay corresponds to half the signal-idler propagation delay τ_0 inside the nonlinear crystal as defined in Eq. 2.4.16. The V-shape of the Hong-Ou-Mandel dip is in excellent agreement with the theory presented by Rubin and coworkers[177] for photon pairs generated by type-II SPDC.[290] Without spectral filtering, the temporal wave function of signal and idler photons exhibits a rectangular shape (see Figs. 2.29 and 2.30). Therefore, the Hong-Ou-Mandel dip – as the self-convolution of the temporal wave function – has a triangular shape:

$$R_{\mathrm{coin}}^{\text{type-II}}(\tau) = c + a\left[1 - \begin{cases} 1 - \left|\tau/\tau_0\right|, & \text{for } \left|\tau/\tau_0\right| < 1 \\ 0, & \text{elsewhere} \end{cases}\right], \tag{2.5.1}$$

where the offset c and the amplitude a are constants. For indistinguishable photons and a Hong-Ou-Mandel interferometer with a classical visibility of $V = 1$, the offset in Eq. 2.5.1 would be $c = 0$. In the following, we discuss why the measured HOM visibility deviates from unity.

Visibility. The *visibility* V of the HOM dip is typically[292] defined by:

$$V = \frac{R_{\mathrm{coin}}^{\max} - R_{\mathrm{coin}}^{\min}}{R_{\mathrm{coin}}^{\max} + R_{\mathrm{coin}}^{\min}}, \tag{2.5.2}$$

where $R_{\mathrm{coin}}^{\max}$ is the maximum of the coincidence rate $R_{\mathrm{coin}}(\tau)$ and $R_{\mathrm{coin}}^{\min}$ is the minimum in the center of the HOM dip.

For the experiment shown in Fig. 2.39, the following imperfections contribute to a degradation of the visibility to $V = 45.4(5)\,\%$: Upon reflection of the

signal photons at the monolithic retroreflector, the linear input polarization was transfered to an elliptical polarization[293] which was not compensated for in the experiment. Thus, the retroreflector limited the indistinguishability of signal and idler photons in polarization. The imperfect spatial mode overlap of signal and idler fields at the beam splitter further limited the HOM visibility. We measure a classical interference visibility of about 80 % for the HOM interferometer. Finally, background fluorescence (see Fig. 2.14) generated inside the nonlinear crystal contributed to the offset of the HOM dip.

The same HOM interferometer is used for the measurements with the cavity-enhanced photon-pair source presented in the subsequent section. Therefore, the visibility measured for the single-pass photon-pair source represents an upper bound for the cavity measurements. Very high visibilities can be achieved with type-II parametric down-conversion.[126,150,290] The visibility measured here is, therefore, not limited by the spectral properties of the generated photon-pairs and can be attributed to the imperfections of the interferometric setup.

2.5.2 | Two-crystal cavity configuration

The cavity configuration with a compensation crystal offers the possibility to tune the signal and idler frequency combs (see section 2.3.3) in perfect degeneracy. On the one hand, the temperature of the conversion crystal determines the degree of degeneracy of the parametric gain envelope for signal and idler fields. On the other hand, by tuning the temperature of the compensation crystal, one can superimpose the individual teeth of the frequency combs.

Typically, the signal and idler frequency combs are superimposed to achieve spectral degeneracy in a central spectral mode. But, by detuning the signal frequency comb with respect to the idler frequency comb, the relative phase $\Delta\Phi$ can be brought to any value between 0 and 2π (albeit with a reduction of the photon-pair generation rate). In this section, we discuss the degenerate case. We will discuss the impact of the phase $\Delta\Phi$ on the shape of the HOM dip in the subsequent section.

Experimental setup. The experimental setup shown in Fig. 2.40 is identical to the Hong-Ou-Mandel interferometer shown in Fig. 2.39 except for the photon-pair source. Instead of the 50 nm bandpass filter, a 1 nm bandpass filter is used to suppress the background fluorescence. Using a grating spectrometer, the signal and idler parametric gain envelope is tuned to degeneracy by adjusting the conversion crystal temperature. Subsequently, to achieve spectral degeneracy of the signal and idler fields, we adjust the temperature and orientation of

the compensation crystal to tune the pump, signal and idler cavity resonance frequencies.

To monitor these resonance frequencies, we use the master laser at 894 nm: While scanning the cavity mirror, a flip mirror directs the master laser to the cavity. We monitor the cavity transmission of the laser with two photodiodes while scanning the cavity mirror position via the piezo-electric transducer attached to the outcoupling mirror (see Fig. 2.12). Simultaneously, a photodiode also records the pump light reflected by the cavity.

The theoretical PD signals are shown in Fig. 2.40c for perfect degeneracy of signal and idler fields and ideal pump resonances. Fig. 2.40e displays the measured photodiode signals. Minor side peaks are detected for the idler field. They are not present for the signal field. By careful alignment of the adjustable cavity mirror, the side peaks for the idler field can be eliminated. But, in this case, we observe side peaks for the signal field. These can be attributed to a birefringence-induced spatial walk-off inside the crystals. This walk-off prohibits the perfect alignment for both signal and idler fields for the chosen crystal orientation.

Once the degeneracy point is detected using the photodiodes, we lock the cavity to the pump beam. We remove the flip mirror and direct signal and idler photons to the HOM interferometer. We measure the coincidence rate for a duration of 20 s for different positions of the retroreflector. Before we will discuss the experimental results, in the following, we present the theoretical expectation for the HOM dip for a triply-resonant cavity-enhanced photon-pair source.

Theory. The Hong-Ou-Mandel dip is expressed as the rate $R_{\mathrm{coin}}(\tau)$ of coincidence events detected with the two single-photon detectors placed behind the two output ports of the beam splitter. The derivation of $R_{\mathrm{coin}}(\tau)$ is similar to the derivation of the signal-idler correlation function (Eq. 2.4.9) and is discussed in detail in the literature.[294,295]

For photon pairs generated by SPDC, the coincidence rate can be expressed solely in terms of the joint spectral amplitude of the biphoton state. The Hong-Ou-Mandel dip is given by:[294–296]

$$R_{\mathrm{coin}}(\tau) \propto \int_{-\infty}^{\infty} \mathrm{d}\omega_{\mathrm{s}} \int_{-\infty}^{\infty} \mathrm{d}\omega_{\mathrm{i}} \left| \psi(\omega_{\mathrm{s}}, \omega_{\mathrm{i}}) e^{i\omega_{\mathrm{i}}\tau} - \psi(\omega_{\mathrm{i}}, \omega_{\mathrm{s}}) e^{i\omega_{\mathrm{s}}\tau} \right|^2 . \tag{2.5.3}$$

Earlier works on the HOM dip did derive analytic expressions for the double integral in Eq. 2.5.3 even for cavity-enhanced type-II SPDC.[121,150,290] But, the

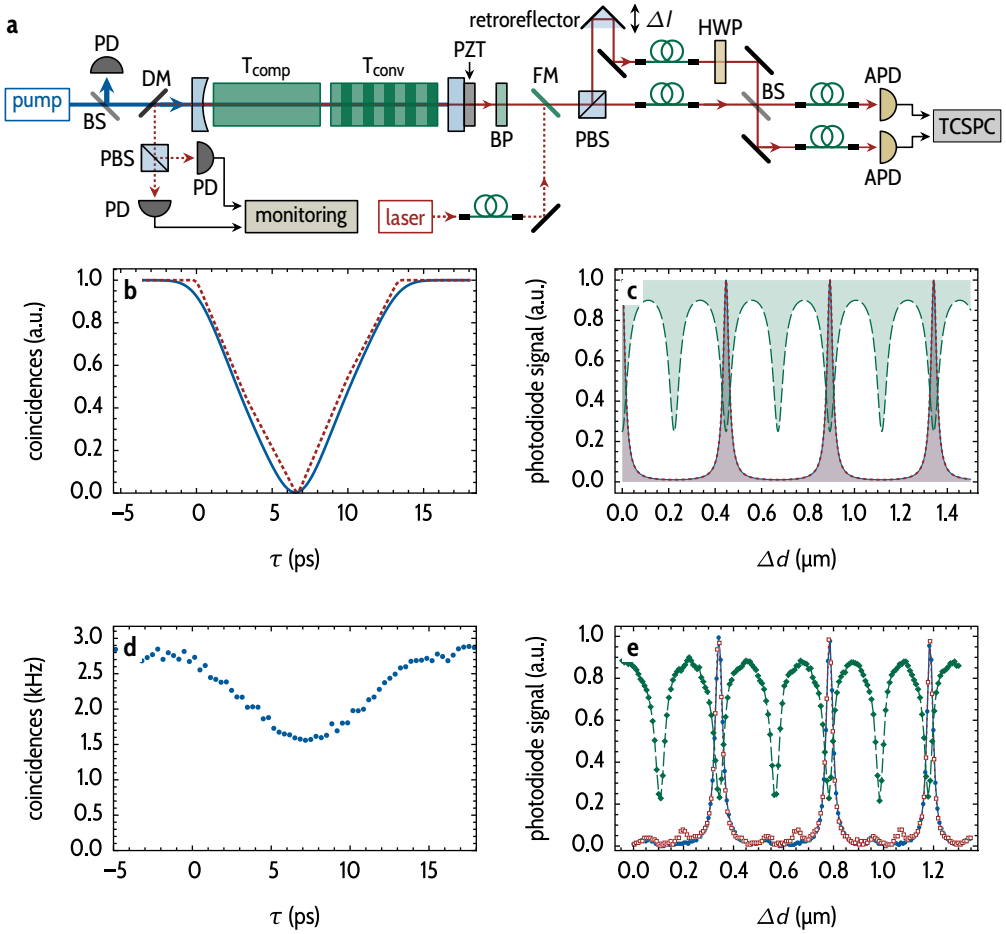

Figure 2.40 | Hong-Ou-Mandel effect measured with a two-crystal cavity. **a**, The experimental setup is identical to the Hong-Ou-Mandel interferometer shown in Fig. 2.39 exept for the photon-pair source. Here, signal and idler photons are generated inside the cavity with compensation crystal. A 1 nm bandpass filter suppresses spurious photons from the background fluorescence. To monitor the signal and idler field resonance frequencies we utilize the master laser. The cavity transmission of the laser is monitored with two photodiodes (PD) while scanning the cavity-mirror position via the piezo-electric transducer (PZT) attached to the outcoupling mirror (see Fig. 2.12). The master laser is directed to the cavity over a flip mirror (FM) which does not block the generated signal and idler photons during the measurement of the Hong-Ou-Mandel effect. **b**, Theoretical simulation of the Hong-Ou-Mandel dip for perfect degeneracy of the signal and idler frequency combs. As measured for this cavity via spectroscopy, the effective reflectivity of the cavity is assumed to be $\bar{r} = 0.9$ (see section 2.3.3). The theoretical model (Eq. 2.5.3) is simulated for a bandpass filter bandwidth of 1 nm (——) and, for comparison, 10 nm (----). **c**, Simulation of the signal (——), idler (----), and pump (– –) photodiode signal as a function of the displacement Δd of the cavity mirror. **d**, Measured Hong-Ou-Mandel dip with a visibility of 39.9(3) %. **e**, Measured signal (——), idler (----), and pump (– –) cavity transmission functions. For the idler field, the presence of side peaks indicates an imperfect alignment of the cavity.

simulation of the theoretical expression shown in this section solely relies on numerical integration of Eq. 2.5.3. This has the advantage that the theoretical predictions can be simulated even for the complicated joint spectral density discussed in the following and, e.g., for arbitrary additional spectral filtering steps.

Two-crystal configuration: joint spectral amplitude. By comparing the experimental data with the theoretical predictions of the HOM dip shape, we can directly verify the explicit expressions for the cavity round-trip phase derived in section 1.2.2. The round-trip phase directly enters the joint spectral amplitude via the cavity transfer functions $\mathcal{T}(\omega)$ of the different fields. A compensation crystal inside the cavity also modifies the phase-balancing amplitude $p(\omega_\mathrm{s}, \omega_\mathrm{i})$.

We can write the joint spectral amplitude of the biphoton state for the two-crystal cavity (with Eq. 1.1.72) as:

$$\psi_\mathrm{cavity}^\mathrm{two\ crystal}(\omega_\mathrm{s}, \omega_\mathrm{i}) \propto \psi_\mathrm{sp}(\omega_\mathrm{s}, \omega_\mathrm{i})\mathcal{T}_\mathrm{p}(\omega_\mathrm{s}+\omega_\mathrm{i})\mathcal{T}_\mathrm{s}(\omega_\mathrm{s})\mathcal{T}_\mathrm{i}(\omega_\mathrm{i})p_\mathrm{cavity}^\mathrm{two\ crystal}(\omega_\mathrm{s}, \omega_\mathrm{i}), \tag{2.5.4}$$

where the cavity transfer functions $\mathcal{T}_\mathrm{n}(\omega_\mathrm{n})$ are given by Eq. 1.1.61 and the corresponding round-trip phases are given by Eq. 1.2.22. Using Eqs. 1.2.38 and 1.2.40 one finds:

$$\begin{aligned}\psi_\mathrm{cavity}^\mathrm{two\ crystal}(\omega_\mathrm{s}, \omega_\mathrm{i}) \propto\ & \psi_\mathrm{sp}(\omega_\mathrm{s}, \omega_\mathrm{i})\mathcal{T}_\mathrm{p}(\omega_\mathrm{s}+\omega_\mathrm{i})\mathcal{T}_\mathrm{s}(\omega_\mathrm{s})\mathcal{T}_\mathrm{i}(\omega_\mathrm{i}) \\ & \times \left[1 + \bar{r}e^{i[\Delta k_\mathrm{qpm} l + 2\Delta k_\mathrm{comp} l + \Delta\Phi_0]}\right],\end{aligned} \tag{2.5.5}$$

where $\Delta k_\mathrm{comp} l$ is the relative phase gathered by the fields inside the compensation crystal and $\Delta\Phi_0$ is the relative phase originating from the mirror phase shifts and the Gouy phase. For the experiments discussed in this section, the Gaussian beam profile of the fields does not affect the shape of the HOM dip since the focussing parameter $\xi \approx 0.2$ is relatively small (see section 1.2.1) for the cavity under investigation. Therefore, we use the plane-wave expression (Eq. 1.1.29) for the signal-pass joint spectral amplitude:

$$\begin{aligned}\psi_\mathrm{cavity}^\mathrm{two\ crystal}(\omega_\mathrm{s}, \omega_\mathrm{i}) \propto\ & s(\omega_\mathrm{s}+\omega_\mathrm{i})\,\mathrm{sinc}\big(\Delta k l/2\big)e^{i\Delta k l/2} \\ & \times \mathcal{T}_\mathrm{p}(\omega_\mathrm{s}+\omega_\mathrm{i})\mathcal{T}_\mathrm{s}(\omega_\mathrm{s})\mathcal{T}_\mathrm{i}(\omega_\mathrm{i}) \\ & \times \left[1 + \bar{r}e^{i[\Delta k_\mathrm{qpm} l + 2\Delta k_\mathrm{comp} l + \Delta\Phi_0]}\right].\end{aligned} \tag{2.5.6}$$

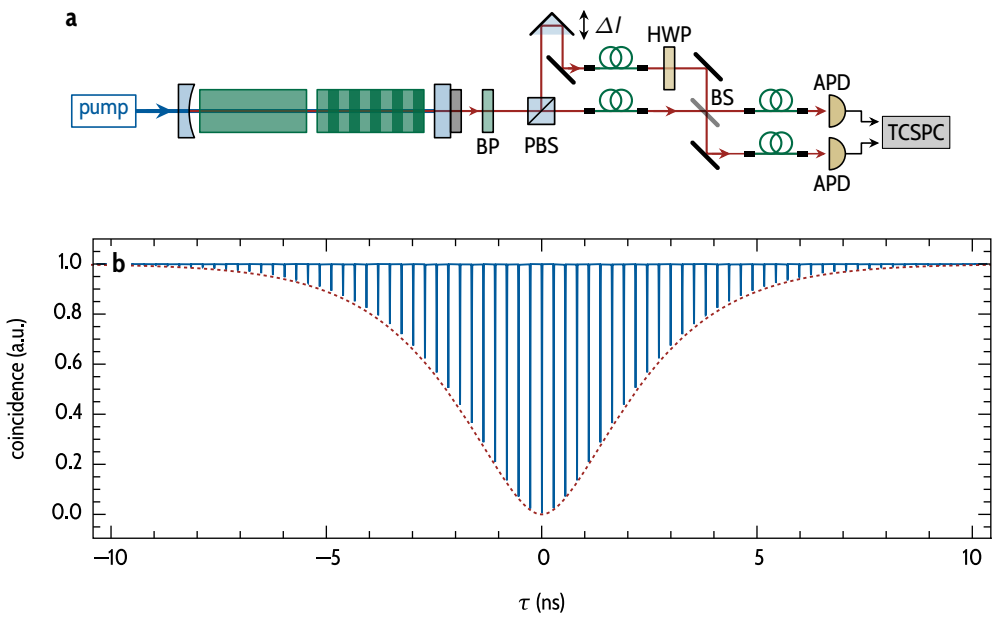

Figure 2.41 | Revivals of the Hong-Ou-Mandel dip for the two-crystal cavity. **a**, Experimental setup. For details refer to Fig. 2.40. **b**, For a cavity-enhanced photon-pair source with compensation crystal and identical signal/idler round-trip times $\Delta t_{\mathrm{rt,\,s/i}}$, we observe a comb of Hong-Ou-Mandel dips spaced by multiples of $\Delta t_{\mathrm{rt,\,s/i}}/2$. For this simulation, signal and idler fields are tuned to perfect degeneracy. The effective reflectivity is $\bar{r} = 1$ and the relative phase is $\Delta\Phi = 0$. Except for their visibility, each of the HOM dips has the same shape (see Fig. 2.40b). Eq. 2.5.8 describes the envelope (----) of the HOM dips.

Hong-Ou-Mandel dip and revivals. Fig. 2.41 shows the coincidence rate $R_{\text{coin}}(\tau)$ simulated with Eqs. 2.5.3 and 2.5.6 for a two-crystal cavity tuned to degenerate triple resonance. The effective reflectivity is set to $\bar{r} = 1$ and the relative phase is $\Delta\Phi = 0$.

Instead of a single Hong-Ou-Mandel dip, we observe a comb of dips separated by multiples of half the signal/idler cavity round-trip time Δt_{rt}.[36,117,119,150] Each of these dips has the same shape as the central dip shown in Fig. 2.40b. Therefore, the adjacent dips are called the revivals of the central Hong-Ou-Mandel dip. But, the individual dips have differing visibilities. While the central dip has a visibility of 1, the visibility of the adjacent dips scales with an inverted bell-shaped distribution with a width determined by the cavity decay rate.

Envelope of the revivals. To analyze the envelope of the dips, we use the idealized single-mode joint spectral amplitude consisting of two Lorentzian contributions with identical cavity decay rates $\Gamma_{s/i}$ (see Eqs. 1.4.14 and 1.4.18):

$$\psi_{\text{single mode}}(\omega_{\text{s}}, \omega_{\text{i}}) = L(\Gamma_{\text{s/i}}, \omega_{\text{s}}) L(\Gamma_{\text{s/i}}, \omega_{\text{i}}). \tag{2.5.7}$$

With Eqs. 2.5.3 and 2.5.7, the normalized HOM dip is:

$$R_{\text{coin}}^{\text{single mode}}(\tau) = 1 - \left[1 + \Gamma_{\text{s/i}}|\tau|\right] e^{-\Gamma_{\text{s/i}}|\tau|}. \tag{2.5.8}$$

The full width at half maximum of this Lorentzian distribution is larger by a factor of ≈2 than the signal-idler correlation function for the same down-conversion cavity configuration (compare Figs. 2.31b and 2.41b). Fig. 2.41 also shows that Eq. 2.5.8 is the envelope for the comb of HOM dips for the two-crystal cavity-enhanced photon-pair source.

Adjacent HOM dips. The presence of the adjacent HOM dips has been confirmed for the two-crystal cavity. But, the shape of the adjacent dips is only identical to the central dips for the idealized parameters chosen for Fig. 2.41. A detailed study of the shapes of the adjacent dips as a function of the compensation crystal temperature, the relative phase $\Delta\Phi$, and the effective reflectivity $\bar{r}$ does not lie within the scope of this thesis. In the following, we will present experimental measurements only for the central HOM dip. Firstly, we discuss how the parameters of the joint spectral amplitude were derived and then present the experimental results.

Parameter values of the joint spectral amplitude. In this section, most of the parameters needed to describe the joint spectral amplitude are taken from the fits to the measurements of the signal-photon spectrum (see Fig. 2.21) and the signal-idler correlation function (see Fig. 2.31). These measurements yield precise values

for the cavity length, the length of the crystals and the reflectivity of the mirrors for the different fields. The only free parameters needed to fully describe the joint spectral amplitude are the offsets to the cavity round-trip phases of the three fields. These offsets shift the resonance frequencies of the three fields to the desired values. To determine these offsets, we would need much more precise absolute values of the mirror spacing, the lengths of the crystals and their precise orientations with respect to the optical axis. We measure changes of the compensation crystal temperature ΔT_{comp} via the set point value of the corresponding temperature controller with an uncertainty of ≈50 mK.

Experimental results. Fig. 2.40d displays the measured central Hong-Ou-Mandel dip for the two-crystal cavity with temperatures and orientations of the crystals optimized for maximum visibility. For each position of the retroreflector, the coincidence rate at the detectors was integrated for 20 s. The shape of the HOM dip is in good agreement with the theory. Instead of a triangular shape, the edges are smoothed out and we observe an inverted Gaussian HOM dip. This smoothing can be attributed to the 1 nm bandpass filter (see Fig. 2.40b).

As expected from the non-resonant measurements with the same HOM interferometer presented in Fig. 2.39, the measured visibility is much lower than the theoretical value of 1. The data shown here is rather noisy due to random fluctuations of the photon-pair generation rate over the measurement duration. Therefore, we do not present a direct fit of the theory to the data points.

2.5.3 | Hong-Ou-Mandel dip and the relative phase $\Delta\Phi$

Note, that the relative phase $\Delta\Phi = 2\Delta k_{\text{comp}} l + \Delta\Phi_0$ in Eq. 2.5.6 can be tuned by changing the compensation crystal temperature T_{comp}. Fig. 2.42a shows this dependency. A full phase shift of $\Delta\Phi = 2\pi$ corresponds to a temperature difference of $\Delta T_{\text{comp}} \approx 0.6$ K.

Temperature tuning of the compensation crystal. In Fig. 2.42b, we simulate the coincidence rate $R_{\text{coin}}(\tau)$ as a function of the compensation crystal temperature. For $\Delta T_{\text{comp}} \approx 0.3$ K (which corresponds to a relative phase difference of $\Delta\Phi \approx \pi$), instead of a reduction of the coincidence rate at $\tau = 0$, we find an increase in coincidence events. Due to the phase relation between the fields inside the cavity, signal and idler photons, now, preferably split at the beam splitter. Therefore, by adjusting the compensation crystal temperature, we can tune the statistics of the generated photons from a bosonic (bunching) to an intermediate or partly fermionic (splitting) characteristic.[297,298] For larger temperature detunings of the compensation crystal ($\Delta T_{\text{comp}} \approx 0.6$ K), the Hong-Ou-Mandel dip is

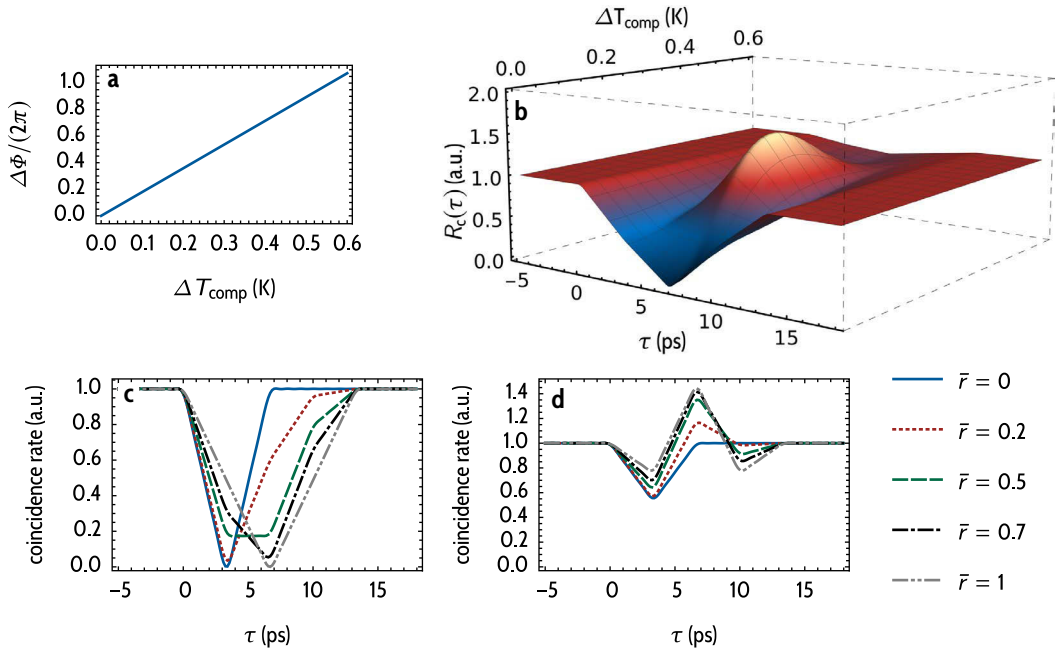

Figure 2.42 | Hong-Ou-Mandel dip depending on compensation-crystal temperature. **a**, Relative phase $\Delta\Phi$ as a function of the compensation-crystal temperature ΔT_{comp}. **b**, Simulation of the coincidence rate $R_c(\tau)$ (Eq. 2.5.3) as a function of the compensation-crystal temperature. The Hong-Ou-Mandel dip is simulated for a 10 nm bandpass filter. For $\Delta T_{comp} \approx 0.3$ K ($\Delta\Phi \approx \pi$), instead of photon bunching, photon antibunching is observed. For $\Delta T_{comp} \approx 0.6$ K ($\Delta\Phi \approx 2\pi$), the HOM dip is restored but the signal and idler photons are spectrally distinguishable, which reduces the visibility. **c**, HOM dip for $\Delta T_{comp} = 0$ ($\Delta\Phi = 0$, perfect spectral indistinguishability) as a function of the effective reflectivity $\bar{r}$. For $\bar{r} = 1$, the width of the HOM dip is doubled compared to $\bar{r} = 0$ due to the doubled parametric interaction length. For $\bar{r} = 0.5$, the visibility of the HOM dip is less than unity since the paths of signal and idler photons are partly distinguishable.[82] **d**, HOM dip for $\Delta T_{comp} = 290$ mK ($\Delta\Phi \approx \pi$) for different values of $\bar{r}$.

recovered, but the visibility is reduced since the individual resonances of the signal and idler fields do not coincide any more such that signal and idler photons are spectrally distinguishable.

Effective reflectivity and indistinguishability. The effective reflectivity $\bar{r}$ determines the shape of the HOM dip (see Figs. 2.42c and 2.42d). For $\bar{r} = 1$ and $\Delta T_{\mathrm{comp}} = 0$, the width of the HOM dip is doubled compared to $\bar{r} = 0$ due to the doubled interaction length. For this situation, photon pairs generated in the forward direction cannot be distinguished from photon pairs generated in the backward direction, in principle.

For $\bar{r} = 0.5$, the visibility of the HOM dip is less than unity since the paths of signal and idler photons are partly distinguishable:[82] Photon pairs generated in the forward direction would require a positive translation $\Delta l > 0$ of the retroreflector to compensate for the time delay with which signal and idler exit the cavity (even for the same number of cavity round-trips). But, photon pairs generated in the backward direction would require a negative translation $\Delta l < 0$ to compensate this time delay. Therefore, there is not value of Δl for which there is no which-way information of the signal and idler paths.

In summary, the measurement of the coincidence rate $R_{\mathrm{coin}}(\tau)$ offers the opportunity to experimentally verify the expression for the joint spectral amplitude (Eq. 2.5.6). Additionally, the parameters $\Delta\Phi$ and $\bar{r}$ can be measured with high resolution by inspecting the HOM dip shape.

Compensation-crystal temperature tuning: experimental results. Fig. 2.43 compares the measured HOM dip for $\Delta\Phi \approx \pi/2$ ($\Delta T_{\mathrm{comp}} \approx 140\,\mathrm{mK}$) with the theoretical predictions. The measurement is in adequate agreement with the theory. The temperature dependent Sellmeier equations of the KTP crystals combined with the full expression of the cavity round-trip phases offer a good estimate of the tuning rates of the individual resonance frequencies. The measured HOM dip shape is compatible with the value $\bar{r} \approx 0.9$ measured for the two-crystal cavity with the high-resolution monochromator (see Fig. 2.21 in section 2.3.3).

As expected, the resonances of signal and idler photons no longer overlap (Fig. 2.43d). Therefore, the photons are partially spectrally distinguishable and we observe low visibilities. In Fig. 2.44 we present the experimental results for two further temperatures of the compensation crystal. These additional measurements fully verify the theoretical model depicted in Fig. 2.42b.

Discussion. When the data discussed in this section was measured,[291] the observed shapes of the Hong-Ou-Mandel dip for the non-degenerate case could not be explained. It was assumed that the shape of the HOM dip for $\Delta T_{\mathrm{comp}} \neq 0$ was caused by the spectral distinguishability of signal and idler fields. But, with

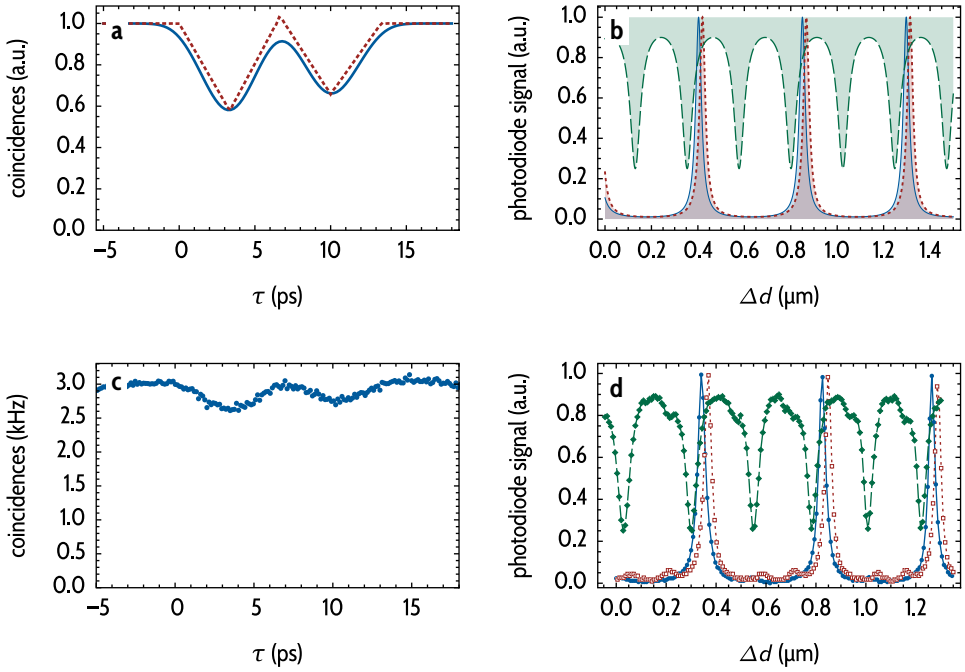

Figure 2.43 | Hong-Ou-Mandel dip for $\Delta\Phi \approx \pi/2$. The same plots as in Figs. 2.40b to 2.40e are shown. The experimental parameters are identical except for the compensation-crystal temperature. Here, the compensation-crystal temperature was shifted by $\Delta T_{\text{comp}} = 140$ mK from the degeneracy point shown in Fig. 2.40. This temperature difference corresponds to a relative phase shift of $\Delta\Phi \approx \pi/2$ (see Fig. 2.42a). **a**, Theoretical model (Eq. 2.5.3) for a bandpass filter bandwidth of 1 nm (——) and 10 nm (----). **b**, Simulation of the signal (——), idler (----) and pump (– –) photodiode signal. **c**, The measured (•) shape of the Hong-Ou-Mandel dip closely resembles the theoretical expecation. Of course, the visibility is lower than in **a** due to the imperfections of the HOM inteferometer. **d**, Measured signal (——), idler (----), and pump (– –) cavity transmission functions. The relative detunings of the resonance frequencies of the different fields are in good agreement with the simulation (**b**). Fig. 2.44 shows the measurement results for $\Delta\Phi \approx \pi$ and $\Delta\Phi \approx 0.8 \times 2\pi$.

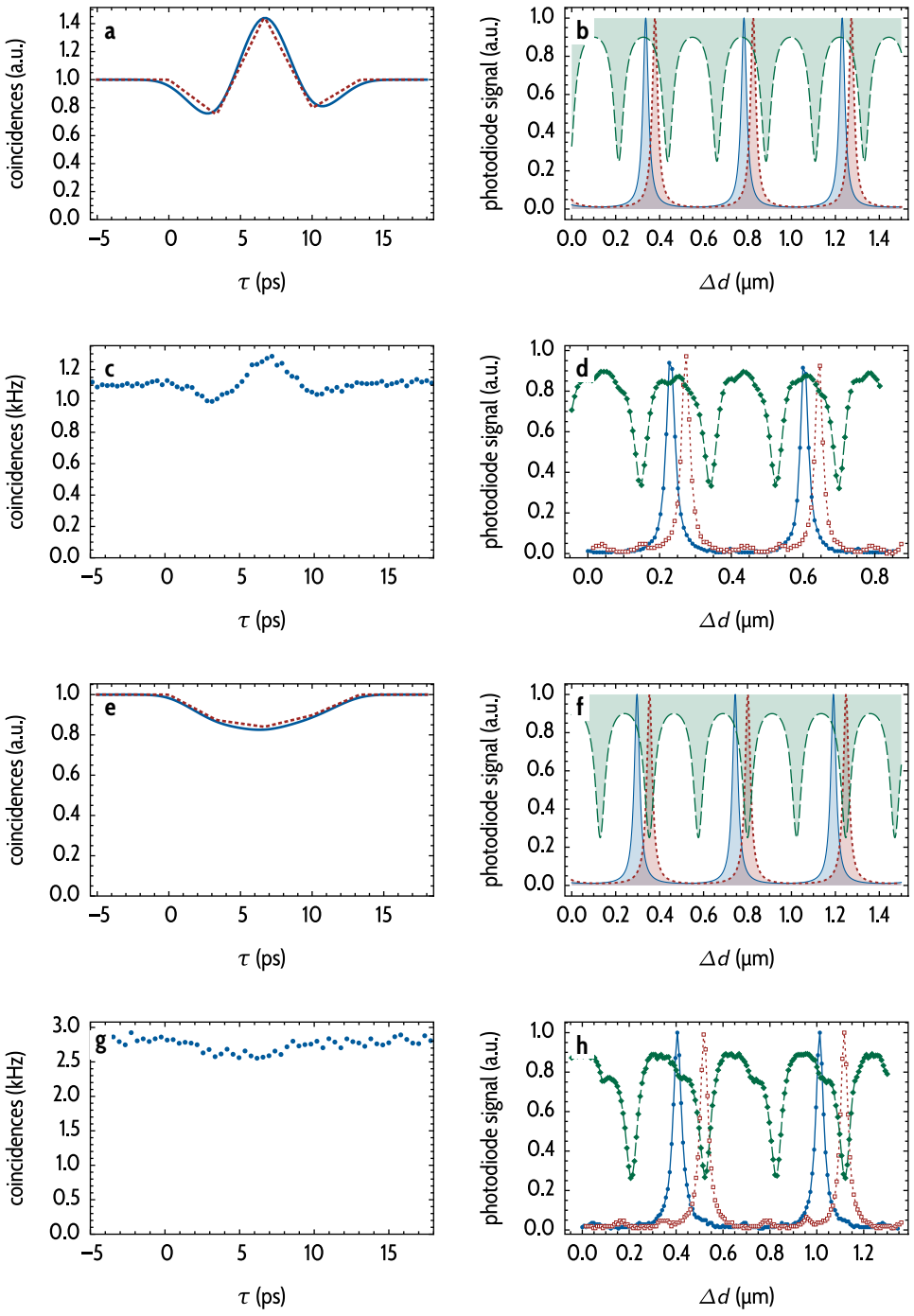

Figure 2.44 | Temperature-dependence of the central HOM dip. Hong-Ou-Mandel dip in the case of a compensation-crystal temperature difference of $\Delta T_{comp} = 290$ mK (figures **a - d**) and $\Delta T_{comp} = 490$ mK (figures **e-h**). The arrangement of both groups of plots is identical to Figs. 2.40 and 2.43.

the theory presented in this thesis, the shape of the HOM dip can be attributed solely to the values of the relative phase $\Delta\Phi$ and the effective reflectivity $\bar{r}$. The spectral distinguishability of signal and idler fields for $\Delta T_{\mathrm{comp}} \neq 0$ plays a minor role as it only limits the visibility of the observed patterns.

We virtually do not require any free parameter to obtain a good agreement between simulations and experimental data (except for the visibility). This is a remarkable result given the complex structure (Eq. 2.5.6) of the joint spectral amplitude.

2.5.4 | Hong-Ou-Mandel effect with single-mode spectral filtering

The Hong-Ou-Mandel dip for the spectrally multi-mode signal and idler fields offers a rich structure. However, the attainable visibility of the HOM dip is limited for a triply-resonant linear cavity without further spectral filtering. In this section, we present the Hong-Ou-Mandel effect with single-mode spectral filtering.

Coherence length with and without spectral filtering. Without external spectral filtering, signal and idler photon wave-packets are localized in narrow time slots during which they can exit the cavity. The temporal width of these time slots is given by the width of the HOM dip ($\Delta\tau_{\mathrm{HOM}} \approx 5\,\mathrm{ps}$). This time delay can easily be compensated by a translation stage since the coherence length is on the order of $\Delta l_{\mathrm{coherence}} = c \cdot \Delta\tau_{\mathrm{HOM}} \approx 1.5\,\mathrm{mm}$.

If only the central mode of the signal and idler frequency comb is spectrally isolated, the spectral bandwidth width of signal and idler photons is on the order of the cavity decay rate $\Gamma_{\mathrm{s/i}}$ (see Eq. 1.3.46). For the two-crystal cavity, $\Gamma_{\mathrm{s/i}} = 2\pi \cdot 120\,\mathrm{MHz}$. This corresponds to a coherence time[173] of $t_{\mathrm{coherence}} = 2/\Gamma_{\mathrm{s/i}} = 2.7\,\mathrm{ns}$ and a coherence length of $\Delta l_{\mathrm{coherence}} = c \cdot t_{\mathrm{coherence}} = 0.8\,\mathrm{m}$. Therefore, a very long translation stage (or an alternative method to introduce a variable time delay between signal and idler photons) would be required to fully sample the HOM dip.

Experimental setup: spectral selectivity. To overcome this experimental challenge, we employ a polarization-based Hong-Ou-Mandel interferometer. Fig. 2.45a shows the experimental configuration: To isolate the central spectral mode of the signal and idler frequency combs, we use the cascaded filter system discussed in section 2.1.3. The cavity resonance of each of the two monolithic filter cavities is tuned to the master-laser frequency. Thus, only the central, degenerate spectral mode of the signal and idler fields is transmitted through the filtering system.

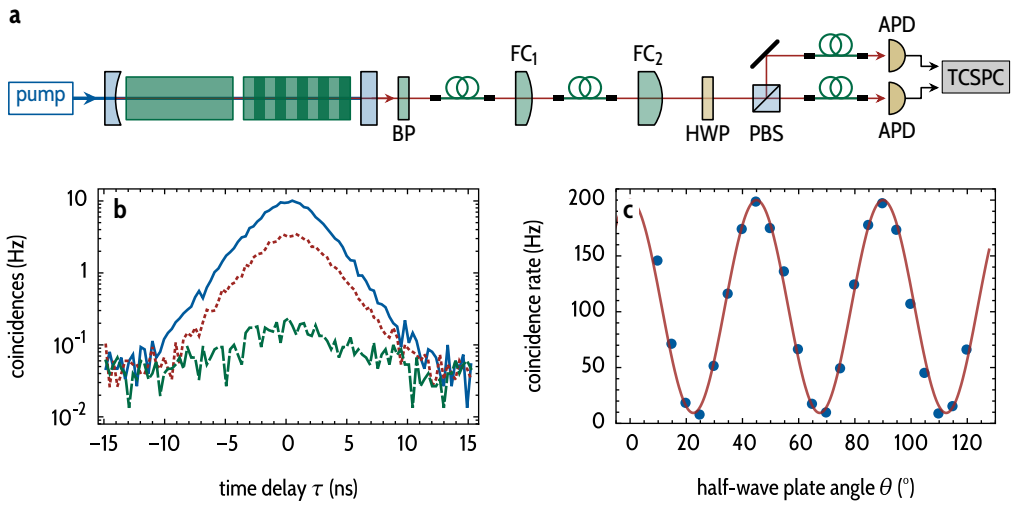

Figure 2.45 | Hong-Ou-Mandel effect with the filtered two-crystal photon-pair source. **a**, The two-crystal cavity is locked to a resonance of the pump beam. The master laser is locked to a hyperfine transition of the cesium D_1-line. A 1 nm bandpass filter blocks the background fluorescence. The resonance frequency of the cascaded filter system (see Fig. 2.10) is also tuned to same hyperfine transition. Therefore, only signal and idler photons generated into the central, degenerate mode of the frequency comb are transmitted by the filtering system. Subsequently, the photons are guided to a polarization-based[126] Hong-Ou-Mandel interferometer. By rotating the half-wave plate (HWP) in front of the polarizing beam splitter, the degree of indistinguishability in the polarization of signal and idler photons can be adjusted. **b**, Start-Stop time-delay histograms measured for $\theta = 0°$ (—), $\theta \approx 10°$ (----) and $\theta = 22.5°$ (– –). The pump-power is 10 mW and the acquisition time is 150 s for the histogram. **c**, Coincidence rate measured (●) without background subtraction and with a coincidence window of 30 ns. A fit (—), results in a visibility of 91(3) %. If we subtract the background caused by uncorrelated photons and detector dark counts, we obtain a visibility of 94(3) %. Figure replicated from Ref. [205].

About 2.5 % of the signal and idler photons are generated into the central spectral mode. All other photons are emitted into the other spectral modes of the frequency combs. The cascaded filtering system nearly completely suppresses these non-degenerate modes: After spectral filtering, approximately 99.6 % of the transmitted photons originate from the central mode. Therefore, the probability to detect two photons from a photon pair which does not originate from the central mode is negligible.

Polarization-based Hong-Ou-Mandel interferometer. Due to this narrow spectral filtering, signal and idler photons can no longer be distinguished by the time delay with which they exit the cavity. Since both signal and idler photons are coupled to a single-mode fiber after spectral filtering, their spatial mode is indistinguishable. Therefore, the polarization of the photons is the only distinguishing degree of freedom.

We measure the Hong-Ou-Mandel effect with a polarization-based HOM interferometer.[126] While a conventional HOM interferometer uses the two spatial input ports of a *non-polarizing* beam splitter, the polarization based HOM interferometer uses a single input port of a *polarization* beam splitter. After spectral filtering, we rotate the polarization direction of signal and idler photons with a half-wave plate and then direct the photons to this polarization beam splitter.

Without the half-wave plate, signal and idler photons are deterministically split at the PBS. But, for a HWP angle of 22.5°, the polarization direction of signal and idler photons is oriented under 45° and −45° with respect to the PBS, respectively. With this input polarization angle, signal and idler photons can no longer be distinguished by their polarization at the PBS. Thus, we observe the Hong-Ou-Mandel effect as a strong reduction of the coincidence rate between detection events recorded with the two APDs behind the output ports of the PBS. Upon rotation of the HWP, we observe a $\cos^2$-shaped oscillation of the coincidence rate.

Experimental results. Figs. 2.45b and 2.45c show the start-stop time-delay histogram and the coincidence rate as a function of the HWP angle θ. For each data point, the integration time is 150 s. For $\theta = 0°$ (distinguishable photons) and a pump power of 10 mW, we detect the maximum coincidence rate of 200 Hz (without correction for the APD detection efficiency) within the coincidence window of 30 ns. For $\theta = 22.5°$ (indistinguishable photons), the coincidence rate drops to 9 Hz.

Visibility. The corresponding HOM visibility is 91(3) %. Detector dark counts and uncorrelated photons generated, e.g. generated by fluorescence, contribute to a background coincidence rate of 4 Hz. With this background rate subtracted, we measure a HOM visibility of 94(3) %. The measured visibility is substantially higher than for the conventional HOM interferometer discussed in the previous section. The main advantage of the polarization-based HOM interferometer is that the spatial modes of signal and idler field are identical at the beam splitter. For a conventional HOM interferometer (Fig. 2.39), alignment of the spatial modes at the HOM beam splitter is necessary. The high visibility reported here also emphasises the polarization-independent operation of the monolithic filter cavities (see Fig. 2.3).

Experimental limitations. But, the visibility is still limited by imperfections of the setup: The polarization-maintaining single-mode fibers preserve only the polarization of either signal or idler photons. Therefore, a degradation of the polarization of at least one field can be expected.

Furthermore, the polarization beam splitter extinction ratio is optimized only for the transmitted beam. The ratio of the transmission of p-polarized photons to transmission of s-polarized photons is $T_p/T_s = 1000$, while for the reflected beam, $R_p/R_s \approx 50(20)$. This limits the maximum achievable visibility of the HOM interferometer to ≈98.5 %.

Finally, we suspect that signal and idler photons exit the cavity with a partial elliptical polarization. We attribute this ellipticity, which limits the attainable HOM visibility, to several factors: On the one hand, the orientation of the crystals' front facets is not perfectly orthogonal to the optical axis such that signal and idler fields are partially mixed due to the spatial walk-off. This corresponds to a configuration where a wave-plate is inserted into a cavity-enhanced photon-pair source to mix signal and idler fields.[53,299] On the other hand, stress-induced birefringence, e.g. inside the outcoupling mirror or the subsequent optical elements, degrades the polarization state of signal and idler photons.

Discussion. For $\theta = 22.5°$, the output state of the polarization-based Hong-Ou-Mandel interferometer is the *NOON-state*:[142]

$$|2002\rangle = |2\rangle_1 |0\rangle_2 + e^{i\phi} |0\rangle_1 |2\rangle_2 , \tag{2.5.9}$$

where the labels 1 and 2 indicate the two output ports of the polarizing beam splitter. The phase shifts for the s- and p-polarization of the dielectric coating of the PBS determines the phase ϕ.

The absolute frequency of the (degenerate) signal and idler photons can be tuned by adjusting the master-laser frequency und optimizing the temperatures and orientations of the crystals inside the cavity. In the above-described experiments, we lock the master laser to an atomic frequency standard. But, in principle, we could lock the master-laser frequency to a resonance of an additional monolithic Fabry-Pérot cavity. We can set the resonance frequency of this locking cavity to any value by temperature tuning. As we discuss in Fig. 2.6, we can stabilize the cavity resonance frequency with a residual drift of less than 5 MHz over a time span of many hours. This frequency deviation is much smaller than the line width of the cavity-enhanced photon-pair source and, thus, should not affect the performance of the photon-pair source negatively for typical applications.

Therefore, with the setup discussed in this section, it is possible to generate a two-photon NOON-state comprised of indistinguishable photons at an arbitrary wavelength. The properties of the photons of a pair are defined in all degrees of freedom: The absolute frequency, the temporal shape of the wave-packet and, thus, the bandwidth are given by the down-conversion process and the filter cavities. The spatial mode is determined by the single-mode fiber after the last

filter cavity. Finally, the polarization is set by the orientation of the polarizing beam splitter.

The two-photon state given by Eq. 2.5.9 can only be verified by post-selection of coincidence events. Due to losses, (e.g. in the filtering system), there is also an admixture of single-photon events for which the corresponding second photon of the pair is missing. Additionally, multi-pair events also degrade the fidelity of the NOON state.

In the following, we will present modified version of the experiment discussed in this section. Instead of the two-crystal cavity, we use the single-crystal configuration. The single-crystal configuration enables us to use a single filtering crystal to obtain (near) single-frequency mode operation of the photon-pair source.

2.5.5 | Single-mode operation of the single-crystal cavity

Fig. 2.46 presents the modified experimental setup for the single-mode operation of the single-crystal cavity. The monolithic low-finesse filtering cavity FC_2 (see section 2.1) selects the central, degenerate spectral mode of the central cluster. The polarization-based HOM interferometer is identical to the previous experiment with the two-crystal photon-pair source.

About 3.5 % of signal and idler photons are generated into the central spectral mode. Due to the low finesse of the filter cavity, the ratio of transmitted photons originating from the central mode to photons originating from other modes is moderately increased to 51 % after the filter cavity. The remaining 49 % of the transmitted signal and idler photons still originate from the other spectral modes or even from other clusters. But, these spurious photons contribute significantly only to the uncorrelated coincidence events in the experiment: The probability to detect both photons from a pair which does not originate from the central mode is below 0.7 %.

Single-crystal cavity Hong-Ou-Mandel dips: theory. The joint-spectral amplitude for a single-crystal cavity is (see Eq. 2.5.4):

$$\psi_{\text{cavity}}^{\text{single crystal}}(\omega_\text{s}, \omega_\text{i}) \propto \psi_\text{sp}(\omega_\text{s}, \omega_\text{i})\mathcal{T}_\text{p}(\omega_\text{s} + \omega_\text{i})\mathcal{T}_\text{s}(\omega_\text{s})\mathcal{T}_\text{i}(\omega_\text{i})p_{\text{cavity}}^{\text{single crystal}}(\omega_\text{s}, \omega_\text{i}). \tag{2.5.10}$$

The single-crystal phase-balancing amplitude is (see Eq. 2.5.5):

$$p_{\text{cavity}}^{\text{single crystal}}(\omega_\text{s}, \omega_\text{i}) = 1 + \bar{r}e^{i\Delta k_\text{qpm} l}. \tag{2.5.11}$$

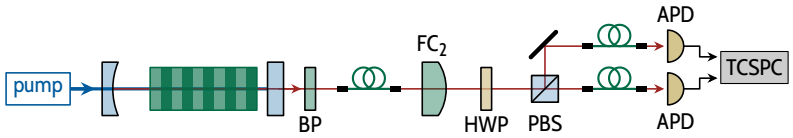

Figure 2.46 | Hong-Ou-Mandel effect – filtered single-crystal cavity. The experimental setup is identical to Fig. 2.43 except for the photon-pair source and the spectral filtering system. Here, the single-crystal cavity is used. In contrast to the Hong-Ou-Mandel experiment performed with the two-crystal cavity, only a single filter cavity with a linewidth of $\Gamma_2 = 2\pi \cdot 885$ MHz is required to achieve (near) single spectral mode operation of the photon-pair source.

Single-crystal Hong-Ou-Mandel dips without narrowband spectral filtering. Without further narrowband filtering, we again observe the full comb of Hong-Ou-Mandel dips (see Fig. 2.47b). Compared to the cavity with compensation crystal (see Fig. 2.41), the visibility of the individual dips is lower. We attribute this reduction of the visibility to two main causes: On the one hand, signal and idler photon generated inside a cavity without compensation crystal are spectrally distinguishable (especially if the spectral mode clusters are not symmetric with respect to the parametric gain envelope as shown in Figs. 2.19 and 2.24). On the other and more importantly, due to the different cavity round-trip times, signal and idler photons do not leave the cavity with equally spaced time delays. The same phenomenon which leads to the splitting of the peaks of the signal-idler correlation function into sub peaks (see Fig. 2.34) results in the broadening of the individual HOM dips. The temporal distinguishability leads to a reduced visibility.

Fig. 2.47c shows the shape of the individual dips for different combinations of the parameters $\bar{r}$ and $\Delta\Phi$. For the idealized case with an effective reflectivity $\bar{r} = 1$ and a relative phase $\Delta\Phi = 0$, each dip has a width of about 40 ps. This is comparable to the width of the substructure of each peak of the signal-idler correlation function (see Fig. 2.36).

As for the photon-pair source with compensation crystal (Fig. 2.42), the shape of the HOM dips depends on the relative phase $\Delta\Phi$ and the effective reflectivity $\bar{r}$. In Fig. 2.47c we plot the shape of the central HOM dip for various parameter combinations. In the ideal case ($\bar{r} = 1$ and $\Delta\Phi = 0$) we find a smooth, asymmetric HOM dip. With a relative phase of $\Delta\Phi = \pi$ we observe strong modulations of the coincidence rate. Again, similar to the results discussed in section 2.5.3, we find time delays τ for which there is a preferred photon splitting instead of photon bunching due to the interference of the three interacting fields inside the cavity. These interference effects have a smaller visibility for smaller values of $\bar{r}$. But, we find a (less pronounced) modulation also for $\Delta\Phi = 0$ and $\bar{r} < 1$.

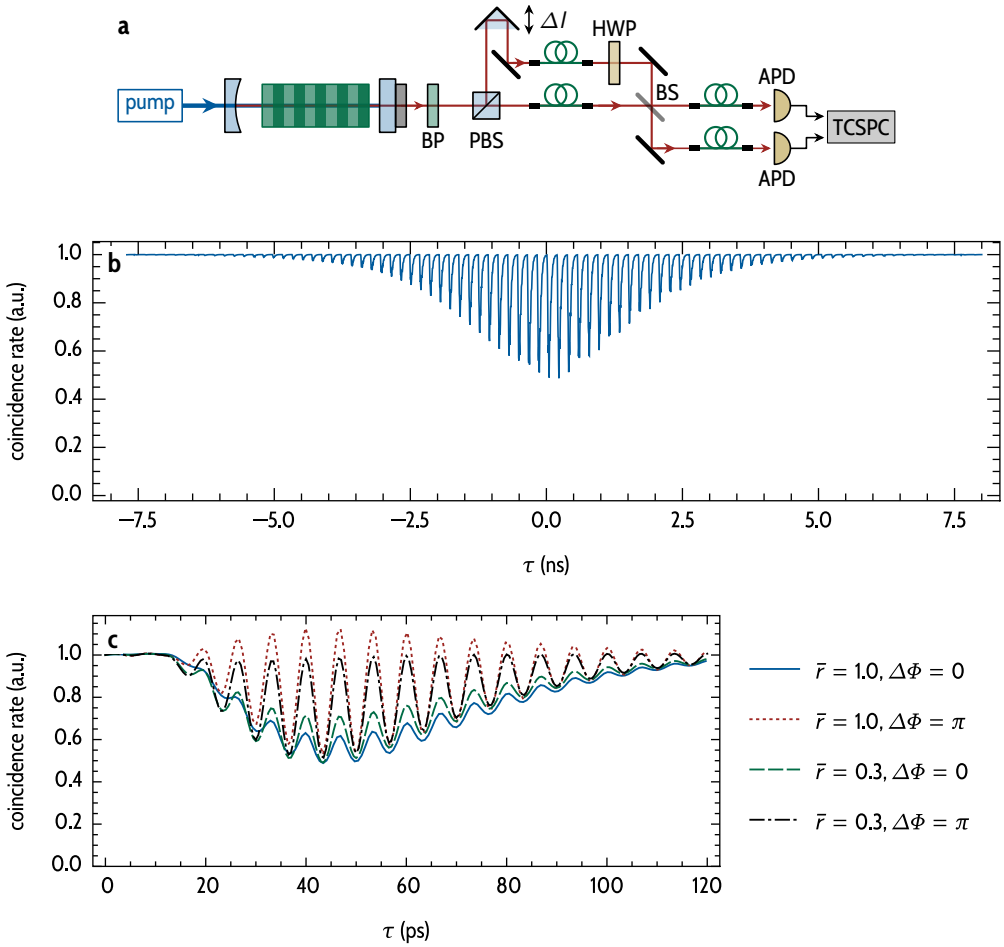

Figure 2.47 | Hong-Ou-Mandel for a single-crystal cavity without narrowband spectral filtering. **a**, Experimental setup. For the details refer to Figs. 2.39 and 2.40. **b**, In contrast to the cavity with compensation crystal, the individual HOM dips have a reduced visibility due to the temporal distinguishability of signal and idler photons. **c**, Detailed view of the central HOM dip. The complicated structure of the two-photon wave packet (see Fig. 2.35) leads to a modulation of the HOM dip. The structure of the adjacent HOM dips is identical to the one shown here. The visibility of the modulation is lower for $\bar{r} = 1$ than for lower values of $\bar{r}$. For a relative phase $\Delta\Phi = \pi$, partial photon anti-bunching (see Fig. 2.42d) can be observed. For all simulations shown here, a 1 nm bandpass filter after the down-conversion cavity is assumed.

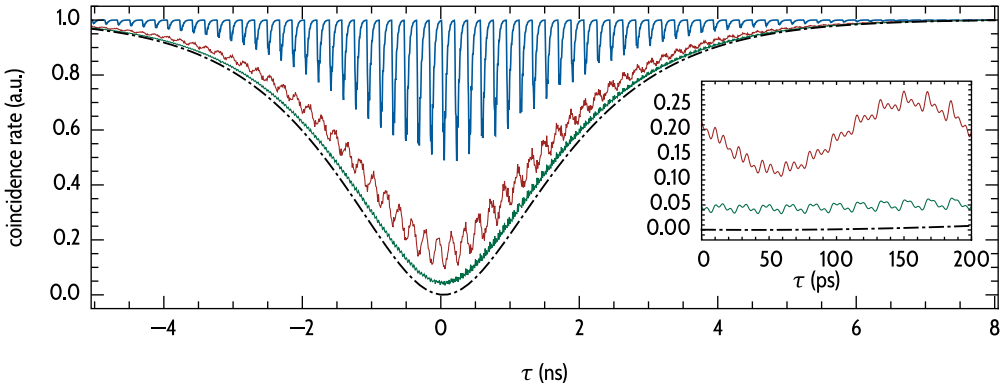

Figure 2.48 | Hong-Ou-Mandel for a single-crystal cavity with narrowband spectral filtering. We plot the coincidence rate (Eq. 2.5.3) without spectral filtering (—), with a single filter cavity (finesse $\mathcal{F} = 10$ (—), finesse $\mathcal{F} = 30$ (—) and a free spectral range of 28 GHz). For comparison, we also show the HOM dip for a single-crystal cavity filtered with two cascaded filter cavities (–·–). For the cascaded filtering system, the free spectral ranges are 28 GHz and 35 GHz, and the finesse is $\mathcal{F}_{1/2} = 30$. The inset is a zoom into the center of the three curves with narrowband filtering. With a single $\mathcal{F} = 10$ cavity, we find a visibility of 84 %. For $\mathcal{F} = 30$, the visibility is 93.7 %. With two cascaded filter cavities, true single-mode operation can be achieved (see Fig. 2.38b). Therefore, we obtain a visibility of 99.9 %.

Single-mode spectral filtering. Spectral filtering with a single cavity modifies the joint spectral amplitude (see Eqs. 1.1.84 and 2.4.20):

$$\begin{aligned}\psi^{\text{single crystal}}_{\text{cavity, filtered}}(\omega_\text{s}, \omega_\text{i}) = \psi^{\text{single crystal}}_{\text{cavity}}(\omega_\text{s}, \omega_\text{i}) \\ \times t_{1\text{s}} t_{1\text{i}} t_{2\text{s}} t_{2\text{i}} t_{\text{sp,s}} t_{\text{sp,i}} \mathcal{T}^{\text{filter}}_{\text{s}}(\omega_\text{s}) \mathcal{T}^{\text{filter}}_{\text{i}}(\omega_\text{i}),\end{aligned} \tag{2.5.12}$$

where $t_{1/2,s/i}$ are the transmission amplitudes of the filter-cavity mirrors for the signal/idler polarization and $t_{\text{sp, s/i}}$ are the signal/idler single-pass transmission amplitudes of the cavity substrate.

In Fig. 2.48 we simulate the coincidence rate $R_{\text{coin}}(\tau)$ (Eq. 2.5.3) for the filtered joint spectral density (Eqs. 2.5.10 and 2.5.12). The plot compares the unfiltered HOM effect (see also Fig. 2.47) with single-cavity filtering to that with cascaded cavity filtering.

Even with a low-finesse cavity ($\mathcal{F} = 10$), there is a strong increase in visibility of the Hong-Ou-Mandel effect from 35 % (unfiltered) to 84 % (filtered). For this moderate spectral filtering, we still observe the revivals of the central HOM dip. For the filter cavity ($\mathcal{F} = 30$) which was used in the experiment (Fig. 2.46), we can no longer detect the revivals and the HOM dip approaches the single-mode regime given by Eq. 2.5.8. But, the visibility with a single filtering cavity is still limited to 94 %. The ragged nature of the plots shown in Fig. 2.48 can be

attributed to an aliasing effect due to the limited number of plot points. The inset in Fig. 2.48 shows that all curves are smooth with small-scale oscillations on top of the envelope.

Fig. 2.48 also shows the HOM dip for a cascaded filtering system with two cavities with finesse of $\mathcal{F}_{1/2} = 30$. From Fig. 2.38b, we can conclude that with this cascaded filtering system, a single-mode regime has been reached. Therefore, we obtain a visibility of the HOM dip of 99.9 %. With a single high-finesse ($\mathcal{F} = 100$) filter cavity, we reach a visibility of just 98.6 %. As discussed in section 2.4.7, these values highlight the advantage of cascaded filtering cavities over single-stage filtering with respect to the mode cleaning.

Experimental results. Figs. 2.49b and 2.49c show the start-stop time-delay histogram and the coincidence rate as a function of the HWP angle θ. For each data point, we choose an integration time of 10 s. For $\theta = 0°$ and a pump power of about 20 mW, we detect the maximum coincidence rate of 23 kHz (without correction for the APD detection efficiency) within the coincidence window of 30 ns. For $\theta = 22.5°$ (indistinguishable photons), the coincidence rate drops below 2 kHz.

As expected, due to the less extensive spectral selectivity of the single filtering stage, the measured visibility of 84(2) % lies below the value observed in the case of the two-crystal cavity. If we correct the data for the uncorrelated background events, we obtain a visibility of 96(4) %. Note that this background subtraction is purely theoretical as the background of uncorrelated photons generated inside the nonlinear crystal cannot be eliminated except by further (single-mode) spectral filtering.

The measured visibility (84(2) %) deviates from the theoretical value 94 % (see Fig. 2.48). The deficiencies of the HOM interferometer discussed in section 2.5.4 also apply here. Additionally, in Fig. 2.49c, there are larger deviations from the ideal $\cos^2$ shape than we would expect from shot noise due to photon counting. The relatively strong deviations, especially at the maxima of the curve, indicate a misalignment of the center of the half-wave plate with respect to the optical axis of the beam behind the filter cavity. This misalignment causes a degradation of the polarization state behind the half-wave plate which results in a lower visibility of the HOM dip.

As expected for a single filtering stage, the visibility is lower than for the two-crystal cavity with the cascaded filtering system (Fig. 2.45). The main advantage of this single-stage filtering is the brightness of the photon-pair source: Compared to the two-crystal configuration with the cascaded filtering system discussed in section 2.5.4, the coincidence rate (at the same pump power) is increased by a factor of 5. This increase can be rationalized as follows:

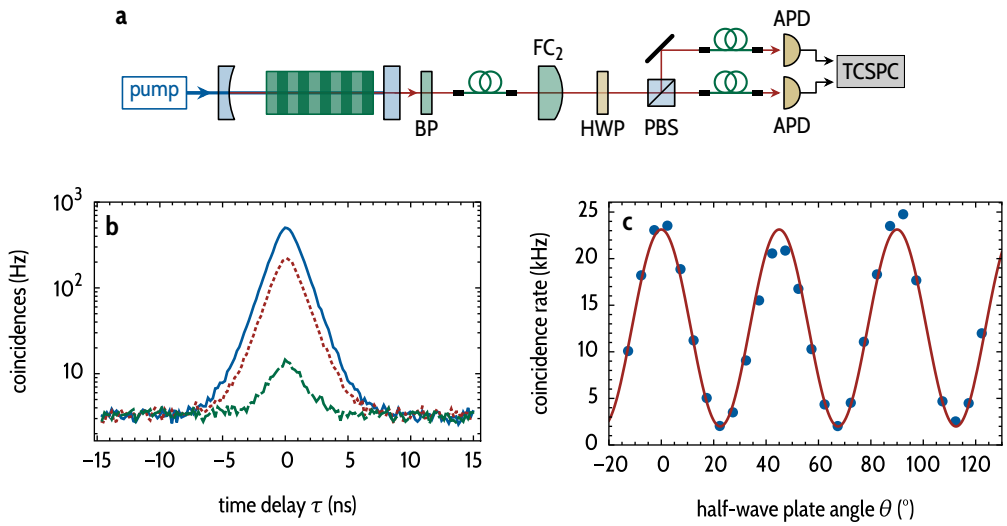

Figure 2.49 | Hong-Ou-Mandel effect – filtered single-crystal cavity. **a**,Experimental setup. For details see Fig. 2.46. **b**, Start-Stop time-delay histograms measured for $\theta = 0°$ (—), $\theta \approx 10°$ (----) and $\theta = 22.5°$ (– –). The pump-power is 20 mW and the acquisition time is 10 s for each histogram. **c**, Coincidence rate measured (•) without background subtraction and with a coincidence window of 30 ns. A fit (—) results in a visibility of 84(2) %. If the background signal caused by uncorrelated background events and detector dark counts is subtracted we obtain a visibility of 96(4) %. Figure replicated from Ref. [138] and extended.

On the one hand, the rate at which photons are generated into the central mode is larger for the single-crystal source (see table 1.1). On the other hand, the transmission of the additional high-finesse filter cavity FC_1, used for the single-mode operation of the two-crystal cavity, is below 35 %.

In the following section, we use the same photon-pair source with single-stage filtering to generate polarization-entangled photons.

2.5.6 | Generation of polarization-entangled photons

In 2002, Kuklewicz and coworkers[118] proposed the usage of cavity-enhanced SPDC as a high-flux source of polarization-entangled photon-pairs. If we spectrally select the central, degenerate mode of a type-II cavity-enhanced down-conversion source, the two photons from a pair are indistinguishable in all degrees of freedom except for their polarization (see Fig. 2.49). With a minor modification of the experimental, we can exploit this indistinguishability to project signal and idler photons into polarization-entangled two-photon state by post-selection.

Probabilistic beam splitting and post selection. In the experimental setup depicted in Fig. 2.49a, we replace the polarizing beam splitter (BS) by a 50/50 non-polarizing beam splitter. This beam splitter probabilistically directs the signal and idler photons to either output port. With a probability of 50 %, signal and idler photons from a pair exit BS at different output ports. In this case where the two photons split, we do not have any *which way* information about which photon exit the BS at the first and the second output port, respectively: The signal and idler photons are indistinguishable in all degrees of freedom except for their polarization.

If we record only those events where there is a photon at either output port of the BS, we project the photons into a polarization-entangled two-photon Bell state:

$$\left|\psi\right\rangle = \left|H\right\rangle_1 \left|V\right\rangle_2 + e^{i\phi} \left|V\right\rangle_1 \left|H\right\rangle_2 , \tag{2.5.13}$$

where the dielectric coating of the beam splitter determines the phase ϕ and the indices 1 and 2 indicate the two output ports of the beam splitter.

Experimental verification. In the following we present an experimental verification that the two photon are entangled by measuring the Bell-state fidelity of the post-selected two-photon state. Fig. 2.50a shows the experimental setup: We use the same setup as in Fig. 2.49 to generate (near) single-mode, degenerate photons with a single-crystal cavity and single-stage narrowband spectral filtering. After probabilistic splitting of the photons at the non-polarizing 50/50 beam splitter, we collect the photons into single-mode polarization-maintaining fibers. In each arm, we use a set of quarter-wave and half-wave plates followed by a linear polarizer to measure the Bell-state fidelity of the generated two-photon state. By rotating the wave-plates with respect to the input polarization axes, we measure coincidence rates between the two single-photon detectors in different polarization bases.

Dietz and Müller present details of this measurement scheme in Ref. [301] and Ref. [300]. An analog characterization of a down-conversion-based entangled photon-pair source has been published in Ref. [292].

Fig. 2.50b shows the experimental results. The rotation angles of the quarter-wave plates determine the measurement basis. For each basis, the coincidence rate at the detectors is measured as a function of the rotation angle of the half-wave plate in the upper arm. We then infer the Bell-state fidelity by computing the visibility of these oscillations measured in each basis.[300,301] The measurement was performed and data kindly provided by Chris Müller

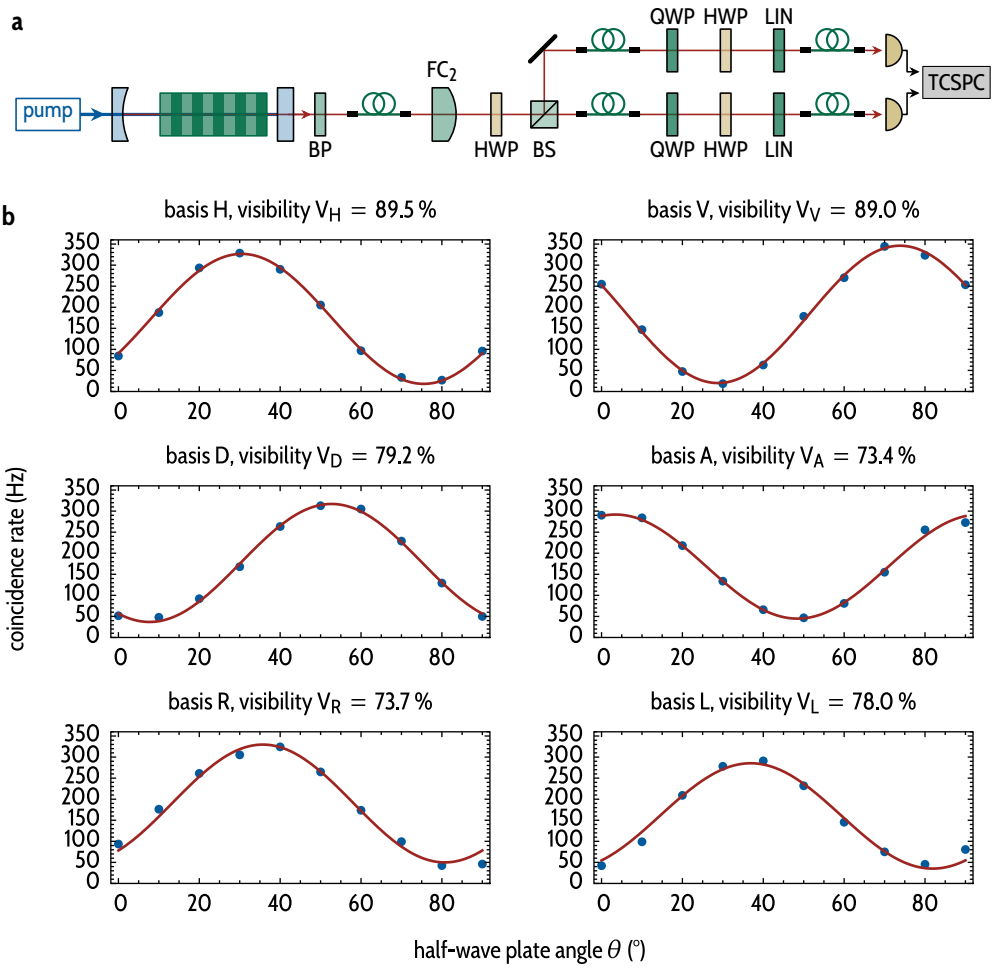

Figure 2.50 | Entanglement verification by measuring the Bell-state fidelity. **a**, We generate photon pairs with the single-crystal cavity with single-stage narrowband filtering identical to Fig. 2.49. A polarization-entangled two-photon state is generated by post-selection of split photon pairs after the non-polarizing beam splitter (BS). After splitting, the photons are collected into single-mode polarization-maintaining fibers. With quarter-wave (QWP) and half-wave (HWP) plates, linear polarizers (LIN) and two avalanche photodiodes, we measure the Bell-state fidelity[292,300] of the generated two-photon state. **b**, The combination of the QWP rotation angles and the angle of the HWP in the lower arm determines the measurement basis (H horizontal, V vertical, D diagonal, A anti-diagonal, R right circular, L left circular). We measure the visibility of the coincidence rate in each basis by rotating the half-wave plate in the upper arm. Measurement performed and data kindly provided by Chris Müller.

Measured Bell-state fidelity. Since, with a single low-finesse filter cavity, we do not observe perfect Hong-Ou-Mandel interference (see Fig. 2.49). Therefore, we expect the visibility of measured oscillations to be on the same order of magnitude as the HOM visibility. Indeed, we measure visibilities in range of 73 % to 89 % with maximum detected coincidence rates of up to 350 Hz at a pump power of 15 mW. These values result in an estimated Bell-state fidelity of 85(4) %.

Discussion. The remaining spectral distinguishability of signal and idler photon after the single-stage filtering directly affects the Bell-state fidelity.[302] Therefore, to improve upon the measured Bell-state fidelity, we need to increase Hong-Ou-Mandel visibility. Here, the same experimental limitations of the spectral filtering and the degradation of the polarization of signal and idler photons apply as discussed in sections 2.5.4 and 2.5.5.

With a two-stage spectral filtering and improved polarization optics a Bell-state visibility well above 95 % should be easily attainable. With an optimized setup, a detected rate of polarization-entangled photons in the range of 100 Hz per mW of pump power is within reach. While this value certainly cannot compete with other state-of-the-art sources of entangled photons,[303,304] it is on the same order of magnitude as other atom-resonant entangled cavity-enhanced down-conversion sources[107,127,142,151]

3 Heralded wave packet manipulation and storage of a frequency-converted pair photon at telecom wavelength

This chapter is a revised and extended version of the article published as Ref. [283].

Contributions. The frequency-conversion setup presented in this article was originally planned and set up by Benjamin Sprenger and reinstalled and operated by Tim Kroh. The single-crystal down-conversion cavity developed for this thesis and discussed in chapter 2 was used as a heralded single-photon source for all experiments presented in this chapter. All authors of the original manuscript planned the experiments and discussed the results. Tim Kroh wrote the original manuscript with detailed contributions from the other authors. The author of this thesis analyzed the data and prepared the figures. Tim Kroh and the author of this thesis contributed equally to the experiments presented in this chapter.

Changes and additions. In contrast to the original manuscript, in this chapter, certain passages (e.g. the description of the photon-pair source) were omitted to avoid the repetition of topics already discussed in other chapters. Furthermore, some sections of the original manuscript were adjusted (e.g. Fig. 3.6) for better readability and adopted to account for the new findings discussed in this thesis. Other parts (e.g. Fig. 3.4 and the accompanying discussion) were either added to relate to the findings of section 2.4 or extended to account for recent results published in the literature. The figures of the original manuscript were optimized for better readability.

Overview. Future optical quantum networks could be based on a hybrid platform of dissimilar quantum systems. Within such a platform, joint quantum states have to be mediated either by single photons, photon pairs or entangled photon pairs. The photon wavelength has to lie within the telecommunication band to enable long-distance fiber transmission. In addition, the temporal shape of the photons needs to be tailored to efficiently match the involved quantum systems. Altogether, this requires the efficient coherent wavelength-conversion of arbitrarily shaped single-photon wave packets.

In this chapter, we demonstrate the wavelength-conversion of heralded single photons generated by cavity-enhanced SPDC and verify the conservation of the temporal wave packets upon conversion. Subsequently, we present the heralded temporal modulation of single-photon wave packets as well as the synchronization of state manipulation and detection. This experiment illustrates that our setup meets common requirements for quantum networks. In a third experiment, we delay a heralded single photon by 45 µs in a fiber spool. We implement all three experiments using commercial telecommunication fiber-optical components which will permit the transition of quantum networks from the lab to real-world application. By combination of the technologies discussed in this chapter, the storage and temporal shaping of single photons in a switchable fiber-loop becomes feasible.

3.1 | Introduction

In this chapter, we propose the implementation of an optical quantum network possessing the following four main properties in reference to David DiVincenzo's criteria[305] for quantum computing:

1. Bright sources of indistinguishable and pure single photons and photon pairs which are standardized in frequency.
2. Quantum frequency conversion of single photons to the telecom band for long-distance transmission of quantum states.
3. Tailoring of the temporal envelope of the photons to optimize their shape for absorption and interaction processes in stationary quantum systems.
4. Storage of quantum states in quantum memories.

Photon-pair states will play a major role in long-distance quantum networks as transmitters of heralded quantum information and as carriers of entanglement between remote nodes.[67,93,94] Many current high-quality sources provide indistinguishable single photons,[102,126,138,260,306–311] and sources of entangled photons[121,312–314] already exist in the near-infrared region.

Requirements on photonic states. However, these photons have to be synchronized[315] and matched with respect to their specific task in the network. For example, the transmission of photons over long distances in optical fibers requires single photons with wavelengths in the telecommunications band to reduce absorption losses to a minimum.[316] Additionally, short-range sections of a network, which perform operations on the quantum states, depend upon shared frequency standards. They are, for example, based on transitions in rubidium[53,317–320]

or cesium (Cs)[65,128,143,205,321] vapor cells to ensure indistinguishability among photons generated by different sources.

The generation of non-degenerate pairs of photons at an atomic transition and in the telecom band has been proposed[322] and implemented.[133,145,146,149,155,273,292] But, quantum communication applications ultimately require[323,324] deterministically generated single photons[213,236,325] and photon pairs,[326,327] e.g. to grant unconditional security.[328–330] If the single-photon sources are based on spontaneous processes (e.g. SPDC or spontaneous four-wave mixing), unconditional security is prohibited by the non-vanishing probability of multi-photon-pair generation.[236,331,332]

Quantum frequency conversion. Fig. 3.1 presents the basic principle of the experiments discussed in this chapter. Single photons are superimposed with a high-power classical laser beam inside a waveguide with a strong $\chi^{(2)}$ nonlinearity. By difference frequency generation, the energy of a pump photon is subtracted from the single photon. The converted photon exits the waveguide with a wavelength in the telecom range at about 1550 nm. The theory of quantum frequency is well established in the literature[333,334] and will be presented elsewhere by Tim Kroh and Chris Müller in detail.

Coherent quantum frequency conversion[333] in nonlinear crystals is a well-established and highly efficient tool to convert photons to the telecom band while preserving important parameters, for example the photon statistics, indistinguishability,[159,338–343] as well as entanglement.[344–348] Also, previous studies demonstrated quantum correlations between atomic ensembles (as an example for a stationary node in a network) and frequency-converted photons in the telecom band.[342,349]

Wave-packet shaping. Besides the frequency, the polarization and the spatio-temporal wave packet of the photons also have to be matched to optimize the storage efficiency in a quantum memory.[350–352] Proposals exist that facilitate full control over the converted photons' waveform by spectral,[353] electro-optic[354] and fast temporal[355,356] modulation of the pump light. So far, only few studies[357–360] exploit nonlinear processes to control and modify single-photon wave packets to improve photon indistinguishability.

Quantum memories. Finally, photon storage is crucial to synchronize the operation of quantum logic gates,[172] error correction,[361–363] or entanglement distillation.[24,364,365] Promising photon storage techniques which utilize neutral atoms or ions as quantum memories require that the involved photons are in resonance with atomic transitions.[366–368] Optical fibers allow for simple realization of broadband, low-loss delay lines and storage devices for photons at

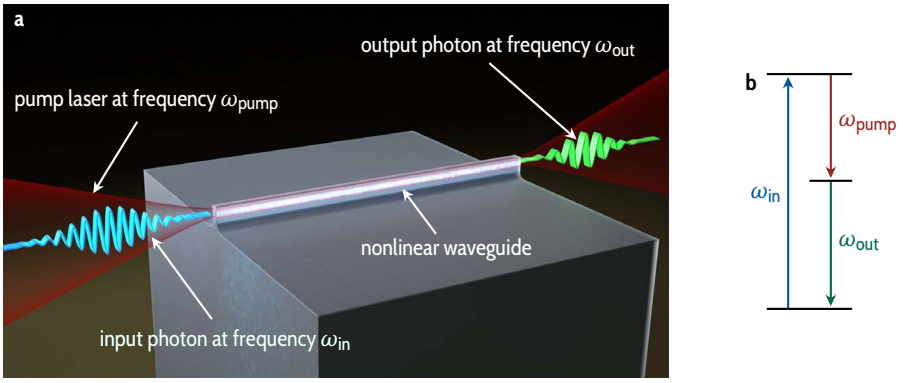

Figure 3.1 | Quantum frequency conversion. **a**, Artistic representation of the process of quantum frequency conversion[333,335] (not to scale): An input photon at frequency ω_{in} is superimposed with a strong classical pump laser at frequency ω_{pump}. The two fields are coupled into a waveguide which guides only a single mode spatial at the pump wavelength.[336] For the input and the output photon wavelength, the waveguide is spatially multi mode. The spatial mode of the input field needs to be matched to the fundamental mode of the waveguide for maximum conversion efficiency. The waveguide is fabricated of a periodically poled nonlinear material and is phase-matched for the desired process. The strong confinement of the fields inside the waveguide enhances the $\chi^{(2)}$-nonlinearity which is utilized for difference frequency generation. **b**, The energy $\hbar\omega_{pump}$ of a pump photon is subtracted from the input photon. After frequency conversion, the output photon has the energy $\hbar\omega_{out} = \hbar\omega_{in} - \hbar\omega_{pump}$. Quantum frequency conversion is a coherent process.[337]

telecom wavelengths. A simple photon storage device could be built with a fiber loop combined with a fast-switching electro-optic modulator to inject and retrieve the photons at discrete times.[369–372]

Storage time-efficiency product. To compare different types of quantum memories, the product of storage time t_{storage} and retrieval efficiency $\eta_{\text{retrieval}}$ represents a common figure of merit.[373] In a delay loop, the storage time is defined by the speed of light in the fiber c_{fiber} and its length L. This would promise arbitrarily long storage times if the non-zero photon absorption in the fiber did not fundamentally limit the transmission due to losses. The global maximum of the time-efficiency product is found at

$$T_{\text{storage}} \cdot \eta_{\text{retrieval}} = 90\,\mu\text{s} \cdot 37\,\%, \tag{3.1.1}$$

for a fiber length of 18.9 km and an absorption coefficient of 0.23 dB/km.

In ultra-cold atomic vapors, storage times of 68 ms and retrieval efficiencies of up to 4 % have been achieved.[374] Other publications report storage-time retrieval-efficiency products of e.g. 3 ms · 78 %[375] or 1 ms · 87 %[373] with ultra-cold atoms.

However, for easily maintainable long-distance networks, simpler solutions, preferably at room temperature, are needed. Similar[376–378] atomic vapor experiments at room temperature only yield up to 1.5 µs · 13 %.[164] Hence, a fiber loop would perform by an order of magnitude better than quantum memories based on neutral atoms at room temperature when comparing the storage-time retrieval-efficiency product. Recently, Katz and Firstenberg[379] reported a storage lifetime of 150 ms of classical pulses in room temperature cesium vapor with an internal storage efficiency of 10 %. But, room-temperature storage of non-classical photonic states on such time scales has not yet been achieved.

Heralded frequency conversion. In this chapter, we approach the implementation of long-distance quantum networks by addressing requirements 2.– 4. that were mentioned in the introduction. We demonstrate the coherent frequency conversion of heralded single photons, initially matched to the cesium D_1 transition at 894 nm, to the telecom band at 1557 nm. In other studies, the temporal envelope was shaped by modulation of the pump field during frequency conversion,[358–360] or photons from an atomic ensemble were electro-optically modulated directly after emission.[380] Here, after frequency conversion to the telecom band, the wave packet of an heralded single photon is modulated with a fast amplitude modulator.

Wave packet modulation and storage. We employ commercial telecom equipment to show heralded shaping of the complex comb-like temporal wave packet of the converted photon at the timescale of a nanosecond. In the last experiment, a frequency-converted photon in the telecom band is further delayed in an optical fiber for 45 µs. The different experiments discussed in this chapter represent key steps towards the realization of synchronized quantum networks. Our approach could then be combined with a fiber-loop photon-storage scheme to create a simple quantum memory consisting of commercially available telecommunication components.

3.2 | Methods

In the following, we present the methods used in the three experiments discussed in this chapter. We introduce the experimental setup of the frequency conversion system in detail. The quantum frequency conversion efficiency as well as the contributing loss factors are discussed. Finally, we quantify the signal-to-noise rate of the measured converted single photons.

3.2.1 | Photon-pair source

All experiments discussed in this chapter utilize the same photon-pair source based on cavity-enhanced SPDC. In principle, any other heralded single-photon source emitting at 894 nm could have been used for the experiments presented here. But, the cavity-enhanced source offers some key advantages: Due to the cavity-enhancement, a high heralding rate can be achieved, giving rise to a high signal-to-noise ratio, even for experiments with high losses. Additionally, the width of the spectrum of the generated photons coincides with the phase-matching bandwidth of the frequency-conversion waveguide. Finally, the comb-like signal-idler correlation function offers interesting temporal properties as it features narrow temporal peaks as well as a moderately long exponential decay constant.

Single-crystal cavity. The single-crystal cavity as presented in section 2.3.1 was used at a pump power of ~20 mW which corresponds to a generation rate of $R \approx 8 \cdot 10^6$ biphotons/s (see table 1.1). This generation rate is divided amongst several spectral modes within the two clusters (see section 2.3.2). The signal-idler second-order correlation function, as discussed in section 2.4.6, plays a fundamental role in this chapter as all experiments discussed here rely on the measurement of $G^{(2)}_{\mathrm{s/i}}(\tau)$.

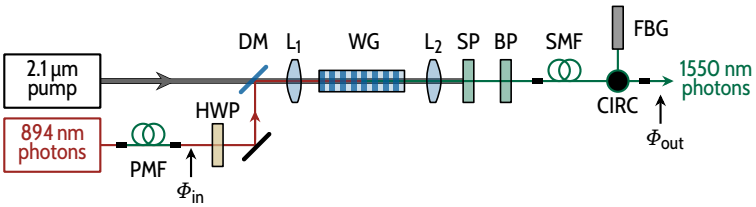

Figure 3.2 | Coherent quantum frequency-conversion setup. Setup for the coherent frequency conversion of single photons. Single photons at 894 nm are collected into a polarization-maintaining fiber (PMF). The polarization can be rotated by a half-wave plate (HWP) to align the photon polarization with the crystal axis for optimum conversion efficiency. Single photons and pump laser light at 2.1 µm are superimposed by a dichroic mirror (DM) and focussed into the conversion waveguide (WG) with lens L_1. The WG is anti-reflection (AR) coated for all three involved wavelengths. The frequency-converted photons are coupled into a single-mode fiber (SMF) by lens L_2 (1550 nm AR coating) after leaving the WG. Remaining pump laser light and unconverted photons at 894 nm are suppressed by a sequence of spectral filters: two dichroic mirrors which act as a 1800 nm shortpass (SP), a 25 nm dielectric bandpass (BP) centered at 1550 nm, and a 3.5 nm fiber Bragg grating (FBG) at 1557 nm connected to a fiber circulator (CIRC). The conversion efficiency is defined as the ratio of photon flux directly after the input fiber Φ_{in} to the photon flux Φ_{out} directly after the FBG. For this setup, a total conversion efficiency of 13(2) % was measured. The internal conversion efficiency was estimated to be 70 %.

The master laser is locked to a hyperfine transition of the cesium D_1-line and the cavity of the photon-pair source is locked via the microcontroller (see section 2.2.2). This allows for arbitrary long integration times for all measurements.

3.2.2 | Coherent quantum frequency-conversion setup

Single photons with a wavelength in the vicinity of the cesium D_1 transition at 894 nm are converted to a telecommunication wavelength in the C-band by generating the difference frequencies at 1557 nm and at the pump wavelength of 2100 nm. We used a strong (~300 mW) continuous-wave laser at 2100 nm as pump (see Fig. 3.2).

Experimental setup. The conversion takes place in a $\chi^{(2)}$ nonlinear 7 mol % ZnO-doped lithium niobate waveguide (NTT electronics) with dimensions 10 µm × 10 µm × 48 mm. The waveguide is placed on top of a lithium tantalate substrate.[338,339,381] A continuous-wave GaSb-based semiconductor disk laser, developed by the Fraunhofer Institute for applied Solid State Physics,[382] generates the pump light at 2100 nm. The pump laser has a linewidth below 100 kHz and an optical power of up to 300 mW in front of the waveguide coupling lens L_1 (see Fig. 3.2).

Conversion efficiency. We define the overall efficiency of our quantum frequency conversion (QFC) setup η_{QFC} as in Ref. [339] to be:

$$\eta_{\mathrm{QFC}} = \frac{\Phi_{\mathrm{out}}}{\Phi_{\mathrm{in}}}. \tag{3.2.1}$$

Here, Φ_{in} is the 894 nm photon flux (in terms of photons per second) directly after the front facet of the input fiber. Φ_{out} is the flux of wavelength-converted 1557 nm photons in the output fiber after all filtering steps (see Fig. 3.2). The maximum efficiency achieved in our setup is $\eta_{\mathrm{QFC}} = 13.1(2)\,\%$. This value is determined by five contributing factors:

$$\eta_{\mathrm{QFC}} \approx \eta_{\mathrm{fs}} \cdot \eta_{\mathrm{c}} \cdot \eta_{\mathrm{int}} \cdot \eta_{\mathrm{fib}} \cdot \eta_{\mathrm{f}}. \tag{3.2.2}$$

The free-space transmission η_{fs} accounts for all losses from the input fiber up to the waveguide coupling lens L_1. The coupling efficiency of the input photons into the waveguide is denoted by η_{c} and the internal conversion efficiency in the waveguide is defined by η_{int}. The fiber coupling efficiency of the converted photons η_{fib} and the transmission through all spectral filters η_{f} determine the losses after the waveguide. In the following, we discuss these contributions in detail.

Loss factors. The first of the aforementioned contributors is the transmission η_{fs} of 894 nm photons from the input fiber to lens L_1, which couples the photons into the conversion waveguide. We use a half-wave plate to optimize the photon polarization direction to the phase-matching axis of the conversion crystal. The losses by absorption or scattering between the fiber front facet and the waveguide are below 2 %. The use of highly reflective coatings for the input photons on the dielectric mirrors and an anti-reflection coating for the half-wave plate results in $\eta_{\mathrm{fs}} > 98\,\%$.

The second factor, $\eta_{\mathrm{c}} \approx 90\,\%$, is the coupling efficiency of the 894 nm photons into the waveguide. We measure η_{c} with a laser at 894 nm. We define the ratio $\eta_c = P_{\mathrm{out}}/P_{\mathrm{in}}$ by the laser power P_{in} just before lens L_1 and by the laser power P_{out} which is coupled into the waveguide mode and detected behind the collimating lens L_2. The spatial mode matching of the input field to the waveguide mode determines the coupling efficiency: The mode matching is mainly defined by the position of lens L_1 with respect to the waveguide front facet and the waveguide geometry.

Internal conversion efficiency. We also use a 894 nm laser to measure the internal conversion efficiency $\eta_{\mathrm{int}} = 70\,\%$. η_{int} is inferred from the 894 nm power depletion after the waveguide when the pump laser is added.[338] In the experiments discussed in the chapter, the internal conversion efficiency has been limited

by the available pump laser power of 300 mW. We extrapolate the maximum internal conversion efficiency for this waveguide to be $\eta_{\mathrm{int}}^{\mathrm{max}} = 79\,\%$ at a pump power of 450 mW.[338]

Fiber coupling efficiency. About $\eta_{\mathrm{fib}} = 35\,\%$ of the converted 1557 nm photons are coupled into an optical single-mode fiber (SMF). The fiber-coupling efficiency is currently limited by imperfect mode matching. In part, one could improve the mode matching with a more advanced lens system in front of the output fiber. But, in principle, the mode matching is limited by the fact that the waveguide is not spatially single-mode at the wavelength of the converted photons. The higher-order modes have a reduced overlap with the Gaussian mode of the collecting fiber.

Spectral filtering. By spectral filtering, we separate the converted light from the pump light, the remaining unconverted input photons at 894 nm, and suppress spurious noise photons in the vicinity of 1557 nm. Broadband noise photons can be generated by the pump e.g. by fluorescence or Raman scattering inside the waveguide.[338,349] Additionally, noise photons could directly be generated inside the laser and subsequently be transmitted through the waveguide.

The spectral filtering setup (see Fig. 3.2) consists of three stages. A dielectric 50 nm bandpass filter centered at 1550 nm (Edmund Optics, transmission $T > 97\,\%$) suppresses 2.1 µm pump light and unconverted 894 nm photons. In a second step, a set of two dielectric 1800 nm longpass filters (Thorlabs, DMLP1880T, used as dichroic mirrors) couples the converted single photons at 1557 nm with a reflectivity $> 98\,\%$ per filter into the SMF. These mirrors, thus, function as shortpass filters for the 1557 nm photons. Further pump light is transmitted ($> 90\,\%$ per filter) and therefore spatially separated from the converted light at the dichroic mirrors.

Finally, the converted photons are reflected at a fiber Bragg grating with a bandwidth of 3.5 nm (Advanced Optics Solutions GmbH) which is spliced to the second port of a fiber circulator (Thorlabs 6015-3-APC). The remaining pump light and 894 nm photons are transmitted by the Bragg grating. Only the converted 1557 nm photons leave the fiber circulator at the output port. We have measured the overall filter transmission to be $\eta_{\mathrm{f}} = 60\,\%$.

Signal-to-noise ratio. At a pump power of 300 mW, the rate of detected noise photons is $N < 5000$ Hz. This rate was measured without any 894 nm input photons present and a detection efficiency of $\eta_{\mathrm{det}} = 14\,\%$ of the superconducting single-photon detector (SSPD, Scontel). Investigations with several additional sets of spectral filters proved that the remaining noise photons are located within the 3.5 nm stopband of the fiber Bragg grating.

Altogether, with a pump power of 20 mW for the cavity-enhanced photon-pair source, we achieved a signal-to-noise ratio for the converted single photons of up to

$$\mathrm{SNR} = \eta_{\mathrm{QFC}} \cdot \eta_{\mathrm{det}} \cdot R/N = 33 \tag{3.2.3}$$

in the experiments discussed in this chapter. The SNR is limited by the random noise detections of rate N as well as by the maximum photon rate R from the photon-pair source before conversion. Reduction and increase of N and R, respectively, could further improve the SNR. In practice, R is usually bound by the saturation of emission rates of single-photon emitters. In the experiments discussed in this chapter, R is limited by the effort to keep the multi-pair generation rate of the photon-pair source low. As will be discussed in section 3.4, we reduced the noise rate N by nearly two orders of magnitude in subsequent experiments without a reduction in conversion efficiency.

3.3 | Results

In this section, we present three experiments performed with the single-crystal photon-pair source and the quantum frequency conversion setup. First, we investigate whether the frequency conversion process has any influence on the temporal wave packet of the heralded single photons. Specifically, we measure the second-order signal-idler correlation function with and without frequency conversion of the signal photons. Implicitly, we find that the influence of the conversion on the single-photon wave packet is so small that it cannot be resolved even with state-of-the-art superconducting single-photon detectors with very low timing jitters.

In the second experiment, we demonstrate how to utilize commercial telecommunication fiber-optical components to arbitrarily shape the temporal wave-packet of the heralded single photons. We verify that the theory detailed in section 2.4 can describe the modulated single-photon wave packet, again, by measuring the second-order signal-idler correlation function. We discuss the limits of the experimental setup as well as its potential for future applications in quantum networks.

Finally, we present a simple form of a quantum memory – the storage of the heralded single photons in a long fiber spool. By analyzing the signal-idler correlation function after storage of the signal photons in a 9.3 km long fiber, we observe a broadening of the peaks in the correlation function due to chromatic dispersion of the photon wave packet. Discussing other experimental factors limiting the temporal resolution of this measurement, we also evaluate the

technical potential of fiber-loop storage systems. These could be combined with the fast amplitude modulation of single-photon wave packets in future quantum communication applications.

3.3.1 | Conversion of the complex temporal wave packet of a photon from a photon pair

In the first experiment discussed in this chapter, we convert a heralded single photon of the single-crystal cavity-enhanced photon-pair source discussed in chapters 1 and 2. We verify that the temporal shape of the single-photon wave packet is not altered by the conversion process. The experimental results are presented in Fig. 3.3.

Experimental setup. The signal and idler photons generated inside the single-crystal photon-pair source are split at a polarizing beam splitter. The second-order signal-idler correlation function was measured with superconducting single-photon detectors $SSPD_1$ and $SSPD_2$. The measurement results have already been discussed in section 2.4. Fig. 3.3b shows the same data points and the same fit function (Eq. 2.4.22) as Fig. 2.35.

Fig. 3.3c shows the measured signal-idler correlation function after conversion of the signal photon. Here, the same fit function as in Fig. 3.3b is plotted with identical parameters except for the overall amplitude. This demonstrates the preservation of the wave packet upon quantum frequency conversion on time-scales accessible with the measurement equipment.

Conservation of the spatio-temporal profile. The wave-packet preservation is a remarkable, although expected,[333,335,383] result. Under the following conditions, in a frequency conversion process, only the central frequency of an electromagnetic wave is changed while its spatio-temporal structure remains unchanged:

1. The phase-matching bandwidth of the nonlinear material is much broader than the spectra of the involved electromagnetic waves.
2. The pump laser spectrum can be approximated as a delta-function.
3. The pump field is not varied in frequency, phase or amplitude in time.[383,384]

In our experiments, the latter two conditions are fulfilled by the continuous-wave pump laser. It emits constantly at 2.1 µm wavelength and its narrow linewidth of $< 100\,\mathrm{kHz}$[382] is very small compared to the spectral width of the photon-pair spectrum of ~100 GHz ($< 0.3\,\mathrm{nm}$, see section 2.3). The first condition is only partially satisfied because the phase-matching bandwidth of the nonlinear process in the waveguide of ~0.3 nm is almost coinciding with the spectral width of the photons.

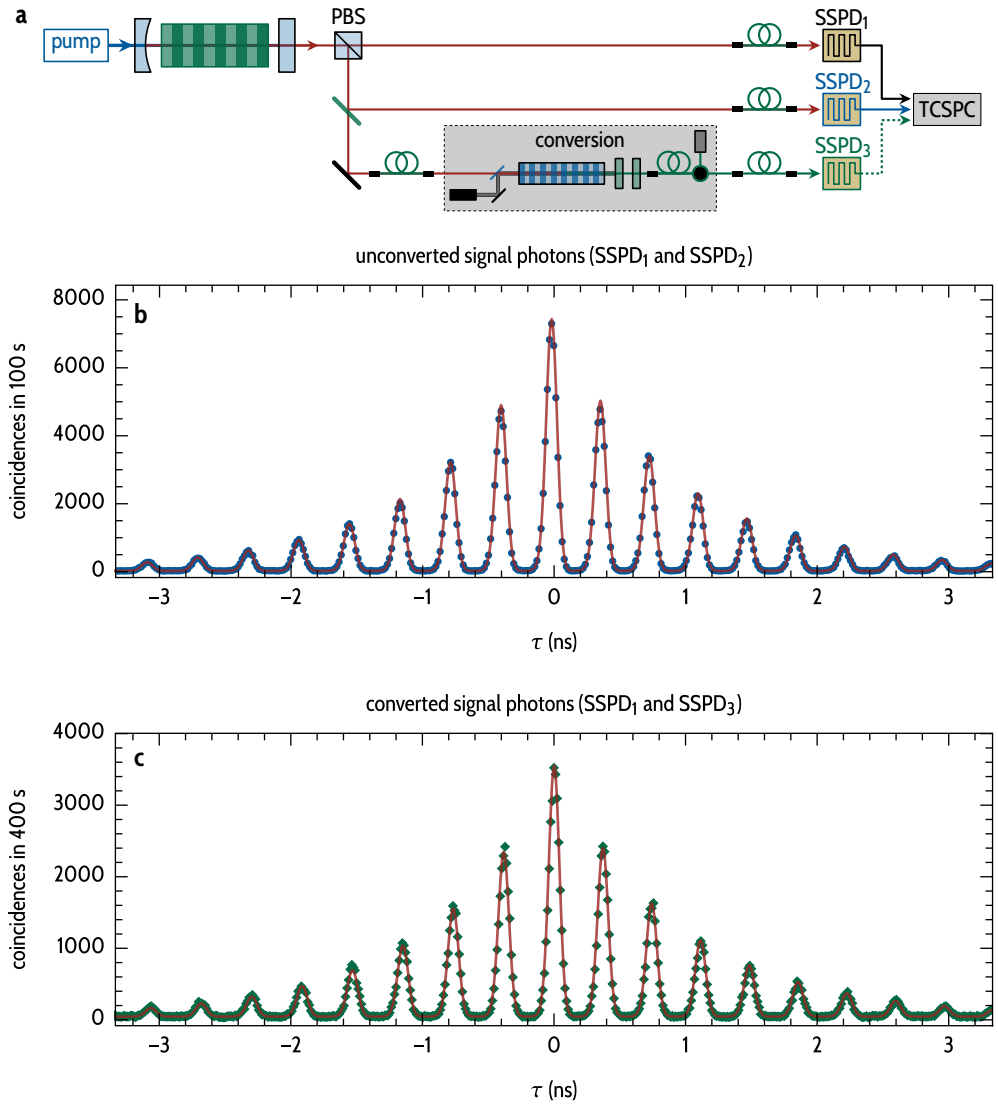

Figure 3.3 | Quantum frequency conversion of a photon from a photon pair. Measurement of the signal-idler second-order correlation function of photon pairs generated by a single-crystal cavity-enhanced down-conversion source with and without conversion. **a**, The signal photons of the photon-pair source are separated from the orthogonally polarized idler photons at a polarizing beam splitter. The idler photons are directly detected by the superconducting single-photon detector $SSPD_1$. The signal photons are either detected directly with $SSPD_2$ or after conversion with $SSPD_3$. **b**, Here, the same data (●) and the same fit function (—) as in Fig. 2.35 is shown. **c**, Coincidence histogram (◆) recorded between idler photons and converted signal photons. The fit from **b** is also plotted in **c** with identical parameters to demonstrate that the conversion does not influence the shape of the wave signal/idler packets. Due to the high signal-to-noise ratio between detected converted photons and detections of uncorrelated photons, no background correction has been performed on both measurements shown here.

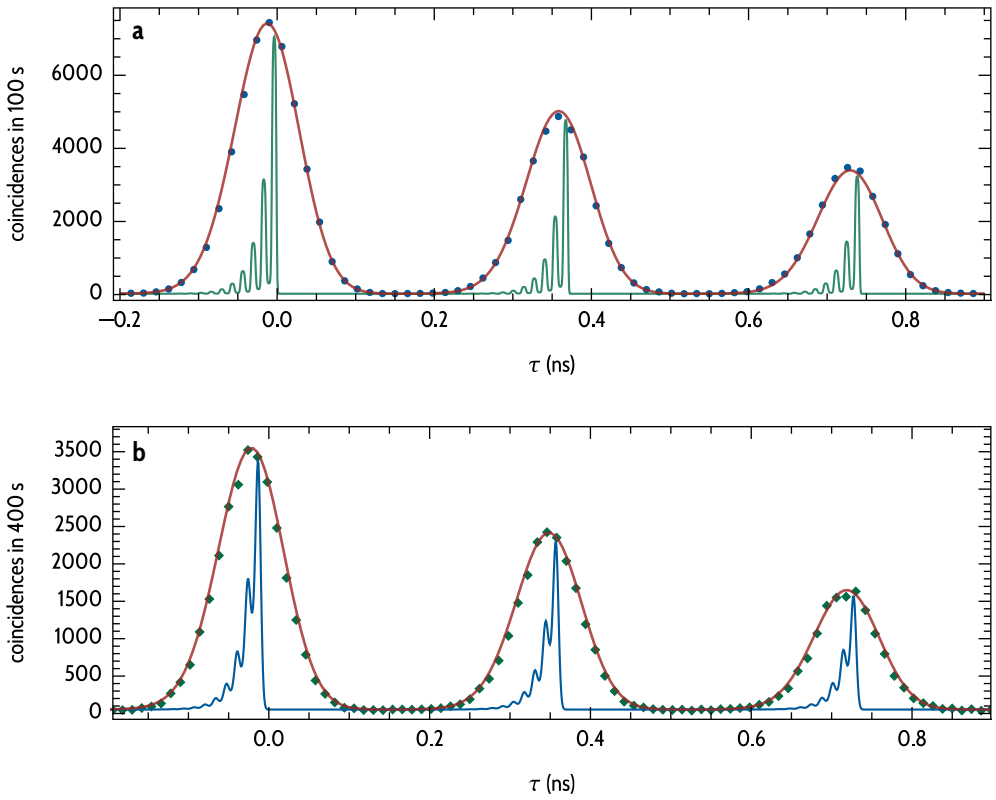

Figure 3.4 | Broadening of the correlation function by frequency conversion. **a**, Zoom into the measured data (●) with the same fit function (—) as shown in Fig. 3.3. The unconvoluted signal-idler correlation function calculated with Eqs. 2.4.9 and 2.4.21 is shown (—). Signal and idler photons have been filtered by a 1 nm bandpass filter. **b**, As a comparison, the unconvoluted correlation function (—) after conversion is broadened. This broadening is caused by the limited phase-matching bandwidth (~0.3 nm) of the conversion process. Due to the width of the instrument response function (~90 ns), this broadening could not be resolved in the experiments. The same fit function (—) as in **a** (except for the global amplitude *a* in Eq. 2.4.22) is plotted here. It still fits the data of the correlation function with converted signal photons (◆) with high fidelity.

Spectral bandwidth of the conversion process. In principle, one can exploit the limited spectral bandwidth of the conversion process to filter out redundant frequency components during conversion.[339] But, in our case, the slight suppression of the shoulders of the parametric gain profile in the converted spectrum causes a broadening of the temporal features in the correlations measurement (Fig. 3.3c). Fig. 3.4 compares the unconvoluted correlation function before and after the conversion process. The phase-matching bandwidth of ~0.3 nm is modelled in Eq. 2.4.22 as an additional spectral filter for the converted photons.

The comparison of the measured signal-idler correlation function shows that the broadening caused by the finite phase-matching bandwidth is too small to be resolved with the IRF of the detection system. In Fig. 3.4, the same fit function with the same parameters (except for the global amplitude a in Eq. 2.4.22) is plotted for both data sets. Within the measurement uncertainty, this fit function is in good agreement with both data sets.

3.3.2 | Heralded shaping of a converted single-photon wave packet

Future quantum networks will, supposedly, require triggered events in successive processes of qubit manipulations and basic shaping of the temporal profile of photons. This shaping has already been demonstrated for heralded single photons from the rubidium ^{85}Rb D_1 transition with an electro-optic modulator at timescale of the lifetime of the atomic excited states of tens to hundreds of nanoseconds.[380] But, in telecom quantum networks, even faster processes will be required to attain high data rates. Fiber-optical equipment for high-speed modulation of light is already commercially available for various applications at telecommunication wavelengths. The frequency conversion of photonic qubits into the telecom band therefore comes with the advantage that this technology can, in many cases, directly be used for experiments at the single-photon level.

In the following, we demonstrate this advantage by showing that we can arbitrarily shape the complex wave packet of the converted signal photons with an off-the-shelf fiber Mach-Zehnder modulator (MZM, Avanex SD20, see Fig. 3.5a).

Experimental setup. The signal and idler photons of a photon pair are separated at a polarizing beam splitter and sent to different parts of the experiment. The detection of an idler photon at $SSPD_1$ triggers an arbitrary waveform generator (Programmable Pulse Generator PPG 512, PicoQuant, 5 Gsamples/s) which sends a voltage pattern to the MZM. The applied voltage defines the transmission of the MZM, continuously adjustable from full transmission to maximum suppression of 21(2) dB. Arbitrary shaping of the outgoing wave packet is possible by means of partial transmission of the wave through the MZM within the

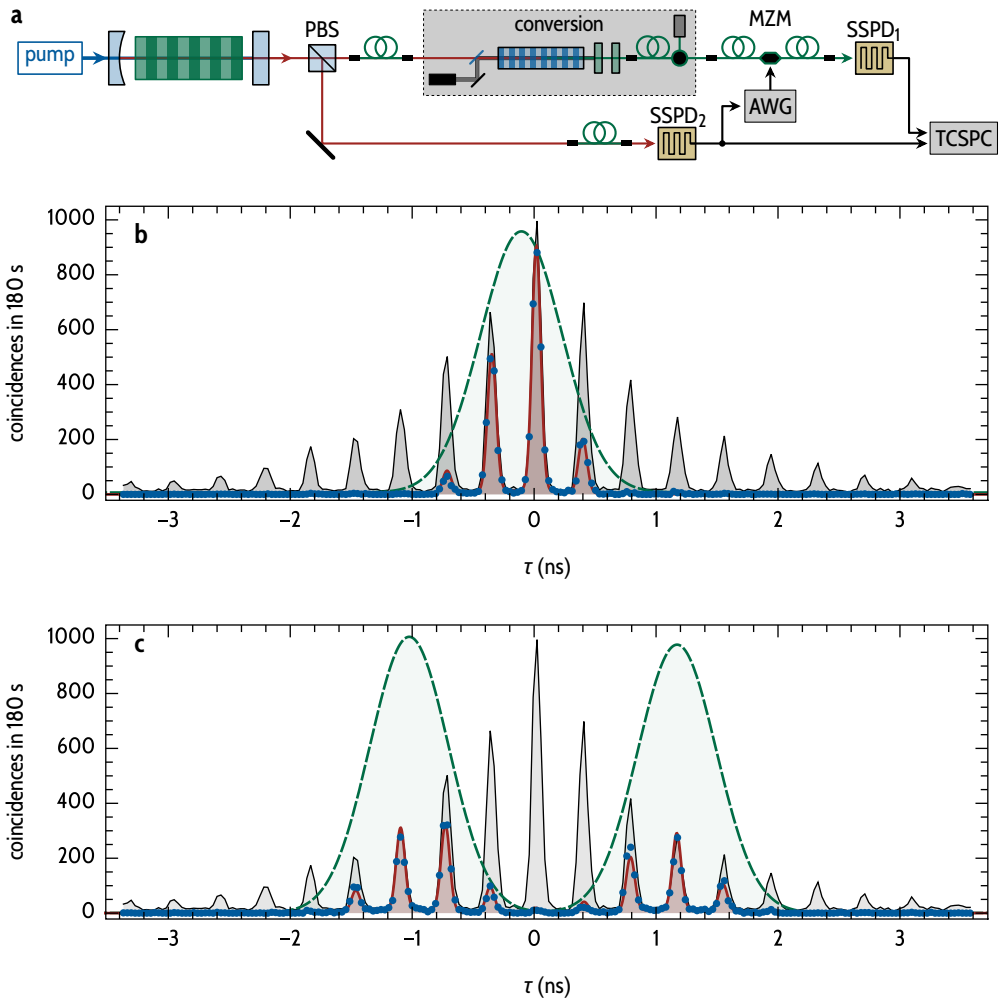

Figure 3.5 | Heralded modulation of a frequency-converted photon. **a**, After separation of signal and idler photons at the PBS, the signal photon is converted to the telecom band and subsequently transmitted to a fiber Mach-Zehnder modulator (MZM). The detection of the idler photon at $SSPD_1$ triggers the generation of pulses of an arbitrary waveform generator (AWG). The AWG pulses control the transmission of the MZM which shapes the converted signal-photon wave packet before it is detected at $SSPD_3$ **b**, and **c**, Measured signal-idler correlation function (●) for two different modulating waveforms. The MZM transmission of a frequency-converted continuous-wave laser was measured in both cases and fit with one and two Gaussians, respectively (– –). These curves were normalized to the reference measurement (——) of the signal-idler correlation function which was measured with permanently transmitting MZM. The timing jitter of the AWG and the trigger electronics add up to a transmitting pulse with minimum width of 1 ns. This timing resolution is well below the capability of the MZM with a bandwidth of 20 GHz. The distinct temporal features of the photon-pair correlation function are not broadened by the modulation process. This is verified by comparison of the measurements with a fit (——) of the product of the unmodulated fit function (see Fig. 3.3) with the transmission function. Only the relative position between modulator transmission and correlation function as well as the transmission amplitude have been used as fitting parameters. All other parameters were taken from the fit of the reference or of the measured transmission function.

resolution limits of the partaking optoelectronics. In the experiment, the signal photon is frequency converted to 1557 nm and transmitted through the MZM. The insertion loss of the MZM of 3.1 dB reduces the telecom single-photon rate at $SSPD_3$ and, consequently, the coincidence rate by roughly 50 %.

Arbitrary waveform generation. The second-order signal-idler correlation measurements are presented in Figs. 3.5b and 3.5c for two exemplary AWG pulse forms. In this experiment, the voltage patterns are compiled from 102.4 ns long sequences of 512 values with 8 bit resolution in amplitude. In both cases, we measured the temporal profile of the MZM transmission as the transmission signal of a continuous-wave laser. The plots display respective fits of the time-dependent transmission $T_i(\tau)$. We achieved transmission pulses with a full width at half maximum of 750(1) ps. The pulse width is mainly limited by the AWG rise time of about 500 ps, while the 20 GHz-bandwidth MZM should assure optical rise times well below 100 ps. The signal-idler correlation measurement demonstrates the modulation of the single-photon wave packet at timescales of nanoseconds.

Theoretical model. To model the expected signal, we extend the convoluted signal-idler correlation function Eq. 2.4.22 by:

$$c + a \cdot T_i(\tau - \tau_0) \cdot \left[\mathrm{IRF} * G^{(2)}_{\mathrm{s/i}}\right](\tau). \tag{3.3.1}$$

For the fit of Eq. 3.3.1 to the data, we only use as fit parameters the amplitude a of the transmission function $T_i(\tau)$ and its relative position τ_0 with respect to the correlation function. Here, we set the global offset c to zero (see section 3.3.3). The parameters of the instrument response function and the correlation function resulted from the fit to a reference measurement performed with constantly transmitting MZM. The accurate overlap of the fit with the data points confirms that no change of the underlying fine temporal features of the signal-idler correlation function is detected within the experiment's timing resolution of 90(2) ps.

Outlook. The major limitation for the fast modulation of the frequency-converted signal photons in this experiment is the bandwidth and the rise time of the AWG. With improved AWGs[385] and MZMs,[386,387] it would be possible to cut out individual temporal peaks of the wave packet. This would be a very useful functionality, for example, in time-bin based quantum keys distribution with larger alphabets.[388]

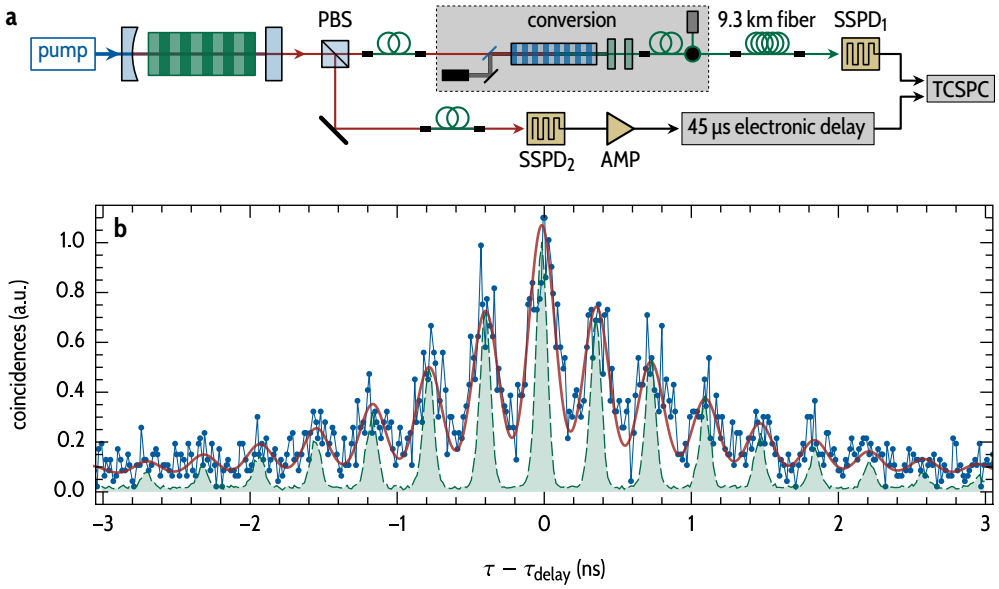

Figure 3.6 | Storage of a converted photon in a 9.3 km long fiber. **a**, Signal and idler photons are split at a polarizing beam splitter. The signal photons are delayed in a 9.3 km long fiber after frequency conversion and forwarded to $SSPD_1$. The idler photons are detected with $SSPD_2$. To reduce the time delay of the start and stop events at the TCSPC electronics, an additional electronic delay of 45 µs is applied to the electronic signal of $SSPD_2$. **b**, Measured correlation function of idler and converted signal photons with 9.3 km delay (–●–) and without fiber delay (– –). The electronic delay box processes only one pulse at a time, resulting in a decreased heralding rate at the correlator. This causes a strong decrease of coincidence events after storage of the signal photons in the fiber. The temporal structure of the signal-photon wave packet is conserved, basically. But, two processes increase the width of the individual peaks of the correlation function. On the one hand, the peaks are broadened by chromatic dispersion in the fiber. On the other hand, the electronic delay and the preceding amplifier (AMP) introduce an additional timing jitter. The measured peak width is the convolution of IRF, chromatic dispersion and timing jitter of the electronic delay. From the fit (—) to Eq. 3.3.1, an IRF peak width of 220(10) ps is inferred. This value is considerably larger than in the case of conversion without an additional fiber delay.

3.3.3 | Storage of a telecom photon wave packet in a fiber

In the final experiment, we demonstrate a straightforward approach to store a frequency-converted photon for the time of 45 µs in a 9.3 km long telecom fiber (SMF-28, Corning) furled on a spool (see Fig. 3.6a).

Experimental setup. The frequency of the signal photons is converted to the telecom band as in the previous experiments. Instead of detecting the signal photons directly after conversion, they are coupled into the 9.3 km fiber spool and detected by a SSPD at the end. Meanwhile, the idler photons are detected at the other SSPD.

A 45 µs electronic delay (Highland Tech., T560) was applied to the detection voltage pulses from the SSPD of the unconverted idler photons. This electronic delay accomplishes almost simultaneous events at the correlation electronics, i.e., it compensates for the optical time-of-flight delay of the signal photons in the fiber loop. We then correlated both electrical detection signals with the TCSPC electronic. The resulting histogram (see Fig. 3.6b) demonstrates the general conservation of the signal-photon wave packets.

Chromatic dispersion. Compared with a measurement where we place the SSPD directly after the conversion (without a fiber delay), the temporal resolution in the correlation measurement is reduced after delaying the signal photons. A fit of Eq. 3.3.1 to the data – using the same fit parameters as in Fig. 3.3 except for the amplitude a, the global offset c, and the width of the IRF – results in a fitted FWHM of the IRF of 220(10) ps. Two main factors originating from the additional equipment contribute to the broadening of the peak in the measured correlation function. The dispersion in the SMF-28 fiber at 1550 nm is ~18 ps/(km nm). With the 9.3 km fiber delay and the spectral width of the converted photons at 1557 nm of ≈0.8 nm (≈100 GHz), the temporal shape of the converted photons is broadened by ≈140 ps at the output of the fiber spool.

Additional timing jitter by electronic noise. Besides wave-package dispersion, the timing jitter of the electronic delay (specified with 50 ps) contributes to the broadening. An quadratic sum of contributions of these uncorrelated broadening effects points out an impact to the data which has so far been unaccounted for. We suspect that the timing jitter (about 150 ps) introduced by the noise of the electronic amplifier (Mini-Circuits, ZFL-500LN-BNC) before the delay box is the cause for the increase of the measured FWHM.

Electronic delay. The strong decrease of the coincidence rate is dominantly caused by the electronic delay box. Each time an electronic pulse is delayed, no other signal will be processed with the 45 µs delay. This limits the detection rate of the signal photons to $1/(45\,\mu s) \approx 22\,kHz$. Therefore, the maximally achievable coincidence rate is reduced by a factor of 38. In comparison, the absorption of the 1557 nm photons in the fiber with an absorption coefficient of 0.23 dB/km causes losses of 39 %. The reduction of the coincidence rate needs to be overcome for the parallel synchronisation of a huge number of correlated photon pairs in future quantum networks. One can avoid this, for example, by using analog delay lines or digital delays with buffers to process multiple pulses simultaneously.

Fiber losses. The fiber loss, on the other hand, implies a fundamental limit to the storage time of a photon in a fiber. This loss cannot be reduced significantly with current fiber technology. A fiber loop photon storage, consisting of a fast switchable four-port fiber Mach-Zehnder-interferometer and a fiber loop, can only reasonably be used in a temporal delay range where its time-retrieval product, as defined in the introduction to this chapter, excels those of other storage mechanisms. We find the optimum to be at 90 µs (see above). This limits the maximum distance at which quantum correlations can reliably be realized to about 18.9 km, or medium-range urban networks.

Outlook. The dispersion of the wave packet in the long fiber reduces the temporal overlap between a photon just after frequency conversion and one at the end of the delay line. In a Hong-Ou-Mandel[32] type experiment where photon indistinguishablity plays a major role, wave-packet dispersion would utterly degrade the performance. This problem could be resolved by the use of fiber optical links with identical lengths or by using dispersion compensating fibers[389,390] in the fiber-loop storage.

3.4 | Discussion

In this chapter, we have experimentally demonstrated the conservation of the complex temporal correlation during coherent quantum frequency conversion between two pair photons which are generated by cavity-enhanced SPDC. We transfered the signal-photon wave packet from the atomic frequency standard of the cesium D_1-line at 894 nm to the minimal absorption wavelength in telecommunication fibers at 1557 nm.

Conversion efficiency. The maximum overall conversion efficiency of our setup $\eta_{\mathrm{QFC}} = (13.1 \pm 0.2)\,\%$ lies below those values (39 %,[391] 32 %,[339] or 22 %,[349]) that were achieved in other experiments. But, we could still improve our conversion efficiency by using an improved telescope in front of the fiber coupler for the 1557 nm photons (up to $\eta_{\mathrm{fiber}} = 70\,\%$) and by reducing the losses during spectral filtering in the fiber circulator system (theoretically up to $\eta_{\mathrm{f}} \approx 100\,\%$). This would result in a possible maximum conversion efficiency of $\eta_{\mathrm{QFC}}^{\mathrm{max}} \approx 40\,\%$.

Noise photon generation inside the pump laser. After completion of the experiments, the rate of detected noise photons N was further reduced to the dark count level of the SSPDs with the help of a 2.0 µm longpass filter for the 2.1 µm pump laser. This verifies that the noise photons were located within the stopband of the fiber Bragg grating at 1557 nm and directly generated inside the pump

laser resonator. The noise rate now lies below $N < 100$ Hz such that the SSPD dark-count rate (≈50 Hz) is an important contributing factor. This noise rate results in a SNR > 1600 for the experiments without the fiber storage spool. Such a high signal-to-noise ratio enables subsequent conversion experiments with single-photon emitters with emission rates that are orders of magnitudes lower than the photon-pair rates reported in this chapters.

Signal-to-noise rate improvement. Recently, Ikuta and coworkers performed a frequency-conversion experiment with correlated photons generated in rubidium vapor with a trade-off between conversion efficiency, and noise detection rate.[349] Due to the low excitation and collection efficiencies they required measurement durations of 200 h. With rates of about 10 kHz of time-energy entangled photons from an InAs quantum dot[392] before frequency conversion and with improved SSPDs with a detection efficiency ≥40 % one could reach rates of entangled photons in the telecom band which are by about one order of magnitude higher than in the above-mentioned study. This corresponds to a reduction in integration time for a similar experiment to one day or less.

Performance with state-of-the-art equipment. Precise heralding of the signal photons and fast temporal modulation of the converted signal photons with commercial fiber telecommunication equipment allows for arbitrary shaping of single-photon wave packets. Though, this arbitrary shaping comes at a cost of photon losses by absorption inside the modulator.

The temporal resolution of this process is only limited by the overall rise time of the arbitrary waveform generator and the optical modulator. A combination of fast temporal switching, as demonstrated in this chapter, with telecom ultra-dense wavelength-division multiplexing[273] would further enhance the attainable complexity of upcoming quantum networks.

Fiber-loop storage. Beyond that, the frequency-converted signal photons have been stored more than 45 µs in a 9.3 km fiber spool and were heralded by the idler photons. With this preparatory work, we propose a fiber-loop storage that would, in addition, shape the single photon with a fast switchable electro-optic modulator at retrieval. Such a device would still outperform current atomic quantum memories at room temperature by one order of magnitude.[164,376] Additionally, it would allow for an immediate technical implementation of a simple storage scheme of single photons at the telecommunication wavelength for medium distance urban quantum networks.

Storage bandwidth. The bandwidth of atom-based quantum memories ranges from a few MHz,[374] over about 100 MHz utilizing electromagnetically induced transparency,[166] to the order of GHz.[164] In molecules, a storage bandwidth of

THz has been shown[393] for classical laser pulses. In nitrogen vacancy centers in diamond, storage of entangled photons with THz-bandwidth has been reported, albeit with storage times on the timescale of picoseconds.[394,395] The bandwidth of an optical-fiber-based memory in the telecom C-band would, in contrast, only be limited by wave packet dispersion. The low-loss transmission window stretches over multiple THz, which makes frequency multiplexing possible.

Further improvements and fundamental limitations. For practical implementations, the idler-photon detection can also be used to add a classical telecom pulse to the transmitting fiber by wavelength division multiplexing, as well as to herald the corresponding signal photon.[396] However, the exponential loss in fibers cannot easily be mitigated and limits storage times to below a millisecond. Therefore, other types of quantum memories are required for long-distance quantum communication.

Outlook. A fiber-loop memory could be a node in the quantum network which merges storage and shaping, thereby reducing the number of incorporated devices and, thus, the overall single-photon losses. This brings recent efforts closer to establish quantum networks in real-world applications. One obstacle to this is the still present modulator insertion loss of about 3 dB. In a fiber loop storage system, this would divide the retrieval probability in half for every round-trip.

3.5 | Conclusion

In the above-described experiments, we have established the frequency conversion of photons generated at the cesium D_1 transition to 1557 nm in the telecom C-band. The overall efficiency lies in the range of other conversion experiments that have recently been conducted and still leaves room for realistic improvement. In the experimental setup, no detectable broadening was introduced into the fine temporal structure of the photon wave packet during frequency conversion.

We have also demonstrated the heralded arbitrary temporal shaping of the converted photons on the timescale of nanoseconds. Such synchronized photon-wave-packet modulation will be of importance for optimal absorption[397] in stationary solid-state or atomic quantum memories.[352] This type of modulation is also essential for quantum protocols that rely on well-defined temporal photon states.[96,398]

We also investigated the influence of chromatic dispersion on the heralded and converted photons that passed through a 9.3 km fiber. For applications requiring indistinguishable photons or for the realization of a basic fiber-loop quantum memory, the temporal broadening observed in the correlation measurements has to be prevented by the use of dispersion compensating fibers and low-timing jitter electronics.

In the future, our setup can be used to build quantum networks consisting of nodes at the cesium D_1 transition and fiber-based channels in the telecom band. The current experiments can be extended by converting entangled photons deterministically generated by a quantum dot[314,392] to enable remote preparation of entangled states. The combination of storage, heralding, arbitrary frequency, amplitude and phase modulation of single-photon wave packets, as well as remote state preparation, will render more complex quantum networks possible.

4 Summary and outlook

This thesis provides an in-depth analysis of triply-resonant cavity-enhanced SPDC. The analysis comprises three aspects: Firstly, a theoretical discussion of cavity-enhanced SPDC, and secondly, the experimental implementation of a cavity-enhanced photon-pair source and the comparison of several experiments with the theory to fully characterize the photon-pair source. In the third part, this thesis presents the results of a series of experiments in the context of hybrid quantum networks that exploit the specific properties of the above-mentioned photon-pair source.

Summary

Theoretical foundations. Chapter 1 presents the theoretical foundations of this thesis. We derive the quantum theory of cavity-enhanced SPDC with a focus on the analysis of double-pass pumping and pump-resonant linear cavities. The main achievement of this chapter is the derivation of a convenient model with which the cavity geometry can be optimized to maximize the photon-pair generation rate while maintaining a high heralding ratio. This model is of great interest for the quantum optics community working towards hybrid quantum systems where photon-pair sources based on cavity-enhanced SPDC are routinely used in state-of-the-art experiments.[107,142–150] For these experiments, the brightness and the heralding ratio of the photon-pair sources are crucial to important experimental parameters, e.g., the success rate and signal-to-noise ratio.

Joint spectral amplitude. At the heart of this theoretical chapter lies the *joint spectral amplitude* of the two-photon state generated by cavity-enhanced SPDC. Building on established theoretical descriptions of triply-resonant cavity-enhanced parametric down-conversion,[111,129,130,136,137,160–162] this thesis refines the expression for the joint spectral amplitude. Specifically, the expression now takes account of the interaction of Gaussian beams inside (linear) cavities. Thereby, for the first time, we discuss the impact of differing confocal parameters of the three involved fields inside the cavity on the Boyd-Kleinman-factor. Additionally, we provide a novel expression for the relative phase of the three fields inside the

cavity. The complete model allows for comparisons between a wide range of different cavity configurations and geometries, which aids in the development and improvement of novel sources.

Heralding ratio. For non-resonant spontaneous parametric down-conversion, it has been found that the heralding ratio decreases with decreasing values of the pump beam waist inside the nonlinear crystal.[59,195,201] Thus, a compromise between brightness and heralding ratio has to be found. However, the theoretical analysis in chapter 1 suggests that this relationship should not apply to the case of high-finesse cavity-enhanced down-conversion. To the best of the author's knowledge, this specific relationship has not been studied in the literature and requires further research.

Photon losses and cavity-escape efficiency. The extended expression for the joint spectral amplitude developed in this thesis also takes the loss of photons inside the cavity and at the cavity mirrors into account. Equipped with this detailed model, chapter 1 highlights the strong impact of photon losses on the brightness and the cavity-escape efficiency for larger values of the cavity finesse. These two parameters cannot be optimized independently. This leads us to conclude that the trade-off between brightness (or linewidth, respectively) and heralding ratio has to be taken into account in the design process of a cavity-enhanced photon-pair source. So far, this trade-off has has not been studied in the literature at this level of detail.

Photon-pair generation rate. The main contribution of the first chapter of this thesis is the derivation and verification of a theoretical expression for absolute values of the photon-pair generation rate. The expression is novel since special care has been taken to specify the brightness only in terms of parameters which are directly accessible in the design process of a new experimental setup. We verify that the model is in good agreement with experimental results gathered for a broad range of different cavity configurations ranging from low-finesse conventional cavities to high-finesse monolithic resonators. This result provides researchers in the field of quantum optics with an approachable, ready-to-use model which serves as a basis for the development and optimization of novel cavity-enhanced photon-pair sources.

Experimental implementation. The second chapter of this thesis describes the experimental implementation of a cavity-enhanced photon-pair source and its characterization. Additionally, from a technical point of view, the thesis addresses two important building blocks for the experimental implementation of cavity-enhanced photon-pair sources: the development of improved monolithic filter cavities as well as the use of digital cavity locking electronics.

Monolithic filter cavities. Monolithic filter cavities are a valuable tool for a broad range of experiments in quantum optics. Chapter 2 presents an important technical improvement to the concept of monolithic cavities. For the first time, we present monolithic filter cavities which allow for *polarization-independent* spectral filtering. This property is important for a wide range of experiments in quantum optics. Additionally, we use the intrinsic frequency stability of the filter cavities to develop a novel high-precision monochromator and a high-resolution spectrum analyzer. We utilized this cascaded setup of filter cavities to fully resolve, for the first time, the comb-like spectral structure of photons generated by cavity-enhanced SPDC.

The employed calibration procedure of the filter cavities, which has been developed in the context of this thesis, currently only allows for a comparison of the measurement results to a given theoretical model. As part of future work the calibration procedure should be improved to allow for precise quantitative measurements of signals with unknown spectral shape. Furthermore, future studies should aim at increasing the cavity transmission, as well as at further optimizing the cavity geometry and thermal properties to reduce thermal settling times.

Digital cavity-locking electronics. Experiments based on cavity-enhanced SPDC with conventional cavities require a sophisticated feedback control system to stabilize the mirror spacing over long measurement durations. We successfully demonstrate that the introduction of a digital locking scheme instead of the previously-employed analog control system leads to a significant improvement of the long-term stability of our experimental setup. Additionally, the digital control system requires significantly less optical components than a comparable analog system.

Microcontrollers are inexpensive, can easily be programmed, and, for many applications, are just as powerful as commercial control systems based on field-programmable gate arrays.[267] Nevertheless, their use in experiments is currently still complex and time-consuming. Further studies should focus on the development of open-source, low-cost, easy-to-use, microcontroller-based feedback control systems with improved electrical noise characteristics. This would enable researches in the quantum-optics community to reduce the complexity of experimental setups without increasing the complexity of the underlying control systems.

Characterization of a triply-resonant photon-pair source. Apart from the technical improvements, chapter 2 also presents an in-depth experimental characterization of cavity-enhanced photon-pair sources. The chapter's main contributions are

the special emphasis on the pump resonance condition and the direct comparison of high-resolution spectral and temporal measurements of the two-photon wave packet. Due to the interference of photons generated in the forward direction and photons generated in the backward direction, a rich spectral and temporal structure is identified and experimentally verified. We find that the theoretical model developed in chapter 1 and the measurements presented in chapter 2 are in excellent agreement, which further corroborates the theoretical description in chapter 1.

For the first time, we not only fully resolve the spectral fine structure of the photons generated by cavity-enhanced SPDC. We also present an experimental analysis of the impact of the relative phase of the three fields inside a linear cavity on the spectral and temporal structure of the two-photon wave packet. This thesis provides the first experimental verification that this relative phase can be measured via the Hong-Ou-Mandel effect. Section 2.4 also theoretically discusses the impact of the relative phase on the second-order signal-idler correlation function. So far, this relationship has not been studied in the literature.

Hybrid quantum networks. Hybrid quantum systems[106] aim at combining different quantum systems with complementary properties and functionalities to overcome fundamental barriers which cannot be overcome by the individual quantum systems. If quantum information is transferred from one such quantum system to another via single photons over optical fibers, often, quantum frequency conversion to telecommunication wavelengths is beneficial to avoid photon losses inside the fiber.

Chapter 3 presents the quantum frequency conversion of heralded single photons generated by the cavity-enhanced photon-pair source presented in chapter 2. We provide evidence that the structure of the temporal wave packets of the heralded photons is unaffected by the conversion process. Operating at telecom wavelength allows us to use advanced telecommunication technology, e.g., for fast wave-packet modulation. Therefore, in chapter 3, we present a route to interface dissimilar quantum system via optical fibers by matching the spectral as well as the temporal wave packets from one quantum system to another and, thus, optimizing their interaction.

Outlook

Applications in quantum communication. The connection of dissimilar stationary quantum systems by tailored photon sources is very promising regarding the mediation of entanglement in quantum networks. This objective is currently investigated within the joint project *Q.Link.X*,[399] funded by the Federal Ministry

of Education and Research, and the *Quantum Flagship*[1,400] initiative, funded by the European Union. Distribution of entanglement over quantum networks is the basis for quantum repeaters[67,93] which can ultimately build the foundation of a unified *quantum internet*.[27,94]

SPDC-based photon sources cannot compete with single photon sources based on isolated quantum systems (e.g. quantum dots[29–31]), especially in terms of on-demand and deterministic generation of single photons, as well as regarding independence of single-photon purity and brightness. But, their spectral flexibility, ease of use, robustness, and maintenance-free operation are still unmatched by single quantum emitters. Therefore, sources of (entangled) photons based on cavity-enhanced SPDC will play an important role in *prove-of-principle* experiments in the development of quantum repeaters.[140,155–159]

Applications in quantum sensing. While photon-pair sources based on spontaneous processes are not ideally suited to large-scale quantum computing or quantum repeaters due to their inherent thermal photon statistics and limited heralding ratios, they have the potential to be vastly beneficial to another area quantum technology that is rapidly gaining in importance: Developments in quantum sensing have sped up in recent years.[19,144,401–405] High-brightness sources of entangled photons operating at room-temperature will play an important role in prototyping and maturing these technologies. Cavity-enhancement and novel approaches such as nonlinear microresonators or waveguides, as well as the miniaturization of the required optical components, will be important driving factors in this field.

Cavity-enhanced spontaneous parametric down-conversion has the potential to provide sources of entangled photons which offer high brightness, spectral purity, tunability in both wavelength and spectral bandwidth, and high heralding ratios while operating at room temperature. Further studies following the line of this thesis should focus on finding and optimizing cavity configurations which combine all of these advantageous properties to harness the full potential of cavity-enhanced spontaneous parametric down-conversion.

Tools and instruments

This thesis was written in LaTeX. All plots and numerical simulations were produced using Mathematica® (Wolfram Research, Inc., Mathematica®, Version 11, Champaign, IL, 2018). With Wolfram Mathematica®, various analytic calculations discussed in this thesis were performed. For the figures, the vector-graphics software IPE (version 7.2 by Otfried Cheong) was used.

The mechanical design of the photon-pair source was created using Autodesk® Inventor® (version 2010/2011). The 3D images of the setup were rendered using Autodesk® 3ds Max® (version 2016). To control the experiments and to collect the experimental data, we used LabView® (version 2010-2012, National Instruments).

The microcontroller for the digital locking scheme discussed in section 2.2.2 were programmed in C using the GNU ARM plugin for the Eclipse Integrated Development Environment. The electronic circuits and the circuit board for the digital locking scheme were designed using EAGLE (version 7, CadSoft Computer GmbH).

	instrument	manufacturer
Narrow-linewidth diode laser	TA pro, DL pro, DL 100	TopticA Photonics AG
Digital laser locking module	DigiLock 110	TopticA Photonics AG
Nonlinear down-conversion crystal	KPT, PPKTP	Raicol Crystals Ltd.
Down-conversion cavity mirrors	SM05-0.050C, PW0537C, custom coating	LASER COMPONENTS GmbH
Avalanche photo diode	τ-SPAD	PicoQuant GmbH
Superconducting single-photon detector	custom design	Scontel Superconducting nano-technology
Time-correlated single-photon counting module	PicoHarp 300	PicoQuant GmbH
Lock-in amplifier	SR810	Stanford Research Systems
Grating Spectrometer	Acton SP2500	Princeton Instruments
Single-mode fiber coupler	60FC, 60SMS	Schäfter + Kirchhoff GmbH
Temperature controller	TEC-1091, TEC-1089-SV	Meerstetter Engineering GmbH
Microcontroller (cavity lock)	STM32F3	STMicroelectronics
$LiNbO_3$ waveguide	custom design	NTT Electronics
2.1 µm semiconductor disk laser	custom design	Fraunhofer Institut for applied Solid State Physics

Table .1 | List of instruments used in the experiments

Publications and outreach

Peer-reviewed publications

1. M. Wahl, T. Röhlicke, H.-J. Rahn, R. Erdmann, G. Kell, A. Ahlrichs, M. Kernbach, A. W. Schell, and O. Benson, Integrated multichannel photon timing instrument with very short dead time and high throughput, Review of Scientific Instruments **84**, 043102 (2013)

2. A. Ahlrichs, C. Berkemeier, B. Sprenger, and O. Benson, A monolithic polarization-independent frequency-filter system for filtering of photon pairs, Applied Physics Letters **103**, 241110 (2013)

3. O. Dietz, C. Müller, T. Kreißl, U. Herzog, T. Kroh, A. Ahlrichs, and O. Benson, A folded-sandwich polarization-entangled two-color photon pair source with large tuning capability for applications in hybrid quantum systems, Applied Physics B **122**, 1–7 (2016)

4. A. Ahlrichs and O. Benson, Bright source of indistinguishable photons based on cavity-enhanced parametric down-conversion utilizing the cluster effect, Applied Physics Letters **108**, 021111 (2016)

5. T. Kroh, A. Ahlrichs, B. Sprenger, and O. Benson, Heralded wave packet manipulation and storage of a frequency-converted pair photon at telecom wavelength, Quantum Science and Technology **2**, 034007 (2017)

Book chapter

A. Ahlrichs, B. Sprenger, and O. Benson, Photon Counting and Timing in Quantum Optics Experiments, in *Advanced Photon Counting: Applications, Methods, Instrumentation*, edited by P. Kapusta, M. Wahl, and R. Erdmann, Springer Series on Fluorescence 15 (Springer International Publishing, Cham, 2015), pp. 319–341

Publications in preparation

1. A. Ahlrichs, and O. Benson, Working title: Triply-resonant cavity-enhanced spontaneous parametric down-conversion. This publication will summarize the so-far unpublished findings of sections 1.1.4, 1.2.3 to 1.2.5, 1.3.2 to 1.3.5, 2.3, 2.4 and 2.5.3
2. C. Müller, A. Ahlrichs, and O. Benson, Working title: Time correlation of photon pairs from a triply-resonant optical parametric oscillator far below threshold.

Talk

Photon Pairs from Cavity-Enhanced Parametric Down-Conversion with Tunable Bandwidth for Quantum Interfaces, Research in Optical Sciences, OSA Technical Digest (Optical Society of America, 2012), paper QT3A.3., Conference on Quantum Information and Measurement, Berlin, 2012.

Patent

C. Müller, A.Ahlrichs, and O. Benson, Verfahren und Einrichtung zur Frequenzumsetzung, Deutsche Patentanmeldung DE 10 2017 223 197.1

Danksagung

An dieser Stelle möchte ich mich herzlich bei allen bedanken, die mich während meiner Promotion unterstützt haben und zur Erstellung dieser Arbeit beigetragen haben.

Ein besonderer Dank gilt meinem Doktorvater Prof. Oliver Benson, der mich in all den Jahren meiner Promotion immer gefördert hat. Ich weiß es sehr zu schätzen, dass er mir bei meiner Forschung viele Freiräume gelassen hat und mir mit Diskussionen und Ratschlägen bei der Umsetzung meiner Vorhaben immer zur Seite stand.

Vielen Dank an Lars Koch, der mich in unsere Versuchsaufbauten eingearbeitet hat und mir im Rahmen vieler Diskussionen geholfen hat, die Grundlage für die Ergebnisse dieser Arbeit zu legen. Martin Kernbach hat sich nicht nur hervorragend für den Umzug und den Neuaufbau unseres Labors in Adlershof eingesetzt. Bei ihm möchte ich mich auch für viele faszinierende Gespräche und eine gute Zusammenarbeit im Labor bedanken. Viele von Martins Ideen sind in das Design der hier vorgestellten Photonpaarquelle eingeflossen.

Mein Dank gilt ebenso Andreas Schell, der mich bei den Experimenten mit viel Geschick und guten Ideen unterstützt hat und immer für spannende Diskussionsthemen gesorgt hat. Es war mir eine Freude, mit Tim Kroh, Benjamin Sprenger und Chris Müller zusammenzuarbeiten. Es freut mich, dass Chris Teile meiner Versuchsaufbauten für seine Experimente weiterverwenden kann.

Bei der gesamten Arbeitsgruppe Nanooptik, insbesondere bei Janik Wolters, Otto Dietz, Günter Kewes, Alexander Kuhlicke und Oliver Neitzke, möchte ich mich für die schöne Zeit bedanken, die wir gemeinsam an den Experimenten und im Büro verbracht haben. Alle Kollegen haben dazu beigetragen, dass die Arbeitsatmosphäre sehr angenehm war. Danke auch an Klaus Palis, der auch bei anspruchsvollen technischen Problemen immer eine Lösung parat hatte. Ein ganz besonderer Dank gebührt Regina Rheinländer dafür, dass sie mich in allen organisatorischen Punkten unterstützt hat. Als gute Seele unserer Arbeitsgruppe ist sie unersetzlich.

Mein größter Dank gilt Hanna, ohne deren kontinuierliche Unterstützung, Zusprache und Geduld ich diese Arbeit nicht hätte abschließen können. Natürlich gilt mein Dank auch meinen Eltern, die mich immer bei all meinen Vorhaben unterstützt haben.

Bibliography

[1] A. Acín et al., The quantum technologies roadmap: a European community view, New Journal of Physics **20**, 080201 (2018), cited on pages 21, 237.

[2] A. Kandala et al., Hardware-efficient variational quantum eigensolver for small molecules and quantum magnets, Nature **549**, 242–246 (2017), cited on page 21.

[3] D. Castelvecchi, Silicon gains ground in quantum-computing race, Nature **553**, 136 (2018), cited on page 21.

[4] N. Moll et al., Quantum optimization using variational algorithms on near-term quantum devices, Quantum Science and Technology **3**, 030503 (2018), cited on page 21.

[5] M. Takita, A. W. Cross, A. D. Córcoles, J. M. Chow, and J. M. Gambetta, Experimental Demonstration of Fault-Tolerant State Preparation with Superconducting Qubits, Physical Review Letters **119**, 180501 (2017), cited on page 21.

[6] A. Bermudez et al., Assessing the Progress of Trapped-Ion Processors Towards Fault-Tolerant Quantum Computation, Physical Review X **7**, 041061 (2017), cited on page 21.

[7] A. Kandala et al., Extending the computational reach of a noisy superconducting quantum processor, (2018), arXiv:1805.04492, cited on page 21.

[8] C. S. Calude and E. Calude, *The Road to Quantum Computational Supremacy*, Technical Report (Department of Computer Science, The University of Auckland, New Zealand, 2017), arXiv:1712.01356, cited on page 21.

[9] A. W. Harrow and A. Montanaro, Quantum computational supremacy, Nature **549**, 203 (2017), cited on page 21.

[10] A. Neville et al., Classical boson sampling algorithms with superior performance to near-term experiments, Nature Physics **13**, 1153–1157 (2017), cited on page 21.

[11] C. Neill et al., A blueprint for demonstrating quantum supremacy with superconducting qubits, Science **360**, 195–199 (2018), cited on page 21.

[12]I. L. Markov, A. Fatima, S. V. Isakov, and S. Boixo, Quantum Supremacy Is Both Closer and Farther than It Appears, (2018), arXiv:1807.10749, cited on page 21.

[13]S. Boixo et al., Characterizing quantum supremacy in near-term devices, Nature Physics **14**, 595–600 (2018), cited on page 21.

[14]J. Zhang et al., Observation of a many-body dynamical phase transition with a 53-qubit quantum simulator, Nature **551**, 601–604 (2017), cited on page 21.

[15]C. Hempel et al., Quantum Chemistry Calculations on a Trapped-Ion Quantum Simulator, Physical Review X **8**, 031022 (2018), cited on page 21.

[16]C. L. Degen, F. Reinhard, and P. Cappellaro, Quantum sensing, Reviews of Modern Physics **89**, 035002 (2017), cited on page 21.

[17]J. Aasi et al., Enhanced sensitivity of the LIGO gravitational wave detector by using squeezed states of light, Nature Photonics **7**, 613–619 (2013), cited on page 21.

[18]T. Ono, R. Okamoto, and S. Takeuchi, An entanglement-enhanced microscope, Nature Communications **4**, 2426 (2013), cited on page 21.

[19]M. Fink et al., Entanglement-enhanced optical gyroscope, (2018), arXiv:1810.02213, cited on pages 21, 237.

[20]S. Slussarenko et al., Unconditional violation of the shot-noise limit in photonic quantum metrology, Nature Photonics, 1 (2017), cited on page 21.

[21]D. D. Awschalom, R. Hanson, J. Wrachtrup, and B. B. Zhou, Quantum technologies with optically interfaced solid-state spins, Nature Photonics **12**, 516–527 (2018), cited on page 21.

[22]J. Yin et al., Satellite-based entanglement distribution over 1200 kilometers, Science **356**, 1140–1144 (2017), cited on pages 21, 22, 25.

[23]J.-G. Ren et al., Ground-to-satellite quantum teleportation, Nature **549**, 70–73 (2017), cited on pages 21, 22.

[24]N. Kalb et al., Entanglement distillation between solid-state quantum network nodes, Science **356**, 928–932 (2017), cited on pages 21, 213.

[25]P. C. Humphreys et al., Deterministic delivery of remote entanglement on a quantum network, Nature **558**, 268–273 (2018), cited on page 21.

[26]C. Simon, Towards a global quantum network, Nature Photonics **11**, 678–680 (2017), cited on page 21.

[27]S. Wehner, D. Elkouss, and R. Hanson, Quantum internet: A vision for the road ahead, Science **362**, eaam9288 (2018), cited on pages 21, 237.

[28]S.-K. Liao et al., Satellite-to-ground quantum key distribution, Nature **549**, 43–47 (2017), cited on page 22.

[29]P. Senellart, G. Solomon, and A. White, High-performance semiconductor quantum-dot single-photon sources, Nature Nanotechnology **12**, 1026–1039 (2017), cited on pages 22, 237.

[30]Y.-M. He et al., Polarized indistinguishable single photons from a quantum dot in an elliptical micropillar, (2018), arXiv:1809.10992, cited on pages 22, 237.

[31]D. Huber et al., Strain-Tunable GaAs Quantum Dot: A Nearly Dephasing-Free Source of Entangled Photon Pairs on Demand, Physical Review Letters **121**, 033902 (2018), cited on pages 22, 25, 237.

[32]C. K. Hong and L. Mandel, Experimental realization of a localized one-photon state, Physical Review Letters **56**, 58–60 (1986), cited on pages 22, 24, 44, 182, 229.

[33]C. K. Hong, Z. Y. Ou, and L. Mandel, Measurement of subpicosecond time intervals between two photons by interference, Physical Review Letters **59**, 2044–2046 (1987), cited on pages 22, 24, 100, 146, 184.

[34]D. Bouwmeester et al., Experimental quantum teleportation, Nature **390**, 575–579 (1997), cited on pages 22, 100.

[35]J.-W. Pan, D. Bouwmeester, H. Weinfurter, and A. Zeilinger, Experimental Entanglement Swapping: Entangling Photons That Never Interacted, Physical Review Letters **80**, 3891–3894 (1998), cited on pages 22, 100.

[36]Z. Xie et al., Harnessing high-dimensional hyperentanglement through a biphoton frequency comb, Nature Photonics **9**, 536–542 (2015), cited on pages 22, 58, 183, 192.

[37]S. Agne et al., Observation of Genuine Three-Photon Interference, Physical Review Letters **118**, 153602 (2017), cited on pages 22, 24.

[38]A. J. Menssen et al., Distinguishability and Many-Particle Interference, Physical Review Letters **118**, 153603 (2017), cited on pages 22, 24.

[39]P. Zarkeshian et al., Entanglement between more than two hundred macroscopic atomic ensembles in a solid, Nature Communications **8**, 906 (2017), cited on page 22.

[40]N. Montaut et al., High-Efficiency Plug-and-Play Source of Heralded Single Photons, Physical Review Applied **8**, 024021 (2017), cited on page 22.

[41]C. K. Hong and L. Mandel, Theory of parametric frequency down conversion of light, Physical Review A **31**, 2409–2418 (1985), cited on pages 22, 24, 39, 40.

[42]Z. Y. Ou and L. Mandel, Violation of Bell's Inequality and Classical Probability in a Two-Photon Correlation Experiment, Physical Review Letters **61**, 50–53 (1988), cited on pages 23, 24.

[43]Y. H. Shih and C. O. Alley, New Type of Einstein-Podolsky-Rosen-Bohm Experiment Using Pairs of Light Quanta Produced by Optical Parametric Down Conversion, Physical Review Letters **61**, 2921–2924 (1988), cited on pages 23, 24.

[44]J. Brendel, E. Mohler, and W. Martienssen, Experimental Test of Bell's Inequality for Energy and Time, EPL (Europhysics Letters) **20**, 575 (1992), cited on pages 23, 24.

[45]A. Mair, A. Vaziri, G. Weihs, and A. Zeilinger, Entanglement of the orbital angular momentum states of photons, Nature **412**, 313–316 (2001), cited on pages 23, 24.

[46]J. C. Howell, R. S. Bennink, S. J. Bentley, and R. W. Boyd, Realization of the Einstein-Podolsky-Rosen Paradox Using Momentum- and Position-Entangled Photons from Spontaneous Parametric Down Conversion, Physical Review Letters **92**, 210403 (2004), cited on pages 23, 24.

[47]J. T. Barreiro, N. K. Langford, N. A. Peters, and P. G. Kwiat, Generation of Hyperentangled Photon Pairs, Physical Review Letters **95**, 260501 (2005), cited on pages 23, 24.

[48]X.-M. Jin et al., Sequential Path Entanglement for Quantum Metrology, Scientific Reports **3**, 1779 (2013), cited on pages 23, 24.

[49]M. Malik et al., Multi-photon entanglement in high dimensions, Nature Photonics **10**, 248–252 (2016), cited on pages 23, 25.

[50]D. Rieländer et al., Frequency-bin entanglement of ultra-narrow band non-degenerate photon pairs, Quantum Science and Technology **3**, 014007 (2018), cited on pages 23, 24, 146.

[51]H. Rütz, K.-H. Luo, H. Suche, and C. Silberhorn, Quantum Frequency Conversion between Infrared and Ultraviolet, Physical Review Applied **7**, 024021 (2017), cited on page 23.

[52]J. Jin et al., Telecom-Wavelength Atomic Quantum Memory in Optical Fiber for Heralded Polarization Qubits, Physical Review Letters **115**, 140501 (2015), cited on page 23.

[53]M. Rambach, A. Nikolova, T. J. Weinhold, and A. G. White, Sub-megahertz linewidth single photon source, APL Photonics **1**, 096101 (2016), cited on pages 23, 26, 87, 161, 166, 201, 212.

[54]L. A. Ngah, O. Alibart, L. Labonté, V. D'Auria, and S. Tanzilli, Ultra-fast heralded single photon source based on telecom technology, Laser & Photonics Reviews **9**, L1–L5 (2015), cited on page 23.

[55]S. Lemieux et al., A Primary Radiation Standard Based on Quantum Nonlinear Optics, in Conference on Lasers and Electro-Optics (2018), paper FW3F.5 (2018), FW3F.5, cited on page 23.

[56]F. Paleari, A. Andreoni, G. Zambra, and M. Bondani, Thermal photon statistics in spontaneous parametric downconversion, Optics Express **12**, 2816–2824 (2004), cited on pages 23, 44.

[57]D. Höckel, L. Koch, and O. Benson, Direct measurement of heralded single-photon statistics from a parametric down-conversion source, Physical Review A **83**, 013802 (2011), cited on pages 23, 132.

[58]I. A. Burenkov et al., Full statistical mode reconstruction of a light field via a photon-number-resolved measurement, Physical Review A **95**, 053806 (2017), cited on page 23.

[59]R. S. Bennink, Optimal collinear Gaussian beams for spontaneous parametric down-conversion, Physical Review A **81**, 053805 (2010), cited on pages 23, 34, 39, 43, 60, 62–65, 71, 72, 74, 76, 77, 88, 234.

[60]K. Banaszek, A. B. U'Ren, and I. A. Walmsley, Generation of correlated photons in controlled spatial modes by downconversion in nonlinear waveguides, Optics Letters **26**, 1367–1369 (2001), cited on page 23.

[61]S. Tanzilli et al., Highly efficient photon-pair source using periodically poled lithium niobate waveguide, Electronics Letters **37**, 26–28 (2001), cited on page 23.

[62]M. Förtsch et al., A versatile source of single photons for quantum information processing, Nature Communications **4**, 1818 (2013), cited on page 23.

[63]M. Förtsch et al., Highly efficient generation of single-mode photon pairs from a crystalline whispering-gallery-mode resonator source, Physical Review A **91**, 023812 (2015), cited on page 23.

[64]S. Ramelow et al., Silicon-Nitride Platform for Narrowband Entangled Photon Generation, (2015), arXiv:1508.04358, cited on page 23.

[65]G. Schunk et al., Interfacing transitions of different alkali atoms and telecom bands using one narrowband photon pair source, Optica **2**, 773–778 (2015), cited on pages 23, 26, 146, 213.

[66]E. Knill, R. Laflamme, and G. J. Milburn, A scheme for efficient quantum computation with linear optics, Nature **409**, 46–52 (2001), cited on pages 24, 25, 100.

[67]L.-M. Duan, M. D. Lukin, J. I. Cirac, and P. Zoller, Long-distance quantum communication with atomic ensembles and linear optics, Nature **414**, 413–418 (2001), cited on pages 24, 25, 212, 237.

[68]D. R. Blay, M. J. Steel, and L. G. Helt, Effects of filtering on the purity of heralded single photons from parametric sources, Physical Review A **96**, 053842 (2017), cited on pages 24, 100.

[69]E. Meyer-Scott et al., Limits on the heralding efficiencies and spectral purities of spectrally filtered single photons from photon-pair sources, Physical Review A **95**, 061803 (2017), cited on pages 24, 100, 164.

[70]P. J. Mosley, Generation of heralded single photons in pure quantum states, Dissertation (University of Oxford, 2007), https://ora.ox.ac.uk/objects/uuid%3A44c36e1e-11ee-41e2-ba29-611c932ce4ff, cited on pages 24, 39.

[71]P. J. Mosley, J. S. Lundeen, B. J. Smith, and I. A. Walmsley, Conditional preparation of single photons using parametric downconversion: a recipe for purity, New Journal of Physics **10**, 093011 (2008), cited on pages 24, 100, 102, 103.

[72]W. H. Louisell, A. Yariv, and A. E. Siegman, Quantum Fluctuations and Noise in Parametric Processes. I., Physical Review **124**, 1646–1654 (1961), cited on page 24.

[73]S. E. Harris, M. K. Oshman, and R. L. Byer, Observation of Tunable Optical Parametric Fluorescence, Physical Review Letters **18**, 732–734 (1967), cited on page 24.

[74]B. R. Mollow and R. J. Glauber, Quantum Theory of Parametric Amplification. I, Physical Review **160**, 1076–1096 (1967), cited on page 24.

[75]B. R. Mollow and R. J. Glauber, Quantum Theory of Parametric Amplification. II, Physical Review **160**, 1097–1108 (1967), cited on page 24.

[76]R. Graham and H. Haken, The quantum-fluctuations of the optical parametric oscillator. I, Zeitschrift für Physik **210**, 276–302 (1968), cited on page 24.

[77]R. Graham, The quantum-fluctuations of the optical parametric oscillator. II, Zeitschrift für Physik **210**, 319–336 (1968), cited on page 24.

[78]D. C. Burnham and D. L. Weinberg, Observation of Simultaneity in Parametric Production of Optical Photon Pairs, Physical Review Letters **25**, 84–87 (1970), cited on page 24.

[79]S. Friberg, C. K. Hong, and L. Mandel, Measurement of Time Delays in the Parametric Production of Photon Pairs, Physical Review Letters **54**, 2011–2013 (1985), cited on page 24.

[80]J. G. Rarity and P. R. Tapster, Fourth-order interference effects at large distances, Physical Review A **45**, 2052–2056 (1992), cited on page 24.

[81]Y. H. Shih, A. V. Sergienko, and M. H. Rubin, Einstein-Podolsky-Rosen state for space-time variables in a two-photon interference experiment, Physical Review A **47**, 1288–1293 (1993), cited on page 24.

[82]C. E. Kuklewicz, F. N. C. Wong, and J. H. Shapiro, Time-Bin-Modulated Biphotons from Cavity-Enhanced Down-Conversion, Physical Review Letters **97**, 223601 (2006), cited on pages 24, 26, 194, 195.

[83]O. Kwon, K.-K. Park, Y.-S. Ra, Y.-S. Kim, and Y.-H. Kim, Time-bin entangled photon pairs from spontaneous parametric down-conversion pumped by a cw multi-mode diode laser, Optics Express **21**, 25492–25500 (2013), cited on page 24.

[84]W.-B. Gao et al., Experimental demonstration of a hyper-entangled ten-qubit Schrödinger cat state, Nature Physics **6**, 331–335 (2010), cited on page 24.

[85]D. Bouwmeester, J.-W. Pan, M. Daniell, H. Weinfurter, and A. Zeilinger, Observation of Three-Photon Greenberger-Horne-Zeilinger Entanglement, Physical Review Letters **82**, 1345–1349 (1999), cited on pages 24, 100.

[86]J.-W. Pan, M. Daniell, S. Gasparoni, G. Weihs, and A. Zeilinger, Experimental Demonstration of Four-Photon Entanglement and High-Fidelity Teleportation, Physical Review Letters **86**, 4435–4438 (2001), cited on page 25.

[87]C.-Y. Lu et al., Experimental entanglement of six photons in graph states, Nature Physics **3**, 91–95 (2007), cited on page 25.

[88]X.-C. Yao et al., Observation of eight-photon entanglement, Nature Photonics **6**, 225–228 (2012), cited on page 25.

[89]B. C. Hiesmayr, M. J. A. de Dood, and W. Löffler, Observation of Four-Photon Orbital Angular Momentum Entanglement, Physical Review Letters **116**, 073601 (2016), cited on page 25.

[90]L.-K. Chen et al., Observation of ten-photon entanglement using thin BiB_3O_6 crystals, Optica **4**, 77–83 (2017), cited on page 25.

[91]X.-L. Wang et al., 18-Qubit Entanglement with Six Photons' Three Degrees of Freedom, Physical Review Letters **120**, 260502 (2018), cited on page 25.

[92]C. H. Bennett et al., Teleporting an unknown quantum state via dual classical and Einstein-Podolsky-Rosen channels, Physical Review Letters **70**, 1895–1899 (1993), cited on pages 25, 100.

[93]H.-J. Briegel, W. Dür, J. I. Cirac, and P. Zoller, Quantum Repeaters: The Role of Imperfect Local Operations in Quantum Communication, Physical Review Letters **81**, 5932–5935 (1998), cited on pages 25, 212, 237.

[94]H. J. Kimble, The quantum internet, Nature **453**, 1023–1030 (2008), cited on pages 25, 212, 237.

[95]M. Pant et al., Routing entanglement in the quantum internet, (2017), arXiv:1708.07142, cited on page 25.

[96]P. C. Humphreys et al., Linear Optical Quantum Computing in a Single Spatial Mode, Physical Review Letters **111**, 150501 (2013), cited on pages 25, 231.

[97]M. A. Nielsen, Optical Quantum Computation Using Cluster States, Physical Review Letters **93**, 040503 (2004), cited on page 25.

[98]B. J. Metcalf et al., Quantum teleportation on a photonic chip, Nature Photonics **8**, 770–774 (2014), cited on page 25.

[99]N. Somaschi et al., Near-optimal single-photon sources in the solid state, Nature Photonics **10**, 340–345 (2016), cited on page 25.

[100]H. Wang et al., Near-Transform-Limited Single Photons from an Efficient Solid-State Quantum Emitter, Physical Review Letters **116**, 213601 (2016), cited on page 25.

[101]J. Huwer et al., Quantum-Dot-Based Telecommunication-Wavelength Quantum Relay, Physical Review Applied **8**, 024007 (2017), cited on page 25.

[102]G. Kiršanskė et al., Indistinguishable and efficient single photons from a quantum dot in a planar nanobeam waveguide, Physical Review B **96**, 165306 (2017), cited on pages 25, 212.

[103]A. Schlehahn et al., A stand-alone fiber-coupled single-photon source, Scientific Reports **8**, 1340 (2018), cited on page 25.

[104]H. Snijders et al., Fiber-Coupled Cavity-QED Source of Identical Single Photons, Physical Review Applied **9**, 031002 (2018), cited on page 25.

[105]H. Wang et al., High-efficiency multiphoton boson sampling, Nature Photonics **11**, 361–365 (2017), cited on page 25.

[106]G. Kurizki et al., Quantum technologies with hybrid systems, Proceedings of the National Academy of Sciences **112**, 3866–3873 (2015), cited on pages 25, 29, 236.

[107]H. Zhang et al., Preparation and storage of frequency-uncorrelated entangled photons from cavity-enhanced spontaneous parametric downconversion, Nature Photonics **5**, 628–632 (2011), cited on pages 25, 26, 105, 146, 210, 233.

[108]G. S. Solomon, E. B. Flagg, S. V. Polyakov, T. Thomay, and A. Muller, Manipulating single photons from disparate quantum sources to be indistinguishable [Invited], Journal of the Optical Society of America B **29**, 319–327 (2012), cited on pages 25, 28.

[109]C. Clausen et al., A source of polarization-entangled photon pairs interfacing quantum memories with telecom photons, New Journal of Physics **16**, 093058 (2014), cited on page 25.

[110]P. S. Michelberger et al., Interfacing GHz-bandwidth heralded single photons with a warm vapour Raman memory, New Journal of Physics **17**, 043006 (2015), cited on pages 25, 33, 93.

[111]Z. Y. Ou and Y. J. Lu, Cavity Enhanced Spontaneous Parametric Down-Conversion for the Prolongation of Correlation Time between Conjugate Photons, Physical Review Letters **83**, 2556–2559 (1999), cited on pages 25–27, 34, 51, 80, 83, 84, 87, 88, 99, 233.

[112]B. Yurke, Use of cavities in squeezed-state generation, Physical Review A **29**, 408–410 (1984), cited on page 26.

[113]M. J. Collett and C. W. Gardiner, Squeezing of intracavity and traveling-wave light fields produced in parametric amplification, Physical Review A **30**, 1386–1391 (1984), cited on pages 26, 51.

[114]L.-A. Wu, H. J. Kimble, J. L. Hall, and H. Wu, Generation of Squeezed States by Parametric Down Conversion, Physical Review Letters **57**, 2520–2523 (1986), cited on page 26.

[115]A. Aiello, D. Fargion, and E. Cianci, Parametric fluorescence and second-harmonic generation in a planar Fabry-Perot microcavity, Physical Review A **58**, 2446–2459 (1998), cited on page 26.

[116]P. Hariharan and B. C. Sanders, Cavity-enhanced parametric down-conversion as a source of correlated photons, Journal of Modern Optics **47**, 1739–1744 (2000), cited on page 26.

[117]J. Shapiro, Coincidence dips and revivals from a Type-II optical parametric amplifier, in Nonlinear Optics: Materials, Fundamentals and Applications, Vol. 79, edited by A. Sawchuk, OSA Trends in Optics and Photonics (2002), FC7, cited on pages 26, 183, 192.

[118]C. E. Kuklewicz, E. Keskiner, F. N. C. Wong, and J. H. Shapiro, A high-flux entanglement source based on a doubly resonant optical parametric amplifier, Journal of Optics B: Quantum and Semiclassical Optics **4**, S162–S168 (2002), cited on pages 26, 31, 98, 207.

[119]Y. J. Lu, R. L. Campbell, and Z. Y. Ou, Mode-Locked Two-Photon States, Physical Review Letters **91**, 163602 (2003), cited on pages 26, 158, 159, 183, 192.

[120]J. H. Shapiro, Generating quantum interference and polarization entanglement with optical parametric amplifiers, in Proceedings of the Sixth International Conference on Quantum Communication, Measurement and Computing (2003), pp. 153–158, cited on page 26.

[121]H. Wang, T. Horikiri, and T. Kobayashi, Polarization-entangled mode-locked photons from cavity-enhanced spontaneous parametric down-conversion, Physical Review A **70**, 043804 (2004), cited on pages 26, 132, 160, 166, 183, 188, 212.

[122]C. E. Kuklewicz, Ultrabright source of polarization-entangled photons from cavity-enhanced downconversion, Dissertation (Massachusetts Institute of Technology, Cambridge, 2005), http://hdl.handle.net/1721.1/33793, cited on pages 26, 159, 173, 183.

[123]J. Laurat, T. Coudreau, and C. Fabre, Type-II Optical Parametric Oscillator: A Versatile Source of Quantum Correlations and Entanglement, in *Quantum Information with Continuous Variables of Atoms and Light* (Imperial College Press, 2007), pp. 197–214, cited on pages 26, 99.

[124]J. S. Neergaard-Nielsen, B. M. Nielsen, H. Takahashi, A. I. Vistnes, and E. S. Polzik, High purity bright single photon source, Optics Express **15**, 7940–7949 (2007), cited on page 26.

[125]X.-H. Bao et al., Generation of Narrow-Band Polarization-Entangled Photon Pairs for Atomic Quantum Memories, Physical Review Letters **101**, 190501 (2008), cited on pages 26, 31, 98, 132, 183.

[126]F. Wolfgramm et al., Bright filter-free source of indistinguishable photon pairs, Optics Express **16**, 18145–18151 (2008), cited on pages 26, 87, 132, 146, 166, 183, 187, 199, 200, 212.

[127]A. Haase, N. Piro, J. Eschner, and M. W. Mitchell, Tunable narrowband entangled photon pair source for resonant single-photon single-atom interaction, Optics Letters **34**, 55–57 (2009), cited on pages 26, 111, 112, 210.

[128]M. Scholz, L. Koch, R. Ullmann, and O. Benson, Single-mode operation of a high-brightness narrow-band single-photon source, Applied Physics Letters **94**, 201105 (2009), cited on pages 26, 31, 73, 87, 89, 90, 94, 109, 112, 132, 134, 166, 176, 177, 180, 213.

[129]Y. Jeronimo-Moreno, S. Rodriguez-Benavides, and A. B. U'Ren, Theory of cavity-enhanced spontaneous parametric downconversion, Laser Physics **20**, 1221–1233 (2010), cited on pages 26, 27, 34, 35, 43, 48, 49, 51, 56, 57, 89, 105, 106, 233.

[130]C.-S. Chuu, G. Y. Yin, and S. E. Harris, A miniature ultrabright source of temporally long, narrowband biphotons, Applied Physics Letters **101**, 051108 (2012), cited on pages 26, 27, 52, 83, 88–90, 176, 233.

[131]O. Morin, V. D'Auria, C. Fabre, and J. Laurat, High-fidelity single-photon source based on a Type II optical parametric oscillator, Optics Letters **37**, 3738–3740 (2012), cited on page 26.

[132]E. Pomarico, B. Sanguinetti, C. I. Osorio, H. Herrmann, and R. T. Thew, Engineering integrated pure narrow-band photon sources, New Journal of Physics **14**, 033008 (2012), cited on pages 26, 106, 146.

[133]J. Fekete, D. Rieländer, M. Cristiani, and H. de Riedmatten, Ultranarrow-Band Photon-Pair Source Compatible with Solid State Quantum Memories and Telecommunication Networks, Physical Review Letters **110**, 220502 (2013), cited on pages 26, 132, 161, 176, 213.

[134]C. Reimer et al., Integrated frequency comb source of heralded single photons, Optics Express **22**, 6535–6546 (2014), cited on page 26.

[135]Z.-Y. Zhou, D.-S. Ding, Y. Li, F.-Y. Wang, and B.-S. Shi, Cavity-enhanced bright photon pairs at telecom wavelengths with a triple-resonance configuration, Journal of the Optical Society of America B **31**, 128–134 (2014), cited on pages 26, 132.

[136]K.-H. Luo et al., Direct generation of genuine single-longitudinal-mode narrowband photon pairs, New Journal of Physics **17**, 073039 (2015), cited on pages 26, 27, 44, 52, 56, 80, 83, 84, 86, 88, 146, 176, 233.

[137]B. Brecht, K.-H. Luo, H. Herrmann, and C. Silberhorn, A versatile design for resonant guided-wave parametric down-conversion sources for quantum repeaters, Applied Physics B **122**, 1–11 (2016), cited on pages 26, 27, 35, 52, 84, 105, 233.

[138]A. Ahlrichs and O. Benson, Bright source of indistinguishable photons based on cavity-enhanced parametric down-conversion utilizing the cluster effect, Applied Physics Letters **108**, 021111 (2016), cited on pages 26, 33, 89–91, 94, 95, 98, 142, 143, 145, 179, 207, 212, 241.

[139]Z.-Y. Zhou et al., Tunable cavity-enhanced photon pairs source in Hermite-Gaussian mode, AIP Advances **6**, 025114 (2016), cited on page 26.

[140]J. Arenskotter, S. Kucera, and J. Eschner, Polarization-entangled photon pairs from a cavity-enhanced down-conversion source in Sagnac configuration, in 2017 Conference on Lasers and Electro-Optics Europe European Quantum Electronics Conference (CLEO/Europe-EQEC) (2017), pp. 1–1, cited on pages 26, 237.

[141]K.-H. Luo, H. Herrmann, and C. Silberhorn, Temporal correlations of spectrally narrowband photon pair sources, Quantum Science and Technology **2**, 024002 (2017), cited on pages 26, 146, 176.

[142]F. Wolfgramm, A. Cerè, and M. W. Mitchell, NOON states from cavity-enhanced down-conversion: high quality and super-resolution, Journal of the Optical Society of America B **27**, A25–A29 (2010), cited on pages 26, 146, 183, 201, 210, 233.

[143]F. Wolfgramm, Y. A. de Icaza Astiz, F. A. Beduini, A. Cerè, and M. W. Mitchell, Atom-Resonant Heralded Single Photons by Interaction-Free Measurement, Physical Review Letters **106**, 053602 (2011), cited on pages 26, 146, 161, 176, 213, 233.

[144]F. Wolfgramm, C. Vitelli, F. A. Beduini, N. Godbout, and M. W. Mitchell, Entanglement-enhanced probing of a delicate material system, Nature Photonics **7**, 28–32 (2013), cited on pages 26, 146, 183, 233, 237.

[145]D. Rieländer et al., Quantum Storage of Heralded Single Photons in a Praseodymium-Doped Crystal, Physical Review Letters **112**, 040504 (2014), cited on pages 26, 148, 176, 213, 233.

[146]A. Lenhard et al., Telecom-heralded single-photon absorption by a single atom, Physical Review A **92**, 063827 (2015), cited on pages 26, 146, 213, 233.

[147]M. W. Mitchell, Generation, Characterization and Use of Atom-Resonant Indistinguishable Photon Pairs, in *Engineering the Atom-Photon Interaction*, Nano-Optics and Nanophotonics (Springer, Cham, 2015), pp. 183–213, cited on pages 26, 233.

[148]K. Huang et al., Experimental quantum state engineering with time-separated heraldings from a continuous-wave light source: A temporal-mode analysis, Physical Review A **93**, 013838 (2016), cited on pages 26, 233.

[149]D. Rieländer, A. Lenhard, M. Mazzera, and H. de Riedmatten, Cavity enhanced telecom heralded single photons for spin-wave solid state quantum memories, New Journal of Physics **18**, 123013 (2016), cited on pages 26, 146, 176, 213, 233.

[150]M. Rambach, Narrowband Single Photons for Light-Matter Interfaces, Dissertation (The University of Queensland, Queensland, Australia, 2017), https://doi.org/10.14264/uql.2017.994, cited on pages 26, 183, 187, 188, 192, 233.

[151]A. Moqanaki, F. Massa, and P. Walther, Generation of Single-mode Narrowband Photons Resonant to Atomic Transitions, (2018), arXiv:1810.02430, cited on pages 26, 148, 210.

[152]J. A. Zielińska and M. W. Mitchell, Atom-resonant squeezed light from a tunable monolithic ppRKTP parametric amplifier, Optics Letters **43**, 643–646 (2018), cited on pages 26, 98, 99, 148.

[153]J. A. Zielińska, Spontaneous parametric down-conversion sources for generation of atom-resonant quantum light, Dissertation (Universitat Politècnica de Catalunya, Catalunya, 2018), http://hdl.handle.net/2117/116304, cited on page 26.

[154]P.-J. Tsai and Y.-C. Chen, Ultrabright, narrow-band photon-pair source for atomic quantum memories, Quantum Science and Technology **3**, 034005 (2018), cited on page 26.

[155]A. Seri et al., Quantum Correlations between Single Telecom Photons and a Multimode On-Demand Solid-State Quantum Memory, Physical Review X **7**, 021028 (2017), cited on pages 26, 146, 213, 237.

[156]A. Seri et al., Laser-written integrated platform for quantum storage of heralded single photons, Optica **5**, 934–941 (2018), cited on pages 26, 237.

[157]D. O. Akat'ev, I. Z. Latypov, A. V. Shkalikov, and A. A. Kalachev, Generation of narrow-band single-photon states via spontaneous parametric down-conversion for quantum memories in doped crystals, Quantum Electronics **48**, 902 (2018), cited on pages 26, 237.

[158]K. Niizeki et al., Ultrabright narrow-band telecom two-photon source for long-distance quantum communication, Applied Physics Express **11**, 042801 (2018), cited on pages 26, 237.

[159]N. Maring, D. Lago-Rivera, A. Lenhard, G. Heinze, and H. de Riedmatten, Quantum frequency conversion of memory-compatible single photons from 606 nm to the telecom C-band, Optica **5**, 507–513 (2018), cited on pages 26, 213, 237.

[160]T. J. Herzog, J. G. Rarity, H. Weinfurter, and A. Zeilinger, Frustrated two-photon creation via interference, Physical Review Letters **72**, 629–632 (1994), cited on pages 27, 45, 51, 233.

[161]M. Scholz, L. Koch, and O. Benson, Analytical treatment of spectral properties and signal–idler intensity correlations for a double-resonant optical parametric oscillator far below threshold, Optics Communications **282**, 3518–3523 (2009), cited on pages 27, 34, 43, 51, 76, 85, 87, 93, 160, 161, 233.

[162]C.-S. Chuu and S. E. Harris, Ultrabright backward-wave biphoton source, Physical Review A **83**, 061803 (2011), cited on pages 27, 34, 45, 47, 52, 58, 76, 83, 86, 88, 93, 160, 233.

[163]M. T. Rakher, R. J. Warburton, and P. Treutlein, Prospects for storage and retrieval of a quantum-dot single photon in an ultracold ^{87}Rb ensemble, Physical Review A **88**, 053834 (2013), cited on pages 28, 93, 126.

[164]K. F. Reim et al., Single-Photon-Level Quantum Memory at Room Temperature, Physical Review Letters **107**, 053603 (2011), cited on pages 28, 215, 230.

[165]K. F. Reim et al., Towards high-speed optical quantum memories, Nature Photonics **4**, 218 (2010), cited on page 28.

[166]J. Wolters et al., Simple Atomic Quantum Memory Suitable for Semiconductor Quantum Dot Single Photons, Physical Review Letters **119**, 060502 (2017), cited on pages 28, 33, 93, 230.

[167]T. Huber et al., Interfacing a quantum dot with a spontaneous parametric down-conversion source, Quantum Science and Technology **2**, 034016 (2017), cited on page 28.

[168]S. V. Polyakov et al., Coalescence of Single Photons Emitted by Disparate Single-Photon Sources: The Example of InAs Quantum Dots and Parametric Down-Conversion Sources, Physical Review Letters **107**, 157402 (2011), cited on pages 28, 111.

[169]C. Matthiesen, A. N. Vamivakas, and M. Atatüre, Subnatural Linewidth Single Photons from a Quantum Dot, Physical Review Letters **108**, 093602 (2012), cited on pages 33, 93, 126.

[170]C. Matthiesen et al., Phase-locked indistinguishable photons with synthesized waveforms from a solid-state source, Nature Communications **4**, 1600 (2013), cited on page 33.

[171]D. G. England et al., High-fidelity polarization storage in a gigahertz bandwidth quantum memory, Journal of Physics B: Atomic, Molecular and Optical Physics **45**, 124008 (2012), cited on page 33.

[172]R. Finkelstein, E. Poem, O. Michel, O. Lahad, and O. Firstenberg, Fast, noise-free memory for photon synchronization at room temperature, Science Advances **4**, eaap8598 (2018), cited on pages 33, 213.

[173]E. Pomarico et al., Waveguide-based OPO source of entangled photon pairs, New Journal of Physics **11**, 113042 (2009), cited on pages 33, 83, 146, 198.

[174]G. D. Boyd and D. A. Kleinman, Parametric Interaction of Focused Gaussian Light Beams, Journal of Applied Physics **39**, 3597–3639 (1968), cited on pages 34, 58, 60, 61, 63–65, 72, 74.

[175]R. W. Boyd, Nonlinear Optics (Academic Press, San Diego, California, 2003), cited on pages 36–38, 60.

[176]P. D. Drummond and M. Hillery, The Quantum Theory of Nonlinear Optics (Cambridge University Press, 2014), cited on page 37.

[177]M. H. Rubin, D. N. Klyshko, Y. H. Shih, and A. V. Sergienko, Theory of two-photon entanglement in type-II optical parametric down-conversion, Physical Review A **50**, 5122–5133 (1994), cited on pages 39, 40, 186.

[178]A. Christ, B. Brecht, W. Mauerer, and C. Silberhorn, Theory of quantum frequency conversion and type-II parametric down-conversion in the high-gain regime, New Journal of Physics **15**, 053038 (2013), cited on page 40.

[179]F. J. Dyson, The Radiation Theories of Tomonaga, Schwinger, and Feynman, Physical Review **75**, 486–502 (1949), cited on page 41.

[180]S. E. Harris, Proposed backward wave oscillation in the infrared, Applied Physics Letters **9**, 114–116 (1966), cited on page 45.

[181]C. Canalias and V. Pasiskevicius, Mirrorless optical parametric oscillator, Nature Photonics **1**, 459–462 (2007), cited on page 47.

[182]J. Bjorkholm, A. Ashkin, and R. Smith, Improvement of optical parametric oscillators by nonresonant pump reflection, IEEE Journal of Quantum Electronics **6**, 797–799 (1970), cited on pages 47, 51.

[183]A. E. Siegman, Nonlinear Optical Effects: An Optical Power Limiter, Applied Optics **1**, 739–744 (1962), cited on page 51.

[184]J. Bjorkholm, Analysis of the doubly resonant optical parametric oscillator without power-dependent reflections, IEEE Journal of Quantum Electronics **5**, 293–295 (1969), cited on page 51.

[185]T. Debuisschert, A. Sizmann, E. Giacobino, and C. Fabre, Type-II continuous-wave optical parametric oscillators: oscillation and frequency-tuning characteristics, Journal of the Optical Society of America B **10**, 1668–1680 (1993), cited on pages 51, 98.

[186]M. Fujimura, T. Suhara, and H. Nishihara, Theoretical analysis of resonant waveguide optical second harmonic generation devices, Journal of Lightwave Technology **14**, 1899–1906 (1996), cited on page 52.

[187]T. Suhara and M. Fujimura, Waveguide Nonlinear-Optic Devices, Springer Series in Photonics (Springer-Verlag, Berlin Heidelberg, 2003), cited on page 52.

[188]R. C. Eckardt, C. D. Nabors, W. J. Kozlovsky, and R. L. Byer, Optical parametric oscillator frequency tuning and control, Journal of the Optical Society of America B **8**, 646–667 (1991), cited on pages 58, 86, 148.

[189]C. Kurtsiefer, M. Oberparleiter, and H. Weinfurter, High-efficiency entangled photon pair collection in type-II parametric fluorescence, Physical Review A **64**, 023802 (2001), cited on page 60.

[190]F. A. Bovino et al., Effective fiber-coupling of entangled photons for quantum communication, Optics Communications **227**, 343–348 (2003), cited on page 60.

[191]R. Andrews, E. R. Pike, and S. Sarkar, Optimal coupling of entangled photons into single-mode optical fibers, Optics Express **12**, 3264–3269 (2004), cited on page 60.

[192]D. Ljunggren and M. Tengner, Optimal focusing for maximal collection of entangled narrow-band photon pairs into single-mode fibers, Physical Review A **72**, 062301 (2005), cited on page 60.

[193]A. Ling, A. Lamas-Linares, and C. Kurtsiefer, Absolute emission rates of spontaneous parametric down-conversion into single transverse Gaussian modes, Physical Review A **77**, 043834 (2008), cited on page 60.

[194]M. W. Mitchell, Parametric down-conversion from a wave-equation approach: Geometry and absolute brightness, Physical Review A **79**, 043835 (2009), cited on page 60.

[195]P. B. Dixon et al., Heralding efficiency and correlated-mode coupling of near-IR fiber-coupled photon pairs, Physical Review A **90**, 043804 (2014), cited on pages 60, 71, 76, 77, 91, 234.

[196]A. E. Siegman, Lasers (University Science Books, 1986), cited on pages 64, 73, 82.

[197]S. Yu and A. M. Weiner, Phase-matching temperature shifts in blue generation by frequency doubling of femtosecond pulses in $KNbO_3$, JOSA B **16**, 1300–1304 (1999), cited on page 64.

[198]P. K. Das, Lasers and Optical Engineering (Springer Science & Business Media, 2012), cited on pages 66, 68.

[199]K. F. Renk, Basics of Laser Physics: For Students of Science and Engineering (Springer Science & Business Media, 2012), cited on page 66.

[200]H. Kogelnik and T. Li, Laser Beams and Resonators, Applied Optics **5**, 1550–1567 (1966), cited on page 66.

[201]T. Guerreiro et al., High efficiency coupling of photon pairs in practice, Optics Express **21**, 27641–27651 (2013), cited on pages 71, 234.

[202]S. Schiller, K. Schneider, and J. Mlynek, Theory of an optical parametric oscillator with resonant pump and signal, JOSA B **16**, 1512–1524 (1999), cited on page 74.

[203]G. Harder et al., An optimized photon pair source for quantum circuits, Optics Express **21**, 13975–13985 (2013), cited on page 74.

[204]P. Maddaloni, M. Bellini, and P. D. Natale, Laser-Based Measurements for Time and Frequency Domain Applications: A Handbook (Taylor & Francis, 2016), cited on page 79.

[205]A. Ahlrichs, C. Berkemeier, B. Sprenger, and O. Benson, A monolithic polarization-independent frequency-filter system for filtering of photon pairs, Applied Physics Letters **103**, 241110 (2013), cited on pages 87, 89, 90, 111, 123, 125, 144, 146, 147, 199, 213, 241.

[206]U. Herzog, M. Scholz, and O. Benson, Theory of biphoton generation in a single-resonant optical parametric oscillator far below threshold, Physical Review A **77**, 023826 (2008), cited on pages 88, 158–161.

[207]G. Hansson, H. Karlsson, S. Wang, and F. Laurell, Transmission measurements in KTP and isomorphic compounds, Applied Optics **39**, 5058–5069 (2000), cited on pages 91, 95.

[208]B. Boulanger, J. P. Fève, G. Marnier, and B. Ménaert, Methodology for optical studies of nonlinear crystals: application to the isomorph family $KTiOPO_4$, $KTIOAsO_4$, $RbTiOAsO_4$ and $CsTiOAsO_4$, Pure and Applied Optics: Journal of the European Optical Society Part A **7**, 239 (1998), cited on page 91.

[209]M. V. Pack, D. J. Armstrong, and A. V. Smith, Measurement of the $\chi^{(2)}$ tensors of $KTiOPO_4$, $KTiOAsO_4$, $RbTiOPO_4$, and $RbTiOAsO_4$ crystals, Applied Optics **43**, 3319–3323 (2004), cited on page 91.

[210]M. M. Fejer, G. A. Magel, D. H. Jundt, and R. L. Byer, Quasi-phase-matched second harmonic generation: tuning and tolerances, IEEE Journal of Quantum Electronics **28**, 2631–2654 (1992), cited on page 93.

[211]J.-J. Zondy, D. Kolker, C. Bonnin, and D. Lupinski, Second-harmonic generation with monolithic walk-off-compensating periodic structures. II. Experiments, JOSA B **20**, 1695–1707 (2003), cited on page 93.

[212]X. Mu, H. Meissner, and H.-C. Lee, Optical parametric oscillations of 2μm in multiple-layer bonded walk-off compensated KTP stacks, Optics Letters **35**, 387–389 (2010), cited on pages 93, 94.

[213]Y.-M. He et al., Deterministic implementation of a bright, on-demand single-photon source with near-unity indistinguishability via quantum dot imaging, Optica **4**, 802–808 (2017), cited on pages 93, 213.

[214]M. J. Missey, V. Dominic, L. E. Myers, and R. C. Eckardt, Diffusion-bonded stacks of periodically poled lithium niobate, Optics Letters **23**, 664–666 (1998), cited on page 94.

[215]G. Qiu et al., Highly efficient intracavity frequency doubling 532-nm laser based on the gray tracking resistance KTP crystal, Laser Physics **20**, 777–780 (2010), cited on page 94.

[216]V. D'Auria, S. Fornaro, A. Porzio, E. A. Sete, and S. Solimeno, Fine tuning of a triply resonant OPO for generating frequency degenerate CV entangled beams at low pump powers, Applied Physics B **91**, 309–314 (2008), cited on pages 98, 140, 148, 149.

[217]J. A. Zielińska, A. Zukauskas, C. Canalias, M. A. Noyan, and M. W. Mitchell, Fully-resonant, tunable, monolithic frequency conversion as a coherent UVA source, Optics Express **25**, 1142–1150 (2017), cited on pages 98, 99, 148.

[218]B. Hardy et al., Compact, single-frequency, doubly resonant optical parametric oscillator pumped in an achromatic phase-adapted double-pass geometry, Optics Letters **36**, 678–680 (2011), cited on page 99.

[219]A. Boucon, B. Hardy-Baranski, and F. Bretenaker, Compact infrared continuous-wave double-pass single-frequency doubly-resonant OPO, Optics Communications **333**, 53–57 (2014), cited on page 99.

[220]K. Makino et al., Synchronization of optical photons for quantum information processing, Science Advances **2**, e1501772 (2016), cited on page 100.

[221]P. J. Mosley et al., Heralded Generation of Ultrafast Single Photons in Pure Quantum States, Physical Review Letters **100**, 133601 (2008), cited on pages 100–102.

[222]C. I. Osorio, N. Sangouard, and R. T. Thew, On the purity and indistinguishability of down-converted photons, Journal of Physics B: Atomic, Molecular and Optical Physics **46**, 055501 (2013), cited on page 100.

[223]E. Megidish et al., Entanglement Swapping between Photons that have Never Coexisted, Physical Review Letters **110**, 210403 (2013), cited on page 100.

[224]S. Barz, G. Cronenberg, A. Zeilinger, and P. Walther, Heralded generation of entangled photon pairs, Nature Photonics **4**, 553–556 (2010), cited on page 100.

[225]W. P. Grice, A. B. U'Ren, and I. A. Walmsley, Eliminating frequency and space-time correlations in multiphoton states, Physical Review A **64**, 063815 (2001), cited on pages 100, 102.

[226]A. B. U'Ren et al., Generation of Pure-State Single-Photon Wavepackets by Conditional Preparation Based on Spontaneous Parametric Downconversion, Laser Physics, 146 (2005), cited on pages 100, 101.

[227]F. Laudenbach, H. Hübel, M. Hentschel, P. Walther, and A. Poppe, Modelling parametric down-conversion yielding spectrally pure photon pairs, Optics Express **24**, 2712–2727 (2016), cited on pages 100, 102.

[228]A. Dosseva, Ł. Cincio, and A. M. Brańczyk, Shaping the joint spectrum of down-converted photons through optimized custom poling, Physical Review A **93**, 013801 (2016), cited on pages 100, 102.

[229]C. Chen et al., Efficient generation and characterization of spectrally factorable biphotons, Optics Express **25**, 7300–7312 (2017), cited on page 100.

[230]F. Graffitti, J. Kelly-Massicotte, A. Fedrizzi, and A. M. Brańczyk, Design considerations for high-purity heralded single-photon sources, Physical Review A **98**, 053811 (2018), cited on page 100.

[231]C. K. Law, I. A. Walmsley, and J. H. Eberly, Continuous Frequency Entanglement: Effective Finite Hilbert Space and Entropy Control, Physical Review Letters **84**, 5304–5307 (2000), cited on pages 101, 102.

[232]M. A. Nielsen and I. L. Chuang, Quantum Computation and Quantum Information: 10th Anniversary Edition (Cambridge University Press, 2010), cited on page 102.

[233]B. M. Nielsen, J. S. Neergaard-Nielsen, and E. S. Polzik, Time gating of heralded single photons for atomic memories, Optics Letters **34**, 3872–3874 (2009), cited on page 106.

[234]C. Song, S. Bao-Sen, and G. Guang-Can, Adjusting the properties of the photon generated via an optical parametric oscillator by using a pulse pumped laser, Chinese Physics B **20**, 114206 (2011), cited on page 106.

[235]Y.-P. Huang, J. B. Altepeter, and P. Kumar, Heralding single photons without spectral factorability, Physical Review A **82**, 043826 (2010), cited on page 106.

[236]A. Christ and C. Silberhorn, Limits on the deterministic creation of pure single-photon states using parametric down-conversion, Physical Review A **85**, 023829 (2012), cited on pages 107, 213.

[237]M. Scholz, New Light Sources for Quantum Information Processing - Single Photons from Single Quantum Dots and Cavity-Enhanced Parametric Down-Conversion, Dissertation (Humboldt-Universität zu Berlin, Berlin, 2009), http://www.logos-verlag.de/cgi-bin/buch/isbn/2220, cited on pages 109, 126, 132.

[238]M. Scholz, L. Koch, and O. Benson, Statistics of Narrow-Band Single Photons for Quantum Memories Generated by Ultrabright Cavity-Enhanced Parametric Down-Conversion, Physical Review Letters **102**, 063603 (2009), cited on pages 109, 146.

[239]P. Palittapongarnpim, A. MacRae, and A. I. Lvovsky, Note: A monolithic filter cavity for experiments in quantum optics, Review of Scientific Instruments **83**, 066101 (2012), cited on pages 109, 111, 112, 114, 115.

[240]M. D. Eisaman, J. Fan, A. Migdall, and S. V. Polyakov, Invited Review Article: Single-photon sources and detectors, Review of Scientific Instruments **82**, 071101 (2011), cited on page 110.

[241]M. Hennrich, T. Legero, A. Kuhn, and G. Rempe, Photon statistics of a non-stationary periodically driven single-photon source, New Journal of Physics **6**, 86 (2004), cited on page 110.

[242]C. Maurer, C. Becher, C. Russo, J. Eschner, and R. Blatt, A single-photon source based on a single Ca + ion, New Journal of Physics **6**, 94 (2004), cited on page 110.

[243]T. Gaebel et al., Stable single-photon source in the near infrared, New Journal of Physics **6**, 98 (2004), cited on page 110.

[244]S. Kako et al., A gallium nitride single-photon source operating at 200 K, Nature Materials **5**, 887–892 (2006), cited on page 111.

[245] A. J. Shields, Semiconductor quantum light sources, Nature Photonics **1**, 215–223 (2007), cited on page 111.

[246] A. B. U'Ren, C. Silberhorn, K. Banaszek, and I. A. Walmsley, Efficient Conditional Preparation of High-Fidelity Single Photon States for Fiber-Optic Quantum Networks, Physical Review Letters **93**, 093601 (2004), cited on page 111.

[247] J. S. Neergaard-Nielsen, B. M. Nielsen, C. Hettich, K. Mølmer, and E. S. Polzik, Generation of a Superposition of Odd Photon Number States for Quantum Information Networks, Physical Review Letters **97**, 083604 (2006), cited on page 111.

[248] S. Riedl et al., Bose-Einstein condensate as a quantum memory for a photonic polarization qubit, Physical Review A **85**, 022318 (2012), cited on page 111.

[249] D. Höckel, E. Martin, and O. Benson, Note: An ultranarrow bandpass filter system for single-photon experiments in quantum optics, Review of Scientific Instruments **81**, 026108 (2010), cited on page 111.

[250] C. Berkemeier, Cascaded Monolithic Fabry-Pérot Filter System for Two-Photon Quantum Interference Experiments, Diplomarbeit (Technische Universität Berlin, Berlin, 2013), cited on page 111.

[251] D. A. Steck, *Cesium D Line Data*, available online at http://steck.us/alkalidata (revision 2.1.4), 2010, cited on pages 114, 146.

[252] C. Pugatschow, Untersuchung des Mollow-Tripletts resonant angeregter InGaAs-Quantenpunkte am Cs-D1-Übergang, Bachelor thesis (Humboldt-Universität zu Berlin, 2016), cited on pages 118, 120.

[253] A. V. Kuhlmann et al., A dark-field microscope for background-free detection of resonance fluorescence from single semiconductor quantum dots operating in a set-and-forget mode, Review of Scientific Instruments **84**, 073905 (2013), cited on pages 120, 121.

[254] O. Gazzano et al., Effects of resonant-laser excitation on the emission properties in a single quantum dot, Optica **5**, 354–359 (2018), cited on page 120.

[255] H. S. Nguyen et al., Optically Gated Resonant Emission of Single Quantum Dots, Physical Review Letters **108**, 057401 (2012), cited on page 120.

[256] B. R. Mollow, Power Spectrum of Light Scattered by Two-Level Systems, Physical Review **188**, 1969–1975 (1969), cited on pages 120, 121.

[257] O. Astafiev et al., Resonance Fluorescence of a Single Artificial Atom, Science **327**, 840–843 (2010), cited on pages 120, 121.

[258] F. Ding et al., Tuning the Exciton Binding Energies in Single Self-Assembled InGaAs/GaAs Quantum Dots by Piezoelectric-Induced Biaxial Stress, Physical Review Letters **104**, 067405 (2010), cited on page 118.

[259]A. Araya et al., Absolute-length determination of a long-baseline Fabry–Perot cavity by means of resonating modulation sidebands, Applied Optics **38**, 2848–2856 (1999), cited on page 122.

[260]S. Ates et al., Two-Photon Interference Using Background-Free Quantum Frequency Conversion of Single Photons Emitted by an InAs Quantum Dot, Physical Review Letters **109**, 147405 (2012), cited on pages 124, 212.

[261]M. Ghali, K. Ohtani, Y. Ohno, and H. Ohno, Generation and control of polarization-entangled photons from GaAs island quantum dots by an electric field, Nature Communications **3**, 661 (2012), cited on page 124.

[262]A. R. McMillan et al., Two-photon interference between disparate sources for quantum networking, Scientific Reports **3**, 2032 (2013), cited on page 126.

[263]E. O. Ammann and P. C. Montgomery, Threshold Calculations for an Optical Parametric Oscillator Employing a Hemispherical Resonator, Journal of Applied Physics **41**, 5270–5274 (1970), cited on page 127.

[264]D. J. McCarron, S. A. King, and S. L. Cornish, Modulation transfer spectroscopy in atomic rubidium, Measurement Science and Technology **19**, 105601 (2008), cited on page 128.

[265]M. Kernbach, Experimentelle Untersuchungen zu schmalbandigen Paarphotonenquellen, Diplomarbeit (Humboldt-Universität zu Berlin, Berlin, 2012), cited on page 128.

[266]S. M. Hegde, K. L. Schepler, R. D. Peterson, and D. E. Zelmon, Room-temperature, near IR fluorescence of high optical quality KTP, in Proc. SPIE 6552, Laser Source Technology for Defense and Security III (2007), p. 65520V, cited on page 131.

[267]K. Huang, H. L. Jeannic, J. Ruaudel, O. Morin, and J. Laurat, Microcontroller-based locking in optics experiments, Review of Scientific Instruments **85**, 123112 (2014), cited on pages 132–134, 235.

[268]T. W. Hänsch and B. Couillaud, Laser frequency stabilization by polarization spectroscopy of a reflecting reference cavity, Optics Communications **35**, 441–444 (1980), cited on page 132.

[269]R. V. Pound, Electronic Frequency Stabilization of Microwave Oscillators, Review of Scientific Instruments **17**, 490–505 (1946), cited on page 132.

[270]R. W. P. Drever et al., Laser phase and frequency stabilization using an optical resonator, Applied Physics B **31**, 97–105 (1983), cited on page 132.

[271]C. Kleine, Locking zweier optischer Resonatoren mittels Mikrocontroller zur Erzeugung schmalbandiger Photonenpaare, Bachelor thesis (Humboldt-Universität zu Berlin, Berlin, 2015), cited on page 134.

[272]S. Emanueli and A. Arie, Temperature-dependent dispersion equations for $KTiOPO_4$ and $KTiOAsO_4$, Applied Optics **42**, 6661–6665 (2003), cited on pages 140, 154.

[273]F. Monteiro, A. Martin, B. Sanguinetti, H. Zbinden, and R. T. Thew, Narrow-band photon pair source for quantum networks, Optics Express **22**, 4371–4378 (2014), cited on pages 146, 176, 213, 230.

[274]C.-H. Wu et al., Bright single photons for light-matter interaction, Physical Review A **96**, 023811 (2017), cited on pages 146, 176.

[275]N. Piro, A. Haase, M. W. Mitchell, and J. Eschner, An entangled photon source for resonant single-photon–single-atom interaction, Journal of Physics B: Atomic, Molecular and Optical Physics **42**, 114002 (2009), cited on page 148.

[276]D. Lee and N. C. Wong, Stabilization and tuning of a doubly resonant optical parametric oscillator, Journal of the Optical Society of America B **10**, 1659–1667 (1993), cited on page 148.

[277]H. Goto, Y. Yanagihara, H. Wang, T. Horikiri, and T. Kobayashi, Observation of an oscillatory correlation function of multimode two-photon pairs, Physical Review A **68**, 015803 (2003), cited on pages 160, 166.

[278]J. W. Cooley and J. W. Tukey, An algorithm for the machine calculation of complex Fourier series, Mathematics of Computation **19**, 297–301 (1965), cited on page 160.

[279]M. Heideman, D. Johnson, and C. Burrus, Gauss and the history of the fast fourier transform, IEEE ASSP Magazine **1**, 14–21 (1984), cited on page 160.

[280]A. Jerri, The Gibbs Phenomenon in Fourier Analysis, Splines and Wavelet (Springer, 1998), cited on pages 162, 163.

[281]K. N. Cassemiro, K. Laiho, and C. Silberhorn, Accessing the purity of a single photon by the width of the Hong–Ou–Mandel interference, New Journal of Physics **12**, 113052 (2010), cited on page 164.

[282]B. A. Korzh et al., Demonstrating sub-3 ps temporal resolution in a superconducting nanowire single-photon detector, (2018), arXiv:1804.06839, cited on page 174.

[283]T. Kroh, A. Ahlrichs, B. Sprenger, and O. Benson, Heralded wave packet manipulation and storage of a frequency-converted pair photon at telecom wavelength, Quantum Science and Technology **2**, 034007 (2017), cited on pages 176, 211, 241.

[284]R. J. Lewis-Swan and K. V. Kheruntsyan, Proposal for demonstrating the Hong–Ou–Mandel effect with matter waves, Nature Communications **5**, 3752 (2014), cited on page 182.

[285]J. G. Rarity and P. R. Tapster, Fourth-order interference in parametric down-conversion, JOSA B **6**, 1221–1226 (1989), cited on page 182.

[286]H. Fearn and R. Loudon, Theory of two-photon interference, JOSA B **6**, 917–927 (1989), cited on page 182.

[287]R. Ghosh, C. K. Hong, Z. Y. Ou, and L. Mandel, Interference of two photons in parametric down conversion, Physical Review A **34**, 3962–3968 (1986), cited on page 182.

[288]R. Ghosh and L. Mandel, Observation of nonclassical effects in the interference of two photons, Physical Review Letters **59**, 1903–1905 (1987), cited on page 182.

[289]T. B. Pittman et al., Can Two-Photon Interference be Considered the Interference of Two Photons?, Physical Review Letters **77**, 1917–1920 (1996), cited on page 182.

[290]A. V. Sergienko, Y. H. Shih, and M. H. Rubin, Experimental evaluation of a two-photon wave packet in type-II parametric downconversion, Journal of the Optical Society of America B **12**, 859–862 (1995), cited on pages 182, 185–188.

[291]R. Mottola, Untersuchung von Photoneninterferenz mit Photonenpaaren aus einem optisch parametrischen Oszillator, Bachelor thesis (Humboldt-Universität zu Berlin, Berlin, 2013), cited on pages 184, 195.

[292]O. Dietz et al., A folded-sandwich polarization-entangled two-color photon pair source with large tuning capability for applications in hybrid quantum systems, Applied Physics B **122**, 1–7 (2016), cited on pages 186, 208, 209, 213, 241.

[293]E. Martin, Konstruktion und experimenteller Aufbau eines Multipass Fabry-Pérot Interferometers zur Einzelphotonenfilterung, Diplomarbeit (Humboldt-Universität zu Berlin, 2009), cited on page 187.

[294]W. P. Grice and I. A. Walmsley, Spectral information and distinguishability in type-II down-conversion with a broadband pump, Physical Review A **56**, 1627–1634 (1997), cited on page 188.

[295]K. Wang, Quantum theory of two-photon wavepacket interference in a beam-splitter, Journal of Physics B: Atomic, Molecular and Optical Physics **39**, R293 (2006), cited on page 188.

[296]T. Gerrits et al., Spectral correlation measurements at the Hong-Ou-Mandel interference dip, Physical Review A **91**, 013830 (2015), cited on page 188.

[297]J. C. F. Matthews et al., Observing fermionic statistics with photons in arbitrary processes, Scientific Reports **3**, 1539 (2013), cited on page 193.

[298]Q. Wang, Y.-S. Zhang, Y.-F. Huang, and G.-C. Guo, Simulating the fourth-order interference phenomenon of anyons with photon pairs, The European Physical Journal D **42**, 179–182 (2007), cited on page 193.

[299]P. Groß, K.-J. Boller, and M. E. Klein, High-precision wavelength-flexible frequency division for metrology, Physical Review A **71**, 043824 (2005), cited on page 201.

[300]C. Müller, Generation of two-color polarization-entangled photon pairs in a folded sandwich configuration, Master thesis (Humboldt-Universität zu Berlin, 2015), cited on pages 208, 209.

[301]O. Dietz, Linear and non-linear properties of light, Dissertation (Humboldt-Universität zu Berlin, Berlin, 2016), https://edoc.hu-berlin.de/handle/18452/18126, cited on page 208.

[302]M. Barbieri et al., What Hong-Ou-Mandel interference says on two-photon frequency entanglement, Scientific Reports **7**, 7247 (2017), cited on page 210.

[303]L. Sansoni et al., A two-channel, spectrally degenerate polarization entangled source on chip, npj Quantum Information **3**, 5 (2017), cited on page 210.

[304]F. Steinlechner et al., A high-brightness source of polarization-entangled photons optimized for applications in free space, Optics Express **20**, 9640–9649 (2012), cited on page 210.

[305]D. P. DiVincenzo, The Physical Implementation of Quantum Computation, Fortschritte der Physik **48**, 771–783 (2000), cited on page 212.

[306]C. Santori, D. Fattal, J. Vučković, G. S. Solomon, and Y. Yamamoto, Indistinguishable photons from a single-photon device, Nature **419**, 594 (2002), cited on page 212.

[307]T. Günthner et al., Broadband indistinguishability from bright parametric downconversion in a semiconductor waveguide, Journal of Optics **17**, 125201 (2015), cited on page 212.

[308]S. Ates et al., Post-Selected Indistinguishable Photons from the Resonance Fluorescence of a Single Quantum Dot in a Microcavity, Physical Review Letters **103**, 167402 (2009), cited on page 212.

[309]Y.-M. He et al., On-demand semiconductor single-photon source with near-unity indistinguishability, Nature Nanotechnology **8**, 213–217 (2013), cited on page 212.

[310]X. Ding et al., On-Demand Single Photons with High Extraction Efficiency and Near-Unity Indistinguishability from a Resonantly Driven Quantum Dot in a Micropillar, Physical Review Letters **116**, 020401 (2016), cited on page 212.

[311]L. Schweickert et al., On-demand generation of background-free single photons from a solid-state source, Applied Physics Letters **112**, 093106 (2018), cited on page 212.

[312]X. Li, P. L. Voss, J. E. Sharping, and P. Kumar, Optical-Fiber Source of Polarization-Entangled Photons in the 1550 nm Telecom Band, Physical Review Letters **94**, 053601 (2005), cited on page 212.

[313]M. Giustina et al., Significant-Loophole-Free Test of Bell's Theorem with Entangled Photons, Physical Review Letters **115**, 250401 (2015), cited on page 212.

[314]D. Huber et al., Highly indistinguishable and strongly entangled photons from symmetric GaAs quantum dots, Nature Communications **8**, 15506 (2017), cited on pages 212, 232.

[315]A. C. Dada et al., Indistinguishable single photons with flexible electronic triggering, Optica **3**, 493–498 (2016), cited on page 212.

[316]S. Miller, Optical Fiber Telecommunications (Elsevier, 2012), cited on page 212.

[317]N. Akopian, L. Wang, A. Rastelli, O. G. Schmidt, and V. Zwiller, Hybrid semiconductor-atomic interface: slowing down single photons from a quantum dot, Nature Photonics **5**, 230 (2011), cited on page 212.

[318]N. Akopian et al., An artificial atom locked to natural atoms, (2013), arXiv:1302.2005, cited on page 212.

[319]J.-P. Jahn et al., An artificial Rb atom in a semiconductor with lifetime-limited linewidth, Physical Review B **92**, 245439 (2015), cited on page 212.

[320]L. Béguin et al., On-demand semiconductor source of 780-nm single photons with controlled temporal wave packets, Physical Review B **97**, 205304 (2018), cited on page 212.

[321]R. Trotta et al., Wavelength-tunable sources of entangled photons interfaced with atomic vapours, Nature Communications **7**, 10375 (2016), cited on page 213.

[322]C. Simon et al., Quantum Repeaters with Photon Pair Sources and Multimode Memories, Physical Review Letters **98**, 190503 (2007), cited on page 213.

[323]K. Azuma, K. Tamaki, and H.-K. Lo, All-photonic quantum repeaters, Nature Communications **6**, 6787 (2015), cited on page 213.

[324]P. Lodahl, Quantum-dot based photonic quantum networks, Quantum Science and Technology **3**, 013001 (2018), cited on page 213.

[325]A. K. Nowak et al., Deterministic and electrically tunable bright single-photon source, Nature Communications **5**, 3240 (2014), cited on page 213.

[326]H. Jayakumar et al., Deterministic Photon Pairs and Coherent Optical Control of a Single Quantum Dot, Physical Review Letters **110**, 135505 (2013), cited on page 213.

[327]I. Schwartz et al., Deterministic generation of a cluster state of entangled photons, Science **354**, 434–437 (2016), cited on page 213.

[328]D. Mayers, Unconditional Security in Quantum Cryptography, J. ACM **48**, 351–406 (2001), cited on page 213.

[329]H. Inamori, N. Lütkenhaus, and D. Mayers, Unconditional security of practical quantum key distribution, The European Physical Journal D **41**, 599 (2007), cited on page 213.

[330]D. Buterakos, E. Barnes, and S. E. Economou, Deterministic Generation of All-Photonic Quantum Repeaters from Solid-State Emitters, Physical Review X **7**, 041023 (2017), cited on page 213.

[331]A. L. Migdall, D. Branning, and S. Castelletto, Tailoring single-photon and multiphoton probabilities of a single-photon on-demand source, Physical Review A **66**, 053805 (2002), cited on page 213.

[332]L. G. Helt, A. M. Brańczyk, M. Liscidini, and M. J. Steel, Parasitic Photon-Pair Suppression via Photonic Stop-Band Engineering, Physical Review Letters **118**, 073603 (2017), cited on page 213.

[333]P. Kumar, Quantum frequency conversion, Optics Letters **15**, 1476–1478 (1990), cited on pages 213, 214, 221.

[334]Z. Y. Ou, Efficient conversion between photons and between photon and atom by stimulated emission, Physical Review A **78**, 023819 (2008), cited on page 213.

[335]J. Huang and P. Kumar, Observation of quantum frequency conversion, Physical Review Letters **68**, 2153–2156 (1992), cited on pages 214, 221.

[336]R. V. Roussev, C. Langrock, J. R. Kurz, and M. M. Fejer, Periodically poled lithium niobate waveguide sum-frequency generator for efficient single-photon detection at communication wavelengths, Optics Letters **29**, 1518–1520 (2004), cited on page 214.

[337]N. Curtz, R. Thew, C. Simon, N. Gisin, and H. Zbinden, Coherent frequency-down-conversion interface for quantum repeaters, Optics Express **18**, 22099–22104 (2010), cited on page 214.

[338]S. Zaske, A. Lenhard, and C. Becher, Efficient frequency downconversion at the single photon level from the red spectral range to the telecommunications C-band, Optics Express **19**, 12825–12836 (2011), cited on pages 213, 217–219.

[339]S. Zaske et al., Visible-to-Telecom Quantum Frequency Conversion of Light from a Single Quantum Emitter, Physical Review Letters **109**, 147404 (2012), cited on pages 213, 217, 218, 224, 229.

[340]J. S. Pelc et al., Downconversion quantum interface for a single quantum dot spin and 1550-nm single-photon channel, Optics Express **20**, 27510–27519 (2012), cited on page 213.

[341]I. Agha, S. Ates, M. Davanço, and K. Srinivasan, A chip-scale, telecommunications-band frequency conversion interface for quantum emitters, Optics Express **21**, 21628–21638 (2013), cited on page 213.

[342]P. Farrera, N. Maring, B. Albrecht, G. Heinze, and H. de Riedmatten, Nonclassical correlations between a C-band telecom photon and a stored spin-wave, Optica **3**, 1019–1024 (2016), cited on page 213.

[343]T. Walker et al., Long-Distance Single Photon Transmission from a Trapped Ion via Quantum Frequency Conversion, Physical Review Letters **120**, 203601 (2018), cited on page 213.

[344]K. De Greve et al., Quantum-dot spin-photon entanglement via frequency downconversion to telecom wavelength, Nature **491**, 421–425 (2012), cited on page 213.

[345]B. Kambs et al., Low-noise quantum frequency down-conversion of indistinguishable photons, Optics Express **24**, 22250–22260 (2016), cited on page 213.

[346]M. Bock et al., High-fidelity entanglement between a trapped ion and a telecom photon via quantum frequency conversion, Nature Communications **9**, 1998 (2018), cited on page 213.

[347]R. Ikuta et al., Polarization insensitive frequency conversion for an atom-photon entanglement distribution via a telecom network, Nature Communications **9**, 1997 (2018), cited on page 213.

[348]A. Lenhard, J. Brito, M. Bock, C. Becher, and J. Eschner, Coherence and entanglement preservation of frequency-converted heralded single photons, Optics Express **25**, 11187–11199 (2017), cited on page 213.

[349]R. Ikuta et al., Heralded single excitation of atomic ensemble via solid-state-based telecom photon detection, Optica **3**, 1279–1284 (2016), cited on pages 213, 219, 229, 230.

[350]M. Fleischhauer, S. F. Yelin, and M. D. Lukin, How to trap photons? Storing single-photon quantum states in collective atomic excitations, Optics Communications **179**, 395–410 (2000), cited on page 213.

[351]A. V. Gorshkov, A. André, M. Fleischhauer, A. S. Sørensen, and M. D. Lukin, Universal Approach to Optimal Photon Storage in Atomic Media, Physical Review Letters **98**, 123601 (2007), cited on page 213.

[352]J. Nunn et al., Mapping broadband single-photon wave packets into an atomic memory, Physical Review A **75**, 011401 (2007), cited on pages 213, 231.

[353]D. Kielpinski, J. F. Corney, and H. M. Wiseman, Quantum Optical Waveform Conversion, Physical Review Letters **106**, 130501 (2011), cited on page 213.

[354]M. Karpiński, M. Jachura, L. J. Wright, and B. J. Smith, Bandwidth manipulation of quantum light by an electro-optic time lens, Nature Photonics **11**, 53–57 (2017), cited on page 213.

[355]B. Brecht, A. Eckstein, A. Christ, H. Suche, and C. Silberhorn, From quantum pulse gate to quantum pulse shaper—engineered frequency conversion in nonlinear optical waveguides, New Journal of Physics **13**, 065029 (2011), cited on page 213.

[356]C. J. McKinstrie, L. Mejling, M. G. Raymer, and K. Rottwitt, Quantum-state-preserving optical frequency conversion and pulse reshaping by four-wave mixing, Physical Review A **85**, 053829 (2012), cited on page 213.

[357]M. T. Rakher et al., Simultaneous Wavelength Translation and Amplitude Modulation of Single Photons from a Quantum Dot, Physical Review Letters **107**, 083602 (2011), cited on page 213.

[358]R. Ikuta et al., Nonclassical two-photon interference between independent telecommunication light pulses converted by difference-frequency generation, Physical Review A **88**, 042317 (2013), cited on pages 213, 215.

[359]R. Ikuta et al., High-fidelity conversion of photonic quantum information to telecommunication wavelength with superconducting single-photon detectors, Physical Review A **87**, 010301 (2013), cited on pages 213, 215.

[360]N. Matsuda, Deterministic reshaping of single-photon spectra using cross-phase modulation, Science Advances **2**, e1501223 (2016), cited on pages 213, 215.

[361]J. Nunn et al., Enhancing Multiphoton Rates with Quantum Memories, Physical Review Letters **110**, 133601 (2013), cited on page 213.

[362]F. Bussières et al., Prospective applications of optical quantum memories, Journal of Modern Optics **60**, 1519–1537 (2013), cited on page 213.

[363]J. R. Wootton, Quantum memories and error correction, Journal of Modern Optics **59**, 1717–1738 (2012), cited on page 213.

[364]S. Bratzik, S. Abruzzo, H. Kampermann, and D. Bruß, Quantum repeaters and quantum key distribution: The impact of entanglement distillation on the secret key rate, Physical Review A **87**, 062335 (2013), cited on page 213.

[365]D. Abdelkhalek, M. Syllwasschy, N. J. Cerf, J. Fiurášek, and R. Schnabel, Efficient entanglement distillation without quantum memory, Nature Communications **7**, 11720 (2016), cited on page 213.

[366]B. Albrecht, P. Farrera, X. Fernandez-Gonzalvo, M. Cristiani, and H. de Riedmatten, A waveguide frequency converter connecting rubidium-based quantum memories to the telecom C-band, Nature Communications **5**, 3376 (2014), cited on page 213.

[367]A. V. Gorshkov, A. André, M. D. Lukin, and A. S. Sørensen, Photon storage in Λ-type optically dense atomic media. I. Cavity model, Physical Review A **76**, 033804 (2007), cited on page 213.

[368]A. V. Gorshkov, A. André, M. D. Lukin, and A. S. Sørensen, Photon storage in Λ-type optically dense atomic media. II. Free-space model, Physical Review A **76**, 033805 (2007), cited on page 213.

[369]J. Franson and T. Pittman, Nonlocality in Quantum Computing, Fortschritte der Physik **46**, 697–705 (1998), cited on page 215.

[370]T. B. Pittman, B. C. Jacobs, and J. D. Franson, Single photons on pseudo-demand from stored parametric down-conversion, Physical Review A **66**, 042303 (2002), cited on page 215.

[371]G. J. Mendoza et al., Active temporal and spatial multiplexing of photons, Optica **3**, 127–132 (2016), cited on page 215.

[372]C. Xiong et al., Active temporal multiplexing of indistinguishable heralded single photons, Nature Communications **7**, 10853 (2016), cited on page 215.

[373]Y.-W. Cho et al., Highly efficient optical quantum memory with long coherence time in cold atoms, Optica **3**, 100–107 (2016), cited on page 215.

[374]A. G. Radnaev et al., A quantum memory with telecom-wavelength conversion, Nature Physics **6**, 894 (2010), cited on pages 215, 230.

[375]X.-H. Bao et al., Efficient and long-lived quantum memory with cold atoms inside a ring cavity, Nature Physics **8**, 517 (2012), cited on page 215.

[376]D. J. Saunders et al., Cavity-Enhanced Room-Temperature Broadband Raman Memory, Physical Review Letters **116**, 090501 (2016), cited on pages 215, 230.

[377]S. E. Thomas et al., High efficiency Raman memory by suppressing radiation trapping, New Journal of Physics **19**, 063034 (2017), cited on page 215.

[378]K. T. Kaczmarek et al., High-speed noise-free optical quantum memory, Physical Review A **97**, 042316 (2018), cited on page 215.

[379]O. Katz and O. Firstenberg, Light storage for one second in room-temperature alkali vapor, Nature Communications **9**, 2074 (2018), cited on page 215.

[380]P. Kolchin, C. Belthangady, S. Du, G. Y. Yin, and S. E. Harris, Electro-Optic Modulation of Single Photons, Physical Review Letters **101**, 103601 (2008), cited on pages 215, 224.

[381]Y. Nishida, H. Miyazawa, M. Asobe, O. Tadanaga, and H. Suzuki, Direct-bonded QPM-LN ridge waveguide with high damage resistance at room temperature, Electronics Letters **39**, 609–611 (2003), cited on page 217.

[382]S. Kaspar et al., Semiconductor disk laser at 2.05 µm wavelength with <100 kHz linewidth at 1 W output power, Applied Physics Letters **100**, 031109 (2012), cited on pages 217, 221.

[383]J. M. Donohue, M. D. Mazurek, and K. J. Resch, Theory of high-efficiency sum-frequency generation for single-photon waveform conversion, Physical Review A **91**, 033809 (2015), cited on page 221.

[384]W. Liu, J. Sun, and J. Kurz, Bandwidth and tunability enhancement of wavelength conversion by quasi-phase-matching difference frequency generation, Optics Communications **216**, 239–246 (2003), cited on page 221.

[385]C. Schmidt, C. Kottke, V. Jungnickel, and R. Freund, High-speed digital-to-analog converter concepts, in Next-Generation Optical Communication: Components, Sub-Systems, and Systems VI, Vol. 10130 (2017), cited on page 226.

[386]C. Haffner et al., All-plasmonic Mach–Zehnder modulator enabling optical high-speed communication at the microscale, Nature Photonics **9**, 525 (2015), cited on page 226.

[387]A. D. Simard, B. Filion, D. Patel, D. Plant, and S. LaRochelle, Segmented silicon MZM for PAM-8 transmissions at 114 Gb/s with binary signaling, Optics Express **24**, 19467–19472 (2016), cited on page 226.

[388]M. Leifgen et al., Practical implementation and evaluation of a quantum-key-distribution scheme based on the time-frequency uncertainty, Physical Review A **92**, 042311 (2015), cited on page 226.

[389]L. Grüner-Nielsen et al., Dispersion Compensating Fibers, Optical Fiber Technology **6**, 164–180 (2000), cited on page 229.

[390]T. Matsui, K. Nakajima, and I. Sankawa, Dispersion Compensation Over All the Telecommunication Bands With Double-Cladding Photonic-Crystal Fiber, Journal of Lightwave Technology **25**, 757–762 (2007), cited on page 229.

[391]R. Ikuta et al., Wide-band quantum interface for visible-to-telecommunication wavelength conversion, Nature Communications **2**, 1544 (2011), cited on page 229.

[392]M. Peiris, K. Konthasinghe, and A. Muller, Franson Interference Generated by a Two-Level System, Physical Review Letters **118**, 030501 (2017), cited on pages 230, 232.

[393]P. J. Bustard, R. Lausten, D. G. England, and B. J. Sussman, Toward Quantum Processing in Molecules: A THz-Bandwidth Coherent Memory for Light, Physical Review Letters **111**, 083901 (2013), cited on page 231.

[394]K. A. G. Fisher et al., Storage of polarization-entangled THz-bandwidth photons in a diamond quantum memory, Physical Review A **96**, 012324 (2017), cited on page 231.

[395]D. G. England et al., Storage and Retrieval of THz-Bandwidth Single Photons Using a Room-Temperature Diamond Quantum Memory, Physical Review Letters **114**, 053602 (2015), cited on page 231.

[396]A. Lenhard et al., Single telecom photon heralding by wavelength multiplexing in an optical fiber, Applied Physics B **122**, 20 (2016), cited on page 231.

[397]N. Yamamoto and M. R. James, Zero-dynamics principle for perfect quantum memory in linear networks, New Journal of Physics **16**, 073032 (2014), cited on page 231.

[398]B. Brecht, D. V. Reddy, C. Silberhorn, and M. G. Raymer, Photon Temporal Modes: A Complete Framework for Quantum Information Science, Physical Review X **5**, 041017 (2015), cited on page 231.

[399]*Website of the joint project Q.Link.X – Building a Quantum Repeater, https://qlinkx.de/*, cited on page 236.

[400]*Quantum Technology - Webportal of the European Quantum Flagship iniative, https://qt.eu/*, cited on page 237.

[401]M. Müller et al., Quantum-Dot Single-Photon Sources for Entanglement Enhanced Interferometry, Physical Review Letters **118**, 257402 (2017), cited on page 237.

[402]E. Oelker et al., Audio-Band Frequency-Dependent Squeezing for Gravitational-Wave Detectors, Physical Review Letters **116**, 041102 (2016), cited on page 237.

[403]A. N. Boto et al., Quantum Interferometric Optical Lithography: Exploiting Entanglement to Beat the Diffraction Limit, Physical Review Letters **85**, 2733–2736 (2000), cited on page 237.

[404]E. D. Lopaeva et al., Experimental Realization of Quantum Illumination, Physical Review Letters **110**, 153603 (2013), cited on page 237.

[405]G. B. Lemos et al., Quantum imaging with undetected photons, Nature **512**, 409–412 (2014), cited on page 237.

[406] M. Wahl et al., Integrated multichannel photon timing instrument with very short dead time and high throughput, Review of Scientific Instruments **84**, 043102 (2013), cited on page 241.

[407] A. Ahlrichs, B. Sprenger, and O. Benson, Photon Counting and Timing in Quantum Optics Experiments, in *Advanced Photon Counting: Applications, Methods, Instrumentation*, edited by P. Kapusta, M. Wahl, and R. Erdmann, Springer Series on Fluorescence 15 (Springer International Publishing, Cham, 2015), pp. 319–341, cited on page 241.